Induced superconductivity in nanoassembled suspended carbon nanotube quantum dot circuits

Zur Erlangung des akademischen Grades eines

Doktors der Naturwissenschaften (Dr. rer. nat.)

von der KIT-Fakultät für Physik des
Karlsruher Instituts für Technologie (KIT)

genehmigte

Dissertation

von

M.Sc. Tim Althuon

aus Pforzheim (Baden-Württemberg)

Tag der mündlichen Prüfung: 23. Mai 2025
1. Referent: Prof. Dr. Wolfgang Wernsdorfer
2. Referent: Prof. Dr. Ralph Krupke

Abstract

A pristine suspended carbon nanotube (CNT) provides an exceptional platform for exploring long-lived quantum states and investigating a broad spectrum of condensed matter physics phenomena, such as the coupling between electronic transport and nanomechanics. A key challenge lies in the integration of the nanotube into the electrical circuit. To address this, we use the advanced nanoassembly technique, in which the CNT is mechanically transferred onto the pre-fabricated electrical circuits at the final stage, yielding ultraclean, high-quality CNT quantum circuits with precise nanotube positioning. However, high CNT-metal contact resistances previously restricted the range of possible experiments to the closed quantum dot regime. In this thesis, we could overcome this limitation by developing a novel contact improvement technique. The resulting transparent CNT-metal interface allows us to reach the open quantum dot regime, as demonstrated by measurements of Fabry-Pérot interferences. Additionally, by incorporating superconducting contacts, nanotube-based Josephson junctions could be realized with proximity-induced supercurrents higher than 3 nA. Furthermore, with two parallel Josephson junctions fabricated from the same CNT, the successful implementation of a suspended CNT superconducting quantum interference device (SQUID) could be demonstrated. The suspended CNT-SQUID enables precise magnetic flux measurements that can be modulated both by variations in the magnetic field and mechanical displacements of the CNT, which alter the SQUID area. This opens up new possibilities for a wide range of experiments, including the precise measurement of single-molecule magnetism and the investigation of optomechanical coupling within a CNT-SQUID integrated into a microwave cavity.

Zusammenfassung

Eine defektfreie, frei hängende Kohlenstoffnanoröhre (CNT) bietet eine herausragende Plattform, um langlebige Quantenzustände zu erforschen und ein breites Spektrum von Phänomenen der Festkörperphysik zu untersuchen, wie beispielsweise die Kopplung zwischen elektronischem Transport und Nanomechanik. Eine der zentralen Herausforderungen besteht in der Integration der Nanoröhre in den elektrischen Schaltkreis. Zur Lösung dieses Problems verwenden wir die fortschrittliche Nanoassemblierungstechnik, bei der das CNT im letzten Schritt mechanisch auf die vorgefertigten Schaltkreise transferiert wird. Dieses Verfahren resultiert in extrem sauberen, hochqualitativen CNT-Quantenschaltkreisen, wobei das CNT sehr präzise im Schaltkreis platziert werden kann. Jedoch beschränkten hohe CNT-Metall-Kontaktwiderstände bisher den Bereich möglicher Experimente auf das geschlossene Quantenpunktregime. In dieser Dissertation überwinden wir diese Einschränkung durch die Entwicklung einer neuartigen Kontaktverbesserungstechnik. Der resultierende transparente CNT-Metall-Kontakt ermöglicht es, das offene Quantenpunktregime zu erreichen, was durch Messungen von Fabry-Pérot-Interferenzen gezeigt wird. Darüber hinaus konnten durch die Integration von supraleitenden Kontakten CNT-basierte Josephson-Kontakte realisiert werden, die induzierte Supraströme größer als 3 nA aufweisen. Zudem konnte die erfolgreiche Implementierung eines supraleitenden Quanteninterferometers (SQUID) mit zwei parallelen Josephson-Kontakten aus demselben CNT demonstriert werden. Das frei hängende CNT-SQUID ermöglicht präzise Messungen des magnetischen Flusses, der sowohl durch Variationen des Magnetfeldes als auch durch mechanische Auslenkung des CNTs und damit einhergehender Veränderung der SQUID-Fläche moduliert werden kann. Dies eröffnet neue Möglichkeiten für eine Vielzahl von Experimenten, einschließlich der präzisen Messung von Einzelmolekülmagneten und der Untersuchung von optomechanischer Kopplung innerhalb eines CNT-SQUIDs, das in einen Mikrowellenresonator integriert ist.

List of Acronyms

ABS Andreev Bound States
AC Alternating Current
CNT Carbon Nanotube
CPR Current-Phase Relation
CVD Chemical Vapor Deposition
DC Direct Current
DI De-Ionized
DMSO Dimethyl sulfoxide
DOS Density of States
ESD Electrostatic Discharge
HAADF High-Angle Annular Dark Field
IPA Iso-propyl-alcohole
LSM Longitudinal Stretching Modes
MARs Multiple Andreev Reflections
NEMS Nanoelectromechanical System
NEP N-Ethyl-2-pyrrolidone
PCB Printed Circuit Board
PMMA Polymethyl methacrylate
RBMs Radial Breathing Modes
RCSJ Resistively-Capacitively Shunted Junction
RSJ Resistively Shunted Junction
RF Radio Frequency
RIE Reactive Ion Etching
RTA Radiative Thermal Annealing
SEM Scanning Electron Microscope/Microscopy
SIS Superconductor-Insulator-Superconductor
SMM Single-Molecule Magnet
SN Superconductor-Normal conductor
SNS Superconductor-Normal conductor-Superconductor
SQUID Superconducting QUantum Interference Device
SU(2) Special Unitary group of degree 2
SU(4) Special Unitary group of degree 4
TEM Transmission Electron Microscope
TMAH Tetramethylammonium hydroxide
VLS Vapor-Liquid-Solid
VSS Vapor-Solid-Solid

Contents

1. Introduction

The year 2025 unfolds during a series of political crises, as the world finds itself in a period of transformation. Following the world's hottest year on record [1], climate change remains a pressing issue. Carbon and carbon emissions are strongly linked to negative environmental impacts. Despite these commonly negative associations with the word carbon, carbon itself is a highly versatile material, widely used in various technological applications, and plays a crucial role in studying fundamental physics phenomena.

Carbon is the sixth element in the periodic system of elements and comes with four valence electrons, which are available for bonds with neighboring carbon atoms. The coupling between different atomic orbitals leads to hybridization, a process related to the mixing of the formerly isolated atomic orbitals (for carbon $2s$ and $2p_x$, $2p_y$ and $2p_z$ orbitals). The hybridization results in a rich plethora of carbon allotropes, which, despite being made of the same element, possess different structural and physical properties depending on the atomic orbitals involved in the hybridization. For example, the exceptional mechanical properties of the 3D material diamond, and its electrical insulating properties, can be explained by tetragonal strong covalent σ-bonds, which can form if one s and the three p orbitals mix to a sp^3-orbital. On the other hand, trigonal σ-bonds arise from sp^2-hybridization, whereas the remaining fourth electron from the p_z-orbital can form delocalized out-of-plane π-bonds, giving rise to the particular electronic properties of the 2D material graphene.

Carbon nanotubes (CNTs)

This work focuses on carbon nanotubes (CNTs), which can be conceived as hollow cylinders made from a rolled-up graphene sheet [2]. In contrast to graphene, electrons in CNTs are confined in the lateral dimension, and thus CNTs can be considered as one-dimensional (1D) materials with diameters on the nanometer scale and length scales in the micrometer range or even longer [3]. Apart from additional boundary conditions along the circumference, CNTs inherit the particular electronic and mechanical properties of graphene.

CNTs have a low mass density of $\rho = 1350\,\mathrm{kg/m^3}$ [4], a high Young's modulus of $\sim 1\,\mathrm{TPa}$ [5, 6] and a high tensile strength of $30\,\mathrm{GPa}$ to $45\,\mathrm{GPa}$ [7, 8], which is more than ten times higher than the highest values reported for steel of $\lesssim 3\,\mathrm{GPa}$ [9]. These properties make CNTs particularly attractive for building nanomechanical resonators. In contrast to other nanomechanical resonators fabricated in a top-down approach with quality factors limited by surface effects [10], potentially defect-free single-walled CNTs are ideal materials for nanoelectromechanical systems (NEMS) with a high quality factor ($Q \sim 10^5$ [11, 4]).

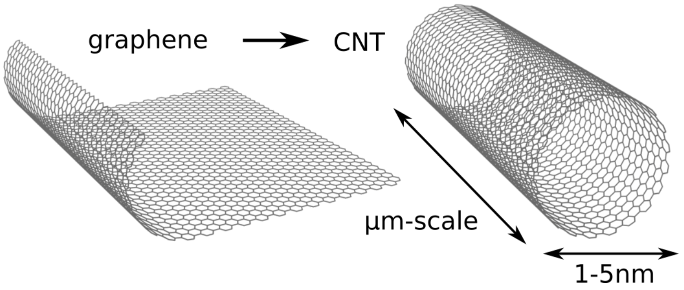

Figure 1.1.: Structure of a CNT. A CNT can be conceived as a rolled-up graphene sheet with nanometer diameter and micrometer length scale.

Owing to Schottky barriers at the CNT contact metal interfaces [12], charges are also confined along the length of the CNT. The confinement in all three dimensions allows for the realization of quantum dots in suspended CNTs and the control of the number of charge carriers in the CNT. In CNT NEMS with high quality factors, strong coupling between single-electron tunneling and nanomechanical motion can be reached [11, 13], giving rise to the detection of mechanical motion by probing the conductance through the CNT. The electrical readout of mechanical motion opens a wide range of applications such as ultrasensitive mass sensing [14, 15, 16] or the readout of a spin coupled to mechanical oscillations [17, 18, 19, 20].

Single-molecule magnets as spin qubits

The spin degree of freedom is a natural candidate for a qubit, the basic building block in a future quantum computer. In our research group, we are interested in studying single-molecule magnets (SMMs) as a promising candidate for spin qubits. An SMM is a molecule with a magnetic core (e.g. a transition metal ion) surrounded by a shell of organic ligands. The anisotropic electron shell of the magnetic core in the molecule together with the chemically engineered ligands induce magnetic anisotropy, which is a crucial requirement for a magnet.

In contrast to other qubit systems, such as superconducting qubits, SMMs are prepared by organic synthesis in a bottom-up approach with high reproducibility and the option of engineering their properties by substituting ligands or magnetic ions. This includes the giant electronic spin of the magnetic molecule, which can be designed up to one to two orders of magnitude larger than the spin of a single electron. A particular candidate that has been investigated with respect to its potential for quantum computing is bis(phthalocyaninato)terbium(III) ($TbPc_2$) [21, 22]. It features a high uniaxial anisotropy with a magnetic ground state of $J = 6$ [20]. For quantum computing, it is beneficial to use the more isolated nuclear spin states of the Tb^{3+}-ion which are coupled to the electronic spin via hyperfine interaction. For the nuclear spin states, relaxation times T_1 on the order of tens of seconds and decoherence times $T_2^* = 64\,\mu s$ have been reported [21].

A key challenge is the electrical readout of the electronic spin state of the molecule. Single-molecule magnets are nanoscale objects which in principle allows a close packing of the

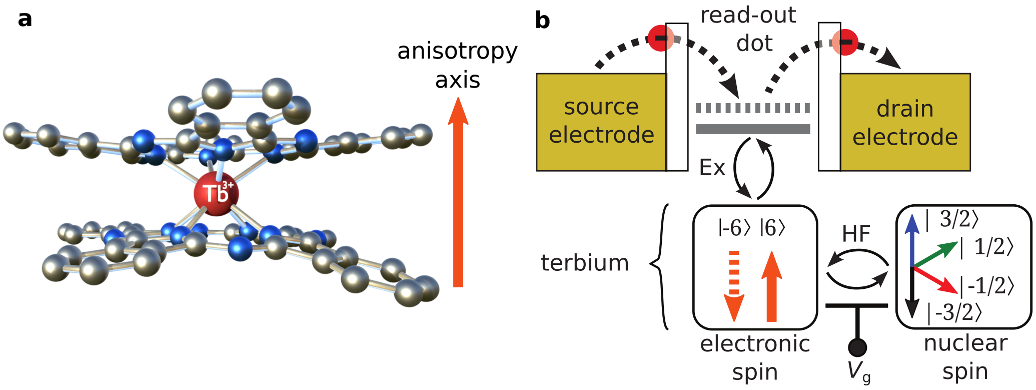

Figure 1.2.: TbPc$_2$-molecule. **a** Sketch of the molecule (blue: nitrogen, grey: carbon and red: terbium atom, diameter: ~ 1 nm) with anisotropy axis leading to a magnetization axis for the electronic spin. **b** Direct readout by connecting the molecule to gold nanojunctions (figure from [21]). The molecule forms a quantum dot and the transport couples to the electronic spin, which is coupled to the nuclear spin via hyperfine interaction (HF). For the indirect readout, the quantum dot is formed in the CNT and the molecule grafted onto the CNT.

qubits. However, due to their small size, the electrical connectivity of the molecules and the individual electrical control remain challenging.

Two different techniques have been proposed: a direct and an indirect coupling scheme [23]. The direct coupling scheme exploits the electrical conductivity of the ligands and the coupling between the giant electronic spin of the SMM and the electronic transport through the ligand. For instance, coherent control of nuclear spin states has been demonstrated using a quantum dot directly formed in an SMM embedded in a gold nanojunction [21]. The indirect coupling scheme relies on grafting an SMM onto a conductor with a diameter comparable to the SMM and the transport through this conductor couples to the giant electronic spin of the SMM.

Readout of molecular spin states using CNTs

Ideal candidates for the indirect coupling scheme are carbon nanotubes which can be fabricated potentially defect-free, show ballistic transport (i.e. without scattering) [24] and exhibit diameters comparable to the diameter of SMMs. For example, by grafting SMMs on a CNT quantum dot on a silicon substrate, the electronic transport through the CNT could be influenced by the orientation of the molecular magnetic moments, which induce a magnetoresistance in the CNT. With this technique a supramolecular spin valve could be demonstrated (cf. figure 1.3a) [25, 26, 27].

In general, when the CNT is placed directly on the substrate, charge noise represents a major source of decoherence, which can be significantly reduced by suspending the CNT. A second major source of decoherence is the spin-phonon coupling. In contrast to a CNT on a substrate, a suspended CNT forms a nanomechanical resonator with a lower, discrete phononic density of states, thereby reducing the phonon-induced relaxation of molecular spin states. Mechanical resonances with high quality factors in CNT NEMS can also be used to couple to molecular magnetic moments. By applying a magnetic field that is not parallel to the easy axis of the SMM, a torque is induced which can shift the resonance frequency as proposed in [18].

Beyond that, the well-controlled phononic environment in such a resonator also allows for a readout of molecular spin states via the coupling between the giant electronic spin of the SMM and phonons inside the CNT resonator. One of the most fundamental principles in physics is the conservation of total angular momentum which has been demonstrated in the Einstein-de-Haas experiment where a freely suspended body will start to rotate when it is magnetized [28]. For SMMs, a change between two different spin states (magnetization reversal) underlies the conservation of angular momentum, which results in the emission of a phonon carrying the difference in angular momentum (cf. figure 1.3b) [20, 17]. It could be demonstrated in [19] that the reversal of the magnetization of a $TbPc_2$-molecule strongly couples to longitudinal stretching modes of the CNT NEMS.

DC Superconducting quantum interference devices (SQUIDs) as magnetometers

The focus of this PhD project is on an alternative approach using a DC-SQUID (Direct Current Superconducting Quantum Interference Device). A DC-SQUID is a highly sensitive magnetometer that provides a direct way to read out extremely weak changes in the magnetic field, which could be induced by single-molecule magnets. It consists of a superconducting loop intersected by two parallel so-called Josephson junctions, which can be realized by embedding a thin insulator, a superconducting constriction or a normal conductor between two superconductors (cf. figure 1.3c).

A SQUID can be considered as the superconducting analogue of the double slit experiment, where electromagnetic waves from a coherent light source pass two parallel slits and interfere at a distant screen. In the case of a SQUID, magnetic flux applied perpendicular to the SQUID loop induces a change in the macroscopic superconducting phase between the supercurrents passing the two parallel Josephson junctions. The phase difference results in an interference pattern in the maximum supercurrent. The period of the current interferences is determined by the flux quantum $\Phi_0 = 2 \times 10^{-15}$ Vs, giving rise to the detection of tiny flux changes due to the low value of Φ_0.

The detection of the magnetization reversal of a single-molecule magnet with a SQUID requires a large flux coupling, i.e. the magnetic field of the SMM has to couple efficiently to the flux penetrating the SQUID loop. This flux coupling can be increased if the molecule is placed at a constriction of comparable diameter within the SQUID loop, which can be achieved by using a CNT as the Josephson junction in a so-called CNT-SQUID (cf. figure 1.3c) [31, 32].

In this PhD project, one of the main objectives was to build a suspended CNT-SQUID with the potential to detect magnetization reversal of SMMs. Due to the suspended nature of the CNT, the SMM is decoupled from the substrate, which reduces charge and phonon noise and should increase the decoherence time of the spin states. The applications of such a device with a suspended CNT are not limited to a direct readout of magnetization

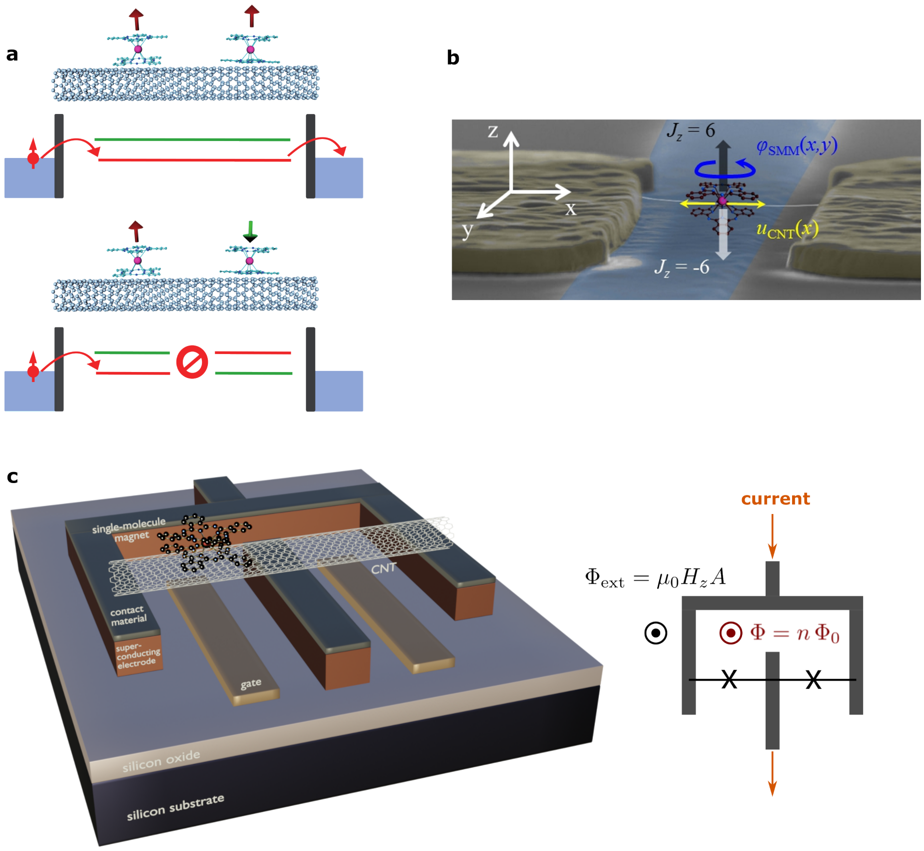

Figure 1.3.: Overview of readout schemes of magnetization reversal using CNT platforms. a Molecular spin valve (figure from [29]). Upper: Parallel orientation of the molecular spins. The energy levels inside the CNT with identical electron spin are aligned over the entire CNT quantum dot (valve opened). Lower: Antiparallel orientation. The energy levels of identical spins in the CNT are reversed, leading to a barrier in electronic transport with reduced conductance (valve closed). **b** Coupling magnetization reversal ($J_z = 6 \rightarrow J_z = -6$) to mechanical motion via conservation of angular momentum. The coupling to mechanical modes depends on the magnetization axis with respect to the CNT axis. In the perpendicular orientation, a coupling to longitudinal stretching modes is expected (figure from [30]). **c** Sketch of a DC CNT-SQUID. The current splits and passes two Josephson junctions (crosses in right schematics) realized by a single CNT and the two currents interfere after the junctions before leaving the SQUID.

reversal via the SQUID. The mechanical degree of freedom allows for a combination of the direct readout with the study of the coupling between molecular spins and mechanical modes of a CNT NEMS similar to [19] and to envisage more complex experiments.

Although SMMs have not been grafted on CNTs in this thesis, already the CNT-SQUID implemented as an NEMS is a very interesting platform by itself. This platform gives rise to an investigation of the interplay between superconductivity and nanomechanical motion in the suspended CNT which could be exploited to observe the Josephson force [33] or to cool the mechanical resonator [34].

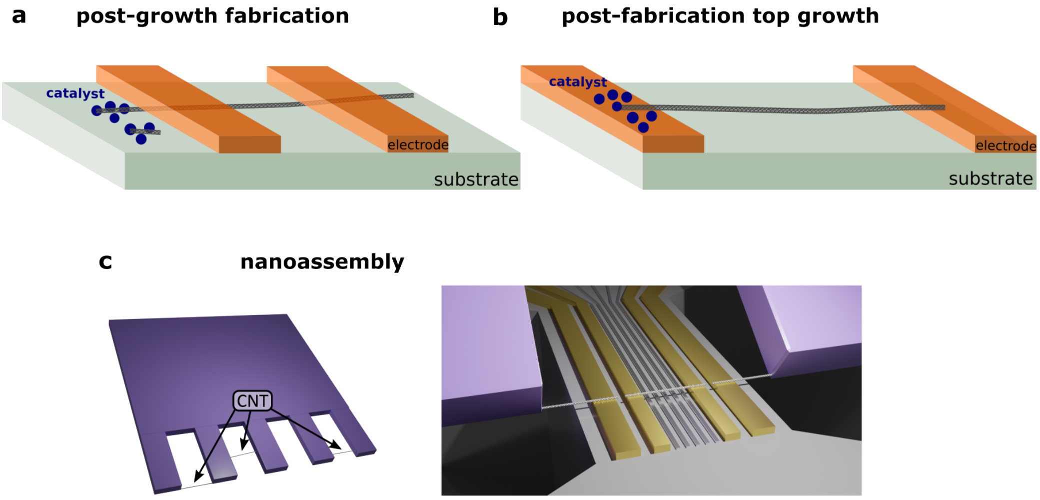

Figure 1.4.: CNT integration techniques. **a** Post-growth fabrication. CNTs are grown on a substrate and electrodes patterned afterwards. **b** Post-fabrication top growth. CNTs are grown on the electrodes. **c** Nanoassembly technique. CNTs are grown on a separate cantilever chip (left) and then integrated into electrical circuits (right).

Integration of CNTs into electrical circuits

To build a functional suspended CNT-SQUID we have to address the fundamental question of how to produce and integrate a CNT into an electrical circuit. Since the discovery of CNTs in 1991 [2], several CNT production techniques have been developed. A method of producing CNTs is their growth from the gas phase using carbon precursors and catalysts at elevated temperatures of 800-900 °C in a process called chemical vapor deposition (CVD).

The techniques of CNT integration can be divided into three classes (cf. figure 1.4). In the first technique, post-growth fabrication [35], CNTs are typically CVD grown or dispersed on a substrate and electrical contacts are established afterwards. This method has the advantage of producing transparent CNT metal contacts because the hot metal is evaporated on top of the CNT. However, the exposure to solvents during the fabrication of the electrodes can lead to contamination of the CNT and a suspension of CNTs can only be achieved by etching the substrate.

In contrast to the method of post-growth fabrication, the post-fabrication top growth (or short top growth) [36] reverses the fabrication order. Here, the chip containing the electrical circuits (circuit chip) is fabricated first and the CNTs are grown in a last step from catalyst islands on the circuit chip. This technique can produce suspended CNTs and yields good CNT metal contacts and is a clean method because the CNTs are not exposed to organic solvents. However, the random growth process leads to a low yield of single suspended CNTs across a desired junction, and the high growth temperature restricts the choice of electrode materials.

In contrast to the methods described above, we use a technique called nanoassembly [37]. Similarly to post-fabrication top growth, we integrate the CNT in the last step. However, instead of growing them on the circuit chip, they are grown on a separate chip ("cantilever chip") that allows for a mechanical transfer of the CNTs onto the circuit chip. With nanoassembly, which is a very controlled integration technique, CNTs can be precisely transferred to the desired position, giving rise for very complex device geometries. Beyond that, the properties of the CNT can be analyzed before the transfer, resulting in potentially high quality CNT devices. On the other hand, the deterministic integration of CNTs is time-consuming, but it allows for automatization of device fabrication with respect to industrial implementations. Although this technique can be performed at room temperature and does not impose constraints on the circuit materials, it has one major drawback, high CNT metal contact resistances. Overcoming this fundamental problem is crucial for the realization of SQUIDs with the nanoassembly technique and was one of the main challenges that was addressed in this PhD.

Outline

This work focuses on the integration of CNTs into electrical circuits with our custom nanoassembly technique. The development of CNT metal contact improvement techniques allows us to reach highly transparent contacts, as demonstrated by reaching the open quantum dot regime [37]. Having reached this milestone, using superconducting electrodes, we could build and investigate superconducting CNT junctions such as SQUIDs. This thesis aims to provide a detailed description of the nanoassembly technique including the fabrication and the improvement techniques and provides a profound analysis of the electronic transport measured at cryogenic temperatures.

This work is structured as follows. Chapter 2 presents the theoretical background regarding the structure, electronic and mechanical properties of carbon nanotubes in the normal conducting state and under the influence of proximity-induced superconductivity. We also address the theory behind possible experiments that can be performed in CNT-SQUIDs. The growth of CNTs with chemical vapor deposition and the detailed analysis of their properties are presented in chapter 3. Chapter 4 reviews the circuit chip design and discusses the nanofabrication process. Having investigated both the growth of CNTs and the fabrication of the circuit chip, chapter 5 focuses on the transfer of the CNTs into the electrical circuits. We explain our custom nanoassembly technique, discuss the optimizations to reduce the CNT metal contact resistance and provide a room temperature analysis of our results. Low temperature electronic transport measurements of CNT devices will be discussed in chapter 6, including normal conducting devices and devices with proximity-induced superconductivity. Finally, chapter 7 concludes the work providing a summary and discussion of the results and an outlook for future experiments.

2. Theoretical background

This section provides the theoretical foundation of the thesis. In the first subsection, the general physical properties of CNTs are introduced before discussing electronic transport in suspended CNT quantum dots in the second subsection. In the third subsection, the theory behind nanomechanics in suspended CNTs is presented, and the coupling to electronic transport. The background behind superconducting CNT-SQUIDs and its application for detecting molecular spins are addressed in the fourth subsection. Lastly, an outlook is provided on the coupling between nanomechanics and superconducting transport in suspended CNTs.

2.1. Physical properties of CNTs

In the following, we will address the structural, electronic and phononic properties of CNTs and start with the sp^2-hybridized material graphene before linking it to CNTs.

2.1.1. Geometric structure of CNTs

Graphene consists of an atomic monolayer of carbon and due to the trigonal arrangement of the σ-bonds in-plane, a planar 2D material with a honeycomb lattice is formed (cf. figure 2.1). It has two atoms per unit cell and is spanned by the unit lattice vectors [38]

$$\mathbf{a}_1 = a \begin{pmatrix} \sqrt{3}/2 \\ 1/2 \end{pmatrix} \qquad \mathbf{a}_2 = a \begin{pmatrix} \sqrt{3}/2 \\ -1/2 \end{pmatrix} \tag{2.1}$$

with $a = \sqrt{3} a_{\mathrm{C-C}}$ and the carbon-carbon bond length of $a_{\mathrm{C-C}} = 0.142\,\mathrm{nm}$. Any lattice vector $\mathbf{C}$ can be constructed as a superposition of these unit lattice vectors

$$\mathbf{C} = n \cdot \mathbf{a}_1 + m \cdot \mathbf{a}_2 \qquad n, m \in \mathbb{Z}. \tag{2.2}$$

A carbon nanotube can be conceived as a rolled-up graphene sheet forming a hollow cylinder with a nanometer diameter, while the length is typically on the order of micrometers. In this case, $\mathbf{C}$ can be used to describe the direction along which the sheet is rolled up and is called a chiral vector with $|\mathbf{C}|$ corresponding to the circumference of the CNT.

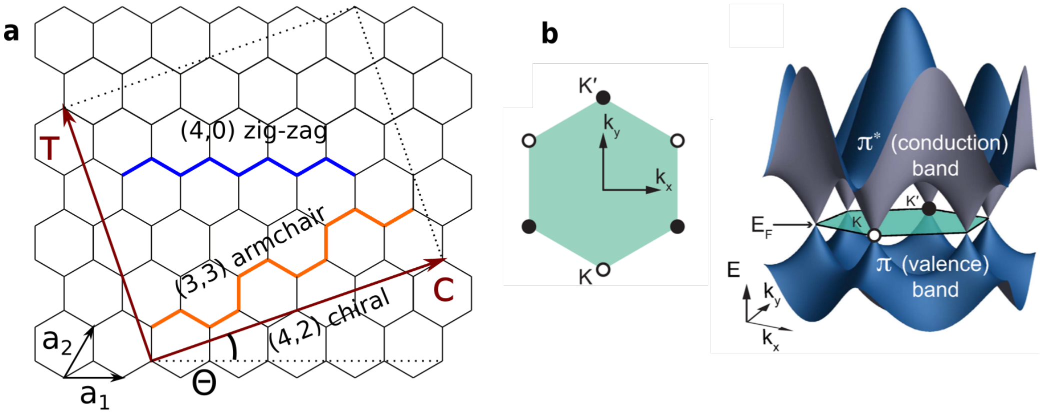

Figure 2.1.: Geometric and electronic structure of graphene. **a** Geometric structure of graphene with unit lattice vectors $\mathbf{a}_1$, $\mathbf{a}_2$. Different directions for chiral vectors are shown in blue, orange and brown. The unit cell of a (4,2) CNT with chiral vector **C**, translation vector **T** and chiral angle Θ is shown. **b** Brillouin zone of graphene with K and K' labelling and the band structure of the π/π^*-band (subfigure from [38]).

The diameter of a CNT can be calculated as $d_{\text{CNT}} = |\mathbf{C}|/\pi$. We can further define a chiral angle Θ as the angle between $\mathbf{a}_1$ and **C**, given by [38]

$$\tan(\Theta) = \frac{\sqrt{3}m}{2n+m}, \qquad 0 \leq |\Theta| \leq 30^\circ. \tag{2.3}$$

Depending on the chiral indices n and m, the chiral vector can point in different lattice directions, and different kinds of CNTs can be classified based on their spatial symmetry. If $n = m$, a CNT is called "armchair" and if $n = 0$ or $m = 0$, the chiral vector follows only one lattice vector resembling a zig-zag line and the CNT is called "zig-zag". If the chiral vector points in any other direction, the CNT is simply called "chiral" due to the lack of symmetries. The CNTs described so far are single-walled carbon nanotubes, but there are also multi-walled CNTs consisting of concentric shells of single-walled carbon nanotubes. Although CNTs can be isolated, it is also possible that CNTs attach to each other and form ropes of CNTs, which are called "bundles". Each conduction channel of another CNT close by will perturb the electronic properties, and therefore, we will only target single-walled CNTs in this thesis.

2.1.2. Electronic properties of CNTs

Electronic properties of graphene

For the derivation of the electronic properties of CNTs, it is again intuitive to start with graphene. Graphene has three sp^2-orbitals, which can hybridize across neighboring atoms, leading to the formation of two bands: a bonding, occupied σ-band with low energy and an anti-bonding, unoccupied σ^*-band higher in energy [38]. The σ-band is located well below the Fermi energy as a result of the strong covalent bond strength, and therefore it is permanently occupied with three electrons per atom and does not participate in electronic transport. The remaining fourth valence electron in the out-of-plane p_z-orbital is odd under z-inversion and decoupled from the σ-band for symmetry reasons. It forms π-bonds to neighboring atoms and leads to the formation of a bonding π-band and an anti-bonding π^*-band which touch at the Fermi level and determine the electronic transport (cf. figure 2.1b).

In $\mathbf{k}$-space, graphene has a hexagonal Brillouin zone with six corners. Due to the two atoms in the unit cell, only three of these corners can be connected with a reciprocal lattice vector, which correspond to equivalent electronic states due to Bloch's theorem [38]. These points are labeled with K, while the other three corners are denoted with K'. The electronic states are degenerate at K and K' and form two valleys around K and K'. For this reason, K and K' are also called valley quantum numbers.

The band structure of the π/π^*-band can be calculated from a tight-binding model and yields in the limit of nearest and next-nearest neighbor interaction with hopping energies of t and t', respectively [39] (cf. figure 2.1b)

$$E(\mathbf{k}) = \pm t\sqrt{3 + f(\mathbf{k})} - t' f(\mathbf{k}) \tag{2.4}$$

$$\text{with} \quad f(\mathbf{k}) = 2\cos(\sqrt{3}k_y a) + 4\cos\left(\frac{\sqrt{3}k_y a}{2}\right)\cos\left(\frac{3k_x a}{2}\right). \tag{2.5}$$

This dispersion relation can be expanded close to the $\mathbf{K}(\mathbf{K'})$ points ($\mathbf{k} = \mathbf{K} + \mathbf{q}$) with the momentum $\mathbf{q}$ measured relative to the $\mathbf{K}(\mathbf{K'})$ points and $|\mathbf{q}| \ll |\mathbf{K}|$. Considering first neighbor interaction only, this results in the following linear dispersion relation

$$E_\pm(\mathbf{q}) \approx \hbar v_\mathrm{F}|\mathbf{q}| + \mathcal{O}[(q/K)^2] \tag{2.6}$$

with the Fermi velocity $v_\mathrm{F} = 3ta/2 \approx 8 \times 10^5\,\mathrm{m/s}$. Since this linear dispersion relation is analogous to massless Dirac fermions, the $K(K')$ points, where the occupied π- and unoccupied π^*-bands touch, are called Dirac points. Graphene can therefore be considered as a semi-metal with a Fermi surface comprising six points.

From graphene to CNTs - the zone-folding approximation

For CNTs additional periodic boundary conditions arise along the circumferential direction due to their cylindrical shape. This has implications on the phase of the wave function and leads to a quantization of $\mathbf{k}$ around the circumference [40]

$$\Psi_\mathbf{k}(\mathbf{r} + \mathbf{C}) = \Psi_\mathbf{k}(\mathbf{r})e^{i\mathbf{k}\cdot\mathbf{C}} = \Psi_\mathbf{k}(\mathbf{r}). \tag{2.7}$$

This equation shows, that only wavevectors with

$$\mathbf{k} \cdot \mathbf{C} = k_\perp \pi d = 2\pi i, \qquad i \in \mathbb{Z} \tag{2.8}$$

are allowed along the circumferential direction. The diameter of a CNT is much larger than the spacing between carbon atoms, and therefore, rolling up the 2D graphene sheet

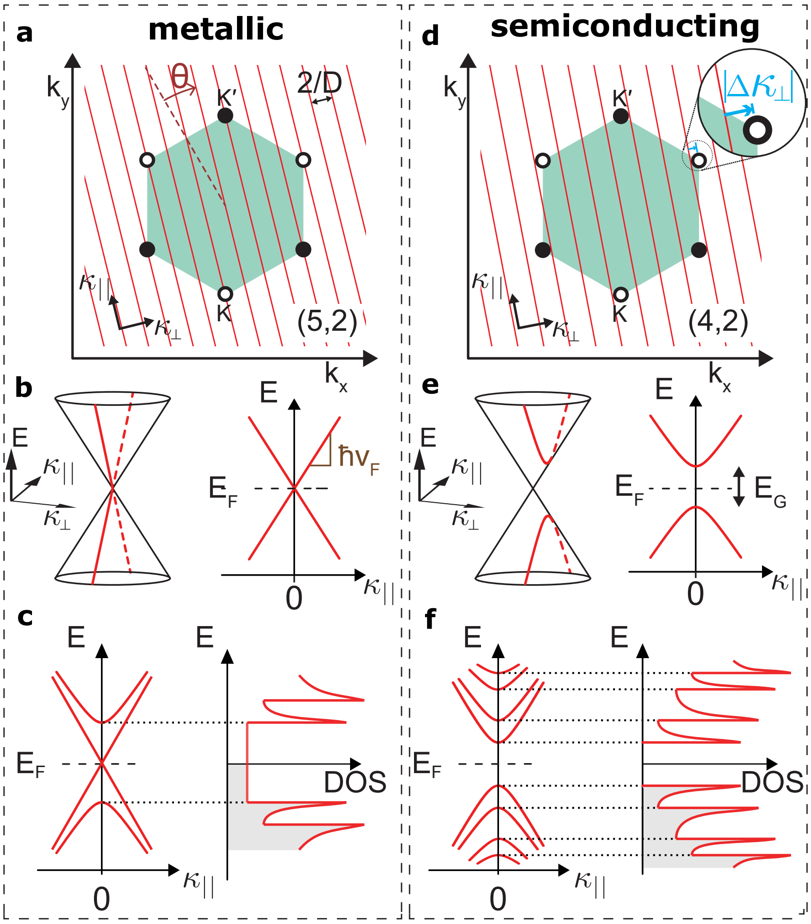

Figure 2.2.: Zone-folding approximation for metallic (left) and semiconducting CNTs (right). a Graphene Brillouin zone with superimposed quantization lines along $\mathbf{k}_\perp$ and chiral angle Θ. For a (5,2) CNT, the quantization lines hit the Dirac cones and the CNT is metallic. **b** A Dirac cone is shown with linear dispersion for one subband. **c** Density of states (DOS) for more than one subband, grey: occupied states. There is a finite DOS at E_F characteristic for a metal. **d,e** If the quantization lines do not intersect the Dirac points, the band gap is determined by the minimum deviation $|\Delta k_\perp|$. **f** For the semiconducting CNT the DOS around E_F is zero. Subfigures a,b,d,e from [38], subfigures c,f inspired by [41].

to a 1D CNT should leave its band structure along the CNT ($\mathbf{k}_{||}$) largely unperturbed if the CNT is long enough (i.e. in units of the translation vector $\mathbf{T}$). The resulting band structure can therefore be considered as a superposition of graphene electronic bands with quantization along the CNT's circumference (zone-folding approximation).

In the first Brillouin zone, the allowed **k**-vectors can be illustrated by a series of parallel quantization lines with spacing $2/d$ (as becomes apparent from equation 2.8) with an angle of $\pi/3 + \Theta$ from the k_x-axis [38]. Each line corresponds to a sub-band of a specific $k_\perp$. The minimum separation of these quantization lines from the Dirac points determines the band gap of the CNT. A band gap of zero occurs, when at least one quantization line crosses a Dirac point, leading to a metallic CNT with linear dispersion of $E(k_{||})$ in the vicinity of the Dirac points. This is the case if $n - m = 3i,\ i \in \mathbb{Z}$, and therefore, for a third of all chiralities and, in particular, for all armchair CNTs with $\Theta = \pi/6$ and $i = 0$.

If the lines do not cross the Dirac points, the band gap is determined by the minimum separation $|\Delta k_\perp|$ from the Dirac points [38]

$$E_\mathrm{G} = 2\hbar v_\mathrm{F}|\Delta k_\perp| = 4\hbar v_\mathrm{F}/3d \approx 700\,\mathrm{meV}/d[\mathrm{nm}]. \tag{2.9}$$

This results in semiconducting CNTs with a hyperbolic dispersion

$$E_\pm(k_\parallel) = \pm\sqrt{\hbar^2 v_\mathrm{F}^2 k_\parallel^2 + E_\mathrm{G}^2/4}. \tag{2.10}$$

For clarity, only the subband closest to the Fermi level is drawn in figure 2.2b,e, while the total number of subbands is equal to the number of carbon atoms in the CNT unit cell (spanned up by **C** and **T**). More subbands are shown in figure 2.2c,f, including the density of states (DOS). The DOS is a measure of the number of available states per energy interval, and in the 1D case of a CNT, the DOS diverges close to the band extrema with a $1/\sqrt{E}$ dependence. This results in spikes in the DOS, the so-called van-Hove singularities (figure 2.2c,f), whereas for other energies the DOS is rather low. Although electronic transport measurements are usually performed in a window of a few meV around the Fermi level and only the energy band close to the Fermi level participates, this has large impacts on optical transitions in CNTs occurring usually at higher energy. These are more likely to occur if the incident photon energy matches the energy difference between two van-Hove singularities. Therefore, the intensity of the optical transitions reflects the DOS, and thus yields direct information on the underlying CNT band structure.

Deviations from the zone-folding approximation

The zone-folding approximation is based on an unperturbed graphene band structure along the CNT. However, this assumption represents a strong simplification. In practice, there are several deviations leading to finite energy gaps, also for CNTs that are considered metallic CNTs according to the zone-folding approximation [38]. Here, we will only discuss the structural origins arising from curvature and strain, leading to narrow energy gaps at the Fermi level.

The curvature of the CNT results in different lengths of C-C bonds in the axial and circumferential direction and induces an angle between neighboring p_z-orbitals that are not aligned in the direction of the CNT axis. Breaking of the planar symmetry gives rise to the mixing of the σ- and π-states and partial sp^3-character [40]. All these effects break the equivalence of the three directions of the σ-bonds and shift the Dirac points away from K and K', which leads to a curvature-induced gap, depending on the chiral angle Θ [38]

$$E_\mathrm{G}^\mathrm{cv} = \frac{50\,\mathrm{meV}}{d^2[\mathrm{nm}]}\cos(3\Theta). \tag{2.11}$$

A close look to equation 2.11 reveals that this band gap is only zero for $\Theta = 30°$, and therefore, armchair CNTs are the only true metallic CNTs when taking curvature effects into account. Strain has similar effects on breaking the equivalence of the three σ-bonds and can induce a band gap of comparable magnitude [38].

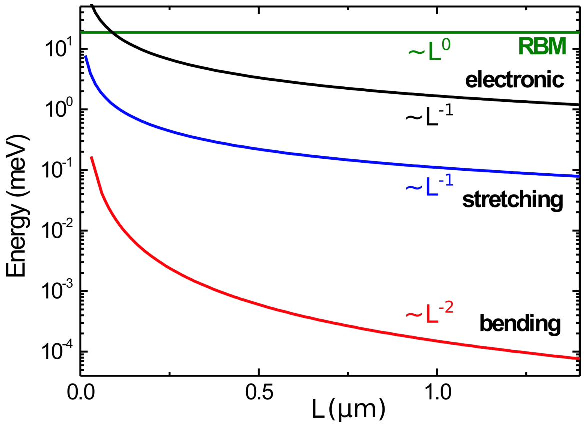

Figure 2.3.: Nanomechanical modes in CNTs. Common low-energy mechanical modes in suspended CNTs and the quantum level spacing with their dependence on the CNT suspension length (calculated for a 1.4 nm diameter CNT, figure from [43])

2.1.3. Phononic properties of CNTs

While the phononic structure of 2D graphene is rather simple with 2 atoms per unit cell and therefore comprises 6 phonon modes (3 optical, 3 acoustic), the situation for CNTs is more complex. First, similar to the electronic DOS of a 1D conductor, the phononic DOS exhibits van-Hove singularities emerging as spikes in the DOS. Second, there exists a significantly higher amount of phonon branches, e.g. for a (10,10) CNT a number as high as 66 phonon branches is expected [42]. In the following, we will quickly review the main phononic modes relevant in the frame of this thesis (cf. figure 2.3).

A CNT can be modeled as a doubly clamped beam and exhibits bending modes, which are transverse modes with polarization perpendicular to the CNT axis. These modes can be excited easily (e.g. by capacitive coupling to a gate) and are the modes that are studied in the nanomechanical experiments with typical frequencies of 50-500 MHz depending on the length of the CNT. These modes are discussed in detail in section 2.3. Longitudinal stretching modes (LSM) are acoustic modes with polarization along the axis of the CNT and thus far higher in frequency (10-100 GHz). They are typically harder to excite, but can be coupled to electron tunneling onto the CNT [43]. Finally, we also address the radial breathing mode, an optical phonon mode in the THz-range, that only occurs in CNTs due to their cylindrical shape and refers to the coherent oscillation of all carbon atoms along the radius of the CNTs (like a CNT breathing). This mode does not depend on the length of the CNT but on the diameter and is commonly used in Raman spectroscopy for the diameter estimation of CNTs.

2.2. Electronic transport in CNTs

Until now, we have only considered free CNTs of infinite length. In order to build devices with CNTs, they have to be integrated into electrical circuits. This inevitably leads to new boundary conditions at the CNT metal contact and opens a unique platform for studying quantum effects in CNTs, which will be discussed in the following.

2.2.1. Electronic transport in 1D

In 3D, the conductance through a wire is proportional to its cross section and inversely proportional to its length. However, in the 1D case, such as for CNTs, the infinitely small cross section requires new theoretical approaches. Within the frame of the Landauer-Büttiker formalism [44, 45], the conductance of a 1D conductor is modeled by the sum of n transmission channels ν with varying transmission coefficients $T_\nu(E)$

$$G = \frac{e^2}{h} \sum_{\nu=1}^{n} T_\nu(E) = \frac{G_0}{2} \sum_{\nu=1}^{n} T_\nu(E). \tag{2.12}$$

The transmission is, in general, energy-dependent, but can be evaluated at the Fermi level for low applied voltages [45]. In the case of a single CNT, there are $n = 4$ channels due to two spin degrees of freedom ($\uparrow$, $\downarrow$) and in addition a two-fold valley degeneracy (K, K'). The four degenerate states are given by $|\uparrow, K\rangle$, $|\uparrow, K'\rangle$, $|\downarrow, K\rangle$ and $|\downarrow, K'\rangle$ and obey the SU(4) symmetry compared to the SU(2) symmetry of a spin 1/2 system. $G_0 = 77\,\mu\mathrm{S}$ is the conductance quantum. For an ideal case with a ballistic CNT (length shorter than mean free path $L < \ell$) and perfect CNT metal contacts, the transmission coefficient for a single CNT is equal to 1, and the conductance sums up to $G = 4e^2/h = 2G_0$, which corresponds to a minimum resistance of $R = 6.4\,\mathrm{k\Omega}$. In practice, the measured resistance is larger due to backscattering in the CNT (if $L > \ell$) and a finite contact resistance R_C [46]

$$R = \frac{h}{4e^2} + \frac{h}{4e^2}\frac{L}{\ell} + R_\mathrm{C}. \tag{2.13}$$

Although clean metallic CNTs with typical channel lengths of $< 1\,\mu\mathrm{m}$ can be considered ballistic [47], it is almost impossible to achieve perfect CNT metal contacts, and the total device resistance is usually dominated by the contact resistance.

2.2.2. CNT metal contact

In general, two types of contacts can be distinguished, end-bonded contacts and side-bonded contacts. For end-bonded contacts, covalent bonds between the sp^2-orbitals and the d-orbitals of the commonly used transition metals lead to a much stronger bonding and usually a lower contact resistance. For example, contact resistances of $25\,\mathrm{k\Omega}$ have been reported for end-bonded contacts with molybdenum, where the current is injected via a MoC_2 interface of only $2\,\mathrm{nm}^2$ [48]. Likewise, carbide formation has been realized in end-bonded contacts with titanium [49, 50].

In the case of side-bonded contacts, the CNT wall is only weakly coupled to the metal (via van-der-Waals interaction), and the bond strength is governed by the overlap of the p_z-orbitals of the CNT and the d-orbitals of the transition metals [51]. With our nanoassembly technique we can only deposit CNTs on top of the electrodes, which naturally leads to side-bonded contacts, and thus we will only focus on these.

For side contacts, it is crucial to choose the appropriate contact metal. First, the wetting of the metal on the curved surface of the CNT matters. Wetting depends not only on the CNT metal interaction, but also on the interaction between the metal atoms [51]. For different metals evaporated on CNTs [52], Au, Al and Fe tend to form clusters on CNTs and a homogeneous coating of the CNT cannot be achieved. Good wetting has been found for Pd, Ni and Ti but also for Pt. Another study [53] investigated the interaction between Pt/Pd and CNTs. The authors evaporated Pt and Pd on CNTs on a gold surface and observed that Pt forms larger clusters than Pd and that smaller clusters adhere better to the CNT. Theoretical calculations [54] support this finding, where it is expected that Pt adheres more to other Pt atoms and is more likely to form clusters compared to Pd despite a stronger bond strength to CNTs. Thus, a more inhomogeneous coating of the CNT and higher contact resistance is predicted for Pt than for Pd.

Second, for the contact resistance, the metal work function has to be compared to the CNT work function which ranges from 4.76-5.05 eV, where bundles are at the lower end and single-walled CNTs at the upper end [55, 56, 57]. A mismatch in work function can lead to the formation of a Schottky barrier, which can be well understood when considering a metal-semiconductor contact [12], as shown in figure 2.4.

For the derivation of the Schottky barrier, it is convenient to start with an isolated consideration of the metal and semiconductor with different Fermi levels, as shown in the left part of figure 2.4. When the metal-semiconductor contact is established, charge carriers will flow across the contact interface until the Fermi levels of the metal and semiconductor are equal. When the Fermi level of the metal is higher (lower) than the Fermi level of the semiconductor, electrons will flow from the metal to the semiconductor (from the semiconductor to the metal). In the metal, the charge carrier density at the Fermi level is high, and charges do not build up. However, in the semiconductor, the exchange of charge carriers results in a zone of negative charges (positive charges) in the semiconductor at the contact interface. The location of the Fermi level in the semiconductor (which is influenced by doping) determines if these charges lead to a depletion or accumulation of majority charge carriers, resulting in a Schottky barrier or an ohmic transparent contact (cf. for n-doping in figure 2.4). The Schottky barrier height is given by

$$\Phi_{\mathrm{B_e}} = \Phi_{\mathrm{metal}} - \chi \qquad \text{for electrons and} \qquad \Phi_{\mathrm{B_h}} = -\Phi_{\mathrm{metal}} + \chi + E_{\mathrm{G}} \qquad \text{for holes.} \tag{2.14}$$

Here Φ_{metal} is the work function of the metal (energy difference between Fermi level and vacuum) and χ the electron affinity of the semiconductor (energy difference between the conduction band edge and the vacuum) and E_{G} the band gap (energy difference between the

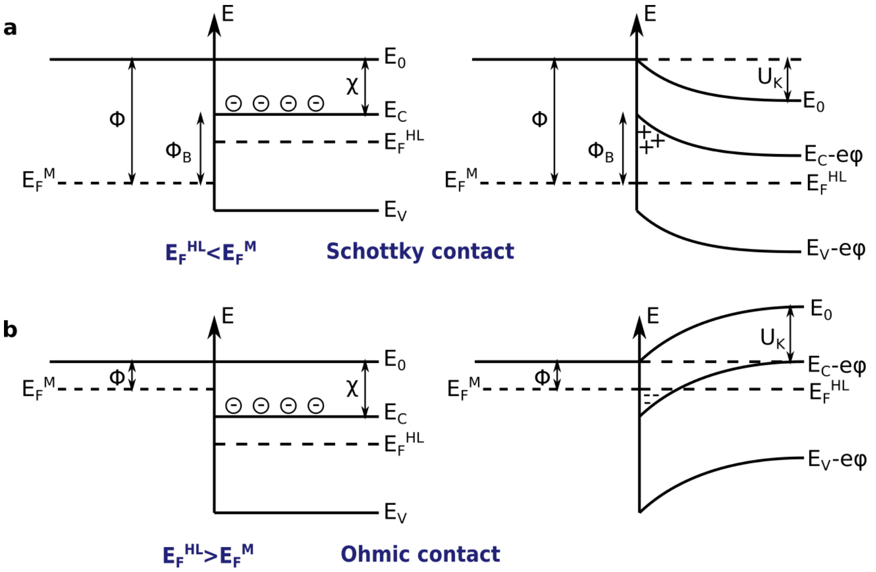

Figure 2.4.: Metal-semiconductor contact. Formation of a contact barrier between a metal and a n-doped semiconductor (left: before making the contact, right: in contact). Φ: metal workfunction, χ: electron affinity in the semiconductor, E_0: vacuum energy, $E_{\mathrm{V,C}}$ energy of the valence/conduction band. **a** Schottky contact. The Fermi level of the semiconductor is higher than the Fermi level of the metal. Electrons (majority charge carriers) flow into the metal and leave a depletion zone denoted with "+" where a potential φ builds up. A Schottky barrier of height Φ_{B} is formed and a contact voltage U_{k} needs to be applied for enabling a current flow. **b** Ohmic contact. The Fermi level of the semiconductor is lower than the Fermi level of the metal. Electrons (majority charge carriers) flow from the metal to the semiconductor and cause an accumulation zone denoted with "-". The contact does not exhibit a barrier, the contact voltage $U_{\mathrm{k}} < 0$.

valence band edge and conduction band edge) [12]. Since charge carriers must overcome the Schottky barrier for a current to flow, an increase in contact resistance is measured. The band gap of a CNT is inversely proportional to its diameter, and thus a larger diameter reduces the height of the Schottky barrier [58].

For typical bulk semiconductors, the Schottky barrier is influenced not only by the workfunction of the metal but also by metal-induced gap states at the interface. These are surface states due to defects, dangling bonds, etc., occurring inside the energy gap of the semiconductor with a high density of states that can pin the Fermi level to their corresponding energy (Fermi-level pinning). In contrast to bulk semiconductors, this effect is less pronounced in CNTs. In particular, for end-bonded contacts with a few atom interface, only a small dipole ring with few surface states can form and the barrier due to Fermi-level pinning is negligible [59, 51]. Even in the case of side-bonded contacts, where the interface is larger, the barrier decays over a few nm [60] which does not restrict the electron tunneling through the barrier. In particular, for the nanoassembly technique, the size of the CNT metal interface is difficult to estimate. Even though an evaporation of metal on CNTs can cover the CNT homogeneously, resulting in a longer contact interface, a dry-transfer of a CNT on a naturally rough surface at ambient temperatures could only lead to local contact points, limiting the number of interface states. In comparison to bulk semiconductors, the negligible Fermi-level pinning allows tuning the contact barrier by choosing a contact metal with a specific work function [59].

Another obvious reason for a high CNT metal contact resistance is the contamination of the contact interface, leading to an insulating barrier between the CNT and the metal. Such a barrier will inevitably reduce the overlap of the electronic wave functions between the CNT and the metal. For example, these contaminations could originate from CNTs with low cleanliness or amorphous carbon coverage on the CNT surface or from the contact electrodes by layers of residual organic solvents or surface oxide layers [61, 37]. In chapter 5, we will see that a clean surface is crucial to establish a good CNT metal contact.

2.2.3. Quantum dots in CNTs

When a 3D system is confined in all dimensions, the system is zero-dimensional and called a quantum dot. The word "quantum" refers to the particular quantum mechanical properties of such a system, that do not occur in the bulk of the same material.

First, the confinement alters the electronic properties which are dominated by Coulomb repulsion. If the dot size is small, the capacitance is small, which means, that adding an additional electron on the dot has a significant cost of energy, given by the charging energy [62]

$$E_\mathrm{C} = \frac{e^2}{2C}. \tag{2.15}$$

This leads to an observable quantization of charges on the dot due to the discreteness of charge.

Second, a confinement in three dimensions sets new boundary conditions for the allowed electron wavefunctions similar to a particle in a 3D box problem, resulting in discrete, quantized energy levels of the dot. These pure quantum effects depend on the dot size. The smaller the dot (the box), the larger the energy spacing ΔE of the discrete energy spectrum and the easier it becomes to observe these effects. For a CNT, the lateral confinement leads to a large energy spacing, while the longitudinal spacing is rather small.

Realization in CNTs

In CNT devices, three-terminal designs are employed [62] (cf. figure 2.5), where two reservoirs (metal electrodes) are coupled to a charge island (CNT). Current is injected into the nanotube via a source electrode and leaves the nanotube via a drain electrode. A gate electrode or a set of gate electrodes is located below the CNT and is only capacitively coupled to the CNT and can change the electrostatic potential in the CNT, thereby influencing the transport properties. The structure of a CNT naturally implies a 1D confinement. A 0D quantum dot can be formed when a contact barrier at the CNT metal interface occurs (e.g. Schottky barrier). A voltage applied to the gate electrodes can further shape the electrical potential seen by the CNT. Similarly to other electrical circuits, these three-terminal building blocks can be combined in series or in parallel, and more complex architectures can be formed.

Energy considerations and electronic transport regimes

Electronic transport through a CNT device depends on the energy scales involved. The properties of the quantum dot are characterized by the previously defined charging energy E_C, which for our CNT devices is on the order of 10 meV, and the quantum level spacing ΔE on the order of meV. These energy scales have to be compared with the thermal energy $k_\mathrm{B}T \approx 25\,\mathrm{meV}$ at room temperature. Therefore, in order to avoid thermal effects on our devices, we operate them at a temperature of $40\,\mathrm{mK} \approx 3.4\,\mu\mathrm{eV}$ in a limit that satisfies the condition $k_\mathrm{B}T \ll E_\mathrm{C}, \Delta E$, and thus the temperature effects can be neglected in the following.

At these low temperatures, electronic transport at the contacts is governed by tunneling. The tunnel coupling is defined as $\Gamma = \Gamma_\mathrm{s} + \Gamma_\mathrm{d}$, with Γ_s denoting the tunnel coupling to the source and Γ_d the tunnel coupling to the drain electrode. The tunnel coupling is related to the tunnel rate $(\Gamma/\hbar)$ of charge carriers at the interface between the metal electrodes and the CNT. The energy scale Γ describes the line broadening of the quantum dot energy levels caused by the coupling between the discrete energy spectrum of the dot and the continuous density of states in the reservoirs.

Depending on the value of the tunnel coupling Γ with respect to charging energy and quantum level spacing, three different transport regimes can be distinguished:

- weak coupling regime: $\Gamma \ll E_\mathrm{C}, \Delta E$
  The device can almost be considered isolated with a fixed number of charges (closed quantum dot). Charging effects govern the transport with sequential single-electron tunneling only and Coulomb blockade.
- intermediate coupling regime: $\Gamma \leq E_\mathrm{C}, \Delta E$
  The larger tunnel coupling increases the probability of higher-order tunneling processes, emerging, for example, as cotunneling or Kondo physics.
- strong coupling regime: $\Gamma \gg E_\mathrm{C}$
  The charging energy is negligible compared to the tunnel coupling which is equivalent to $\hbar/\Gamma \ll \hbar/E_\mathrm{C}$. More than one electron can tunnel at the same time (open quantum dot). If $\Gamma \leq \Delta E$, the transport is dominated by quantum interference analogous to an open cavity (Fabry-Pérot regime). If $\Gamma \gg \Delta E$, the physics can no longer be modeled by a quantum dot.

The tunnel coupling is inherently related to the energy barrier at the CNT metal interface, but the large tunability of the electrostatic potential in the CNT through the gates allows a modification of Γ, as well [63]. Thus, a great advantage of CNTs is that the three transport regimes can be accessed within the same CNT for different gate voltage ranges [31, 37].

2.2.4. Weak coupling regime

General notions

To start with, we define the chemical potentials of the two reservoirs, the source μ_s and the drain μ_d as the energy of adding an additional electron to the Fermi level of the source or the drain. The Fermi levels (and chemical potentials) can be shifted between source and drain by applying a bias voltage which gives the so-called bias window

$$-eV_\mathrm{sd} = \mu_\mathrm{s} - \mu_\mathrm{d}. \tag{2.16}$$

Likewise, we define the chemical potential of the quantum dot as the difference in total energy U by addition of an N^th electron

$$\mu(N) = U(N) - U(N-1). \tag{2.17}$$

In the weak coupling regime, the charging energy dominates, and the dot is characterized by a series of sharp and well-defined energy levels. The density of states of a single level at an energy $E_0 = \mu(N)$ can be modelled by a Lorentzian lineshape [62] with $\Gamma = \Gamma_\mathrm{s} + \Gamma_\mathrm{d}$

$$D(E) = \frac{1}{2\pi}\frac{\Gamma}{(E-E_0)^2 + (\Gamma/2)^2}, \tag{2.18}$$

which evolves into a delta-function for vanishing Γ. When a charge carrier has tunneled onto the quantum dot, the corresponding energy level is occupied. Due to strong electrostatic repulsion, the next free energy level is separated in energy by E_C (and depending on the spin and valley degeneracy in addition by ΔE), and thus cannot be occupied. No current can flow until the charge has left the dot. For this reason, the tunneling of charge carriers via a single level occurs only one by one (sequential tunneling). If there is no level available inside the bias window (given by the difference of the Fermi level of source and drain, eq. 2.16), electronic transport is blocked, a phenomenon called Coulomb blockade. When V_sd is increased and $V_\mathrm{sd} > E_\mathrm{C} + \Delta E$, multiple levels can be located within the bias window and contribute to electronic transport. In the following, we only consider a single level that contributes to transport and low V_sd.

Constant-interaction model

The constant-interaction model represents a semi-classical description of the total energy of the electrons on the quantum dot and a simple way to calculate the transport through a quantum dot in the weak coupling regime. It is based on two fundamental assumptions [65] for a model of a quantum dot visualized in figure 2.5a.

1. All electrostatic interactions are described by a single and constant capacitance which is the sum of the capacitances to the source, the drain and the gate

$$C = C_\mathrm{s} + C_\mathrm{d} + C_\mathrm{g}. \tag{2.19}$$

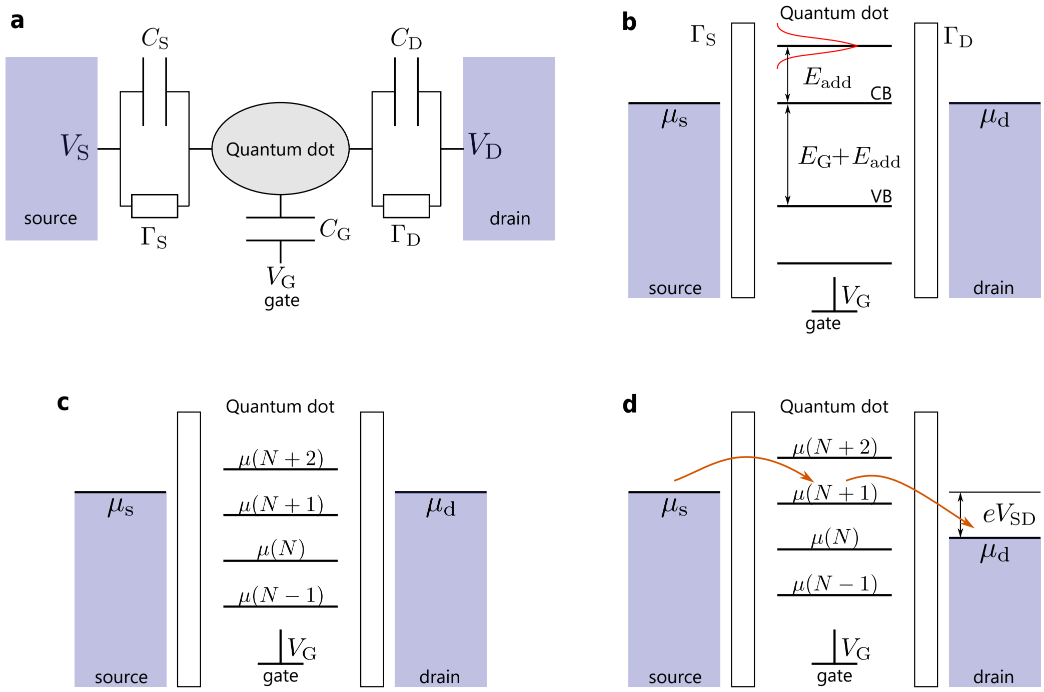

Figure 2.5.: Model of a quantum dot in the constant-interaction model. **a** Equivalent circuit of a quantum dot with the source and drain modelled as big reservoirs and a small quantum dot capacitively coupled to the source and drain with tunnel coupling Γ and purely capacitively coupled to the gates without any conduction channel (inspired by [64]). **b** Schematic of the potential landscape if the dot is implemented in a semiconducting CNT with valence band (VB) and conduction band (CB) and semiconducting energy gap E_G. The barriers are drawn simplified as rectangular, but in reality, their shape can be more complex. Each level is drawn with a δ-lineshape. In reality a Lorentzian lineshape has to be assumed as indicated in red. μ_s and μ_d separate occupied states from unoccupied states in the reservoir. **c** Quantum dot in the Coulomb blockade, no level is inside the bias window. **d** Applying a bias between source and drain V_{sd} opens a bias window and a change in the gate voltage brings a single level inside the bias window, which can contribute to electronic transport, as indicated by the arrows.

2. The quantum level spacing ΔE is independent of the number of charge carriers on the dot.

The total energy $U(N)$ of N electrons on the dot in the ground state is given by [38, 65]

$$U(N) = \frac{(-eN + C_s V_s + C_d V_d + C_g V_g)^2}{2C} + \sum_{i=1}^{N} E_i. \tag{2.20}$$

The first term represents the electrostatic energy stored in the capacitances due to the external voltages applied and the charge on the dot itself, whereas the second term sums up the confinement energies E_i for each single electron level.

The chemical potential can be obtained with eq. 2.17

$$\mu(N) = (N - 1/2)E_C - \frac{E_C}{e}(C_s V_s + C_d V_d + C_g V_g) + E_N. \tag{2.21}$$

With this result we can calculate the addition energy which determines the spacing between two successive chemical potentials

$$E_{\mathrm{add}} = \mu(N+1) - \mu(N) = E_{\mathrm{C}} + \Delta E \tag{2.22}$$

and comprises the quantization of charge and the quantization due to the 0D confinement of the electron spatial wave functions. In the constant-interaction model, this addition energy leads to an almost regularly spaced ladder of levels, as shown in figure 2.5. Each level is occupied by a single electron because the addition of one electron has to be paid by the corresponding charging energy. With regard to the quantum level spacing ΔE (usually $E_{\mathrm{C}} > \Delta E$) the situation is more complex. Due to the fourfold degeneracy arising from spin and valley degrees of freedom, a new shell is filled for every fourth electron and only in this case $\Delta E \neq 0$.

Charge stability diagram

In the experiment, we are interested in the areas in V_{sd}-V_{g} space where a current is measured or where transport is blocked and the number of charges on the quantum dot fixed. For this purpose, we define the charge stability diagram as a 2D map with the source-drain voltage V_{sd} on the y-axis and the gate voltage V_{g} on the x-axis, while either the current I through the device or the differential conductance $\mathrm{d}I/\mathrm{d}V$ is measured. The current visualizes the conducting areas, whereas the differential conductance is sensitive to changes of these areas, and therefore better suited to measure transitions between areas with different conductance. Similarly to the plots in figure 2.5, areas with $I \neq 0$ can only be found when a level $\mu(N)$ is inside the bias window, which implies $\mu_{\mathrm{s}} \geq \mu(N) \geq \mu_{\mathrm{d}}$. In the V_{g}-V_{sd} plane, this condition corresponds to sets of lines which are determined by an alignment of μ_{s} or μ_{d} to a level $\mu(N)$ on the quantum dot. For a grounded drain ($\mu_{\mathrm{d}} = 0$), as indicated in figure 2.6, the slopes of the lines are given by [62]

$$\beta = \frac{C_{\mathrm{g}}}{C_{\mathrm{g}} + C_{\mathrm{d}}} \ (\mu(N) \text{ aligned to source}) \text{ and } \gamma = -\frac{C_{\mathrm{g}}}{C_{\mathrm{s}}} \ (\mu(N) \text{ aligned to drain}). \tag{2.23}$$

The lines occur in a checkerboard pattern with diamond-like shaped areas (cf. figure 2.6). Outside these white areas a current can flow, but inside the number of charges on the quantum dot is fixed and no current will flow, the dot exhibits Coulomb blockade. For this reason, these areas are also called Coulomb diamonds. The height of a diamond, measured from $V_{\mathrm{sd}} = 0$, is given by E_{add}/e and the width is given by $E_{\mathrm{add}}/(\alpha e)$. $\alpha = C_{\mathrm{g}}/C$ is the lever arm of the gate, a measure of how an applied gate voltage translates into a change in potential in the quantum dot or in the language of the plots in figure 2.5 by how much $\mu(N)$ is shifted in energy by applying a gate voltage.

We can again see the fourfold periodicity due to spin and valley degeneracy as every fourth diamond being larger. If the valley degeneracy is broken (i.e. K and K' states can mix), there is an additional splitting δE. Valley splitting can be induced by spin-orbit coupling (for CNTs rather small and difficult to observe), external magnetic field, or intervalley scattering, whereas the latter one can be due to electrical disorder in the CNT [38].

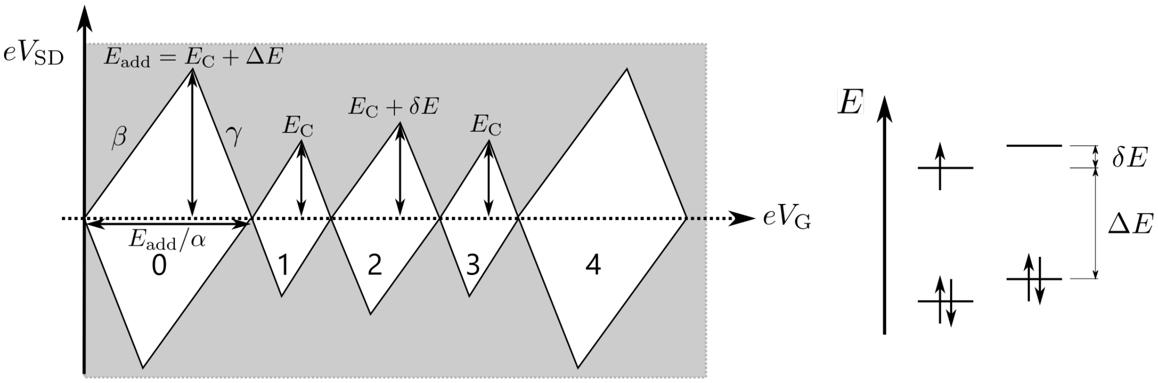

Figure 2.6.: Charge stability diagram. The differential resistance dI/dV is shown in grey as a function of the energies $eV_{\mathrm{sd/g}}$. Inside the white areas the current is zero, the number of charges is fixed. The pattern repeats with a period of 4 diamonds, here the fourth diamond is similar to the zeroth. If the valley degeneracy is broken, the second diamond shows an additional splitting δE as illustrated on the right side. If $\Delta E \sim \delta E$, the pattern is only two-fold periodic instead of fourfold. β and γ indicate the slopes of the diamonds and α is the gate lever arm.

For this reason, the observation of 4-fold degeneracy is a signature of a clean CNT [66]. If only a twofold degeneracy due to spin degeneracy occurs ($\Delta E \simeq \delta E$), the CNT is likely to exhibit some defects.

Deviations from the constant-interaction model

The constant-interaction model gives a simple description of electronic transport through a quantum dot. However, in real measurements, we can observe some deviations from the sketch of an idealized charge stability diagram in figure 2.6. In experiments, there is usually a region close to the first charges on the dot (about $-5 \leq N \leq 5$), where the diamonds appear larger than for high $|N|$ and a decreasing envelope can be distinguished (cf. figure 2.7).

This behavior can be explained by a modification of the contact barrier when a gate voltage is applied. The contact barrier itself has a finite width and height and the effective electrostatic potential arises from a superposition of the contact barrier and the electrostatic potential in the CNT induced by the gate. Although the potential barrier for high charge number $|N|$ is located at the CNT metal contact barriers (hard confinement), in general, this is not true for low $|N|$. In a simple quantum dot with only one gate, a low gate voltage needs to be applied for a few electron occupation. Depending on the geometry of the device (gate width, gate CNT separation and CNT suspension length), the potential barrier for low gate voltage can still be defined within the CNT only (soft confinement). The boundary conditions affect not only the charging energy but also the quantum level spacing which is usually smaller (cf. figure 2.7). The width of the confinement potential increases quadratically until it reaches the hard boundary at the CNT metal contact (the width corresponds to L) and does not increase further and ΔE approaches a constant.

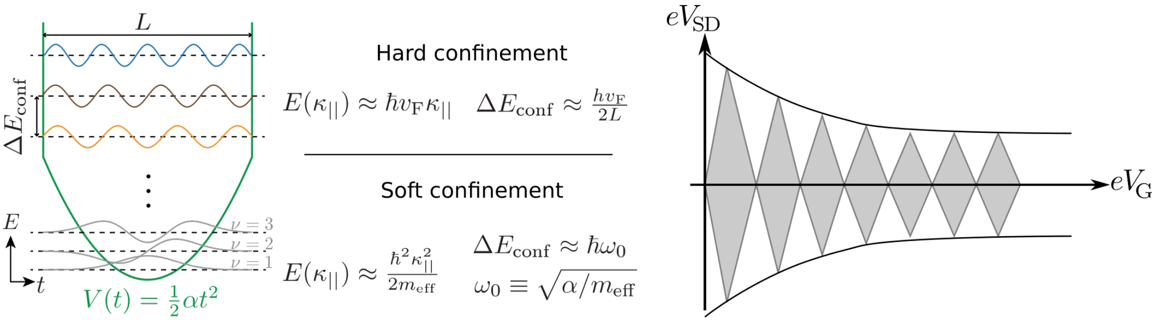

Figure 2.7.: Deviation from the constant-interaction model. Left: Soft and hard confinement in a CNT of length L (figure from [38]). Right: Decreasing envelope of Coulomb diamond height (fourfold periodicity not shown).

Likewise, it has to be emphasized that the gate-induced change of the shape of the contact barrier can have an impact on the tunnel coupling Γ, which leads to higher conductance for higher $|N|$.

With respect to the first assumption of the constant-interaction model, the constant capacitances covering all electrostatic interactions represent a strong simplification. We only want to point towards one obvious effect which is not taken into account. The gate voltage does not only influence the number of charges, but because the CNT is suspended, a higher gate voltage will pull the CNT closer to the gate and will thereby change the capacitance C_g.

Excited states

Until now, we have only considered energy levels $\mu(N)$ in the ground state. However, similar to atoms, quantum dots as artificial atoms can have excited electronic states. These states belong to the same electron number N, and can be located between two levels $\mu(N)$ and $\mu(N+1)$ (cf. figure 2.8d). They are separated from the ground state $\mu(N)$ (or other excited states) by a corresponding excitation energy $\Delta E_{\mathrm{ex}}^{(i)}$ for an excited state i. Every time an excited state enters the bias window, an additional transport channel opens up, resulting in lines of high conductance running parallel to the edges of the Coulomb diamonds.

Excited states in suspended CNTs can also occur due to vibronic excitations of the CNT, owing to the strong electron-phonon coupling g. Particularly strong electron-phonon coupling ($g > 1$) has been observed for longitudinal stretching modes in CNTs [67, 43]. The situation for strong and weak electron-phonon coupling g is schematically shown in figure 2.8, where the vibron potential is sketched. Tunneling of an electron onto the quantum dot will shift the equilibrium coordinate of the vibron potential due to electron-phonon coupling. The Franck-Condon model gives a description of the transition probability of such an electron tunneling process. Due to a negligible mass of electrons compared to nuclei, the nuclear positions remain essentially unchanged and in figure 2.8 only vertical transitions are possible.

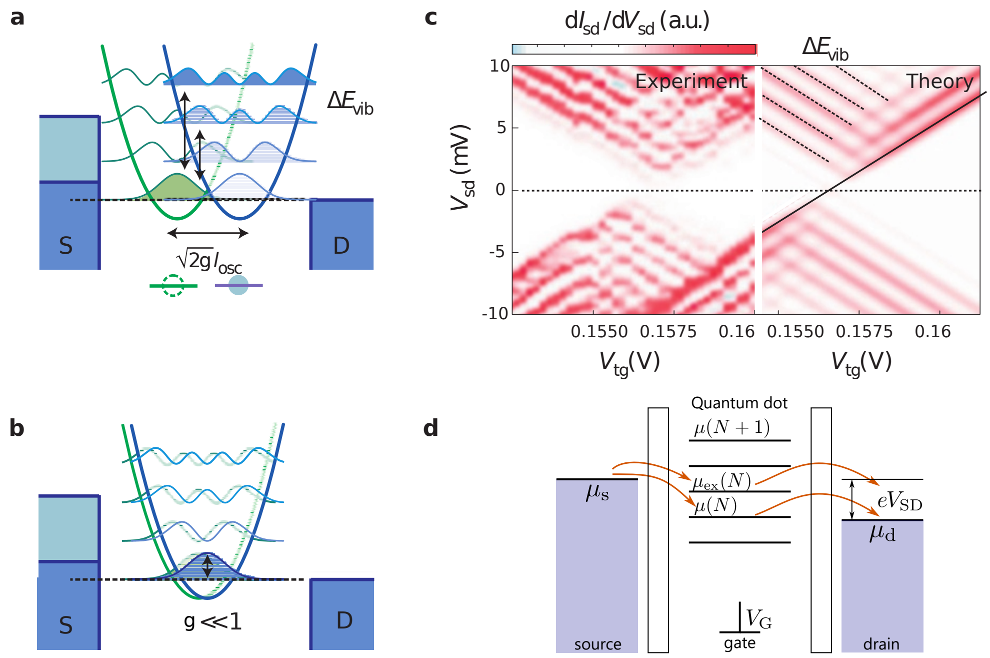

Figure 2.8.: Vibrational excitations in CNTs and electronic excitations. **a**,**b** Sketch of the vibron potential for N (green) and $N+1$ electrons (blue). **a** Large electron-phonon coupling g shifts the equilibrium position by $\sqrt{2}gl_{\mathrm{osc}}$ with the vibron's oscillator length $l_{\mathrm{osc}} = \sqrt{\hbar/M\omega}$. A large overlap between vibronic wave functions only exists for higher excitations, as marked by the arrow. **b** For low electron-phonon coupling, the overlap between the ground states is still large and higher excitations show a lower overlap. **c** Measurement showing the vibrational sidebands spaced by ΔE_{vib}. The asymmetry is due to asymmetric tunnel coupling Γ_{s} and Γ_{d}. **d** Energy diagram of a quantum dot showing electronically excited states participating in transport when they enter the bias window. Subfigures a-c adapted from [67] with permission from Springer Nature.

The transition probability is proportional to the Franck-Condon factor, given by the square of the overlap integral between the two vibrational wave functions before and after tunneling [43]. This overlap depends on the displacement of the two vibron potentials, and thus on the electron-phonon coupling. In case of strong electron-phonon coupling, the overlap of the two vibronic ground states is small, resulting in a suppression of current at low bias (Franck-Condon blockade, cf. figure 2.8c). A larger overlap can only be found between the vibronic ground state before tunneling and higher vibronic states after tunneling. For these transitions to occur, the source-drain bias V_{sd} does not only need to provide the energy to open a bias window around a level on the dot but also the energy required for the respective vibronic excitations. This leads to vibrational sidebands, which can be observed as equidistant lines (for harmonic vibron potential) running parallel to the edges of the Coulomb diamonds similar to electronic excited states. In case of weak electron-phonon coupling, the vibronic ground states before and after tunneling are almost unchanged, resulting in a large overlap between the ground states, and the overlap to excited vibronic states is negligible. Vibrational sidebands are suppressed. The spacing between the vibrational sidebands corresponds to the energy of the vibronic excitations, and can be used to compare to different mechanical modes. In case of a longitudinal stretching mode, this energy is given by $\Delta E_{\mathrm{vib}} = \hbar v_{\mathrm{ph}} q$ with $q = n\pi/L$ for a mode n and L the suspension length of the CNT [67].

2.2.5. Intermediate coupling regime

In the intermediate coupling regime, the tunnel coupling Γ is of the same order as the charging energy E_C and the quantum level spacing ΔE. The higher tunnel coupling gives rise to higher-order tunneling processes which scale proportionally to Γ^n [1] and were therefore suppressed in the weak coupling regime. A higher tunnel coupling increases the probability of coherent electron tunneling, i.e. electron tunneling onto the dot and out of the dot on a time scale preserving its coherence.

Elastic and inelastic cotunneling

Not only the states inside the bias window can contribute to electronic transport. Within a time scale set by the energy-time uncertainty, an intermediate state can be occupied that is not inside the bias window and would be classically forbidden as it violates energy conservation (virtual state). If the electron leaves this intermediate state to the drain electrode, a charge has been transferred via a classically forbidden state without changing the dot's electron occupation and conserving the total energy of this two-electron tunneling process. According to the energy-time uncertainty relation, these processes are more likely to occur when the time scale $\sim \hbar/\Gamma$ set by the tunnel coupling is comparable to the time scale $\sim \hbar/\delta\epsilon$ where $\delta\epsilon$ is the energy difference from the intermediate state to the Fermi level of the source and the drain. Such a second-order process requires two tunneling processes within this short time window and is therefore called cotunneling.

In contrast to first-order tunneling, where the current depends linearly on the tunnel rate $\Gamma_\mathrm{s}\Gamma_\mathrm{d}/(\Gamma_\mathrm{s}+\Gamma_\mathrm{d})$, the current for cotunneling scales proportionally to $\Gamma_\mathrm{s}\cdot\Gamma_\mathrm{d}$ [62]. The next higher-order terms for electron transport from source to drain would be of fourth order and is, for instance, required for Cooper pair transport through a CNT. For now, we will only focus on the second-order cotunneling processes and discuss different configurations leading to non-zero conductance inside the Coulomb diamonds.

One can differentiate between elastic and inelastic cotunneling. Elastic cotunneling takes place at zero bias ($\mu_\mathrm{s} = \mu_\mathrm{d}$) and leaves the dot energy unchanged. The mechanism involves a single virtual state, as explained above (cf. figure 2.9a), and is visible as a gate-independent line at zero bias in $\mathrm{d}I/\mathrm{d}V$ in the charge stability diagram (cf. blue line in figure 2.9c). Elastic cotunneling is significantly enhanced when a spin-flip is involved in the process (usually for odd electron occupation), as we will see in the next subsection when the Kondo effect in CNTs will be discussed in more detail.

Inelastic cotunneling requires a finite bias, which must be larger than the excitation energy to an excited state (cf. figure 2.9b). A level $\mu(N)$ is occupied with an electron below the Fermi levels of source and drain, and thus the bias window does not cover this level, and the dot would classically be in the Coulomb blockade regime. If the electron escapes to the drain (virtual state) and another electron tunnels into the dot into an excited state,

---

[1] note: Γ refers here to the tunnel coupling of a single barrier and n is the order of the tunneling process

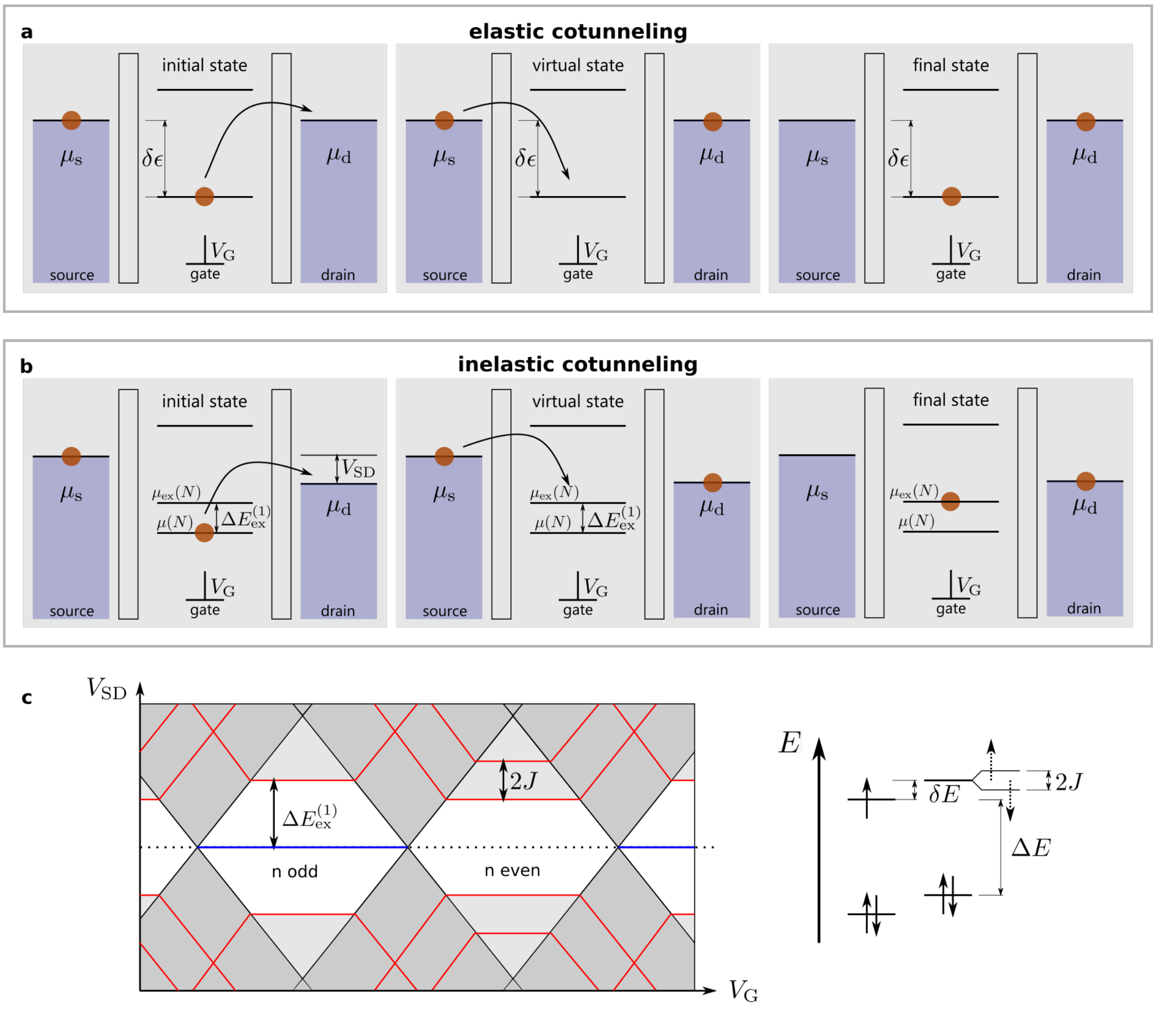

Figure 2.9.: Schematics of the cotunneling processes. **a** Elastic cotunneling. An electron (brown circle) can tunnel out and a virtual state is formed as shown in the center image. If another electron tunnels into the dot, energy is conserved when comparing the initial and final state. **b** Inelastic cotunneling leaving the dot in an excited state and the energy is supplied by the bias voltage. Only the first excited state is shown. **c** Charge-stability diagram for the cotunneling processes. Blue: Zero-bias line due to elastic cotunneling, as typically observed for odd electron occupation. Red: Inelastic cotunneling lines and excited states. For even electron occupation and broken valley degeneracy there can be two configurations for the excited state, depending on the ferromagnetic exchange interaction J. Figure inspired by [62, 68].

the total energy is conserved and the cotunneling process allowed. However, this can only occur if the source drain bias voltage covers at least the energy difference from the ground state to an excited state i ($|eV_{sd}| \geq \Delta E_{ex}^{(i)}$). In the charge stability diagram, inelastic cotunneling appears as horizontal lines in the differential conductance located at $\pm\Delta E_{ex}^{(i)}$ inside the Coulomb blockade area (cf. figure 2.9c). Note that these lines simply join the parallel lines of excited states running along the edges of Coulomb diamonds when the respective excited state enters the bias window in addition to the ground state (cf. excited states in 2.2.4 and figure 2.8d).

A particular type of excited states can be encountered in the case of broken valley degeneracy with $\delta E < E_\mathrm{C}$. In this case, the second shell with K' can play a role similar to that of excited electronic states. For odd electron occupation, this effect manifests itself as peaks in the differential conductance located at $eV_\mathrm{sd} = \pm\delta E$. For diamonds with even occupation, one can sometimes observe a splitting of the inelastic cotunneling line into two nearby cotunneling lines. The two electrons in the ground state have opposite spin due to the Pauli principle. When one electron occupies an excited state, however, the spin is no longer fixed. The low energy splitting between the two excited states can be explained by a singlet-triplet splitting of the two spin configurations that depends on the magnetic exchange interaction J between the electron spin in the ground state and the excited state [62].

Kondo effect in CNTs

One special type of elastic cotunneling in CNTs is spin-flip cotunneling, also called "Kondo effect". In metals, the Kondo effect is usually associated with a resistance increase in low-temperature electronic transport when magnetic impurities are added [69]. The magnetic moments of the local impurities can interact with the spins of the delocalized conduction electrons at the Fermi level of the metals. An antiferromagnetic exchange interaction leads to a screening of the impurity by electrons with spins opposing the magnetic moment of the impurity, forming a correlated electron state, the Kondo cloud. The scattering of conduction electrons at the Kondo cloud causes a resistance increase.

In CNT quantum dots for an odd electron occupation, the resulting unpaired spin 1/2 electron can be considered as a magnetic impurity in the 1D conduction channel between the two reservoirs [70]. If the contact barriers are sufficiently transparent ($\Gamma \geq E_\mathrm{C}$), an antiferromagnetic exchange coupling between the spin on the dot and the conduction electrons of source and drain can arise. This interaction is responsible for the screening of this magnetic spin 1/2 impurity, with the majority spin in the leads opposing the spin of the electron on the dot. As a consequence, at the end of a cotunneling process, the spin of the initial and final states of the spin 1/2 impurity changes sign (spin-flip cotunneling). The Kondo effect can be considered as a many-body phenomenon since many conduction electrons at the Fermi level of the reservoirs are involved [71]. A new strongly correlated state arises between the energy level on the dot and the conduction electrons of the reservoirs. In contrast to bulk metals, where a resistance increase is observed when magnetic impurities are added, in 1D conductors, such as CNTs, the correlations enhance the elastic cotunneling processes considerably and open up a highly transmitting channel at zero bias, the Kondo resonance. To the width of this resonance, one can associate a Kondo temperature T_K [62]

$$k_\mathrm{B}T_\mathrm{K} = \frac{\sqrt{\Gamma E_\mathrm{C}}}{2} \exp\left(\frac{\pi\delta\epsilon(\delta\epsilon + E_\mathrm{C})}{\Gamma E_\mathrm{C}}\right). \tag{2.24}$$

Here $\delta\epsilon$ is the energy difference from the level $\mu(N)$, which hosts the magnetic impurity, to the Fermi level of the reservoirs (cf. figure 2.10).

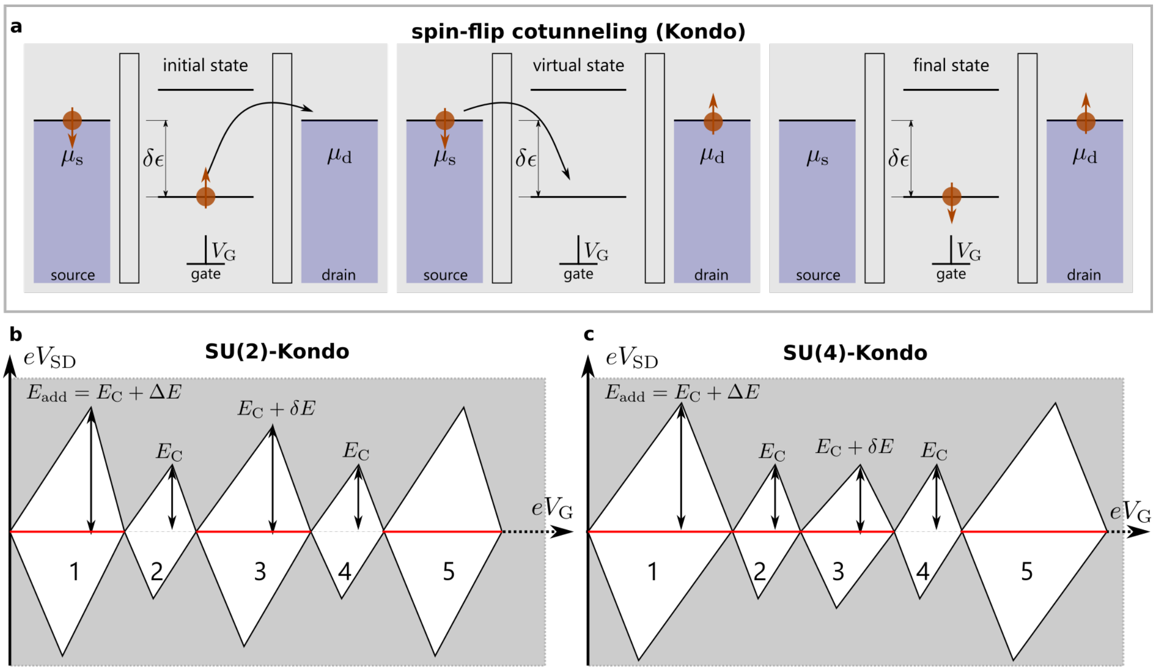

Figure 2.10.: Kondo effect in CNTs. a Spin-flip cotunneling process, **b** Charge stability diagram with SU(2) Kondo effect in the case of broken valley degeneracy. Elastic cotunneling lines appear for every odd diamond. **c** Charge stability diagram with SU(4) Kondo effect in the case of approximate valley degeneracy. Elastic cotunneling lines appear for a sequence of three diamonds.

So far we only investigated the standard spin 1/2 Kondo effect (SU(2) Kondo), but in principle Kondo resonances can also be mediated by other degrees of freedom under the condition that they are conserved during cotunneling processes [72]. For CNTs, depending on spin-orbit coupling [73], valley splitting [74], etc., many other types of Kondo effects can arise. We will only focus on the SU(4) Kondo effect due to the fourfold degeneracy occurring in the limit $\Delta_{KK'}, \Delta_{SO} \ll k_B T_K$. Here, in addition to diamonds with odd electron occupation, resonances can also be observed when the fourfold shell is occupied with two electrons. For two electrons and therefore half occupation of the shell (spin and valley) the situation is analogous to two independent unpaired impurities. This results in a maximum conductance of $4e^2/h$ instead of $2e^2/h$ for the SU(2) Kondo effect. For the third diamond, there is only one unpaired electron, and the situation is similar to the first diamond, and a maximum conductance of $2e^2/h$ can be reached.

2.2.6. Strong coupling regime

If the transparency of the contact barrier is increased, such that the tunnel coupling Γ dominates the charging energy E_C, the electrostatic interaction between electrons in the CNT is negligible and the addition energy depends only on the quantum level spacing ΔE. As a consequence, more than one electron can tunnel at a time.

For a ballistic CNT without scattering inside the CNT, this results in electron interference from multiple reflections at the CNT metal contact interface [47]. These interferences can

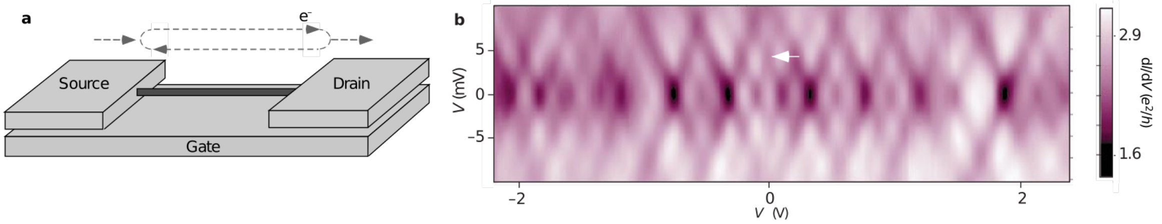

Figure 2.11.: Fabry-Pérot regime. a Schematic of the electron interferences. **b** Charge stability diagram with Fabry-Pérot interference pattern with height indicated by the white arrow. Figure from [47].

be compared to the photonic analogue of Fabry-Pérot interferences in an optical cavity (cf. figure 2.11), and this regime is called the Fabry-Pérot regime or the open quantum dot regime. In the optical analogue of a cavity with fixed length, the resonance condition can be tuned by changing the wavelength of the light. For a CNT quantum dot, V_g changes the position of the Fermi level in the CNT and the associated Fermi wave number which is related to the Fermi wavelength $k_\mathrm{F} = 2\pi/\lambda_\mathrm{F}$. Therefore, the oscillations in the charge stability diagram exhibit a dependence on the gate voltage. The height of the pattern, indicated by the white arrow in figure 2.11, shows an inverse dependence on the length L of the CNT quantum dot and if $E_\mathrm{C} \ll \Delta E$, the height corresponds to the quantum level spacing, which for a metallic, ballistic CNT is similar to the hard confinement condition in figure 2.7 and given by [47]

$$\Delta E = \frac{h v_\mathrm{F}}{2L}. \tag{2.25}$$

This equation can be used to calculate the length L of the CNT quantum dot.

2.3. Nanomechanics of transverse bending modes in suspended CNTs

Due to their low mass and high Young's modulus, CNTs are ideal candidates for nanoelectromechanical systems (NEMS), with potential applications ranging from force and mass sensors to a versatile platform for exploring fundamental physics questions. A key challenge is to transduce mechanical vibrations into a measurable electrical signal [75]. In this chapter, we will review the mechanics of transverse bending modes and discuss how motion can be driven and detected in suspended CNTs.

2.3.1. Mechanics of a doubly clamped beam

A suspended CNT can be modelled by the Euler-Bernoulli equation of a doubly clamped beam with cylindrical cross section [76]

$$\rho A \frac{\partial^2 u}{\partial t^2} + D \frac{\partial^4 u}{\partial x^4} - T \frac{\partial^2 u}{\partial x^2} = F(t). \tag{2.26}$$

Here, the CNT axis is in x-direction and the vibration amplitude $u(x,t)$ in z-direction. The first term in equation 2.26 represents the acceleration with the mass density ρ and the cross section $A = \pi r^2$ for a CNT with radius r. The second term is related to the bending of the beam and depends on the bending rigidity $D = EI/(1-\nu^2) \approx EI$ with the Young's modulus E, the second moment of inertia I, and the Poisson's ratio ν, which is often negligible for CNTs since the application of axial strain only induces weak transverse strain in CNTs. The third term takes tension into account, which in the limit of small beam deflections ($\partial u/\partial x \ll 1$) is given by $T = T_0 + \frac{EA}{2L}\int_0^L \left(\frac{\partial u}{\partial x}\right)^2 \mathrm{d}x$ and includes some initial tension T_0 and a tension related to the elongation of the beam. The tension induced by elongation introduces a nonlinearity in equation 2.26 that makes an analytical solution impossible [77].

$F(t)$ is a time-dependent external force driving the CNT. In case of a capacitive actuation at angular frequency ω via a gate below the CNT in the limit of weak drive $V_\mathrm{g}^\mathrm{AC} \ll V_\mathrm{g}^\mathrm{DC}$, this force can be written as [76]

$$F(t) = \frac{1}{2}\frac{\partial C_\mathrm{g}}{\partial u}V_\mathrm{g}^2(t) = \frac{1}{2}\frac{\partial C_\mathrm{g}}{\partial u}\left(V_\mathrm{g}^\mathrm{DC} + V_\mathrm{g}^\mathrm{AC}(t)\right)^2 \tag{2.27}$$

$$\approx \frac{1}{2}\frac{\partial C_\mathrm{g}}{\partial u}\left((V_\mathrm{g}^\mathrm{DC})^2 + 2V_\mathrm{g}^\mathrm{AC}(t)V_\mathrm{g}^\mathrm{DC}\right) = F_\mathrm{DC} + F_\mathrm{AC}\cos(\omega t). \tag{2.28}$$

The partial derivative $\partial C_\mathrm{g}/\partial u$ takes the modification of the gate capacitance into account induced by a CNT oscillating with deflection u. Note that doping of the CNT can shift the Fermi level of the CNT to a non-zero gate voltage. Beyond that, the equation for the force is based on a continuous charge distribution on the beam. In the case of Coulomb blockade, the discreteness of charge can induce a finite electrostatic potential on the dot itself, which is discussed in detail in section 2.3.4. Both effects lead to a non-zero potential on the dot, denoted V_0, which must be subtracted, leading to a substitution of $V_\mathrm{g}^\mathrm{DC} \rightarrow V_\mathrm{g}^\mathrm{DC} - V_0$ [13].

For now, we neglect the AC part of the external force. The DC part of the external force induces tension in the CNT which can be approximated by $T \propto F_\mathrm{DC}$ [78]. In the following, we give approximations for the fundamental mode for different limits, including second-order corrections from [79] (cf. figure 2.12).

- bending limit: $T \ll \frac{EI}{L^2}$: The tension-based term can be neglected and the solution is

  $$\omega_0 = \frac{22.4}{L^2}\sqrt{\frac{EI}{\rho A}} + 0.28T\sqrt{\frac{1}{\rho EIA}}. \tag{2.29}$$

  Therefore a $\omega_0 \sim L^{-2}$ dependence is expected for the resonant angular frequencies and a $\omega_0 \sim T \sim (V_\mathrm{g}^\mathrm{DC})^2$ dependence for the DC part of the gate voltage. CNTs with high Young's modulus $E = 1\,\mathrm{TPa}$ [80] are expected to be bending dominated. Indeed, the quadratic dependence on the gate voltage is typically observed in our experiments, indicating that we work in the bending limit.

- catenary regime: When the tension is increased and $T \gtrsim \frac{EI}{L^2}$, the bending term becomes negligible and the leading term is determined by the resonant angular

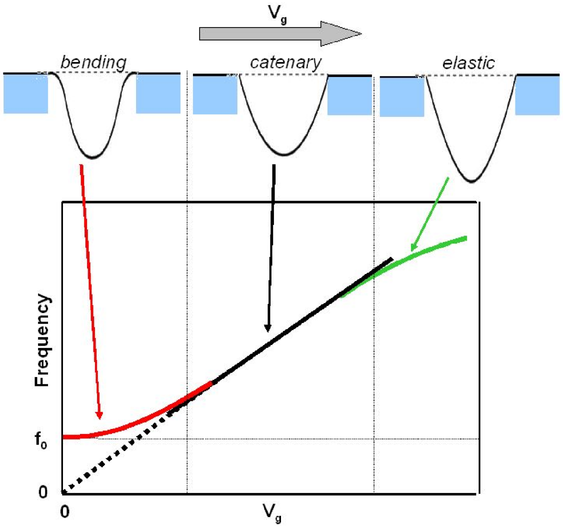

Figure 2.12.: Limits of the Euler-Bernoulli equation. Resonant frequency as function of gate voltage with the three different regimes. Figure from [78].

frequencies of a guitar string (scaling of $1/L$). Since $\omega_0 \sim \sqrt{T} \sim V_g^{DC}$ a linear dependence on the DC part of the gate voltage is observed.

- tension limit: $T \gg \frac{EI}{L^2}$: The bending term is completely negligible. The second term of the tension T dominates and the tension starts saturating [79]

$$\omega_0 = \frac{\pi}{L}\sqrt{\frac{T}{\rho A}} + \frac{2\pi}{L^2}\sqrt{\frac{EI}{\rho A}}. \tag{2.30}$$

2.3.2. Duffing oscillator

The equation 2.26 can be approximately transformed into the equation of a so-called Duffing oscillator, a model of a harmonic oscillator with non-linearities absorbed in a cubic u^3-term [77, 80]. The according differential equation for a periodic drive force and an additional damping term (with damping rate γ) writes as [80, 81]

$$\ddot{u}(t) + \gamma\dot{u}(t) + \omega_0^2 u(t) + \alpha u^3(t) = \frac{F_0}{m}\cos(\omega t). \tag{2.31}$$

The cubic dependence of the nonlinearity implies, that for low drive power, the linear system with Lorentzian resonance is retained. The onset of nonlinearity has been calculated for a nanotube in [80]

$$a_c = \frac{2}{\sqrt[4]{3}}\sqrt{\frac{1}{Q}\left(\frac{d^2}{4} + \frac{4T_0}{\pi^3 E}\frac{L^2}{d^2}\right)}. \tag{2.32}$$

For nanoassembled CNTs we expect a low initial tension, since the CNT is mechanically transferred at ambient temperature, and thus the second term can be neglected.

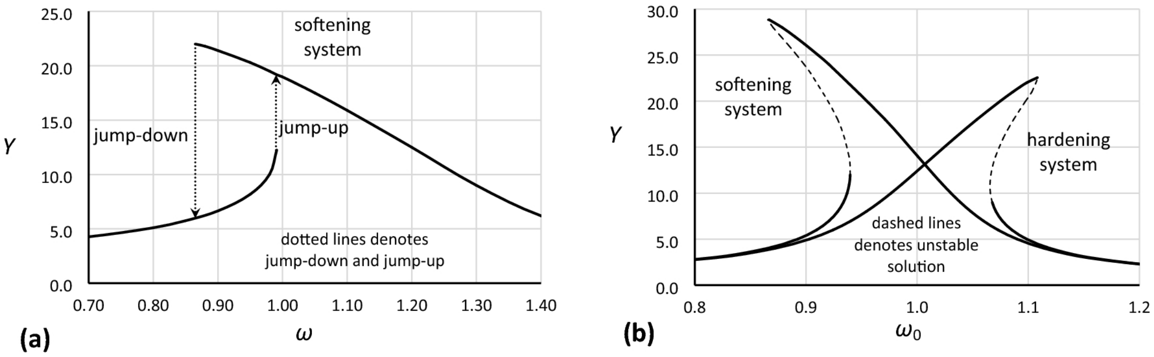

Figure 2.13.: Duffing oscillator resonance lineshape. Resonance (amplitude Y in arbitrary units) as function of resonance frequency ω. The resonance is softened for $\alpha < 0$ and hardened for $\alpha > 0$. **a** Observable hysteresis for increasing and decreasing frequency sweeps. **b** Theoretical result for the two cases $\alpha < 0, \alpha > 0$. Figure from [82].

Due to the low diameter, the onset of nonlinearity is expected at comparably low power, making CNT nanomechanical oscillators ideal platforms for an operation in the nonlinear regime (e.g. as threshold detectors).

For higher power, the cubic term dominates and the peak is pulled to higher (or lower) frequencies depending on the sign of the Duffing parameter $\alpha > 0$ ($\alpha < 0$) (cf. figure 2.13b, for a detailed calculation of α see [80]). For an even stronger drive, there are three solutions for the amplitude u in a specific frequency range. Only two of these solutions are stable, the one on the upper branch and the other on the lower branch. The system's change from the upper branch to the lower branch and vice versa depends on the direction of the frequency drive. In the example shown in figure 2.13a, we assume $\alpha < 0$ and the resonance is pulled to the left side and multivalued due to the high drive power. A downward frequency sweep will leave the resonator in the upper branch until it reaches the maximum, and then a sudden jump into the lower branch occurs. For an upward frequency sweep, the situation is different. The system stays in the lower branch until it reaches the highest frequency value possible on this branch, and then it will jump into the upper branch. The result is a sharp hysteresis in the shape of the resonance.

2.3.3. Detection of mechanical resonances

Motion can be driven in a suspended CNT by applying an AC voltage either at the local gate electrodes or via a distant RF antenna following equation 2.28. When the applied frequency matches the resonance frequency of the CNT $\omega_0/2\pi$, the amplitude u_0 of the transverse bending mode becomes significant. The high resonance frequencies in the MHz-GHz range exceed the measurement bandwidth in the kHz-range (limited by an effective low-pass filter due to the device resistance and the cable capacitances), and therefore, direct, real-time measurements of the oscillations are not possible. For CNT bending modes, two readout techniques are commonly used, which we will discuss in the following.

Current rectification

The rectification of a time varying current signal in a device results in a non-zero DC signal if the conductance is nonlinear. For CNTs such nonlinear conductance can, for instance, occur due to Coulomb oscillations. A mechanical displacement of the CNT $u(t) = u_0 \cos(\omega_0 t)$ at resonance $\omega_0/2\pi$ periodically modifies the distance between the position of the CNT and the gate electrode, resulting in a modulation of the gate capacitance. This effect can be modeled by adding an alternating capacitance $C_\mathrm{g}^\mathrm{AC}(t) = \partial C_\mathrm{g}/\partial u \cdot u(t)$ to the static capacitance C_g^DC which affects the gate induced charge $q_\mathrm{c} = V_\mathrm{g} C_\mathrm{g}$, and therefore the current through the CNT. With our low measurement bandwidth in the kHz range we measure the effect of mechanical oscillation on the time-averaged current given by [4]

$$\langle I(u_0, V_\mathrm{g}) \rangle = I(V_\mathrm{g}) + \frac{u_0^2}{4} \left(\frac{V_\mathrm{g}}{C_\mathrm{g}} \frac{\partial C_\mathrm{g}}{\partial u} \right)^2 \frac{\partial^2 I}{\partial V_\mathrm{g}^2} + O(u_0^4). \tag{2.33}$$

The time-averaged current is proportional to the local curvature $\partial^2 I/\partial V_\mathrm{g}^2$ of the gate dependent current $I(V_\mathrm{g}) = G(V_\mathrm{g}) V_\mathrm{sd}$, which has important implications on the measurements. First, in order to measure a mechanically-induced change in the time-averaged current signal, it is beneficial to choose a gate voltage at which the current has maximum curvature. Second, in the Coulomb blockade regime, the curvature is negative around the maximum of a Coulomb peak and a dip in the current is expected when the tube oscillates at resonance, while the curvature is positive on the flanks resulting in a peak in the current.

Frequency mixing

In a frequency mixing technique, two RF signals at frequencies f_1 and f_2 are applied to an electric circuit and an output signal is generated with frequencies different from the input frequencies f_1 and f_2. The output signal usually has two frequency components at the sum and the difference of the input frequencies $f_1 \pm f_2$. For CNT resonators, the downward mixed component at the difference of the input frequencies can be chosen to be within the measurement bandwidth of the setup. Similarly to rectification, the oscillating CNT leads to an AC component of the gate capacitance C_g^AC. However, a second microwave drive tone is now applied to the source electrode, and the CNT is used as a frequency mixer.

The magnitude of the current through the suspended CNT device is given by the product of the modulated conductance δG due to mechanical oscillation and the applied RF voltage at the source with amplitude $V_\mathrm{sd}^\mathrm{AC}$ [78]

$$\delta I = \delta G V_\mathrm{sd}^\mathrm{AC} = \frac{1}{\sqrt{8}} \frac{\mathrm{d}G}{\mathrm{d}V_\mathrm{g}} \left(V_\mathrm{g}^\mathrm{AC} + V_\mathrm{g}^\mathrm{DC} \frac{C_\mathrm{g}^\mathrm{AC}}{C_\mathrm{g}} \right) V_\mathrm{sd}^\mathrm{AC}. \tag{2.34}$$

In distinction to the current rectification, the amplitude of the current does not depend on the second-order derivative (curvature) of the conductance but on the first-order derivative (slope).

A modified approach involves an impedance matching circuit transforming the device impedance to 50 Ω at the resonance frequency $\omega_0/2\pi$ of the CNT [83, 84, 75]. This setup allows for a measurement of the current noise, which is related to the displacement noise, giving rise to the detection of thermal vibrations and the determination of the thermal occupation of the resonator in the absence of driving [84].

2.3.4. Impact of Coulomb blockade on mechanical bending modes

In the previous section, we presented two measurement schemes for the changes in the current and the differential conductance induced by the mechanical resonance. On the other hand, the single-electron tunneling represents an external perturbation to the mechanical oscillations. In the following, we will calculate the modifications in the mechanical resonance due to single-electron tunneling in the Coulomb blockade regime, where we will follow the supplementary material from [13, 11].

We start with the electrostatic force between the quantum dot and the gate which is a modified version of the DC part of equation 2.28

$$F_{\mathrm{dot}} = \frac{1}{2}\frac{\partial C_{\mathrm{g}}}{\partial u}(V_{\mathrm{g}}^{\mathrm{DC}} - V_{\mathrm{dot}})^2 \approx \frac{1}{2}\frac{\partial C_{\mathrm{g}}}{\partial u}((V_{\mathrm{g}}^{\mathrm{DC}})^2 - 2V_{\mathrm{g}}^{\mathrm{DC}}V_{\mathrm{dot}}) \qquad V_{\mathrm{g}}^{\mathrm{DC}} \gg V_{\mathrm{dot}}. \tag{2.35}$$

Here V_{dot} is the electrostatic potential of the quantum dot which consists of two terms, a first term with the electrostatic potential arising from N charges on the dot and a second term generated by the applied gate voltage

$$V_{\mathrm{dot}} = \frac{-N|e|}{C} + \frac{C_{\mathrm{g}}V_{\mathrm{g}}^{\mathrm{DC}}}{C} = \frac{q_{\mathrm{dot}} + q_{\mathrm{c}}}{C}. \tag{2.36}$$

C is the total capacitance of the dot which could be modeled within the constant-interaction model following equation 2.19, q_{dot} the charge on the dot and $q_{\mathrm{c}} = C_{\mathrm{g}}V_{\mathrm{g}}^{\mathrm{DC}}$ the control charge. A non-zero V_{dot} is a direct consequence of the discreteness of charge in single-electron tunneling. In the absence of Coulomb blockade ($k_{\mathrm{B}}T \gg E_{\mathrm{C}}$), when the charge q_{dot} on the dot is continuous, the potential on the dot is $V_{\mathrm{dot}} = 0$ since $q_{\mathrm{dot}} = -q_{\mathrm{c}}$.

Equation 2.35 thus reduces to a force only determined by the DC gate voltage (cf. F_{DC} in equation 2.28). In equation 2.36 the charge on the dot q_{dot} is assumed as a staircase, as is the case for $T \longrightarrow 0, \Gamma \longrightarrow 0$. In practice, we operate in the limit $k_{\mathrm{B}}T \ll \Gamma$ and the charge steps are smeared out. At the transition from N to $N+1$ charges, it makes sense to talk in terms of average electron numbers $\langle N\rangle$ which are no longer restricted to integer charges (cf. figure 2.14a). This allows us to write q_{dot} as

$$q_{\mathrm{dot}} = -|e|\langle N(q_{\mathrm{c}})\rangle. \tag{2.37}$$

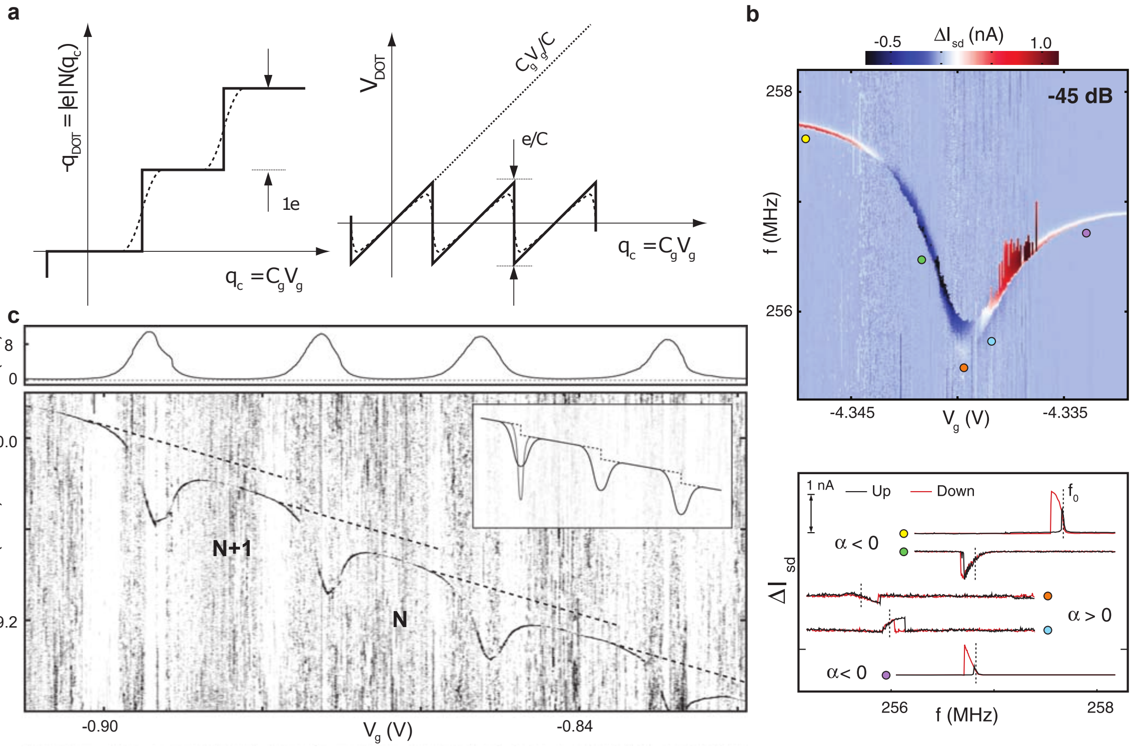

Figure 2.14.: Overview of the spring softening of the mechanical resonance. **a** Definition of the charge on the quantum dot at $T, \Gamma = 0$ (solid line) and finite T, Γ (dashed line) and definition of the dot potential V_{dot} with the sawtooth dependence on the control charge q_{c}. **b** Spring softening dip for the Duffing oscillator at a Coulomb diamond with change of the sign of the Duffing parameter α at the inflection points and respective resonance shape. The bifurcation broadens the areas with positive current (red) and negative current (blue). The background has been subtracted. **c** Measurement data for the spring softening. Upper: Current as a function of gate voltage showing Coulomb peaks. Lower: Spring softening at the Coulomb peaks and linear frequency dependence for diamonds corresponding to N holes. Inset: theoretical curve. Subfigures taken from [11].

In the following, the case of a mechanically excited CNT oscillating at a frequency f will be addressed. We can calculate the modification of the spring constant due to single-electron tunneling with equation 2.35 as follows

$$\delta k = -\frac{\mathrm{d}F_{\mathrm{dot}}}{\mathrm{d}u} = -\frac{\mathrm{d}}{\mathrm{d}u}\left(\frac{1}{2}\frac{\partial C_{\mathrm{g}}}{\partial u}(V_{\mathrm{g}}^{\mathrm{DC}} - V_{\mathrm{dot}})^2\right) = (V_{\mathrm{g}}^{\mathrm{DC}} - V_{\mathrm{dot}})\frac{\partial C_{\mathrm{g}}}{\partial u}\frac{\mathrm{d}V_{\mathrm{dot}}}{\mathrm{d}u} + \mathcal{O}\left(\frac{\partial^2 C_{\mathrm{g}}}{\partial u^2}\right) \qquad (2.38)$$

$$\delta k \approx \frac{V_{\mathrm{g}}^{\mathrm{DC}}(V_{\mathrm{g}}^{\mathrm{DC}} - V_{\mathrm{dot}})}{C}\left(\frac{\partial C_{\mathrm{g}}}{\partial u}\right)^2\left(1 - |e|\frac{\mathrm{d}\langle N(q_{\mathrm{c}})\rangle}{\mathrm{d}q_{\mathrm{c}}}\right). \qquad (2.39)$$

With $G = \Gamma/2 \cdot |e| \cdot C \cdot \mathrm{d}\langle N\rangle/\mathrm{d}q_{\mathrm{C}}$, for $\Delta E \gg k_{\mathrm{B}}T$, the result can be expressed in terms of Γ and the conductance

$$\delta k = \frac{V_{\mathrm{g}}^{\mathrm{DC}}(V_{\mathrm{g}}^{\mathrm{DC}} - V_{\mathrm{dot}})}{C}\left(\frac{\partial C_{\mathrm{g}}}{\partial u}\right)^2\left(1 - \frac{2G}{C\Gamma}\right). \qquad (2.40)$$

Equation 2.40 implies a softening of the spring constant due to the last term in brakets which depends on the conductance G. We therefore expect the respective dips in frequency to occur only in the vicinity of the Coulomb diamonds (cf. eq. 2.39, figure 2.14c).

The frequency shift of the mechanical resonance f_0 due to single-electron tunneling is given by

$$\delta f = f_0 \frac{\delta k}{2k} = \frac{f_0}{2k} \frac{V_{\mathrm{g}}^{\mathrm{DC}}(V_{\mathrm{g}}^{\mathrm{DC}} - V_{\mathrm{dot}})}{C} \left(\frac{\partial C_{\mathrm{g}}}{\partial u} \right)^2 \left(1 - \frac{2G}{C\Gamma} \right). \tag{2.41}$$

The frequency shift depends on V_{dot}. Its sawtooth dependence on $V_{\mathrm{g}}^{\mathrm{DC}}$ results in frequency shifts each time a charge is added to the quantum dot. This can be seen in discrete spacings between the resonance frequencies in the Coulomb blockade areas between the dips of softening.

Until now, we only considered small oscillation amplitudes for the resonator in the linear regime. For stronger drive, the complete Duffing equation 2.31 must be taken into account, including the nonlinear term, and the spring constant has to be modified $k \longrightarrow k + \alpha u^2$. The softening or hardening of the spring constant is determined by the sign of α. We can calculate α as the third derivative of the force with respect to the amplitude (neglecting second order derivatives of C_{g})

$$\alpha = -\frac{\mathrm{d}^3 F}{\mathrm{d}u^3} = \frac{\mathrm{d}^2}{\mathrm{d}u^2} \delta k(q_{\mathrm{c}}) = (V_{\mathrm{g}}^{\mathrm{DC}})^2 \left(\frac{\partial C_{\mathrm{g}}}{\partial u} \right)^2 \frac{\mathrm{d}^2 \delta k}{\mathrm{d}q_{\mathrm{c}}^2}. \tag{2.42}$$

Note that δk is the same as in the linear case and can be taken from equation 2.40. The Duffing parameter α is proportional to the curvature of $\delta k = \delta k(q_{\mathrm{c}}) = \delta k(V_{\mathrm{g}}^{\mathrm{DC}})$ and will change its sign at the inflection points of the frequency dip, as it becomes apparent in figure 2.14b.

2.4. Superconductivity in carbon nanotubes

Building superconducting circuits with CNTs is not straightforward, since single carbon nanotubes are not intrinsically superconducting. Potential signatures of intrinsic superconductivity have only been found in ropes of CNTs [85]. However, a supercurrent can be injected via the superconducting proximity effect when the CNT is contacted by a superconductor. This chapter is dedicated to the superconducting proximity effect in CNTs. We will first review the basic physics of superconductivity, discuss the transport through a superconductor - normal conductor - superconductor weak link and apply the theory of CNT quantum dots presented in chapter 2.2.3 to superconducting contacts. The last part focuses on the dynamics of the Josephson junction and SQUIDs.

2.4.1. Basics of superconductivity

Superconductivity is a many-body, quantum mechanical phenomenon that occurs in certain materials when they are cooled below a critical temperature T_{c}. At this critical temperature, the material undergoes a phase transition from the normal conducting into the superconducting state, which is characterized by zero electrical resistance and perfect diamagnetism[2]. The latter one is also known as the Meissner-Ochsenfeld effect and is caused by screening currents flowing on the surface of the superconductor that expel the magnetic field inside the superconductor.

On a microscopic level, these effects can be explained by the BCS theory [86]. Two electrons can combine to a so-called Cooper pair with less energy than the kinetic energy of the two individual electrons. For this to be energetically favorable, an attractive electron-electron interaction needs to be established between two electrons, which can, for instance, be mediated by the lattice in the form of phonons [87]. The corresponding pairing energy of two electrons or the breaking energy of a Cooper pair is 2Δ, where Δ is called the superconducting gap. In the case of conventional superconductivity, the spin part of the wave function is antisymmetric and the two electrons of a Cooper pair have opposite momentum and spin ($|\mathbf{k}\uparrow, -\mathbf{k}\downarrow\rangle$). The integer spin results in a behavior similar to bosons, and thus all Cooper pairs form a single coherent macroscopic state, the BCS ground state with a single macroscopic phase φ, which is given by [88]

$$|\Psi_{\mathrm{BCS}}\rangle = \prod_k \left(|u_k| + |v_k| e^{\mathrm{i}\varphi} c^\dagger_{k,\uparrow} c^\dagger_{-k,\downarrow}\right) |0\rangle \tag{2.43}$$

with the vacuum state $|0\rangle$, creation operator of an electron $c^\dagger_{k,\sigma}$ with momentum k and spin σ and the probability of an occupied pair state $|v_k|^2$ and unoccupied pair state $|u_k|^2$.

Excitations from the BCS ground state result in the creation of pairs of quasiparticles, and each pair requires an energy of $> 2\Delta$. The dispersion relation of a single quasiparticle relative to the chemical potential μ is given by [88]

$$E_k = \sqrt{\Delta^2 + \epsilon_k^2} = \sqrt{\Delta^2 + \left(\frac{\hbar^2 k^2}{2m} - \mu\right)^2}. \tag{2.44}$$

The hyperbolic dispersion relation is drawn in figure 2.15 and we can see that the superconducting gap leads to a mixing of electron-like and hole-like excitations, which is different in a normal metal ($\Delta \to 0$) where both contributions can be separated. There are no quasiparticle states available for $E \leq \Delta$ and the quasiparticle density of states can be computed as [88]

$$D_{\mathrm{sc}}(E) = \begin{cases} D_{\mathrm{nc}}(\mu) \frac{E}{\sqrt{E^2 - \Delta^2}}, & E \geq \Delta \\ 0, & \text{else.} \end{cases} \tag{2.45}$$

$D_{\mathrm{nc}}(\mu)$ denotes the DOS in the normal conducting state and is assumed to be constant around the chemical potential. A common representation of the quasiparticle density of states is the semiconductor model [88], as shown in figure 2.15b. We will later use this representation to explain tunneling processes of quasiparticles.

---

[2] for type I superconductors

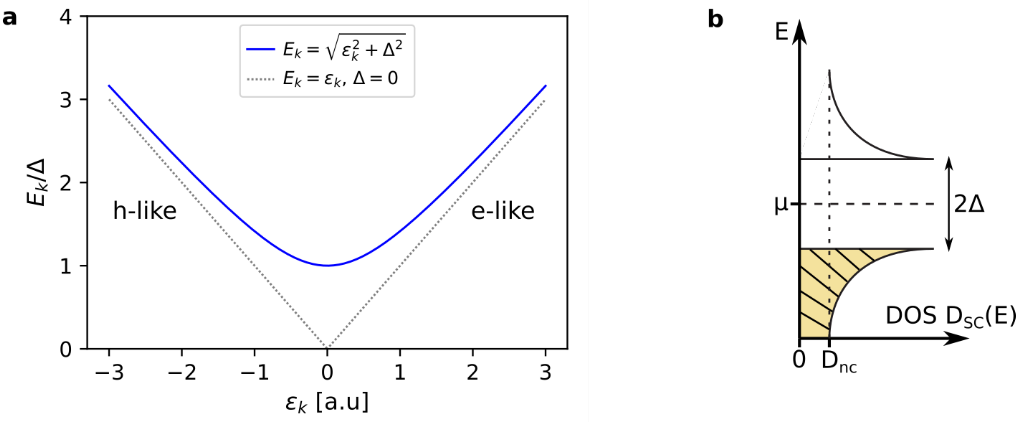

Figure 2.15.: Quasiparticle dispersion and density of states. a Energy dispersion of quasiparticles and comparison to pure electronic/hole excitations (grey dashed). **b** Quasiparticle density of states (DOS) in the semiconductor model with occupied states below the chemical potential μ marked in yellow (at $T = 0$).

The BCS theory also yields a characteristic BCS coherence length related to the superconducting gap [88]

$$\xi_{\mathrm{BCS}}(T) = \frac{\hbar v_{\mathrm{F}}}{\pi \Delta(T)}. \tag{2.46}$$

For clean superconductors (electron mean free path shorter than the average distance of the two electrons of a single Cooper pair) this BCS coherence length describes the spatial extension of a Cooper pair (at zero temperature) also known as the superconducting coherence length $\xi_0 \equiv \xi_{\mathrm{BCS}}(0)$. Likewise, it can be seen as the distance over which the superconducting electron density changes from zero on the surface to the bulk value of the superconductor [89].

Since the binding energy of a Cooper pair is finite as well as the number of accessible Cooper pair states[3], magnetic fields are only expelled up to a critical field $H_{\mathrm{c}}(T)$ which is inherently related to a maximum supercurrent density j_{c} that is linked to a critical current I_{c}. In general, two types of superconductors can be distinguished. In a type I superconductor, the perfect diamagnetism (Meissner phase) persists until the phase transition, while in a type II superconductor, two phases exist below the transition to the normal state. The first phase is a Meissner phase until a first critical field H_{c1} when magnetic flux can partially penetrate the superconductor and form vortices until superconductivity is broken at a second critical field H_{c2} (Shubnikov phase). The main superconductor used in this work is molybdenum rhenium and a type II superconductor.

---

[3] For phononic interaction only electrons with one particle energies $\mu < E < \mu + \hbar\omega_{\mathrm{D}}$ with the Debye frequency ω_{D} can participate in pairing which restricts the corresponding k-states.

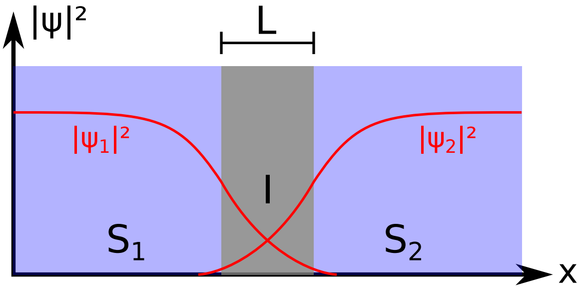

Figure 2.16.: Josephson effect for an insulator (I) sandwiched between two superconductors (S_1, S_2). The wave functions overlap in the normal conductor and Cooper pairs can tunnel through the junction of length L. Inspired by [90].

2.4.2. Superconducting proximity effect

In the previous sections, we focused only on isolated superconductors, now we will discuss a system consisting of two superconductors S_1 and S_2 separated by a normal conductor (N) or insulator (I), denoted SNS or SIS junction. In our case, the CNT can be approximated as a normal conductor and the two superconductors consist of the same material (with the same superconducting gap Δ, but different superconducting phases φ_1 and φ_2).

Josephson effect

In a normal metal - insulator contact, the wave function of electrons decays exponentially in the insulator region. If this insulator is thin and encapsulated by two normal conducting regions, the exponentially decaying electron wave functions of the two metals can overlap in the insulator region and a finite tunneling current can be measured. Replacing the normal conductor with a superconductor implies that there are no electrons around the Fermi energy available for tunneling and the tunnel current should be negligible. However, the superconducting correlations also extend into the insulating region, as shown by the overlap of the macroscopic wave functions in figure 2.16. As Josephson [91] predicted, Cooper pairs can tunnel as one entity through the insulating junction, which can be interpreted as tunneling of the macroscopic wave function. The effect of supercurrent flowing through a non-superconducting region between two superconductors is referred to as the Josephson effect, and the corresponding junction is called a Josephson junction.

This supercurrent depends on the phase difference $\varphi = \varphi_1 - \varphi_2$ of the two superconductors across the junction and for an SIS junction it has the following current-phase relation (CPR), known as first Josephson equation

$$I = I_\mathrm{c} \sin(\varphi). \tag{2.47}$$

I_c is the critical Josephson current determined by the coupling strength of the two superconductor and gives the maximum Josephson current. Compared to a normal metal, where a current is only driven by a difference in the electrical potential, for a superconductor, the phase difference drives a supercurrent through the Josephson junction, which in the absence of external voltages is constant (DC Josephson effect). Note that the simple sinusoidal dependence of the CPR of equation 2.47 is only applicable to junctions in the weak coupling limit (e.g. SIS tunnel junction), while the 2π periodicity of the phase difference φ is a fundamental property independent of the material, geometry, and model used for the derivation [92].

The application of a finite bias voltage across the junction results in a phase evolution, given by the second Josephson equation with the flux quantum $\Phi_0 = h/2e$

$$\frac{\mathrm{d}\varphi}{\mathrm{d}t} = \frac{2eV}{\hbar} = \frac{2\pi}{\Phi_0}V. \tag{2.48}$$

An integration of this equation over time and insertion into the first Josephson equation results in an alternating current across the junction for $V \neq 0$. This effect is known as the AC Josephson effect with the characteristic Josephson frequency $\omega_\mathrm{J} = 2eV/\hbar$.

In the case of an SIS junction with two identical superconductors, the BCS theory can yield a relation between the normal state resistance and the critical current, known as Ambegaokar-Baratoff relation [93]

$$I_\mathrm{c}(T)R_\mathrm{N} = \frac{\pi\Delta(T)}{2e}\tanh\left(\frac{\Delta(T)}{2k_\mathrm{B}T}\right) \xrightarrow{T\to 0} \frac{\pi\Delta(0)}{2e}. \tag{2.49}$$

SN contact

From now on the insulator is replaced by a normal conductor to model our CNT. Transport through the normal conductor could still occur through direct Cooper pair tunneling, as it is the case for the usually few nm thick insulators (cf. figure 2.16). However, in SNS tunneling experiments, a non-zero supercurrent can still be observed over a distance ranging from 100 nm to several µm much larger than the superconducting coherence length, which must rely on other mechanisms. In contrast to the insulator in an SIS junction, the normal conducting metal in an SNS junction has electronic states available at the Fermi level, which may suggest supercurrent transport through the SNS junction via electron hole pairs in the normal conducting region.

In the following, we assume $\Delta \gg k_\mathrm{B}T$ and consider a normal conductor shorter than the phase coherence length $L \ll L_\phi$. The transport through an SNS junction can be divided into different regimes depending on the ratio of the junction length L to the superconducting coherence length $\xi = \pi\xi_0$ and the electron mean free path ℓ in the normal metal.

The transport through a normal conductor is ballistic, when its length is shorter than the electron mean free path ℓ, i.e. $L < \ell$ and diffusive when $L > \ell$. Transport in CNT junctions with $L <$ 1 µm can typically be considered ballistic.

An SNS junction operates in the short-junction regime, when $\xi \gg L$ and in the long-junction regime when $\xi \lesssim L$ [94]. An alternative definition of the short- and long-junction regime can be given in terms of classical energy scales. The energy scale of an electron

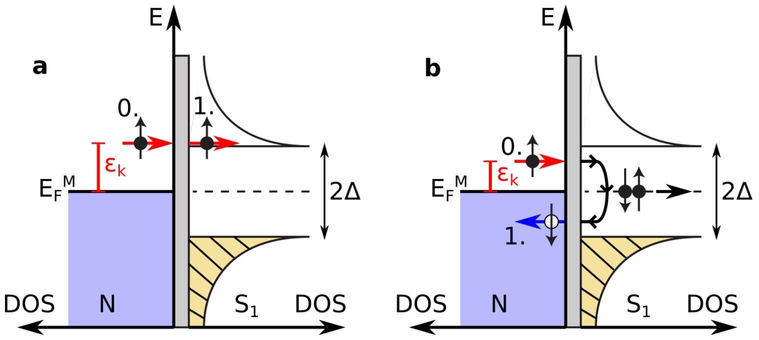

Figure 2.17.: Normal conductor-superconductor (NS) contact. Andreev reflection occurs for high contact transparency $T_\nu \longrightarrow 1$. **a** If the kinetic energy is larger than the superconducting gap $\epsilon_k > \Delta$ an incoming electron can find unoccupied quasiparticle states and can tunnel. **b** If the kinetic energy of the incoming electron is not sufficient to overcome the superconducting gap $\epsilon_k < \Delta$, the electron can be Andreev reflected as a hole with inverse $\mathbf{k}$ and under simultaneous injection of a right-moving Cooper pair in the superconductor S_1. The occupied states in the normal conductor are shown in blue and in hatched yellow in S_1. Note that the DOS in the normal conductor is modified close to the interface due to the proximity effect, the DOS drawn here is far away from the interface.

that passes the normal conductor can be expressed in the diffusive and ballistic limit as follows

$$\tilde{E} = \begin{cases} \frac{\hbar v_F}{L}, & \text{ballistic limit} \\ \frac{\hbar D}{L^2}, & \text{diffusive limit.} \end{cases} \tag{2.50}$$

The energy $E_{th} = \frac{\hbar D}{L^2}$ with diffusion constant $D = \ell v_F/3$ is called the Thouless energy [95]. This allows us to express the short-junction regime equivalently as $\tilde{E} \gg \Delta$ and the long-junction regime as $\tilde{E} \leq \Delta$. For a junction length of $L < 500\,\text{nm}$ in this work and a Fermi velocity of $v_F \approx 8 \times 10^5\,\text{m/s}$, we can calculate $\tilde{E} > 1\,\text{meV}$. In the cryogenic measurements in chapter 6.3, the proximity-induced gap is estimated for our devices to $\sim 1.5\,\text{meV}/4$, which places us slightly in the short-junction limit.

For the derivation of the microscopic process at the SN junction, we consider a simple NS_1 junction and an electron in the normal metal approaching the contact interface with kinetic energy ϵ_k, where ϵ_k is measured relative to the Fermi level. The contact itself has a transparency of $0 < T_\nu < 1$. If the contact is opaque ($T_\nu \longrightarrow 0$), the electron cannot enter the superconductor and will be reflected as an electron (normal reflection). For a transparent contact ($T_\nu \longrightarrow 1$) the situation is more interesting. If $\epsilon_k > \Delta$, there are empty quasiparticle states in the superconductor and the electron can tunnel into these states with the result of a quasiparticle in the superconductor. The conduction is determined by the quasiparticle density of states and reaches a maximum when $\epsilon_k = \Delta$. However, if $\epsilon_k < \Delta$, there are no quasiparticle states available in the superconductor. In this case, the electron can be reflected back as a hole if energy, charge, and momentum are conserved in a process called Andreev reflection. Energy is conserved by reflection as a hole with energy $-\epsilon_k$. Charge conservation requires that the charge of $2e$ must be transferred to the superconductor, which can be realized if the reflection process generates a Cooper pair in the superconductor. The momentum of a Cooper pair is $2\mathbf{k}_F$ and momentum conservation requires $2\mathbf{k}_\mathrm{F} = \mathbf{k}_e + \mathbf{k}_h$, which implies an opposite propagation direction of the hole compared to the incident electron. Andreev reflection leads to a phase shift of the reflected hole or electron, which is given by [45]

$$\phi_h - \phi_e = \pm\varphi_1 + \arccos\left(\frac{\epsilon_k}{\Delta}\right) \qquad \begin{cases} +, & \text{incident electron} \\ -, & \text{incident hole.} \end{cases} \tag{2.51}$$

Similar to a particle incident from the normal conducting side, Andreev reflection can also occur if a Cooper pair from the superconducting side penetrates the contact interface, resulting in the formation of an electron hole pair in the normal conductor which is also called Andreev pair. Equation 2.51 implies that this Andreev pair carries information about the superconducting phase φ_1, and thus superconducting correlations also spread into the normal conductor and induce a (reduced) superconducting gap in the vicinity of the interface. This is the superconducting proximity effect. The characteristic length scale ξ_n over which the proximity-induced superconductivity decays, is determined by the coherence length of the *e*-*h* pair in the normal conductor ($\xi_\mathrm{n} = \hbar v_\mathrm{F}/2\pi k_\mathrm{B}T$ in the clean limit [88], e.g. for a ballistic CNT).

SNS contact with zero voltage bias

We consider a S_1NS_2 junction with the two superconductors S_1 and S_2 with the same superconducting gap Δ but different phases φ_1 and φ_2 and a normal conductor in between and the following process.

a

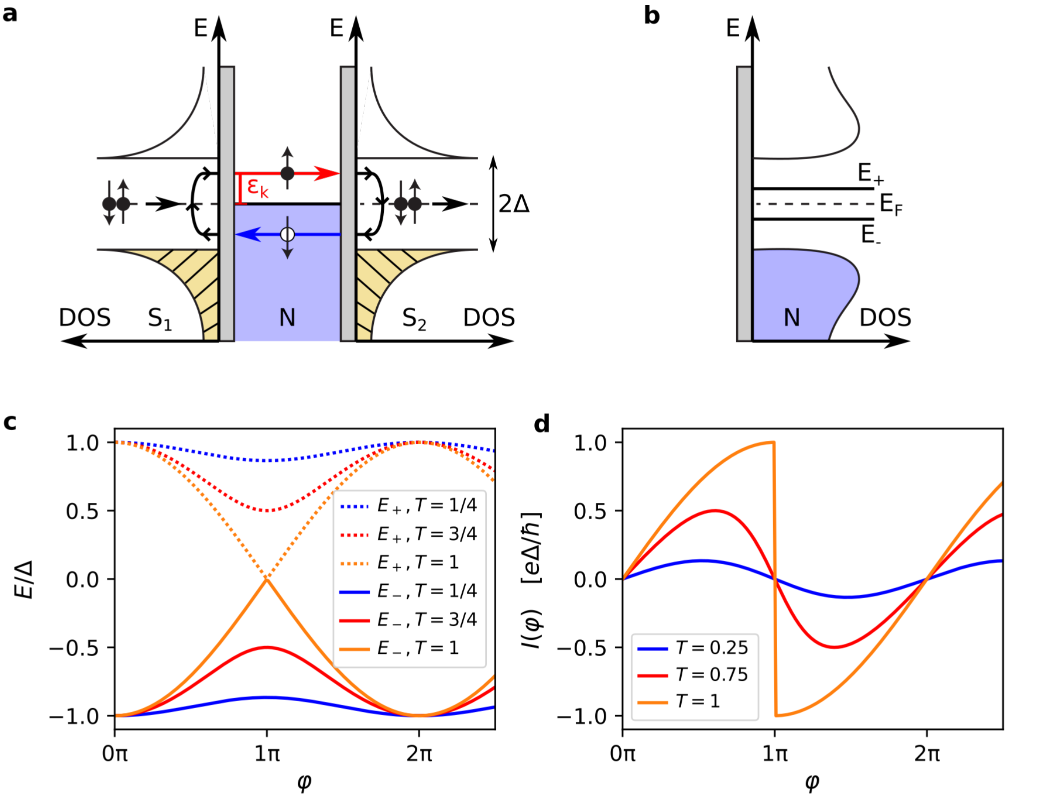

Figure 2.18.: SNS contact and Andreev bound states (ABS). a Andreev reflections of an electron at kinetic energy ϵ_k at the two NS interfaces result in a closed loop transporting supercurrent through the normal conductor. **b** The DOS in the normal conductor is actually not constant as drawn in **a** for simplicity, but modified due to the proximity effect and the emergence of ABS (inspired by [97]). **c** Energy dispersion of the ABS for different junction transparencies (cf. eq. 2.53). The ground state E_- is occupied at $T = 0\,\mathrm{K}$ and the excited state E_+ unoccupied. **d** Current-phase relation (CPR) for different junction transparencies (cf. eq. 2.55), differing fundamentally from the sinusoidal CPR for $T_\nu \longrightarrow 0$.

For now we assume a short junction, $L \ll \xi$, i.e. negligible phase evolution due to propagation in the normal conductor. The energy of the ABS below the superconducting gap Δ with ν transmission channels in the normal conductor and a non-perfect transmission T_ν gives the expression [45, 92]

$$E_\nu(\varphi) = \pm\Delta\sqrt{1 - T_\nu \sin^2(\varphi/2)}. \tag{2.53}$$

From this expression, the current-phase relation $I(\varphi)$ can be inferred by using

$$\frac{\mathrm{d}E}{\mathrm{d}t} = \frac{\partial}{\partial\varphi}\sum_\nu E_\nu(\varphi)\frac{\mathrm{d}\varphi}{\mathrm{d}t} = VI \tag{2.54}$$

and the second Josephson equation 2.48, linking the phase derivative to the voltage. The CPR at zero temperature for positive ABS energy is given by [45]

$$I(\varphi) = -\frac{2e}{\hbar}\sum_\nu \frac{\partial E_\nu}{\partial\varphi} = \frac{e\Delta}{2\hbar}\sum_\nu \frac{T_\nu \sin\varphi}{\sqrt{1 - T_\nu \sin^2(\varphi/2)}}. \tag{2.55}$$

One can see that the energy of the ABS oscillates periodically with the phase difference φ, which in the optical analogue, corresponds to a change in the cavity length by moving the mirrors [97]. A phase difference of $\varphi = 0$ for any transmission T_ν implies that the two ABS hit the superconducting gap and start to show quasiparticle-like behavior, resulting in a zero net current across the junction. In general, the CPR itself differs from the CPR of the first Josephson equation 2.47, but in the limit of opaque contact barriers $T_\nu \ll 1$ the CPR 2.47 is recovered with $I(\varphi) = I_\mathrm{c} \sin(\varphi)$, where $I_\mathrm{c} = (e\Delta/2\hbar) \sum_\nu T_\nu = (\pi\Delta/2e)G_\mathrm{N}$ [45], and therefore, it is proportional to the normal state conductance G_N and in agreement with the Ambegaokar-Baratoff relation 2.49. This is fundamentally different in the limit of transparent contact barriers $T_\nu \longrightarrow 1$, where one obtains $I(\varphi) = I_\mathrm{c} \sin(\varphi/2)$ (for $-\pi < \varphi < \pi$) and a discontinuity at $\varphi = \pm\pi$ with $I_\mathrm{c} = (\pi\Delta/e)G_\mathrm{N}$, as shown in figure 2.18.

SNS contact with finite bias voltage

In the previous section, we considered ABS at zero bias voltage across the junction. The finite voltage will induce a linear time evolution of the phase difference, and at low bias $eV \ll \Delta$, the oscillating ABS energy will simply result in an AC current, following equation 2.48 and 2.55. However, if $eV \lesssim \Delta$, the rate at which the phase difference changes and therefore the Josephson frequency is of the same order as the ABS energy. The adiabatic assumption that the ABS energies follow the time evolution of the phase is no longer fulfilled [45].

The dominant charge carrier transport is via multiple Andreev reflections (MAR) of quasiparticles [98], which will be discussed in the semiconductor picture. If $eV > 2\Delta$, a quasiparticle from an occupied state in superconductor S_1 can find an unoccupied state in superconductor S_2 and a current can be measured only due to quasiparticle tunneling. If $eV < 2\Delta$, there are no states available in the superconductor S_2 and multiple Andreev reflections can occur, leading to subgap conductance resonances.

The MAR process can be described in terms of the same two Andreev reflection processes $\mathbf{a_i}$ and $\mathbf{b_i}$ involved in ABS with the only difference that the Fermi energies of the two superconductors are shifted due to the applied voltage bias and that two quasiparticle tunneling processes need to be added at the start and the end. We start with an electron from an occupied state at the Fermi level of the left electrode entering the normal region in a normal tunneling process. This is the initial condition in $\mathbf{a_1}$, and after propagation in the normal conductor, the electron at energy $-\epsilon_k$ below the Fermi level at S_2 is Andreev reflected at the NS_2 interface as a hole at energy ϵ_k, and the process $\mathbf{b_1}$ starts with the hole propagating to the NS_1 interface and Andreev reflection. Due to the finite voltage, the hole energy and the energy of the initial electron entering the normal region are not symmetric with respect to the Fermi level in S_1. Therefore, in contrast to the zero voltage case, the loop is not closed and the energy of the Andreev reflected electron at the NS_1 interface is different from the initial electron. A succession of these processes leads to an increase in electron energy in the normal conductor and when the energy exceeds the gap of the superconductor S_2 or S_1, the quasiparticle can find free states and tunnel into the superconductor in a normal tunneling process. The probability of the normal tunneling

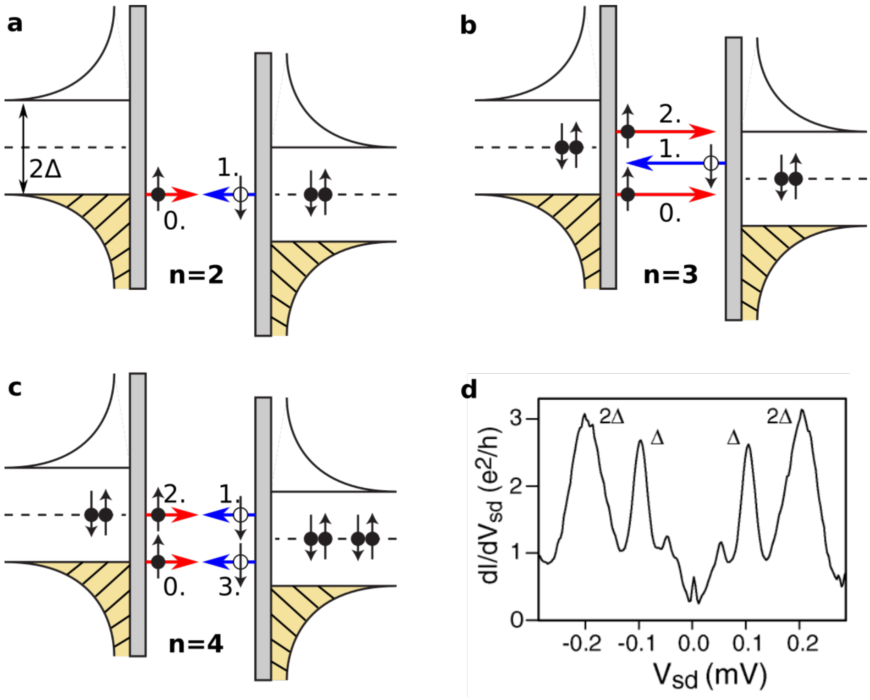

Figure 2.19.: Multiple Andreev reflections (MARs). Schematic representation of the energy as function of quasiparticle DOS with different multiple Andreev reflection processes. **a** MAR of second order ($eV_{sd} = 2\Delta/2$): A quasiparticle tunnels into the normal conductor, leaves a hole in the valence band of S_1 (0.) and is Andreev reflected at the NS_2 interface under emission of a hole (1.) and a Cooper pair in S_2. The hole can tunnel into S_1, and thus two charges are transferred. **b** MAR of third order ($eV_{sd} = 2\Delta/3$): Similar to before a quasiparticle tunnels into the normal conductor, leaves a hole in the valence band of S_1 (0.) and is Andreev reflected at the NS_2 interface under emission of a hole (1.) and a Cooper pair in S_2. The hole is again Andreev reflected as electron (2.) at the NS_1 interface by elimination of a Cooper pair. It has sufficient energy to tunnel into the unoccupied states in S_2, and thus 3 charges are transferred. **c** MAR of fourth order ($eV_{sd} = 2\Delta/4$): The quasiparticle is Andreev reflected at the NS_2 interface as hole (1.) with transfer of a first Cooper pair in S_2, the hole is Andreev reflected as electron (2.) at the NS_1 interface under elimination of a Cooper pair. The electron (2.) is again Andreev reflected as hole (3.) at the NS_2 interface with the transfer of a second Cooper pair. The resulting hole (3.) can tunnel into the valence band of S_1. In total 4 charges are transferred. **d** Measurement of MARs from [99] together with the quasiparticle onset at 2Δ. The second-order process ($eV_{sd} = \Delta$) has high differential conductance, but higher orders are suppressed.

processes at the beginning and at the end is higher if these processes are resonant with the van-Hove singularities in the DOS of S_1 and S_2. This leads to conductance peaks at multiples of $eV = 2\Delta/n$.

The first three MAR processes at energies $eV = \Delta, 2\Delta/3, 2\Delta/4$ are shown in figure 2.19. For n odd, the electron and reflected hole always have different energies, and the electron ends up in the empty states of the conduction band of superconductor S_2. On the contrary, for n even, electron and Andreev reflected hole can have the same energy and the MAR process ends with a hole in the valence band of the superconductor S_1 where the initial electron originated from. In general, an MAR process of order n transports n charges through the junction and involves $n-1$ Andreev reflections. Usually, the transmission at the NS interfaces is $T_\nu < 1$, and thus higher-order MAR processes scaling with T_ν^n are suppressed.

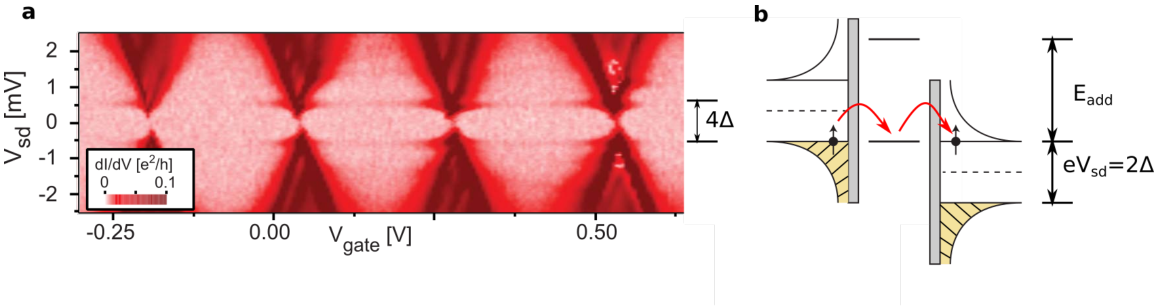

Figure 2.20.: Superconducting quantum dot in the weak coupling regime. a Differential conductance map showing Coulomb diamonds pushed 4Δ apart (subfigure from [101]). **b** Corresponding DOS in the semiconductor image.

2.4.3. Induced superconductivity in quantum dots

In the previous section, we have assumed a constant DOS at the Fermi level of the normal conductor, as it is approximately the case for many metals. However, for CNTs, electronic transport is better modeled by a quantum dot with discrete energy levels, as described in section 2.2.3. The aim of this section is to extend these findings to a CNT quantum dot with superconducting leads. The relevant energy scales are the charging energy E_C, the quantum level spacing ΔE, the tunnel coupling Γ, and additionally the superconducting energy gap Δ[4]. The different regimes are now discussed following the review [100].

Weak coupling regime

In the weak coupling regime $\Gamma \ll E_C, \Delta$, higher-order tunneling processes are suppressed and supercurrent transport cannot be observed. First-order tunneling processes dominate in the Coulomb blockade regime and only quasiparticle transport takes place. The differential conductance in the charge stability diagram shows Coulomb diamonds where the conducting regions are pushed apart by 4Δ (cf. figure 2.20). This is due to the absence of single-particle states within the superconducting gap and in order to align occupied quasiparticle states and free quasiparticle states, the energy $|eV| > 2\Delta$ needs to be supplied[5]. The non-constant quasiparticle DOS modulates the differential conductance and due to the divergence in the DOS, a conductance peak occurs at $\pm\Delta$, followed by a zone with negative differential conductance [100]. In the case of normal conducting electrodes, we saw that elastic cotunneling can occur if the tunnel coupling is increased and the chemical potentials of source and drain are aligned. For superconducting electrodes, however, due to the superconducting gap, no quasiparticle tunneling processes can occur below $|eV| < 2\Delta$.

---

[4] In the experiment, a non superconducting top contact material is used (e.g. Pd or Pt) and the superconducting gap has to be replaced by a reduced superconducting gap Δ^* at the electrode surface.

[5] Since in the charge stability diagram V_{sd} is swept from negative to positive, the superconducting gap is visible as $2 \cdot 2\Delta$ in the charge stability diagram and figure 2.20b only shows the situation for $V_{sd} > 0$.

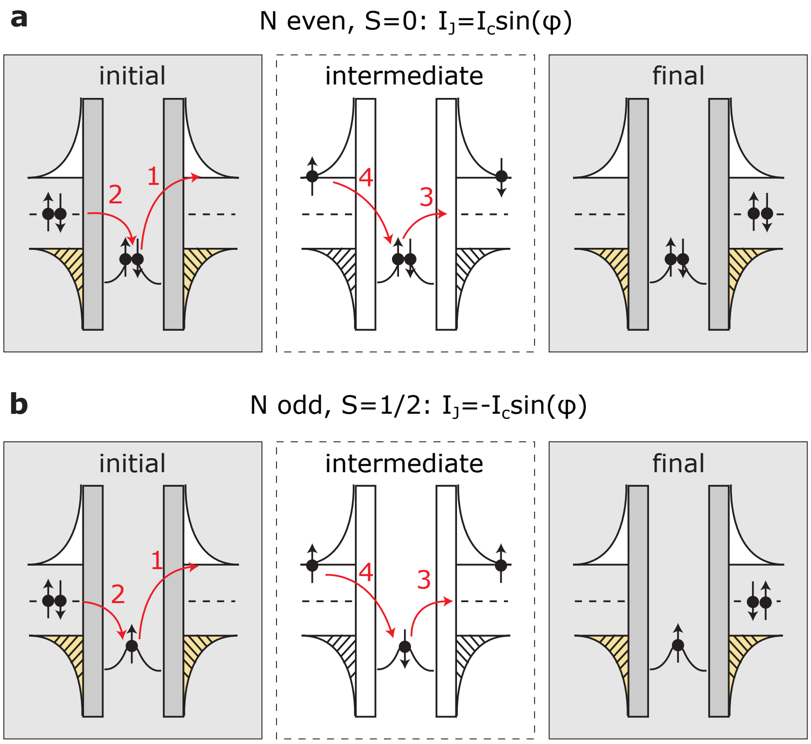

Figure 2.21.: Cotunneling for even and odd electron occupation. Shown for spin degeneracy neglecting valley degeneracy and for BCS singlet superconductors with zero spin. **a** For an even dot occupation two electrons with opposite spin are in the highest shell and due to Pauli's principle, the electron tunneling onto the dot in the virtual process must have the same spin as the one leaving the dot. This leaves the dot's spin state unchanged in the intermediate state and forms a 0-junction transferring a Cooper pair without an additional phase shift. **b** If the occupation is odd, in order to recombine to a Cooper pair at the final stage, an electron of opposite spin must tunnel onto the dot in the intermediate state and the spin ordering of the Cooper pair in the final state $|\psi\rangle_\mathrm{f}$ is reversed, leading to a phase shift of π: $|\psi\rangle_\mathrm{f} = (|\downarrow\uparrow\rangle - |\uparrow\downarrow\rangle) = e^{i\pi}|\psi\rangle_\mathrm{i} = -|\psi\rangle_\mathrm{i}$. Such a junction is called π-junction and characterized by a reversal of the supercurrent. Adapted from [100] with permission from Springer Nature.

Intermediate coupling regime

The intermediate coupling regime is defined by $\Gamma \sim E_\mathrm{C} \sim \Delta$. In contrast to the weak coupling regime, the condition $\Gamma \sim \Delta$ gives rise to a measurable supercurrent when an energy level of the quantum dot is aligned with the Fermi level of source and drain (resonant transport). Beyond that, when $\Gamma \sim E_\mathrm{C}$, higher-order cotunneling processes are more likely to occur, as is also the case in the normal conducting state. In the superconducting case, fourth-order cotunneling processes contribute to a smaller but detectable off-resonant supercurrent, which depends on the occupation parity of the dot (cf. figure 2.21). For even occupation, Cooper pair transfer occurs without phase shift (0-junction), while for odd occupation, the transferred Cooper pair accumulates a phase shift of π, which results in an inversion of the supercurrent (π-junction). Note that the interplay with the Kondo effect and the fourfold degeneracy of a CNT can lead to more complicated physics [102, 103, 104, 105], which will not be discussed in this chapter.

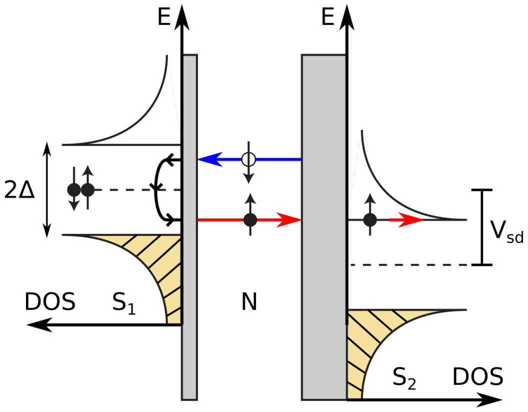

Figure 2.22.: Andreev bound state spectroscopy for asymmetric barriers. The ABS is pinned to the stronger coupled superconductor S_1, while the quasiparticle DOS in the weaker coupled superconductor S_2 can be used as probe. By changing the bias voltage, the spike in the quasiparticle DOS in the probe can scan the subgap of the better coupled superconductor. Conductance resonances occur when the quasiparticle DOS matches the energy of an ABS. Inspired by [108].

At finite bias, MARs start to emerge with increasing tunnel coupling Γ. They are located at $eV = 2\Delta/n$ and their intensity strongly depends on the DOS in the quantum dot, favoring processes that pass through an energy level of the quantum dot.

Strong coupling regime

In the strong coupling regime characterized by $\Gamma \gg E_C$ and $\Gamma \gg \Delta$, Coulomb blockade is absent and the addition energy is only specified by the quantum level spacing ΔE, and thus more than one electron can be added to the quantum dot. The transport depends on the ratio of V_{sd} and Γ.

For $|eV_{sd}| > 2\Delta$, Fabry-Pérot interferences can be observed for quasiparticles when $\Delta E \geq \Gamma$. Below the gap ($eV_{sd} < 2\Delta$), Andreev reflections are likely to occur due to the high transmission coefficient T_ν. At finite bias, the current is transported through MARs. At zero bias, the supercurrent is mediated through ABS and manifests itself as a high conductance line in the case of symmetric contact barriers ($\Gamma_s \approx \Gamma_d$) [106]. If the SN contacts are highly asymmetric, the ABS are pinned to the better coupled superconductor and the weaker coupled superconductor can be used as a probe for the dispersion of the ABS [107, 108, 97] (cf. figure 2.22).

The critical current also shows a periodic gate dependence, and is maximum when a level in the quantum dot is aligned with the Fermi energy of the superconductors. The maximum critical current has been calculated in [109] for the case of equal barriers ($\Gamma_s = \Gamma_d = \Gamma$) and zero temperature to

$$I_c^{\max} = \frac{e}{\hbar}\frac{\Delta\Gamma}{\Delta + \Gamma}. \tag{2.56}$$

In the limit of $\Gamma \gg \Delta$, this expression can be written in terms of the conductance quantum $G_0 = 2e^2/h$, and for a spin-degenerate channel, the maximum supercurrent is also quantized [100], similarly to the Landauer-Büttiker formalism (cf. eq. 2.12)

$$I_c^{\max} = \frac{\pi\Delta}{e} G_0. \tag{2.57}$$

2.4.4. Circuit description of Josephson junctions

In the last sections, we discussed the microscopic origin of the Josephson effect in SNS junctions. In real circuits, the total current includes contributions from other sources beyond the supercurrent. As we will see in the following, the essential physics of Josephson junctions in the voltage state can also be modeled by classical circuit elements. This provides an alternative simplified description that can be used to understand the measurements in the experiment.

In the following, we consider the two limits (i) $T \longrightarrow 0\,\mathrm{K}$ and (ii) $|eV| \ll 2\Delta$. In this case, the Josephson junction dynamics is governed by the DC Josephson effect (eq. 2.47), resulting in a supercurrent without electrical resistance at zero bias voltage and the AC Josephson effect at finite voltage (eq. 2.48). The time oscillations in the CPR at finite bias voltage cannot be resolved in DC measurements which detect only the time-averaged current $\langle I \rangle$. Thus, the supercurrent for a simple tunnel junction is only given by the DC part

$$I_J = I(\varphi) = I_c \sin(\varphi). \tag{2.58}$$

Releasing the first condition (i), at finite temperature, a part of the Cooper pairs is thermally excited and broken up to quasiparticles. Regarding the second condition (ii), a finite voltage can also break up Cooper pairs. Quasiparticles do not contribute to the current in the zero-voltage state, but as soon as a finite voltage is applied to a junction, the resistive quasiparticle current must be taken into consideration. For an SNS junction, the resistance of the quasiparticle current is proportional to the normal state resistance of the SNS junction [88]

$$I_N = \frac{V}{R_N}. \tag{2.59}$$

In addition, there is also a capacitive effect, which arises from the two superconductors facing each other. For an SIS junction, the capacitance can be large, but for a CNT Josephson junction, it is typically small. A non-zero time derivative $\mathrm{d}V/\mathrm{d}t$ causes a displacement current proportional to the junction capacitance [110]

$$I_D = C\frac{\mathrm{d}V}{\mathrm{d}t}. \tag{2.60}$$

RCSJ model

The dynamics of a Josephson junction in the finite voltage state can be described by the three contributions, the superconducting channel I_J, the resistive channel I_N and the capacitive channel I_D, which can be modeled in a parallel junction (cf. inset in figure 2.23a). The model is called RCSJ or Resistively Capacitively Shunted Junction model [88, 110]. The second Kirchhoff's law states

$$I = I_\mathrm{J} + I_\mathrm{D} + I_\mathrm{N} = I(\varphi) + C\frac{\mathrm{d}V}{\mathrm{d}t} + \frac{V}{R_\mathrm{N}}. \tag{2.61}$$

By multiplying with $\hbar/2e$ and with the help of the second Josephson equation 2.48 one obtains

$$\frac{\hbar}{2e}(I(\varphi) - I) + C\left(\frac{\hbar}{2e}\right)^2 \ddot{\varphi} + \frac{1}{R_\mathrm{N}}\left(\frac{\hbar}{2e}\right)^2 \dot{\varphi} = 0. \tag{2.62}$$

For an SNS junction with arbitrary transmission coefficients T_ν, the CPR can be complicated (cf. eq. 2.55). Here the focus will be on the simple case of $T_\nu \ll 1$, when the sinusoidal CPR 2.58 is valid. With the Josephson energy

$$E_\mathrm{J0} = \hbar I_\mathrm{c}/2e \tag{2.63}$$

one can transform the equation 2.62 to

$$\underbrace{C\left(\frac{\hbar}{2e}\right)^2}_{M} \ddot{\varphi} + \underbrace{\frac{1}{R_\mathrm{N}}\left(\frac{\hbar}{2e}\right)^2}_{\eta} \dot{\varphi} + \frac{\mathrm{d}}{\mathrm{d}\varphi}\underbrace{\left(E_\mathrm{J0}\left(-\cos(\varphi) - \frac{I}{I_\mathrm{c}}\varphi\right)\right)}_{E_\mathrm{pot}(\varphi)} = 0. \tag{2.64}$$

To the phase difference φ across the Josephson junction one can associate a displacement x. Equation 2.64 corresponds to the differential equation describing the motion of a particle with mass M and damping η in a potential $E_\mathrm{pot}(x)$. With the CPR 2.58, this potential takes the form of a tilted washboard potential, where the tilt is determined by the total current I (cf. figure 2.23a).

In this picture, when the "phase particle" is trapped inside a local minimum, the average phase does not change ($\dot{\varphi} = 0$), and the junction is in the zero voltage or superconducting state. When the particle runs along the slope of the washboard potential, its average phase changes and the junction becomes normal conducting ($\dot{\varphi} \neq 0$). Due to the cosine shape of the potential, the particle periodically accelerates and decelerates, and thus $\dot{\varphi}$ is not constant, which translates to an oscillation of the voltage. With a DC measurement setup this oscillation vanishes, and only the average voltage is detected, which is proportional to $\langle\dot{\varphi}\rangle$. The critical current I_c can be interpreted as the slope of the tilted washboard potential, where the local minima correspond to saddle points and the phase particle is not confined any more. Note that in the experiment, an escape of the phase particle usually occurs at a lower current, the switching current $I_\mathrm{sw} < I_\mathrm{c}$, due to thermal fluctuations or tunneling of the phase particle through the confinement potential.

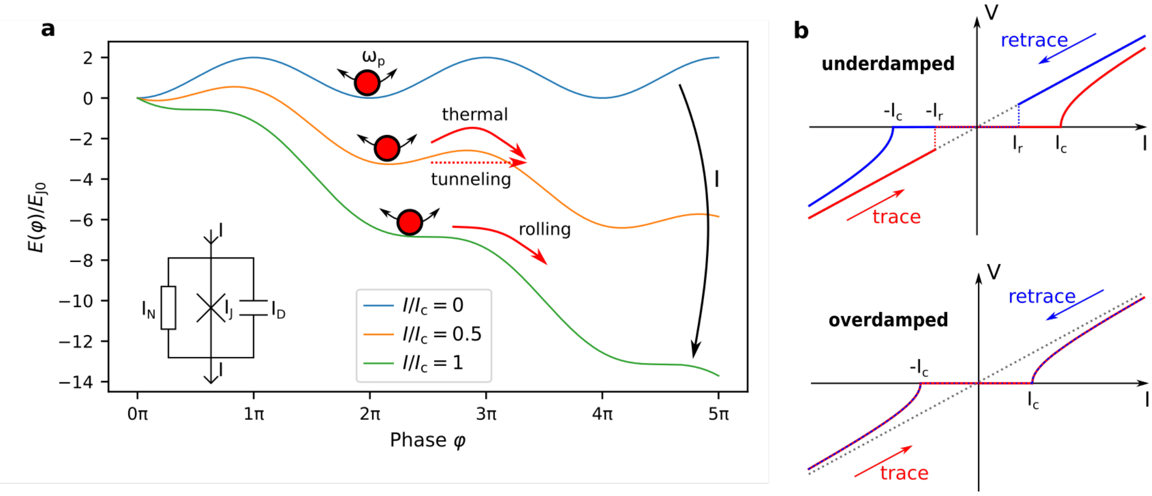

Figure 2.23.: RCSJ model and I-V characteristics. a Sketch of the potential energy $E_{\mathrm{pot}}(\varphi)$ for different currents (tilts). The phase particle oscillates with the Josephson plasma frequency ω_{p} and can overcome the barrier thermally or by tunneling, leading to a switching current lower than the critical current. At $I = I_{\mathrm{c}}$, the potential barrier has vanished and the phase particle can roll down the energy landscape. The inset shows the lumped circuit considered in the RCSJ model. **b** Two limiting cases of the RCSJ model. In the underdamped case $\beta_{\mathrm{C}} \gg 1$, there is a hysteresis between trace and retrace, while in the overdamped case, the trace and retrace overlap. The normal state resistance is shown in dashed grey.

Before discussing I-V characteristics within the RCSJ model (eq. 2.64), we will define some characteristic quantities [110].

- Josephson plasma frequency ω_{p}: In the limit of $\eta \longrightarrow 0$, $I \longrightarrow 0$, the phase difference $\varphi(t)$ oscillates within a local minimum of the tilted washboard potential. Eq. 2.64 becomes the differential equation of a harmonic oscillator with the characteristic frequency

$$\omega_{\mathrm{p}} = \sqrt{\frac{2eI_{\mathrm{c}}}{\hbar C}}. \tag{2.65}$$

- Characteristic frequency ω_{c}: The superconducting channel of a Josephson junction has a nonlinear inductance $L = L_{\mathrm{c}}/\cos(\varphi)$ (here for a tunnel junction CPR, which can be derived by time derivation of the CPR 2.47 and insertion of eq. 2.48) with $L_{\mathrm{c}} = \hbar/2eI_{\mathrm{c}}$. The characteristic frequency is defined as the frequency corresponding to the junction voltage at the transition from superconducting to normal conducting state $V_{\mathrm{c}} = I_{\mathrm{c}}R_{\mathrm{N}}$

$$\omega_{\mathrm{c}} = \frac{R_{\mathrm{N}}}{L_{\mathrm{c}}} = \frac{2e}{\hbar}V_{\mathrm{c}}. \tag{2.66}$$

- Stewart-McCumber parameter β_{C} [111, 112]: This is a dimensionless parameter defined as the square of the quality factor Q, and therefore a suitable parameter to discuss different damping scenarios

$$\beta_{\mathrm{C}} = \left(\frac{\omega_{\mathrm{c}}}{\omega_{\mathrm{p}}}\right)^2 = \frac{2e}{\hbar}I_{\mathrm{c}}R_{\mathrm{N}}^2C = Q^2. \tag{2.67}$$

> An underdamped junction $\beta_c \gg 1$ corresponds to large C (mass) or large R_N (low friction) and an overdamped junction $\beta_c \ll 1$ to low C or low R_N. In the overdamped junction regime, the displacement current is negligible, and the RCSJ model can be analytically solved.

In the following, the RCSJ model will be used to explain the *I*-*V* characteristics (cf. figure 2.23b). The starting point is at $I = 0$ and the current corresponding to the slope of the potential increased. At $I > I_{sw}$ the phase particle can escape and roll along the slope of the tilted washboard potential, the junction enters the finite voltage state. The exact shape of the *I*-*V* curve around I_{sw} depends on β_c, but for $I \gg I_{sw}$, the normal state resistance is recovered. In the overdamped case in the finite voltage state ($I > I_{sw}$), the average voltage calculates to [88]

$$\langle V \rangle = R_N \sqrt{I^2 - I_{sw}^2}. \tag{2.68}$$

During the retrace (decrease in current), the slope is reduced and for $I < I_c$ a potential barrier emerges. It depends on β_c when the phase particle is retrapped, and the junction returns to the superconducting state. In the overdamped case, the kinetic energy of the phase particle is quickly reduced since the friction term dominates the mass term and the inertia of the phase particle. The phase particle will be trapped directly at the critical current, and the *I*-*V* curve does not exhibit hysteresis. The situation is fundamentally different for the underdamped case (large mass/inertia and low friction), where the kinetic energy is sufficiently high to overcome the potential barrier and the phase particle is re-accelerated after each barrier. As a result, the phase particle is trapped and returns to the superconducting state at a much lower retrapping current $I_r < I_c$. The *I*-*V* curve in the underdamped case exhibits a hysteresis between trace and retrace. The value of the retrapping current can be expressed in terms of β_c and I_c (neglecting thermal fluctuations) as [113]

$$I_r = \frac{4I_c}{\pi\sqrt{\beta_c}}. \tag{2.69}$$

2.4.5. External microwave radiation on Josephson junctions

It has already been discussed that the AC Josephson effect leads to an oscillation of the current when a finite bias voltage is applied (cf. eq. 2.48). If an additional AC voltage is applied by irradiating the junction with microwaves, voltage plateaus in the time averaged *I*-*V* characteristic can occur, the so-called Shapiro steps [114]. The voltage applied to an irradiated Josephson junction is given by

$$V = V_{DC} + V_{AC}\cos(\omega t). \tag{2.70}$$

The phase difference $\varphi(t)$ can be calculated with eq. 2.48

$$\varphi(t) = \varphi_0 + \underbrace{\frac{2eV_{DC}}{\hbar}}_{\omega_0} t + \frac{2eV_{AC}}{\hbar\omega_{AC}}\sin(\omega_{AC}t). \tag{2.71}$$

This expression can be inserted into the CPR. For a sinusoidal CPR (eq. 2.47) and the Bessel functions of first kind J_n, we obtain the following supercurrent [88, 89]

$$I_\mathrm{J}(t) = I_\mathrm{c} \sum_{n=-\infty}^{\infty} (-1)^n J_n\left(\frac{2eV_\mathrm{AC}}{\hbar\omega_\mathrm{AC}}\right) \sin((\omega_0 - n\omega_\mathrm{AC})t + \varphi_0). \tag{2.72}$$

A DC contribution of the Josephson current only exists when the time oscillating part vanishes, $\omega_0 = n\omega_\mathrm{AC}$, which is equivalent to

$$V_\mathrm{DC} = n\hbar\omega_\mathrm{AC}/2e. \tag{2.73}$$

This contribution leads to current spikes in the $I(V)$ characteristic or to plateaus in the $V(I)$ characteristic whose width is given by [88]

$$\langle I_{\mathrm{J},n}(t)\rangle = 2I_\mathrm{c}\left|J_n\left(\frac{2eV_\mathrm{AC}}{\hbar\omega_\mathrm{AC}}\right)\sin(\varphi_0)\right|. \tag{2.74}$$

The Bessel function contains the amplitude of the AC drive V_AC, and therefore, the current spikes have a characteristic power dependence, as shown in figure 2.24c. For a CNT Josephson junction in the overdamped regime, this power dependence has been measured in [115] and data are shown in figure 2.24d.

In figure 2.24b, the I-V characteristic of an overdamped junction is presented. The spacing between the current jumps is given by eq. 2.73 and the height by eq. 2.74. In the case of an underdamped junction, the I-V characteristic shows hysteretic behavior between the current steps.

The existence of Shapiro steps can be explained by a locking of the change in phase difference to the externally applied RF frequency. This can be nicely illustrated within the RCSJ model for an overdamped junction [110] (cf. figure 2.24a). RF irradiation induces an alternating current with small amplitude I_AC that modulates the slope I of the tilted washboard potential around its DC value I_DC.

If I_DC is chosen close to I_c, the alternating current I_AC determines whether the phase particle enters in a rolling state or stays trapped, and therefore has a direct influence on the phase dynamics. The motion of the phase particle can be synchronized with the frequency of the RF drive, in a way that during one cycle of the RF drive the phase particle rolls down n minima (cf. figure 2.24a). The corresponding phase change equals to

$$\dot{\varphi} = n\omega_\mathrm{AC} \tag{2.75}$$

and with the second Josephson equation, the average DC voltage calculates to

$$\langle V\rangle = n\frac{\hbar\omega_\mathrm{AC}}{2e} \tag{2.76}$$

which is exactly the voltage condition for a non-vanishing average Josephson current from eq. 2.72.

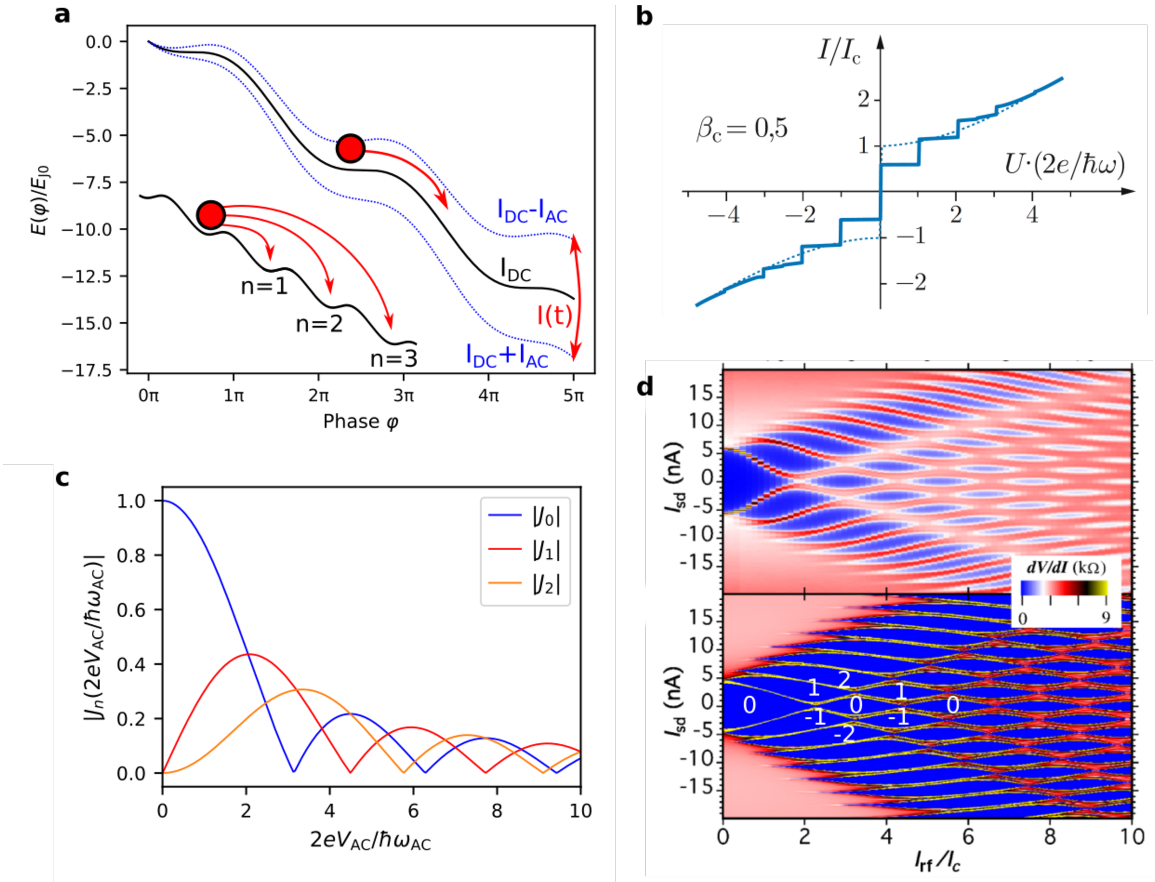

Figure 2.24.: Josephson junction under microwave irradiation. **a** An AC current drive periodically modulates the slope of the tilted washboard potential. Inset: When the RF drive is synchronized with the motion of the phase particle, the particle rolls down *n* minima during one RF oscillation (only schematic). **b** Current-voltage characteristic of an irradiated Josephson junction in the overdamped regime, showing Shapiro steps at fixed voltages. The voltage steps are quantized. The dashed line shows the junction behavior without RF (figure from [116] with data from [117]). **c** Power dependence of the first three Bessel functions of first kind. **d** RF power dependence of the Shapiro steps measured in a CNT (with current drive instead of voltage drive, upper: data, lower: simulation for the overdamped regime with $I_D \to 0$, subfigure from [115]). Blue areas mark Shapiro steps with widths given by the Bessel function behavior from **c**. The first steps are indicated.

2.4.6. SQUIDs

A Superconducting QUantum Interference Device (SQUID) consists of an electric circuit with one or more Josephson junctions in a closed superconducting loop. In this thesis, we investigate a DC-SQUID which consists of two Josephson junctions that are DC-wise connected to the measurement electronics. As mentioned in the introduction chapter 1, a DC-SQUID can be conceived as the superconducting analogue of a double-slit experiment. Instead of electromagnetic waves diffracted at the two slits and interfering on a distant screen in position-space, the supercurrent described by the macroscopic phase difference across the two Josephson junctions shows an interference pattern. A SQUID combines the two fundamental phenomena, (i) the Josephson effect and (ii) the fluxoid quantization in a

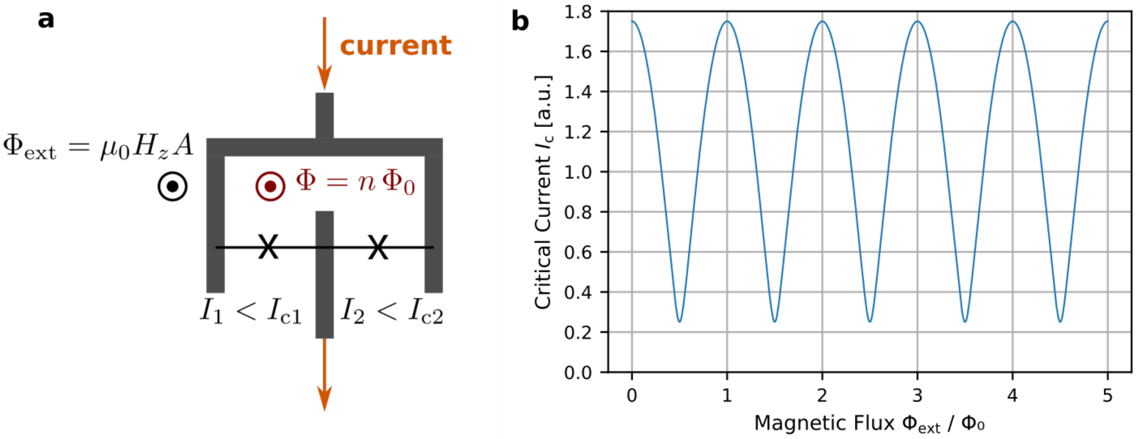

Figure 2.25.: Schematics and critical current of a DC-SQUID. a The two Josephson junctions of the DC-SQUID are formed in a single suspended CNT. An external field H_z is applied perpendicular to the SQUID loop and the flux threading the loop can only be multiples of the flux quantum Φ_0. **b** Critical current dependence on the external flux (cf. eq. 2.79) for asymmetric critical currents: $I_{c1} = 0.75 I_{c2}$.

superconducting loop, i.e. the flux Φ penetrating the superconducting loop can only be multiples of the flux quantum $\Phi_0 = h/2e$. This flux quantization has its origin in the phase of the macroscopic wave function, which has to be continuous and can only change by multiples of 2π along the closed loop ($\oint \nabla\varphi \mathrm{d}\mathbf{l} = 2\pi n,\ n \in \mathbb{N}_0$).

In the following, the dependence of the current through the SQUID as a function of the external applied flux Φ will be derived. For this, a device geometry as in figure 2.25 is considered. The current enters the device at a source electrode, splits and propagates through the two Josephson junctions in parallel with critical currents I_{c1} and I_{c2} and phase differences φ_1 and φ_2 and leaves the device via a drain electrode.

Application of second Kirchhoff's law allows to describe the Josephson effect (i) for the system (assuming a tunnel junction CPR, $T_\nu \longrightarrow 0$)

$$I = I_1 + I_2 = I_{c1}\sin(\varphi_1) + I_{c2}\sin(\varphi_2) \tag{2.77}$$

The fluxoid quantization (ii) implies for an external applied flux $\Phi_{\rm ext}$ [88]

$$\varphi_1 - \varphi_2 = 2\pi n + \frac{2\pi\Phi_{\rm ext}}{\Phi_0}. \tag{2.78}$$

This relation can be inserted into eq. 2.77 to obtain the external flux dependence of the supercurrent. The maximum supercurrent (or the critical current of the SQUID) is given by [118]

$$I_c = \sqrt{(I_{c1} - I_{c2})^2 + 4 I_{c1} I_{c2} \cos^2(\pi\Phi_{\rm ext}/\Phi_0)}. \tag{2.79}$$

For the special case of two identical Josephson junctions ($I_{c1} = I_{c2} = I_{c0}$) this expression reduces to the pure cosine relation similar to the double-slit experiment

$$I_c = 2 I_{c0} \left|\cos\frac{\pi\Phi_{\rm ext}}{\Phi_0}\right|. \tag{2.80}$$

The critical current of the SQUID has its maximum when $\Phi_{\text{ext}} = n\Phi_0$, and the two currents I_1 and I_2 interfere constructively. A minimum occurs for destructive interference ($\Phi_{\text{ext}} = (2n+1)\Phi_0/2$). The critical current of the SQUID goes to zero for a symmetric SQUID or is reduced to the difference of the critical currents of the two junctions for an asymmetric SQUID.

Note that in the discussions here the inductance L of the SQUID loop has been neglected, which adds to the external applied flux as $\Phi_L = L(I_1 - I_2)/2$. To estimate the inductance contribution, the screening parameter $\beta_L = 2LI_c/\Phi_0$ is introduced [119]. It describes the ratio of the maximum circulating current $I_1 = -I_2$ to the corresponding trapped flux $\Phi_0/2$.[6] In the case of CNTs, the critical current is on the order of 100 pA to ~ 10 nA, and therefore, $\beta_L \ll 1$ and the inductive effects due to the circulating current are negligible. Beyond that, CNT nano-SQUIDs allow one to tune the gate voltage below each weak link independently and to adjust the critical current, enabling the construction of a symmetric SQUID with higher flux modulation and sensitivity.

SQUID sensors

The oscillations of the critical current of a SQUID as a function of the external applied flux $\Phi_{\text{ext}} = BA$ penetrating the SQUID area A have a periodicity given by the flux quantum $\Phi_0 = 2 \times 10^{-15}$ Vs. It is this small flux scale that provides the high sensitivity of SQUID sensors.

In general, SQUID sensors are operated in the overdamped regime (to avoid hysteresis) and in the voltage state ($I > I_{c1} + I_{c2}$). In the zero-voltage state, the supercurrent would need to be gradually increased and only once the SQUID reaches its critical current I_c (detected as a jump in $\mathrm{d}V/\mathrm{d}t$) a data point $I_c(\Phi_{\text{ext}})$ can be acquired. For an overdamped SQUID in the voltage state, the average voltage is given by (cf. eq. 2.68)

$$\langle V(\Phi_{\text{ext}})\rangle = R_N\sqrt{(I/2)^2 + (I_c((\Phi_{\text{ext}})/2)^2}, \quad I > I_c. \tag{2.81}$$

The voltage is also periodically modulated by Φ_{ext}, which can be seen when inserting eq. 2.79 into eq. 2.81. The highest sensitivity is reached when the first term in the square root of eq. 2.81 is minimum, which is fulfilled for $I = I_c + \epsilon,\ \epsilon/I_c \ll 1$.

To measure a signal with a SQUID, a pick-up circuit is commonly used, which converts a signal to a flux and the flux can be coupled into the SQUID [120, 121]. The SQUID is used as a flux-to-voltage transducer, where the voltage is measured with some readout electronics. The signal could for instance be a magnetic field for magnetometer application, but also a current or voltage for amperemeter or voltmeter applications.

---

[6] This is not the current from source to drain, which is minimum for this flux, but the current circulating in the loop itself, which generates the additional flux contribution.

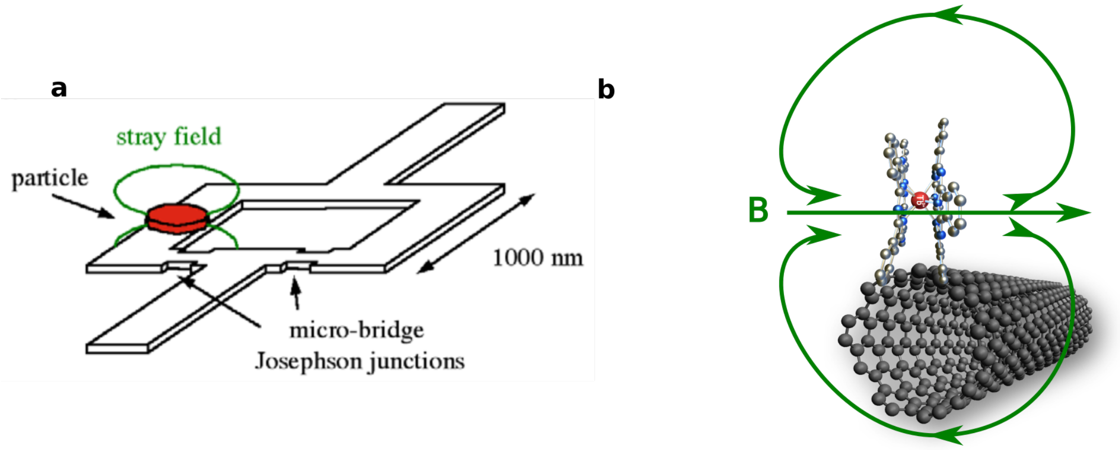

Figure 2.26.: Measurement of the magnetization change of single-molecule magnets. **a** A micro-SQUID is ideal for measuring the magnetization change from a molecular crystal with similar dimensions as the SQUID electrodes, the flux overlap with the SQUID loop is large. From [118].**b** For SMMs, the flux coupling for a micro-SQUID would be too small. A CNT, however, with comparable diameter integrated in a nano-SQUID can provide a good flux coupling between a SMM and the SQUID loop.

SQUID as sensor for magnetic molecules

In our group, we are interested in using the SQUID technology for the detection of the magnetization reversal of a single-molecule magnet (SMM) or crystals of SMMs. Due to the small dimensions of the submicrometer-sized samples, the flux coupling is too small in a setup where the flux is picked up in an external circuit. The coupling can be improved by a direct coupling of the magnetic sample to the SQUID loop without a pick-up circuit, e.g. by placing a molecular crystal on a planar micro-SQUID [118] or evaporating single molecules on a CNT nano-SQUID [32].

The magnetization change due to the reversal of magnetic moment ΔM translates into a change of the flux $\Delta\Phi$ threading the SQUID loop that depends on the flux coupling, i.e. a measure of how well the stray field of the magnetic sample penetrates the SQUID loop. A few examples are shown in figure 2.26, where a micro-SQUID can be used to detect magnetization reversal of a molecular crystal with a rather large magnetic stray field, penetrating the SQUID loop efficiently. However, when an SMM is placed on a micro-SQUID, the stray field penetrating the SQUID loop is too low to be detected. A natural solution is based on decreasing the junction diameter by using a CNT in a nano-SQUID with a diameter comparable to an SMM. In [118] the signal $\Delta\Phi$ due to the magnetization reversal of a Mn_{12} SMM is estimated to be on the order of $10^{-4}\Phi_0$, which is larger than the sensitivity of a nano-SQUID of $10^{-5}\Phi_0$ [32].

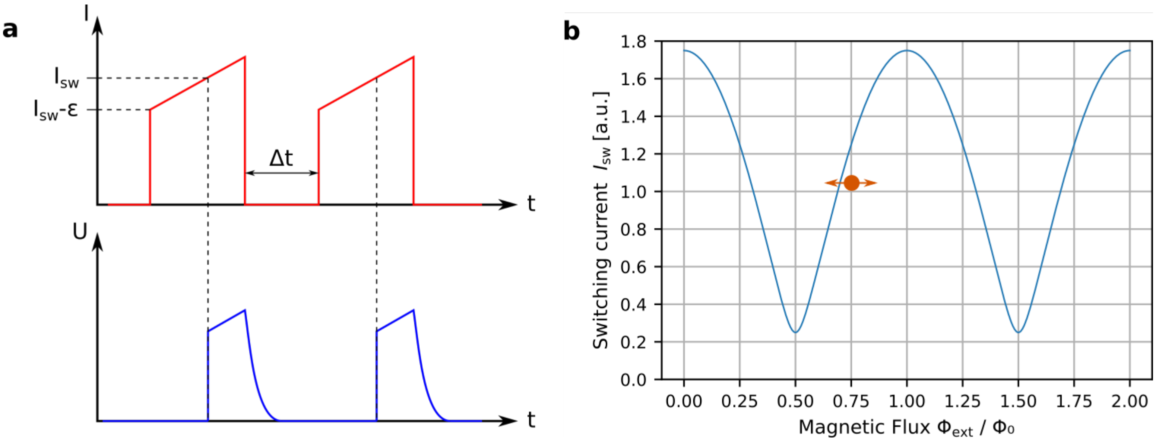

Figure 2.27.: SQUID measurements. a Measurement principle for direct switching current measurements. **b** Threshold detector at the working point close to the transition to the resistive state (marked in orange)

Measurement principle

The measurement principle differs from the standard SQUID measurements explained in the previous chapter [118]. Since the magnetic field applied to the magnetic molecule can also couple to the SQUID loop, the application of high magnetic fields is limited to the SQUID plane. A standard measurement in the finite voltage state would permanently heat up the SQUID and the sample, which is undesired. Therefore, measurements are performed mainly in the zero-voltage state where the magnetic flux dependence of the switching current (eq. 2.79) is probed. A magnetization reversal of the magnetic molecules changes the flux Φ through the SQUID loop and the switching current $I_{\mathrm{sw}}(\Phi)$, which can be detected using the following two methods (cf. figure 2.27).

- Direct switching current measurement: Here, the SQUID current is set close to the switching current $I = I_{\mathrm{sw}} - \epsilon$ and periodically ramped above I_{sw}. Each time when $I > I_{\mathrm{sw}}$, a finite voltage is detected $\mathrm{d}V/\mathrm{d}t \neq 0$ and to avoid excessive Joule heating the current is directly reduced below I_{sw} and a new cycle is restarted. A more precise measurement of I_{sw} can be achieved when synchronizing a clock with the switching current ramp and converting the time when $\mathrm{d}V/\mathrm{d}t \neq 0$ to the corresponding switching current.
- Threshold detector ("cold" mode): The detection mechanism in the former method is based on periodically entering the dissipative, finite-voltage state of the SQUID which leads to undesired Joule heating. Using the SQUID as a threshold detector allows one to permanently stay in the zero-voltage state close to the switching current, and only when a magnetization reversal of the molecules occurs, the flux through the SQUID changes. If a suitable working point is chosen, the SQUID enters the normal conducting state, and a finite voltage is measured.

2.5. Coupling nanomechanics and superconductivity in suspended CNTs

Apart from measuring single-molecule magnets, the platform of a suspended CNT-SQUID could also be used to investigate the interplay between mechanical displacement of the CNT resonator and the Josephson effect in the CNT weak link. Two coupling mechanisms have been suggested, a capacitive coupling due to the Coulomb force between the CNT and the gate, which is expanded by an additional Josephson force in the case of proximity-induced superconductivity [33, 122], and an inductive coupling due to the Lorentz force in an applied magnetic field [123, 113]. The purpose of this section is to discuss possible ideas for studying the interplay between nanomechanics and superconductivity in suspended CNTs.

2.5.1. Capacitive coupling

The actuation and read-out mechanism for normal conducting electrodes has been discussed in chapter 2.3. We recall the different contributions from eq. 2.28 in the limit of a weak drive $V_\mathrm{g}^\mathrm{AC} \ll V_\mathrm{g}^\mathrm{DC}$ for the oscillation amplitude u. There is a static force that pulls the CNT to the gate and can tune its resonant frequency

$$F_\mathrm{g}^\mathrm{DC} = \frac{\partial C_\mathrm{g}}{\partial u}\frac{(V_\mathrm{g}^\mathrm{DC})^2}{2} \tag{2.82}$$

and an AC force $F_\mathrm{g}^\mathrm{AC}(t) = F_\mathrm{g}^\mathrm{AC}\cos(\omega t)$ due to the oscillating RF voltage at the gate with amplitude

$$F_\mathrm{g}^\mathrm{AC} = \frac{\partial C_\mathrm{g}}{\partial u} V_\mathrm{g}^\mathrm{DC} V_\mathrm{g}^\mathrm{AC}. \tag{2.83}$$

Josephson force

In the case of superconducting electrodes another force term emerges, which is discussed in detail in [33, 122] and called Josephson force due to its dependence on the superconducting phase difference φ across the Josephson junction. The total Josephson energy is defined as the energy stored in a Josephson junction in the zero-voltage state and depends on the phase difference φ and the charge q on our quantum dot. With eq. 2.63 it can be expressed as

$$E_\mathrm{J}(q,\varphi) = E_\mathrm{J0}(q)(1-\cos(\varphi)) = \frac{\hbar}{2e} I_\mathrm{c}(q)(1-\cos(\varphi)). \tag{2.84}$$

The total Josephson energy depends on the critical current, which for a CNT quantum dot depends on the induced charge. The charge itself depends on the capacitance that is modulated when the CNT oscillates, and therefore, the Josephson energy is sensitive to the

CNT displacement. The corresponding Josephson force can be calculated as the gradient of the Josephson energy $\mathbf{F}_\mathrm{J} = -\nabla E_\mathrm{J}$, which for us is only non-zero along the polarization axis of the mechanical bending mode u. We can therefore write the Josephson force as

$$F_\mathrm{J} = -\frac{\mathrm{d}E_\mathrm{J}(q,\varphi)}{\mathrm{d}u} = -\frac{\partial E_\mathrm{J}(q,\varphi)}{\partial q}\frac{\mathrm{d}q}{\mathrm{d}u} = -\frac{\partial C_\mathrm{g}}{\partial u}V_\mathrm{g}^\mathrm{DC}\frac{\partial E_\mathrm{J}(q,\varphi)}{\partial q}. \tag{2.85}$$

The structure is analogous to eq. 2.83 when we associate the term $\partial E_\mathrm{J}(q,\varphi)/\partial q$ with an AC drive voltage V_g^AC. However, the time dependence of the Josephson force depends on the phase dynamics and not on an external drive voltage.

Potential measurement schemes for the Josephson force

The Josephson force has only been theoretically proposed [33] and has not yet been experimentally observed. In [122] potential signatures of the Josephson force have been measured, but the superconducting phase could not be changed, and thus the phase dependence of the Josephson force could not be probed. Here, we will focus on one potential measurement; for more proposals see [33].

A potential measurement scheme could be based on the phase dependence of the Josephson force. We assume a constant phase bias, and the Josephson force can be considered as a static force that acts on the CNT in addition to the static gate force F_g^DC. It modifies the tension in the CNT and shifts the resonant frequency by [33]

$$\Delta\omega_0(\varphi) \sim \omega_0\frac{F_\mathrm{J}(\varphi)}{F_\mathrm{g}^\mathrm{DC}} \sim \omega_0\frac{E_\mathrm{J0}}{eV_\mathrm{g}^\mathrm{DC}}\cos(\varphi). \tag{2.86}$$

The frequency shift depends on the superconducting phase that can be controlled in a CNT-SQUID in a four-point current-biased setup. The frequency shift depends on E_J0, and therefore the magnitude of the critical current. Hence, it is favorable to have the highest critical current possible to measure the frequency shift. In principle, we could follow the protocol:

1. Left junction in the "on" state: The biasing current is swept and the gate voltage of the left gate is stepped and we measure the voltage drop across the left junction of the SQUID (right junction is in the "off" state). The left gate voltage is set to obtain maximum critical current and a sharp transition between superconducting and normal conducting state.

2. Right junction in the "on" state: The measurement is repeated for the right gate voltage with the left gate voltage tuned according to (1). The right gate voltage is chosen to obtain a maximum and sharply defined critical current and the two junctions of the SQUID in the "on" state.

3. Finding the mechanical resonance: The current is swept at fixed gate voltages, cf. (1) and (2), and the applied RF frequency is stepped, and we measure the voltage drop across the SQUID. Hitting the resonance frequency should modulate the gate capacitance, and the critical current should depend on the frequency.

4. Probing the phase dependence of the resonance: To distinguish from the gate forces F_g^{DC} and F_g^{AC}, the resonance frequency must be analyzed as a function of φ. If the mechanical resonance depends on the Josephson force, it should shift following eq. 2.86. The phase can be changed by applying a magnetic field perpendicular to the SQUID plane, e.g. repeating measurement (3) for different magnetic fields. However, note that a change in φ will also affect the maximum supercurrent according to the flux dependence of the SQUID $I_c(\Phi_{ext})$ (cf. eq. 2.79), and thus only the frequency of the mechanical resonance can be compared.

2.5.2. Inductive coupling

The inductive coupling is based on driving the resonator by applying a magnet field and exploiting the Lorentz force when a DC current flows through the resonator. The general model has been theoretically studied by [123, 124, 113]. We will now review the model and derive the coupling mechanism following [125, 126].

Model for inductive coupling

The device consists of two superconducting electrodes connected via a suspended weak link (e.g. a CNT) forming a nanomechanical resonator of length L (cf. figure 2.28). The junction is current-biased by a DC current I in x-direction and an in-plane magnetic field is applied in y-direction. The CNT can oscillate in the z-direction in the fundamental transverse bending mode with deflection u. The current and the CNT oscillations are coupled via the Lorentz force mediated by the in-plane magnetic field in two different ways. First, mechanical oscillation can modulate the current and redistribute the current over the different channels of the RCSJ model. Second, an AC current through the junction can lead to mechanical oscillations in the CNT.

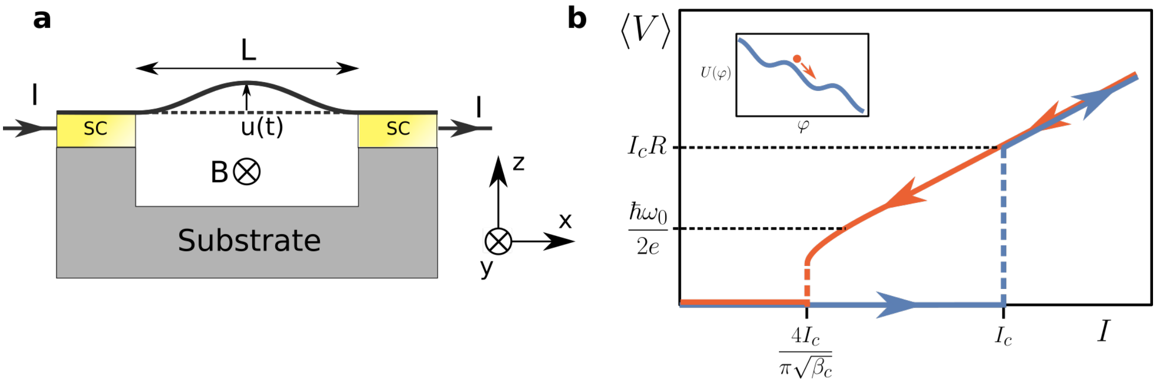

Figure 2.28.: Model for the inductive coupling from [113]. a Geometry, **b** Frequency matching condition on the decreasing current sweep.

With respect to the electrical part, the changes in current arising from mechanical oscillations can be calculated under the approximation of a uniform displacement of the weak link. The normal current density is given by

$$\mathbf{J}_\mathrm{N} = \sigma_\mathrm{N}(\mathbf{E} + \mathbf{v} \times \mathbf{B}) = \frac{\sigma_\mathrm{N}}{L}\left(\frac{Q}{C} - BL\frac{\mathrm{d}u}{\mathrm{d}t}\right)\mathbf{e}_\mathrm{x}. \tag{2.87}$$

Here, σ_N denotes the normal metal conductivity, $\mathbf{E} = Q/(CL)\mathbf{e}_\mathrm{x}$ the electric field across the weak link due to charge accumulation Q at the superconductor weak link interface and $\mathbf{e}_\mathrm{x,y,z}$ unit vectors in x, y, z-direction. The voltage drop across the junction is given by $V = \int \mathbf{E}\mathrm{d}\mathbf{l} = Q/C$. The normal current can be expressed as

$$I_\mathrm{N} = \frac{1}{R_\mathrm{N}}\left(V - BL\frac{\mathrm{d}u}{\mathrm{d}t}\right). \tag{2.88}$$

The applied magnetic field $\mathbf{B} = B\mathbf{e}_\mathrm{y}$ modifies the superconducting phase $\varphi \longrightarrow \varphi - 2e/\hbar \int \mathbf{A}\mathrm{d}\mathbf{l}$ where the vector potential can be chosen as $\mathbf{A} = Bu\mathbf{e}_\mathrm{z}$ and the integration is along the length L of the weak link.

This results in a modified second Josephson equation (cf. eq. 2.48)

$$\frac{\mathrm{d}\varphi}{\mathrm{d}t} = \frac{2e}{\hbar}\left(V - BL\frac{\mathrm{d}u}{\mathrm{d}t}\right). \tag{2.89}$$

With eq. 2.61 and 2.88, assuming a sinusoidal CPR eq. 2.47, and using eq. 2.89 we obtain

$$\begin{aligned} I &= I_\mathrm{J} + I_\mathrm{D} + I_\mathrm{N} && (2.90)\\ &= I_\mathrm{c}\sin(\varphi) + C\frac{\mathrm{d}V}{\mathrm{d}t} + \frac{1}{R_\mathrm{N}}\left(V - BL\frac{\mathrm{d}u}{\mathrm{d}t}\right) && (2.91)\\ &= I_\mathrm{c}\sin(\varphi) + \frac{\hbar}{2eR_\mathrm{N}}\frac{\mathrm{d}\varphi}{\mathrm{d}t} + \frac{\hbar C}{2e}\frac{\mathrm{d}^2\varphi}{\mathrm{d}t^2} + CBL\frac{\mathrm{d}^2u}{\mathrm{d}t^2}. && (2.92) \end{aligned}$$

Eq. 2.92 only differs from eq. 2.62 of the RCSJ model without magnetic field by the last additional current term, absorbing the coupling between nanomechanics of the weak link and the I-V relationship of the junction. When the weak link oscillates at resonance, this last term oscillates with the resonance frequency ω_0 and can be considered as an AC current which could potentially be measured as plateaus in the I-V characteristics of the junction at $V_0 = \hbar\omega_0/(2e)$ in analogy to Shapiro steps.

For the mechanical motion on the other hand, the Lorentz force acts as external force driving the resonator $F = BI_\mathrm{eff}L$. The current I_eff, which has to be taken into account, differs from the previously defined current I in eq. 2.92 since the displacement current does not flow through the weak link and only emerges from charge accumulation at the interface between superconductor and weak link. The magnitude of the Lorentz force acting on the resonator is given by

$$F = BL(I_\mathrm{c}\sin(\varphi) + I_\mathrm{N}) \tag{2.93}$$

and can be inserted in eq. 2.31

$$\ddot{u}(t) + \gamma \dot{u}(t) + \omega_0^2 u(t) + \alpha u^3(t) = BL(I_\mathrm{c} \sin(\varphi) + I_\mathrm{N}). \tag{2.94}$$

The coupled differential equations 2.92, 2.94 are solved in [113] and discussed in detail for different couplings.

Experimental feasibility

In this section, a realistic parameter check will be performed to discuss the experimental feasibility of the proposal. The key of the proposal, the driving of motion in the weak link relies on an alternating current $I_\mathrm{eff}(t)$ through the CNT. Otherwise, the Lorentz force would only act as a static force. Since $I_\mathrm{eff}(t) = I_\mathrm{J}(t) + I_\mathrm{N}(t)$, the addition of the Josephson and normal current should not cancel the oscillating time dependence. In an overdamped junction, however, the oscillating Josephson current is mainly compensated for by the oscillating normal current, while the displacement current is approximately DC. We should therefore be in the underdamped regime, where the Josephson current is compensated by the displacement current and the normal current approximately DC [126]. Then the effective current in eq. 2.94 passing the junction and the Lorentz force acting on the junction oscillate in time, which enables the driving mechanism.

The condition for mechanical resonance requires the supercurrent frequency to match the mechanical resonance frequency $\mathrm{d}\varphi/\mathrm{d}t = \langle V \rangle = \hbar\omega_0/(2e)$, and thus the junction needs to be operated in the finite voltage state. The minimum frequency at finite voltage is given by the characteristic frequency $\omega_\mathrm{c} = 2eR_\mathrm{N}I_\mathrm{c}/\hbar$, which for a typical junction with a CNT with minimum $R_\mathrm{N} = 6.5\,\mathrm{k\Omega}$ and $I_\mathrm{c} = 1\,\mathrm{nA}$, calculates to $\omega_\mathrm{c}/2\pi = 3.13\,\mathrm{GHz}$. This value has to be compared to the mechanical resonance frequency which can be estimated to $f_0 \approx 313\,\mathrm{MHz}$, and therefore, the ratio $\omega_0/\omega_\mathrm{c} \sim 0.1$ is similar to [113]. The conclusion is the same as in [113], the condition cannot be fulfilled on the increasing current path and could potentially be valid for the decreasing path for a hysteretic junction where the retrapping current $I_\mathrm{r} = 4I_\mathrm{c}/(\pi\sqrt{\beta_\mathrm{c}}) < I_\mathrm{c}$. The condition to observe the mechanical resonance on the decreasing current path translates to

$$\frac{I_\mathrm{r}}{I_\mathrm{c}} < \frac{\omega_0}{\omega_\mathrm{c}} \Leftrightarrow \beta_\mathrm{c} > \left(\frac{4}{\pi}\frac{\omega_\mathrm{c}}{\omega_0}\right)^2 \Leftrightarrow \beta_\mathrm{c} \gtrsim 100. \tag{2.95}$$

Although it is suggested in [126, 125] that this value of β_c is in experimental reach, our underdamped junctions have a β_c on the order of $\lesssim 10$. It is further proposed that a shunt capacitor could be added in parallel to the junction to increase β_c. However, the main limitation is the voltage $\langle V \rangle = \hbar\omega_0/(2e)$ that matches the resonance frequency. For a resonance frequency of 313 MHz it would only be 1.3 µV which would be very challenging to measure. In conclusion, a direct realization of this proposal in [113] is beyond the state-of-the-art.

3. Synthesis of CNTs and analysis

In this chapter we will focus on the core of our device, the carbon nanotube, and discuss how we produce CNTs. We will review the synthesis process and present the experimental setup in the first part. The second part of this chapter contains the analysis of the properties of the CNTs which are later on used in the experiments.

3.1. Chemical vapor deposition of CNTs

Carbon nanotubes were synthesized for the first time in 1991 [2] using the so-called arc-discharge method. Here, carbon atoms are evaporated by applying an electric arc between two graphite electrodes [127, 128] and the carbon gas can then crystallize into carbon allotropes, including CNTs. An alternative method is laser ablation, where the energy required for the evaporation of carbon is supplied by a laser [129, 130].

In contrast to carbon deposition from the gas phase, the synthesis method used in this work is chemical vapor deposition (CVD), which is based on the thermal decomposition of a hydrocarbon vapor at metal catalyst sites [131]. This method has multiple benefits compared to arc-discharge or laser ablation. First of all, it is a technically simple and low-cost method with a high yield of single-walled CNTs and high purity [131]. Second, the influence of the growth parameters (such as temperature, gas flow and composition and the type of catalyst) allows to easily modify the properties of the synthesized CNTs [132]. Lastly, for our application, the nanoassembly of CNTs, it is desired to synthesize CNTs at predefined positions to be able to transfer them onto our circuit chips. Because CNTs only grow from catalyst particles, the positioning of the catalyst allows local growth of CNTs on predefined sites.

3.1.1. Principle of chemical vapor deposition

Chemical vapor deposition requires a steady supply of a carbon source in the gas phase (precursor) and elevated temperatures between 600-1200 °C, as well as catalyst particles for the chemical reactions to occur efficiently [131]. For this purpose, the substrate on which to grow CNTs is commonly placed inside a quartz glass tube that can be heated by a surrounding radiative oven.

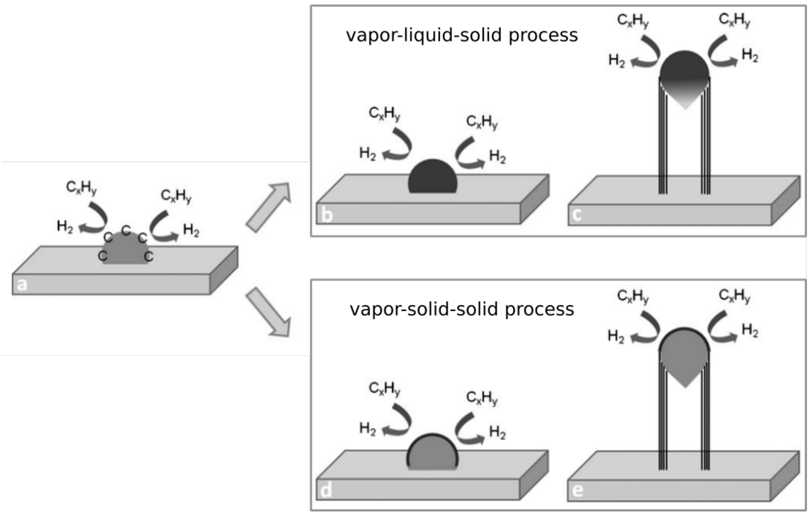

Figure 3.1.: CNT growth processes. Three steps are involved in the vapor-liquid-solid process (VLS) (a,b,c) or vapor-solid-solid process (VSS) (a,d,e) process in the case of tip-growth. Details see text. Figure adapted from [132] with permission from John Wiley & Sons - Books.

CNT growth mechanism

The most generally accepted mechanism for CNT growth can be described by the vapor-liquid-solid (VLS) process [133, 134], comprising the following intermediate reactions involved in the growth process (cf. figure 3.1) [131, 132].

(a) Adsorbation of precursor gas with carbon (e.g. methane) on the hot catalyst surface and dissociation into elementary carbon and hydrogen species.

(b) Dissolution of the carbon atoms in the bulk of the catalyst nanoparticle, diffusion into the catalyst and formation of a metastable carbide.

(c) Saturation at the carbon solubility limit, nucleation and precipitation of solid carbon on the other side of the catalyst nanoparticle, crystallizing into a nanotube. The formation of a carbon nanotube is energetically stable due to the absence of dangling bonds.

The whole mechanism is continuously driven by a temperature gradient in the nanoparticle [131]. This gradient occurs due to the different reaction kinetics in hydrocarbon decomposition and carbon crystallization because the hydrocarbon decomposition is an exothermic process releasing heat, while the carbon crystallization is an endothermic process absorbing heat. The process is stopped when the continuous supply of carbon is interrupted. For instance, this occurs when the catalyst nanoparticle is covered by a thin layer of carbon.

Another growth mechanism that has been suggested is the vapor-solid-solid (VSS) growth, where the second step differs compared to the VLS process (cf. figure 3.1d). Here, instead of dissolving into the catalyst, carbon only diffuses along the surface before precipitation. The proponents of this mechanism highlight the lower activation energy for surface diffusion compared to bulk diffusion. Which of the two mechanisms occurs also depends on the type of catalyst and the growth temperature [132].

For both mechanisms, we can further differentiate between two cases, depending on the interaction strength between the catalyst particle and the substrate. In the case of weak interaction, the catalyst detaches from the substrate and the CNT starts growing from the tip, with the catalyst moving upward at the tip of the CNT (tip growth). On the other hand, in the case of strong interaction, the catalyst particle adheres to the substrate and remains in its original position, and growth is initiated from the bottom of the CNT (base growth) [131, 135]. Unfortunately, in this work, we could not identify which one of the two mechanisms prevails in our growth.

After initiation, the CNT growth is influenced by two flows. The growth direction is mainly guided by the horizontal gas flow direction. However, there is a second less obvious vertical flow in the CVD oven. The substrate usually has a higher temperature compared to that of the freshly entering precursor gas. This temperature gradient results in a vertical gas density gradient that initiates a convection flow lifting the CNT (buoyant effect) [136, 137]. The ratio of the two gas flows depends on the horizontal gas flow and the temperature in the oven. In the case of tip growth, the catalyst particle can fly like a kite in the wind and collect precursor gas efficiently (kite mechanism), which can result in a rapid growth of single-walled CNTs up to 18.5 cm [138].

Role of the catalyst

The decomposition of methane is thermodynamically favored at temperatures above 900 °C [139]. With the use of catalyst, the decomposition temperature can be reduced to 600 °C, but the reaction rates are too slow, and therefore, temperatures above 850 °C are commonly used [132]. The key function of the catalyst is hydrocarbon dissociation and carbon solubility [140]. Transition metal catalysts (in this work iron) are commonly used due to their partially filled 3d orbitals, which can pair with the carbon radicals formed during hydrocarbon decomposition. When the catalyst has a high carbon solubility and a high carbon diffusion rate, carbon can dissolve into the catalyst nanoparticle efficiently [131]. In addition to iron, we add molybdenum to the catalyst. Molybdenum can promote the aromatization of methane at elevated temperatures. Since the iron and molybdenum sites are in close proximity, it is argued that aromatic species from the molybdenum sites can directly promote growth at the iron sites [141].

The size of the catalyst nanoparticle is crucial and is a result of the preparation process, but it is also influenced by the temperature during the growth process [132]. The melting temperature depends on the diameter of the nanoparticle [140], and thus the size determines whether the catalyst is in a liquid or a solid state at the growth temperature. Furthermore, the size of the CNT cap in the nucleation process depends on the catalyst size, resulting in a correlation between the catalyst size and the nanotube diameter. Smaller diameter nanoparticles are too active, dissolve carbon too fast, and when nucleating, a continuous thin layer of graphite will form around the nanoparticle. This interrupts the carbon supply, and thus no CNT can grow anymore (catalyst poisoning). On the other hand, nanoparticles with too large diameter reduce the hydrocarbon decomposition and do not provide sufficient carbon for the nucleation and growth of CNTs [142].

The metal catalyst is usually not applied directly on the substrate and a metal oxide catalyst support is used (in this work alumina Al_2O_3). Due to the strong interaction between the catalyst and the metal oxide support [141], the metal catalyst can be stabilized, which prevents the coalescence of the nanoparticles during growth [143]. This is essential to maintain the optimum diameter of the nanoparticles required for an efficient growth. In addition, the support allows the distribution of the catalyst particles to be adjusted by simply varying the size or density of the support [132].

Apart from the precursor methane as carbon feedstock, we also add hydrogen to the gas flow for two reasons. First, the catalyst nanoparticles are usually exposed to air before being transferred into the CVD oven and quickly oxidized. Hydrogen gas can reactivate the catalyst by reducing the metal oxide to pure metal [131]. Second, hydrogen prevents nucleation of carbon species on the catalyst surface, which can lead to the formation of a carbon layer around the catalyst (catalyst poisoning) and growth inhibition [135, 144].

3.1.2. Setup and process flow

Cantilever chip

We use special cantilever chips to transfer the CVD-grown CNTs onto circuit chips using our nanoassembly technique. It is a custom design fabricated by Micromotive[1]. A schematic of a cantilever chip is shown in figure 3.2. This silicon chip consists of a 3 mm × 3 mm support to allow easy chip handling and a comb of 500 µm long cantilevers which is attached to the support. We aim for a high number of suspended CNTs between pairs of cantilevers, which should preferably grow close to the tip since we can only transfer CNTs from the top 20 µm.

CVD oven

We use a CVD oven[2] with a heating zone of about 15 cm (cf. figure 3.3). The oven encloses a 2.5 cm diameter quartz glass tube, which serves as a reaction chamber. In addition to methane and hydrogen, argon is used as an inert gas to flush the tube, vent the reaction chamber, and during heating to reach the growth temperature. On the right side of the tube at the inlet, the gas flow enters and can be adjusted by three mass flow controllers (MFC), one for each gas. The outlet on the left is connected to a scroll pump, which can evacuate the reaction chamber to about 10^{-2} mbar. The cantilever chips are loaded via a top loadlock onto a quartz arm which can be slided into the reaction chamber to position

---

[1] Micromotive GmbH, Carl Zeiss Str. 18-20, 55129 Mainz

[2] Carbolite Gero 3000, Carbolite Gero GmbH, Hesselbachstr. 15, 75242 Neuhausen

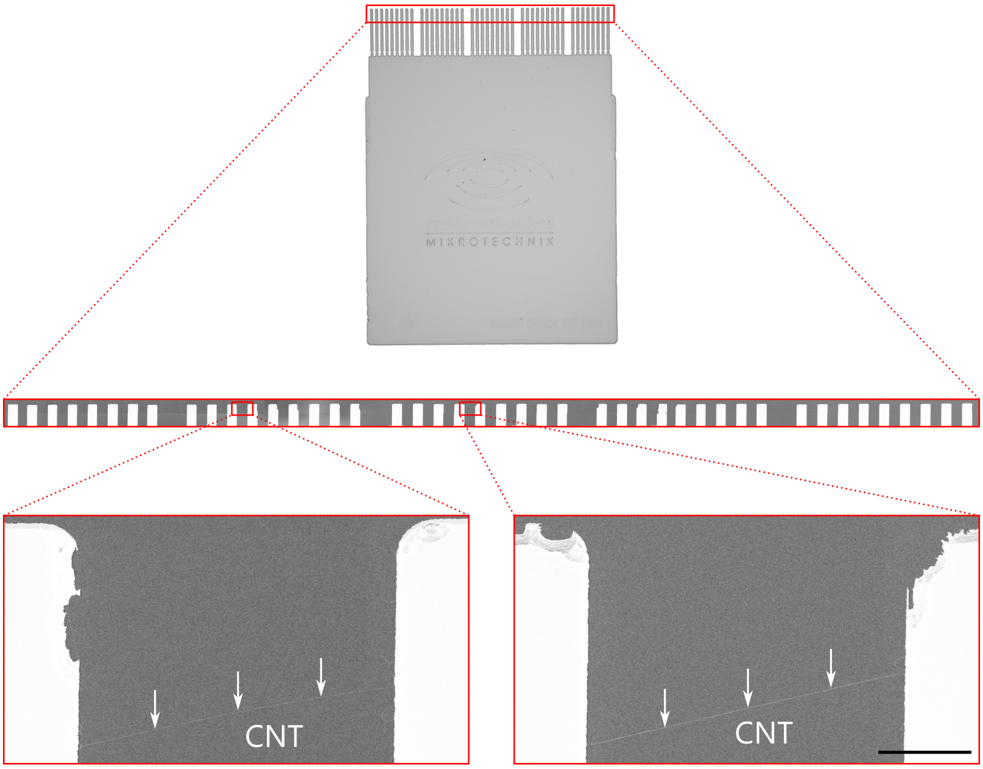

Figure 3.2.: Overview of a cantilever chip. The scanning electron micrograph shows CNTs suspended between white cantilevers. Scale bar: 10 µm. From [37].

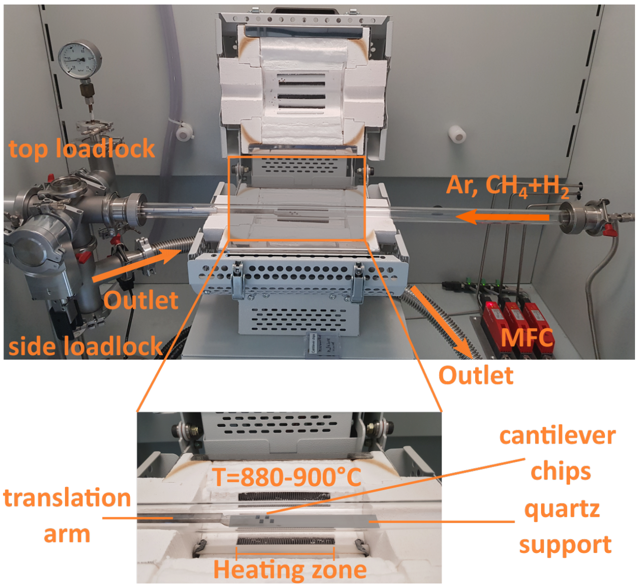

Figure 3.3.: Image of the CVD oven in an opened position. Details see text.

the cantilever chips inside the heating zone. At the front (side loadlock) a vacuum transfer arm can be connected to unload the cantilever chips after the growth and to transfer them to the scanning electron microscope for pre-characterization.

Process parameter

A detailed description of the growth recipe is given in the appendix B.1. Here, we only give a brief summary of the growth parameters.

- Catalyst: $Fe(NO_3)_3 \cdot 9H_2O$, MoO_2 as active catalysts in a proportion of $\approx$ 8 %-at. Mo similar to [145]. Alumina (Al_2O_3) as catalyst support. IPA is used as a solvent. The cantilever chips are dipped in a catalyst dilution (and IPA) and blow dried.
- Temperature: Standard oven temperature 880 °C. Low number of suspended CNTs below 860 °C and too much amorphous carbon at >920 °C. Note that the exact temperature in the oven is unknown.
- Gas flow: 75 sccm CH_4 and 50 sccm H_2 (low flow) or 600 sccm CH_4 and 300-200 sccm H_2 (high flow).
- Growth duration: 15 min.
- Position in the oven: Cantilever chips are oriented perpendicular to the flow direction (i.e. in figure 3.2 the flow goes from right to left) and are positioned in the last third of the heating zone.

3.2. Techniques for analyzing the CNTs

In our experiment, we probe the electronic transport of our CNT devices. The transport properties strongly depend on the structure of the individual CNT. Instead of relying on room temperature and cryogenic temperature electronic transport measurements, it is more convenient to directly characterize the properties of the CNTs before integration into electric circuits. This section is dedicated to a pre-characterization of the grown CNTs which is required to evaluate and optimize the growth process. We are mainly interested in the following information:

- Ratio of number of single-walled with respect to multi-walled CNTs
- Ratio of number of single tubes with respect to bundles of tubes
- CNT diameter
- Contamination with amorphous carbon
- Contamination by electron beam induced hydrocarbons during pre-analysis with scanning electron microscopy.

Characterization techniques

Among the many methods for investigating CNTs, atomic force microscopy can be used to determine the diameter of the tubes, but it is limited to CNTs lying on a substrate and cannot be applied on our suspended CNTs [146] and is disregarded. Scanning electron microscopy can be used to detect the position of CNTs and to estimate their density [147]. We typically employ this method to select the CNTs and align them during the transfer onto the circuit chip. Raman spectroscopy is another option to determine the diameter and defects of individual CNTs based on vibration modes [42]. The last method used in this work is transmission electron microscopy (TEM), which directly gives us information on the structure of the CNT [2]. The advantages and drawbacks of the different methods are opposed in the following:

Scanning electron microscopy:

+ Simple and fast characterization based on contrast in e-beam imaging (larger diameter, potential contamination or multiple tubes (bundles, multi-walled CNTs) have a higher contrast than small diameter, clean, single-walled CNTs).
+ Possible directly on cantilever chips.
- No characterization of the internal structure possible.
- Electron-beam induced contamination. E-beam exposure leads to the hydrocarbon deposition from the remaining species in the vacuum chamber.

Raman spectroscopy:

+ Simple characterization under ambient conditions. On the basis of the Raman shift phonon modes can be extracted, yielding precise information on the structure of the CNT (e.g. semiconducting/metallic CNT, defects, and CNT diameter).
+ Possible directly on cantilever chips.
+ The number of radial breathing modes (RBM) allows to differentiate between bundles or multi-walled CNTs, and potentially single-walled CNTs showing only one RBM
- No differentiation between multi-walled CNTs and bundles possible.
- High signal only when the resonance condition between the incident laser energy and electronic transition is fulfilled. In a non-resonant process, it is easy to miss some modes and information. Potential single-walled CNTs can therefore still be bundles with additional CNTs that do not show RBMs.

Transmission electron microscopy:

+ Direct characterization based on e-beam scattering. Precise information on the structure of the CNT (diameter, contamination e.g. with amorphous carbon, number of walls, differentiation between bundle and multi-walled possible).
- Not possible on long suspended CNTs on cantilevers due to mechanical vibrations upon e-beam exposure. We have to use special grid chips with a different geometry and smaller suspension length instead.
- Time-consuming, expensive.

3.3. Experimental results

This section focuses on the internal structure of CNTs and therefore concentrates on the Raman and TEM characterization of the growth.

3.3.1. Raman characterization of the growth

The Raman characterization has been done together with Niklas Martin in the framework of a supervised bachelor's thesis [148], using two different setups. Initial measurements were conducted with a commercial Renishaw Raman microscope at the INT[3], but due to the restriction of only one laser wavelength ($\lambda_{\text{green}} = 532\,\text{nm}$, $P = 3\,\text{mW}$) and a large cutoff of the elastic Rayleigh scattering peak, we missed some RBMs and all vibration modes below $70\,\text{cm}^{-1}$. For the reliable determination of the RBMs we cooperated with the startup C12[4], where a detailed analysis of CNTs on two cantilever chips was performed using four different laser wavelengths ($\lambda_{\text{blue}} = 457\,\text{nm}$, $\lambda_{\text{green}} = 532\,\text{nm}$, $\lambda_{\text{red}} = 633\,\text{nm}$ and $\lambda_{\text{IR}} = 786\,\text{nm}$, $P = 1\,\text{mW}$).

In the following, we will discuss these measurements, which were performed directly on our cantilever chips. The CNTs on these cantilever chips have been preselected based on their shape and not primarily on low SEM contrast. It is therefore likely that the study also includes CNT bundles with higher SEM contrast than single CNTs, as well. CNTs that split into multiple tubes ("spider webs"), which are obvious bundles were excluded. All measurable Raman peaks (RBMs, D, G, G') have been analyzed in [148]. The discussion, however, will be limited to the most conclusive results. In particular, we did not perform an analysis of the G peak to infer the chirality of the CNT (semiconducting or metallic), because with our final process flow of the nanoassembly this information can only be verified in electronic transport measurements after the CNT transfer.

Principle of Raman spectroscopy and inference on the internal structure of CNTs

Raman spectroscopy relies on the inelastic scattering of light in the investigated structure. In a resonant Raman process, a photon excites an electron, which can then interact with phonons (Stokes process=phonon emission or anti-Stokes process=phonon absorption), and then relaxes back to the ground state under emission of a photon with different wavelength [42]. The measurement of the difference in the inverse wavelengths of incident and scattered photons ($1/\lambda_{\text{in}} - 1/\lambda_{\text{out}}$) is called the Raman shift and is given in units of 1/cm. The Raman shift contains information on the phonons involved in the Raman process. The phonons themselves have discrete frequencies depending on the phononic density

---

[3] Institute of Nanotechnology, KIT-Campus North, H.-von-Helmholtz-Platz 1, 76344 Eggenstein-Leopoldshafen, Germany

[4] C12 Quantum Technologies, 26 rue des Fossés Saint-Jacques, 75005 Paris, France

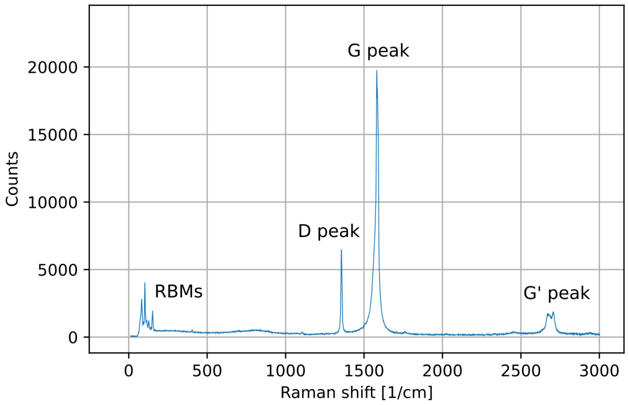

Figure 3.4.: Example of Raman spectroscopy of a CNT. Measured with the Renishaw Raman microscope with indicated phonon modes.

of states, and thus the measurement of the intensity of the Raman shift allows to obtain internal structural information of the material under investigation.

In the following, we will focus on the internal structure of CNTs and discuss the main phononic modes and their detection with Raman spectroscopy [42, 149]. An example Raman spectrum is given in figure 3.4.

- Radial-breathing modes (RBMs): These phononic modes ($\sim 100\,\mathrm{cm}^{-1}$-$300\,\mathrm{cm}^{-1}$) occur only in CNTs due to the cylindrical shape and not in other graphene-based materials and refer to the coherent oscillation of all carbon atoms along the radius of the CNTs (like a CNT breathing). The frequency is inversely proportional to the diameter of the CNT. For suspended CNTs, we use the formula from [150], where they calibrated their Raman data with TEM.

$$\omega_{\mathrm{RBM}} = 228/d \quad [\mathrm{cm}^{-1}] \tag{3.1}$$

- D mode: The defect-induced peak at $\sim 1350\,\mathrm{cm}^{-1}$ due to the first-order component of the hexagonal breathing mode. This mode can only become Raman active when the hexagon exhibits some defects and can therefore be used to quantify the amount of defects in CNTs.
- G-mode: The in-plane C-C bond stretching mode in the hexagonal lattice at $\sim 1585\,\mathrm{cm}^{-1}$. In contrast to graphene, we observe a splitting into a G_+ and G_- peak for CNTs due to different bond strengths in the axial and circumferential directions due to curvature-induced strain. From the shape of the G peak we can also determine whether the CNT is metallic or semiconducting [149].
- G' mode: Overtone of the D mode at $\sim 2700\,\mathrm{cm}^{-1}$ that is Raman active independent of the number of defects.

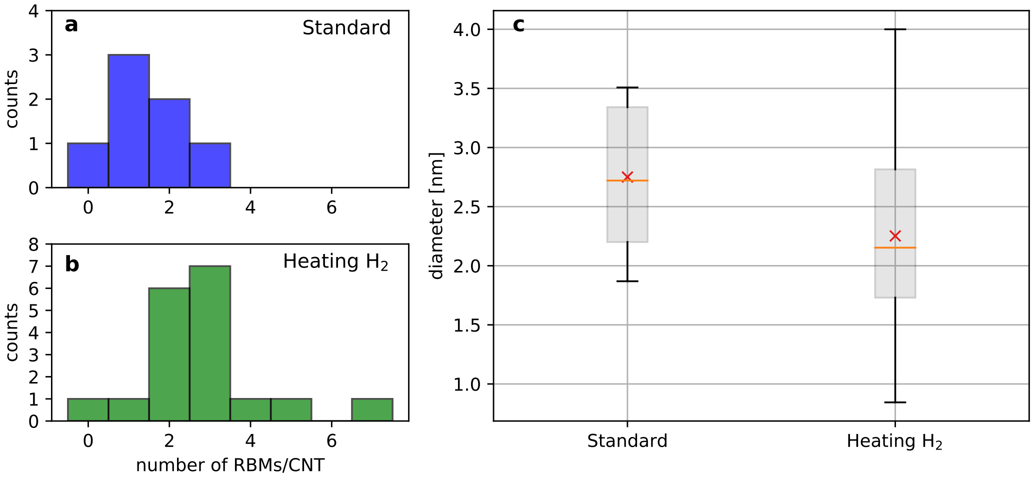

Figure 3.5.: RBMs and CNT diameter estimation. Data based on RBMs from the two cantilever observed by C12 with the standard recipe and the hydrogen addition during heating. **a** number of RBMs per CNT for the standard growth and **b** number of RBMs per CNT for the hydrogen addition during heating of the oven. **c** Boxplot with diameter distribution for the two chips (cross: mean value, bar: median, grey box: interquartile range and whiskers: 1.5 interquartile range). Calculated from the RBMs using $d = 228/\omega_{\mathrm{RBM}}$.

Diameter distribution based on RBMs

Two cantilever chips were sent to C12, one grown with the standard recipe (cf. appendix B.1) and the other one grown with the addition of 200 sccm hydrogen during the heating time of the oven. Most of the observed CNTs showed more than one RBM, as illustrated in figure 3.5a,b, but there are also CNTs with only one RBM, which could potentially be single CNTs. The few CNTs with only one RBM also have a very low SEM contrast, hinting towards a first correlation between SEM contrast and number of tubes (parallel tubes=bundles or concentric tubes=multi-walled CNTs). The two chips also had one CNT each where no RBMs could be detected, showing that we can also miss some RBMs even with 4 different laser wavelengths.

The diameter distribution of these two chips is illustrated in figure 3.5c calculated from eq. 3.1. For the standard recipe, the mean diameter is 2.75 nm ± 0.59 nm. For the recipe with hydrogen addition during the heating process, we observe a slightly smaller CNT diameter with a mean of 2.25 nm ± 0.75 nm.

Regarding a possible impact of hydrogen addition during heating, it must be mentioned that only two cantilever chips have been investigated by C12. On the basis of the data, it appears that hydrogen addition leads to a reduction of the diameter and an increase of the number of RBMs per CNT.

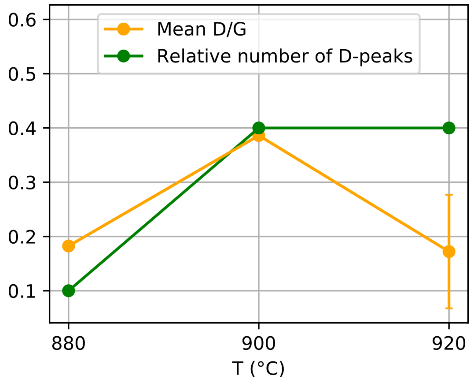

Figure 3.6.: Investigation of D peaks. Mean intensity ratio from D to G peak and relative number of D peaks for three cantilever chips grown at different temperatures. Figure taken from [148].

Choice of growth temperature based on the D peak

This study was performed with the Renishaw Raman microscope and included three chips with CNTs grown at 880 °C, 900 °C and 920 °C. In contrast to the RBM detection, the Renishaw microscope is better suited to detect the D and G peaks, whereas the latter peak could almost be found for all observed CNTs. The CNTs on the cantilever chip grown at 880 °C show the lowest relative number of D peaks with 1/10, while the higher growth temperatures both have a ratio of 2/5 (cf. figure 3.6). The mean intensity ratio from D peak to G peak in figure 3.6 indicates the amount of defects normalized to the overall signal, but due to the low number of D peaks it is not possible to draw any conclusion from these data. We decided to fix the growth temperature to 880 °C due to the lowest number of D peaks and a sufficient number of suspended CNTs, which were significantly reduced for lower growth temperatures.

3.3.2. TEM characterization of the growth

The TEM observation was performed by Di Wang with a Thermofisher Scientific Themis Z transmission electron microscope located at the KNMF[5]. Unfortunately, cantilever chips could not be loaded into the TEM and on top of that, due to the long suspension length of 30 µm large mechanical oscillations are expected upon e-beam irradiation, blurring the image and making an observation impossible. For these reasons, we grow CNTs on dedicated grid chips with a silicon nitride membrane, which contains arrays of 1 µm diameter holes[6]. TEM imaging is performed at an acceleration voltage of 60 kV, well below the threshold energy of 86 keV, where electrons can knock out carbon atoms and induce defects in the CNT [151].

---

[5] Karlsruhe Nano Micro Facility, KIT-Campus North, H.-von-Helmholtz-Platz 1, 76344 Eggenstein-Leopoldshafen, Germany

[6] PELCO Holey Silicon Nitride Support Film, 200nm thick, 1000nm pores, 0.5 x 0.5mm window, diameter 3mm

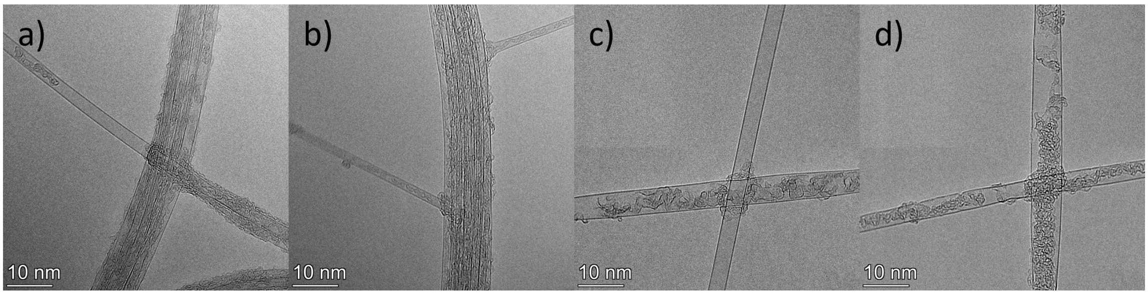

Figure 3.7.: Overview of TEM images. a) Single-walled CNT covered with carbon (right) and filled with carbon (left) and a contaminated bundle. **b)** Single-walled CNTs emerging from a bundle. **c)** Clean single-walled CNT. **d)** Varying diameter for CNTs grown at 920 °C.

In the following study four different growth tests are included: a) standard growth recipe (75 sccm CH_4 and 50 sccm H_2, 880 °C, 2 grid chips), b) growth recipe (75 sccm CH_4 and 50 sccm H_2, 920 °C, 1 grid chip), c) growth recipe (600 sccm CH_4 and 200 sccm H_2, 880 °C, 1 grid chip) and d) growth recipe (600 sccm CH_4 and 300 sccm H_2, 880 °C, 1 grid chip).

Overview

In this section we want to summarize the main observation results of our CNTs. The corresponding images can be found in figure 3.7.

- Single-walled to multi-walled CNT ratio: We observe a share of single-walled CNTs around 90 % independent of the recipe which is satisfying (cf. table 3.1).
- CNT bundles: Almost each grid hole has at least one CNT bundle, which is probably due to a high coverage of catalyst on these chips. Many single CNTs start off from bundles, but we can also observe pure single CNTs. The ratio between individual CNTs and bundles is therefore difficult to estimate properly.
- Uniformity of CNTs: For all growth tests, the CNT diameter looks uniform, except for the CNTs grown at 920 °C (cf. fig. 3.7d). There is a large diameter variation along an individual CNT, which could point towards a large variation in the reaction dynamics at this temperature. The variation of diameter is caused by defects along the CNT, and thus a lower growth temperature is desirable.
- Contamination: Most CNTs are contaminated with hydrocarbons or amorphous carbon. The bundles show more contamination than the individual CNTs (cf. fig. 3.7a,b). Sometimes the contamination is also only inside the CNTs (cf. fig. 3.7a), indicating that the contamination occurs during the growth process and not afterwards due to air exposure. Some CNTs are clean (cf. fig. 3.7c). We performed one of our main contact improvement techniques, radiative thermal annealing (RTA, cf. chapter 5), for 45 min at 5.6 W and 11 W on a grid chip with CNTs to investigate the impact on contamination. There was no evidence that the degree of contamination changed after RTA.

Table 3.1.: Ratio of single-walled (SW) and multi-walled (MW) CNTs. **a** Standard growth recipe (75 sccm CH_4 and 50 sccm H_2, 880 °C, 2 grid chips), **b** growth recipe (75 sccm CH_4 and 50 sccm H_2, 920 °C, 1 grid chip), **c** growth recipe (600 sccm CH_4 and 200 sccm H_2, 880 °C, 1 grid chip) and **d** growth recipe (600 sccm CH_4 and 300 sccm H_2, 880 °C, 1 grid chip).

growth	number of SW	number of MW	ratio SW	ratio MW
a	67	4	94%	6%
b	25	2	93%	7%
c	15	3	88%	12%
d	18	2	90%	10%

Diameter of CNTs

TEM images have also been used to determine the diameter of individual single-walled CNTs (bundles are excluded) for four different growth recipes. In general, all average diameters are around 2-2.5 nm with the exception of a few CNTs with diameter larger than 5 nm, observed only for low precursor flows (cf. fig. 3.8a,b). Interestingly, we cannot observe CNTs with a diameter of around 4 nm. Due to the large deviation, these outliers are not included in the average values. There is a slight tendency for smaller diameter CNTs in the high precursor flow recipes (cf. fig. 3.8c,d) and higher growth temperature could result in a larger CNT diameter than the standard temperature (cf. fig. 3.8a,b).

Comparison with Raman data

- The Raman and TEM data both show that the number of defects increases when the growth temperature is increased to 920 °C. We should therefore target the lowest temperature possible.
- The average values for the CNT diameter are comparable. This would mean that the results from the TEM study performed on dedicated grid chips could also be valid for CNTs grown on our cantilever chips. However, it must be noted that the Raman study also includes RBMs from bundles, while the TEM study only contains true single tubes.
- There is a tendency that hydrogen addition during heatup and a surplus of hydrogen can lead to a smaller CNT diameter and a higher proportion of multi-walled CNTs.

Elementary analysis of a catalyst island

With the TEM it is also possible to perform a high-angle annular dark field (HAADF) analysis. Here, the e-beam is focused on the sample and scans a predefined area (cf. fig. 3.9b) and the angular scattering due to Rutherford scattering is measured. The intensity of angular scattering of electrons depends on the atomic number ($\sim Z^{1.7}$ [152]) and allows distinguishing between chemical elements.

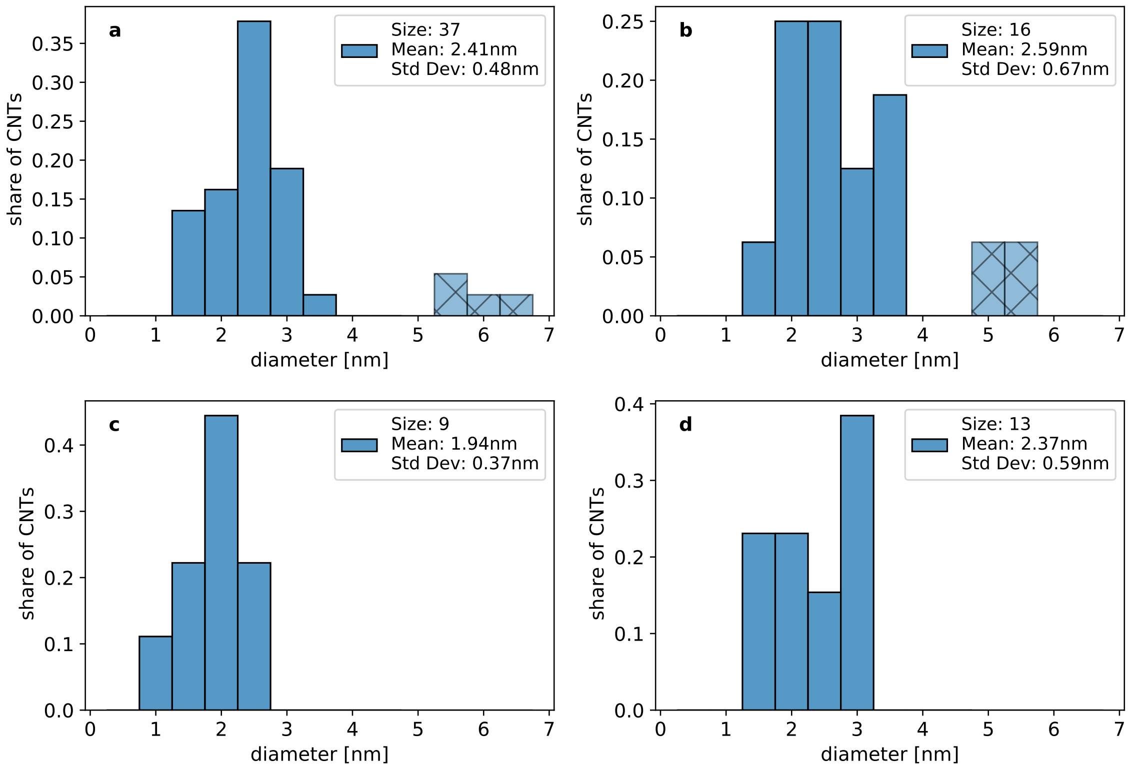

Figure 3.8.: Diameter calculation from TEM images. **a** standard growth recipe (75 sccm CH_4 and 50 sccm H_2, 880 °C, 2 grid chips), **b** growth recipe (75 sccm CH_4 and 50 sccm H_2, 920 °C, 1 grid chip), **c** growth recipe (600 sccm CH_4 and 200 sccm H_2, 880 °C, 1 grid chip) and **d** growth recipe (600 sccm CH_4 and 300 sccm H_2, 880 °C, 1 grid chip). For the mean values only diameters <5 nm have been considered and the hatched share of CNTs has been excluded.

Such an analysis was performed on a catalyst island in figure 3.9b. The elementary analysis shows that iron nanoparticles have a diameter of about 10 nm with a rather low size deviation. The formation of bigger nanoparticles is not observed, even if the nanoparticles touch each other (cf. figure 3.9c). This could hint towards the desired strong interaction between the alumina support and the nanoparticles. Molybdenum, on the other hand, forms much smaller nanoparticles which are homogeneously distributed with a slight accumulation in the vicinity of the iron nanoparticles (cf. figure 3.9d). It has to be mentioned that the observation took place after a growth and that during the growth at elevated temperatures this distribution might look different. In particular, we cannot infer the size of the nanoparticles from which CNT growth is initiated. Nonetheless, the distribution of molybdenum near to the iron sites agrees with the theory that molybdenum could promote growth at the iron sites as described in section 3.1.1.

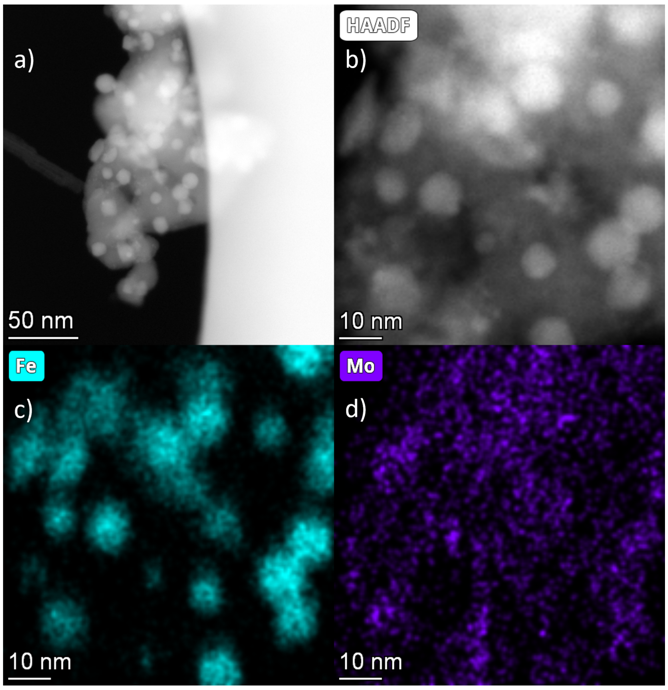

Figure 3.9.: Catalyst analysis with HAADF-TEM. a) Image of a big catalyst island, **b)** a zoom into the analyzed area, **c)** the elementary analysis of iron and **d)** the elementary analysis of molybdenum.

3.3.3. Calibration of SEM CNT images with the TEM images

With TEM we can resolve the internal structure of the CNT, while with SEM it is only possible to characterize CNTs based on imaging contrast and apparent width. In this section, TEM and SEM images are opposed to set the SEM contrast into reference with the internal structure of the CNTs. In figure 3.10 and 3.11, we compare two out of six observed grid holes.

- A very high SEM contrast originates from bundles that are usually covered with more amorphous carbon (figure 3.10 b & c, figure 3.11 a & c).
- Single-walled CNTs can also have a high contrast when they are contaminated with carbon (figure 3.10 a & c, figure 3.11 b).
- There are single-walled CNTs with low contamination and large diameter $\approx 5\,\text{nm}$ that also show a comparably high contrast but lower contrast than the contaminated CNTs (figure 3.10 a & d, figure 3.11 c).
- Single-walled CNTs with a diameter of 1-3 nm with low contamination have the weakest contrast (figure 3.10 a & d). In general, these CNTs are also less contaminated.

From the comparison in figure 3.10 and 3.11 we can conclude that SEM contrast is a reliable quantity to preselect CNTs. CNTs with large SEM contrast are most likely bundles or very contaminated tubes and should not be used for devices. The weaker the contrast, the smaller the CNT, the more likely it is a single CNT and the lower the contamination. Therefore, we should select CNTs with the lowest SEM contrast possible.

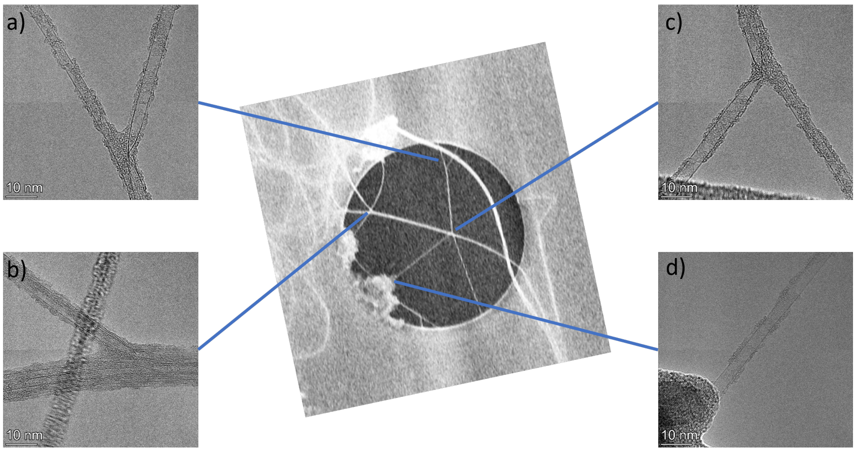

Figure 3.10.: Comparison of TEM images and corresponding SEM image. The blue lines map the CNTs on the SEM image (center) to the TEM images **a)**-**d)**. Taken from a 1 µm diameter grid hole.

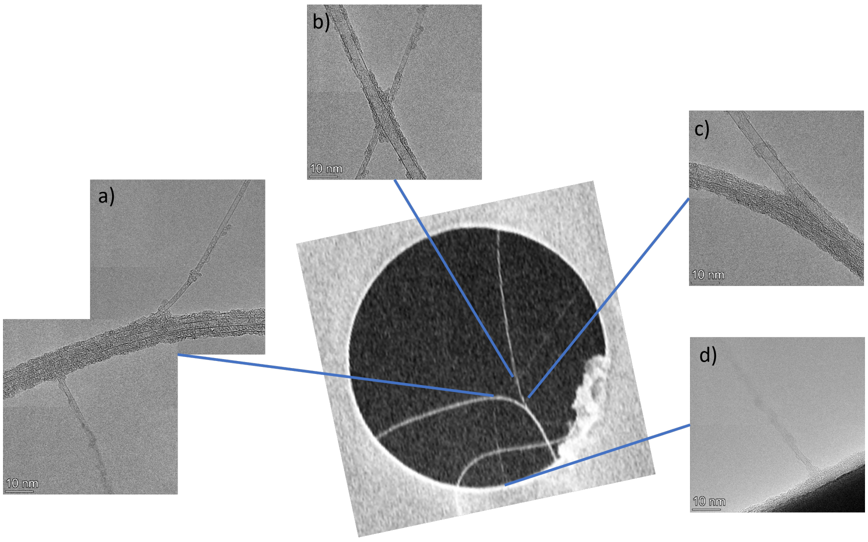

Figure 3.11.: Comparison of TEM images and corresponding SEM image. The blue lines map the CNTs on the SEM image (center) to the TEM images **a)**-**d)**. Taken from another 1 µm diameter grid hole.

3.3.4. Discussion on e-beam induced contamination

Before transferring a carbon nanotube, we localize the carbon nanotubes on the cantilever chip with scanning electron microscopy and select a suitable CNT based on shape, position and e-beam contrast. Electron-beam exposure of carbon nanotubes is expected to induce the deposition of hydrocarbons on the nanotube, which originate primarily from residual precursor species in the direct vicinity of the CNT [153]. The precursors could originate from the vacuum chamber, but the substrate surface is probably the strongest source of precursors.

The presence of hydrocarbons on the surface of the CNT can form an insulating barrier between the CNT and the metal of the contact electrodes, and can thereby deteriorate the CNT metal contact. Likewise, on the suspended part of the CNT, hydrocarbons could potentially lead to charge fluctuations impeding the electronic transport through the CNT quantum dot. It is therefore essential to limit the hydrocarbon deposition to a minimum. In the following, we want to discuss the e-beam induced contamination of our CNTs in more detail according to the supplementary notes of [37] and provide additional TEM data on SEM e-beam induced contamination in our setup.

Reduction of hydrocarbon deposition

For our setup we expect only a low deposition of hydrocarbons on the suspended nanotubes for the following reasons.

1. Small exposed area of suspended CNTs: Hydrocarbon deposition is mainly caused by low energy ($< 50\,\mathrm{eV}$) secondary electrons [154], and therefore, it is crucial to reduce the number of secondary electrons in the vicinity of the CNT. The secondary electrons occur as a product of the interaction of primary electrons with atoms, e.g. on the substrate or the CNT. In our case, the CNTs are suspended between pairs of cantilevers, and compared to the CNTs on the substrate, the limited number of atoms in the vicinity of a CNT reduces the emission of secondary electrons. In particular, the CNT section that is later embedded in the devices is in the center of the 30 μm long suspended nanotube, and thus far away from the potential secondary electron emission induced by the cantilevers. This becomes also visible in figure 3.2, where we measure the secondary electrons with the Inlens detector of the SEM. We can clearly see the low contrast between the suspended CNT and the background, while the electron count on the cantilevers is completely saturated (white color).
2. High acceleration voltage of the e-beam: The acceleration voltage determines the penetration depth of the electrons where the interaction with the atoms and the emission of secondary electron occurs. Therefore, the amount of hydrocarbon deposited on a substrate surface strongly depends on the acceleration voltage of the e-beam. This is demonstrated on a silicon substrate in figure 3.12, where the higher the acceleration voltage, the lower the deposition of hydrocarbons on the surface. Compared to a standard low acceleration voltage of 1-2 kV [153], we use a relatively high acceleration voltage of 8 kV.
3. High vacuum: The hydrocarbon deposition depends on the number of precursor species for hydrocarbon formation, mainly coming from the residual vacuum, the surfaces in the chamber [153] or from the substrate. For this reason, we work at low pressure ($P = 2.5 \times 10^{-6}$ mbar), and for suspended CNTs, the central section, which is integrated into devices, is approximately 10 μm away from the cantilever substrate.

The parameters used during the SEM exposure are the following: Acceleration voltage: 8 kV, chamber pressure: $p = 2.5 \times 10^{-6}$ mbar, beam current: 70 pA, pixel size: 27.9 nm × 27.9 nm, exposure time per pixel: 2.5 μs

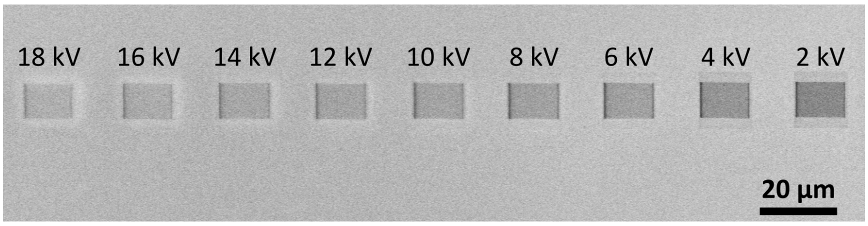

Figure 3.12.: Hydrocarbon deposition. Exposure of a predefined area with different acceleration voltages and resulting hydrocarbon deposition taken from [37], supplementary notes.

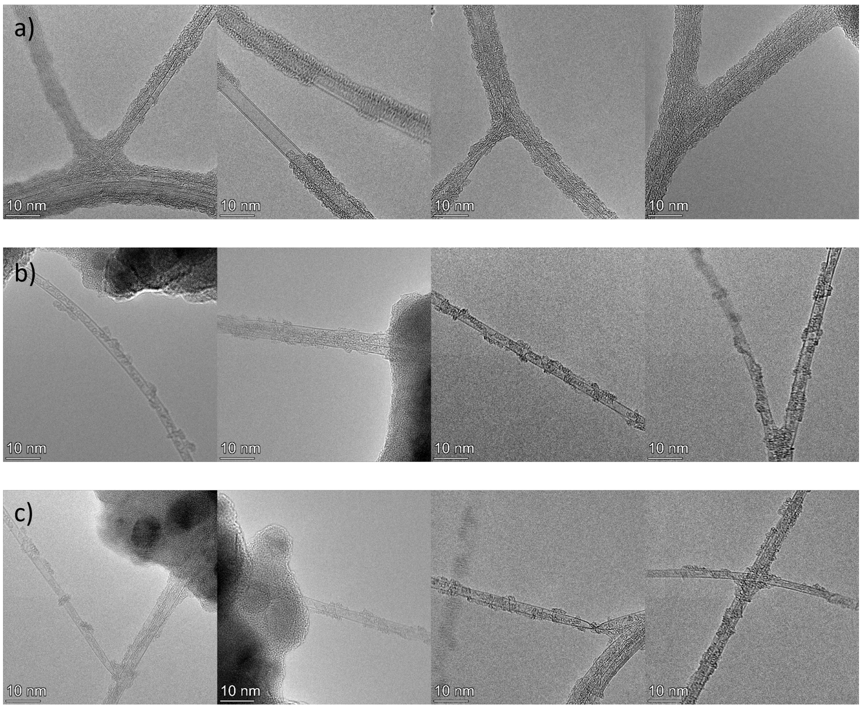

Figure 3.13.: Comparison of different SEM exposure duration and magnification observed with TEM. a) 10 min, magnification 22000, **b)** 1 scan with the usual scanning parameters, magnification 2000 and **c)** no imaging before TEM.

TEM characterization of SEM induced contamination

TEM provides a direct image of contamination on CNTs and is therefore used to determine the contamination of CNTs that have been exposed to the e-beam during scanning electron microscopy. As a benchmark, we exposed an area at magnification 22000 for 10 min, where we can clearly see the contamination covering large parts of the CNTs in figure 3.13a. In contrast to this high exposure dose, we cannot observe a difference in contamination between an exposure with the usual scanning parameters from above in figure 3.13b and no exposure at all in figure 3.13c. This provides further evidence that contamination during our SEM precharacterization is probably negligible.

4. Design and fabrication of circuit chips

4.1. Design and material selection

4.1.1. Design overview

In this thesis, the term "chip" refers to a larger chip of 15 mm × 15 mm or 20 mm × 20 mm. This chip, as represented in figure 4.1, hosts a number of "circuit chips" that contain the electrical circuits making the connection to the CNT. The term "sample" refers to a circuit chip with a transferred CNT. In early designs, a circuit chip can host two CNTs and therefore two samples. Each sample can contain a number of CNT junctions, which form CNT quantum dots or SQUIDs. We call these junctions "devices".

In other CNT integration techniques based on a stochastic process, such as top growth, the yield of successfully suspended CNTs can be drastically increased by scaling up the number of devices per chip. The deterministic nanoassembly approach, on the contrary, allows one to separate the circuit chip fabrication from the CNT synthesis and to reduce the number of devices to a few per circuit chip. This offers more flexibility in the design, and the remaining space on the circuit chip can be used to easily include additional components on the chip, especially required for hybrid architectures, such as microwave filters or cavities. An overview of the two device geometries investigated in this thesis is given in figure 4.1. In the following, we will discuss key elements of circuit chip design.

Trench

Despite the many benefits of the nanoassembly technique, there is a major spatial constraint on the circuit chip required to align the desired CNT on the cantilever chip with the transfer position on the circuit chip. Since the suspended CNT on the cantilever chip needs to be brought into mechanical contact with the circuit electrodes, and most of the CNTs are not on the tip of the cantilever chip, the cantilever chip needs to be lowered below the chip surface. For this purpose, we etch material from the circuit chip next to the transfer area and build two cavities on either side of the transfer position with a depth of 10-15 µm. In the following, we call these cavities simply trenches. Since we transfer the CNTs under an angle, this trench depth allows to reliably transfer CNTs up to 20 µm away from the cantilever tip.

The upper limit for the width of the area between the trenches (which we call “bridge“ in the following) is determined by the distance between a pair of cantilevers which measures

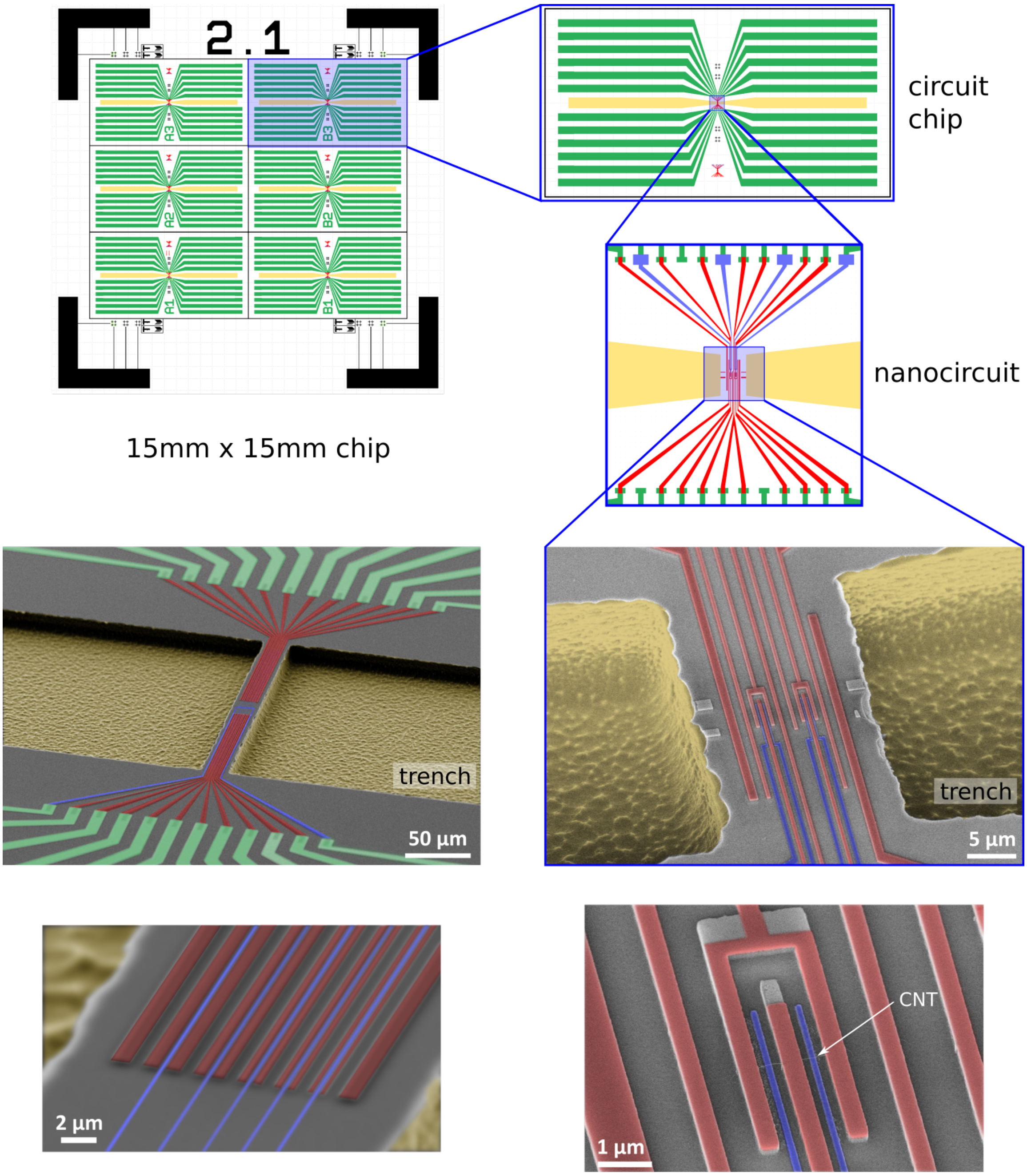

Figure 4.1.: Overview of circuit chip design. Upper: 15 mm × 15 mm chip with 6 circuit chips and zoom into a nanocircuit. Green: DC lines, yellow: trench and nanocircuit with red: contact electrodes and blue: gate electrodes. **Bottom:** False colored scanning electron micrographs with zoom into the two nanocircuit designs: **Left:** Basic circuit used for contact tests with pairs of parallel electrodes for a set of quantum dots and zoom into the center of the bridge. **Right:** Circuit with superconducting electrodes with zoom on a SQUID with a transferred CNT (white). The DC lines are outside the imaging window in these images.

30 µm. To have some additional freedom for aligning the CNT, we use bridges measuring about 20-25 µm in width and 40 µm or 200 µm in length.

DC lines

Each chip contains 24 DC lines which have bondpads on the edge of the chip to connect the lines on the chip with the measurement setup. Microwaves to drive motion in the CNT are also applied through these DC lines. The large DC lines end about 100 µm away from the bridge, where 12 of these lines arrive from the bottom of the bridge and 12 lines from the top. At this position, the DC lines are connected to the so-called nanocircuit, which refers to the circuit with the smallest electrode width in the nanometer range around the CNT transfer area on the bridge. This modular approach, separating the large DC lines from the nanocircuits, allows us to easily modify the design of the nanocircuit for each chip or experiment independently from the design of the large DC lines, which can usually be kept unchanged.

Nanocircuit

The nanocircuit is the core of each circuit chip. The nanocircuit comprises two different types of electrodes: Contact electrodes which make electrical contact to the CNT and gate electrodes which are located below the CNT and couple capacitively to the CNT to control its chemical potential. In the frame of this thesis, two main designs have been used, one with pairs of parallel contact electrodes and a gate electrode in between for simple quantum dots and one for SQUIDs with a fork-like geometry for the contact electrodes and two gate electrodes to control either of the two quantum dots on the SQUID. At the end of the CNT transfer process, we aim for suspended CNTs, also when a gate voltage of up to 10 V is applied. This results in constraints in the ratio between the height of the gate electrode and contact electrodes, depending on the suspension length of the CNT. Different transfer tests on junctions as long as 1200 nm showed that a ratio of suspension length to height difference between gates and contacts of 10 to 1 still reliably produces suspended CNTs. However, in most cases, we aim for short CNT junctions of 200-500 nm, and the ratio is more on the order of 5 to 1 or even lower. This leads to contact electrode thicknesses on the order of 100 nm and gate electrode thicknesses of about 20 nm. The width of the gate electrodes can impact the shape of the potential in the CNT quantum dot. However, for short suspension lengths the contact resistance is dominant and the width is usually chosen to fit easily within the contact electrodes measuring around 100-200 nm. For contact electrodes, the width is crucial, as it can have a large impact on the contact and the contact improvement techniques (cf. chapter 5). Here, we varied the width between 50 nm and 1000 nm. Independent of the circuit, we always have two electrodes on the left and right side, which make the first contact with the CNT and are used to cut the CNT before retracting the cantilever chip.

4.1.2. Material of circuit chip

Chip material

The chip itself is mainly used as carrier substrate and consists of 525 µm p-doped <100>silicon (Czochralksi-process, resistivity 1-5 mΩ cm) with a layer of amorphous, 290 nm thick SiO_2 fabricated by dry oxidation. We use silicon due to its comparably easy nanotechnology processing, while the doping allows to potentially use a backgate and charges can drain more easily than on undoped silicon facilitating the fabrication process. The SiO_2 top layer forms an insulating barrier between the metal electrodes of the nanocircuit and the silicon, preventing an electrical shunt between the metal electrodes. The chips are commercially bought[1] in the form of 4 inch wafers and then diced into 20 mm × 20 mm or 15 mm × 15 mm chips. Each chip can then host between 6 and 10 circuit chips of about 3-4 nm × 6-7 nm.

Gate electrode material

There is no general constraint on the material of the gate electrode. At the beginning we used aluminum electrodes with a thickness of about 10 nm with a thin layer of 8 nm amorphous aluminum oxide to insulate the gates from potentially touching CNTs. Later, we moved to platinum without an additional oxide layer. Platinum has the advantage of a higher melting temperature, and thus a higher resilience during heat application in contact improvement techniques, and proved to be more robust with respect to electrostatic discharge (ESD) in particular for gate electrode arrays with widths on the order of 50 nm. A second advantage is lower charge noise in the vicinity of the CNT compared to other materials, such as aluminum, due to the absence of surface oxides. In addition, we use a titanium adhesion layer between the gate metal and the silicon oxide whose thickness varies between 3 nm and 20 nm, depending on the surface roughness after the previous fabrication steps. Titanium is commonly used due to its ability to form chemical bonds between the substrate and the metal [155].

Contact electrode material

The material choice for the contact electrodes is more delicate since it has a direct impact on the CNT metal contact and electronic transport through the CNT. In order to make a good electrical contact to the CNT, at least 3 nm of a noble material are required on top of the electrode with a high work function, comparable to the one of the CNT (4.76-5.05 eV, where bundles are on the lower end and single-walled CNTs on the upper end)[55, 56, 57]. Likewise, it should have good wetting properties to the CNT. We achieved the lowest contact resistance using platinum and palladium. Regarding the core material, basic contact improvement tests have been performed on electrodes with core materials

---

[1] SIEGERT WAFER GmbH, Charlottenburger Allee 7, 52068 Aachen

such as gold, aluminum, niobium, molybdenum, palladium and titanium. Aiming for a proximity-induced supercurrent through the CNT, the core of the contact electrode should consist of a superconductor as source of superconductivity. For the superconducting devices presented in chapter 6 the alloy and type 2 superconductor MoRe is used. Similar to the gate electrodes a thin layer of adhesive material needs to be added. In most cases, it consists of few nanometers titanium, whereas for molybdenum-based core electrodes molybdenum shows similar adhesion and the titanium layer is not required. The core of the contact electrode has also an impact on the surface roughness and the heat transport, which can both affect the CNT metal contact and the different contact improvement techniques in chapter 5. To apply the radiative thermal annealing (cf. chapter 5.4.3), it is crucial that the core material is not affected by the heating process.

4.2. Basic techniques in nanofabrication

This section will be dedicated to the fundamental processes in nanofabrication and will explain how structures can be patterned on empty chips. These processes will then be applied to the fabrication of normal and superconducting circuit chips. Although some parts of the fabrication have been carried out at the Physikalisches Institut (PHI), all chips have been mainly processed in the ISO 6/ISO 7 cleanroom of the Nanostructure Service Lab (NSL) at the CFN institute to guarantee a high cleanliness, and thus a high yield of functional devices.

In order to add to or remove parts from the chip locally, the rest of the chip needs to be protected by a mask which needs to be removed at the end of the process. This mask has to be patterned with the desired design in a process called lithography. For structural dimensions in the nanometer and micrometer range, organic resist masks are most commonly used. These are polymers that are sensitive to electron-beam exposure or optical exposure and are either crosslinked (negative resist) or scissioned (positive resist) upon exposure. In a subsequent step, the development, the exposed positive resist or unexposed negative resist is dissolved in organic or alkaline solvents and the mask can be used for metal deposition (lift-off process, cf. figure 4.2a) or as a protective mask during etching (etching process, cf. figure 4.2b). At the end of the process, the mask can be dissolved in organic solvents and the pattern on the chip remains. The basic techniques will now be explained in detail.

4.2.1. Fabricating the mask

Resist deposition

The resist must be deposited homogeneously on the chip. The technique of choice is spin coating. Here, the chip is sucked with a vacuum pump onto a rotating chuck, the resist is dropcast on the chip, and the chuck is rotated to distribute the resist homogeneously. The

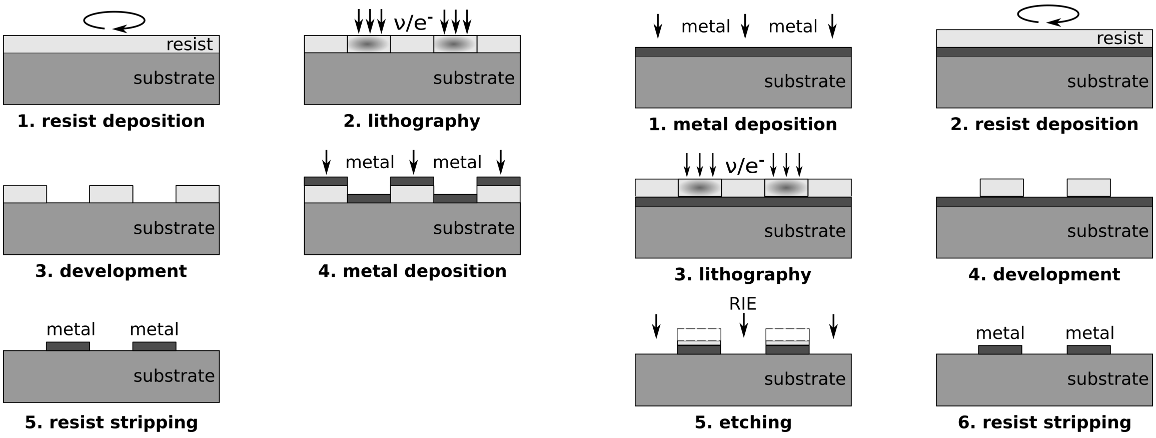

(a) Lift-off process **(b)** Etching process

Figure 4.2.: Overview of the different steps in lift-off (for positive resist) and etching process (for negative resist). Drawn without considering the undercut in the resist profile. The individual steps are described in the text.

final thickness depends on the spinning speed (1000-6000 rpm) and the resist viscosity. In a subsequent step, the hard bake, the chip is heated on a hot plate above the evaporation temperature (T = 90-180 °C) and the resist mask becomes solid.

Optical and electron-beam lithography

The resist mask needs to be patterned and, depending on the sensitivity of the resist, this can be done with photon or electron exposure at the energy scissoring or crosslinking the resist and an appropriate intensity or dose. The electron-beam lithography is performed by Silvia Diewald (NSL), where an electron-beam with an acceleration voltage of 50 kV scans the desired pattern and modifies the resist[2]. This direct lithography technique is used for the nanocircuits due to the small dimensions below the optical resolution limit. Likewise, the pattern can be easily adapted from chip to chip. For larger structures with minimum widths of > 2 µm optical lithography is used. Here, we make use of a mask aligner[3]. Light from a Hg-Xe gas lamp exposes the resist through a separate quartz mask containing the pattern, which is aligned and brought into contact with the circuit chip. Because the full mask can be exposed homogeneously within a few seconds, this method is faster than electron-beam lithography and is mainly used for large structures on the circuit chip that are rarely modified, such as the trenches and the large DC lines.

Resist development

After the exposure, the final pattern needs to be formed. For this purpose, the chip is inserted into a developer bath. In case of a positive resist, the exposed parts with broken

---

[2] Jeol JBX-5500, JEOL Ltd. Akishima Tokyo Japan

[3] Mask Aligner Süss MA/BA 6, SUSS MicroTec SE Schleißheimer Str. 90, 85748 Garching

polymer chains are dissolved in some organic solvent, while the unexposed parts with long polymer chains still remain. For a negative resist, we typically use an alkaline developer which etches the unexposed parts and leaves the exposed crosslinked resist largely unaffected. In practice, however, the developer always attacks the remaining resist, as well, a process referred to as dark erosion. Therefore, a second bath, the stop bath, is used to prevent further resist erosion after the development and residual developer is removed. In general, the profile and width of the electrodes depend on the sensitivity and thickness of the resist, the exposure dose due to scattering effects, and the development time, which all have to be chosen carefully. In some cases, e.g. to facilitate a lift-off process, it might be desired to create some undercut profile, and a stack of two resists with different sensitivity can be used.

4.2.2. Structuring using the resist mask

Metal deposition

In this thesis, two different metal deposition techniques have been used: Sputtering and e-beam evaporation. Sputtering refers to a process in which the impingement of accelerated ions on a metal target leads to momentum transfer, and atoms are kicked out of a target and then hit the sample. In our case, for sputtering, a flow of argon is led into the vacuum chamber, and an argon plasma is lit at a sputter gun in the vicinity of the target. We distinguish between DC magnetron sputtering and RF sputtering, where a DC electric field or an AC electric field generates the plasma, respectively. RF sputtering is commonly used for insulating materials when applying a bias between the gun cathode and the target becomes difficult. Sputtering requires pressures on the order of 10^{-3} mbar to have a sufficient number of argon atoms in the vacuum chamber to excite the plasma. This comparably high pressure reduces the mean free path of the target atoms to tens of centimeters, making sputtering a less directive process. Therefore, sputtering is not suitable for lift-off processes, since the metal film would climb up the resist walls impeding resist removal. Therefore, it is only used for global metal deposition on the chip prior to resist application. Sputtering has a major benefit over evaporation when metal alloys are deposited. For evaporation, this would require the complex and expensive installation of two electron guns due to the difference in evaporation temperatures of different metals, while for sputtering, either premixed targets can be used or metal from targets of two sputter guns can be sputtered simultaneously, independent of their evaporation temperature (cosputtering).

For e-beam evaporation, the metal is filled in a crucible and heated beyond the evaporation temperature. In our case, we use electron-beam evaporation, where an electron beam heats up the metal, and the metal film is then deposited on the sample positioned above the crucible. The evaporation takes place in high vacuum at pressures ranging from 10^{-7}-10^{-6} mbar at which the mean-free path largely exceeds the dimensions of the vacuum chamber. Therefore, thermal evaporation can be considered as a directive deposition method and is the choice for lift-off processes.

Etching

In this work we use two different dry etching techniques, Reactive Ion Etching (RIE)[4] and argon milling[5]. Both are based on a plasma, separating the gas in the chamber in electrons and ions, whereas the ions are accelerated to the sample by electric fields. The impingement of ions leads to a momentum transfer, ejecting atoms from the sample. In RIE chemical reactive ions are used. In addition to the physical impact, they can react with the sample atoms and form volatile chemical components which can then be removed from the reaction chamber by pumping. Thus, RIE can be considered to be a combination of chemical and physical etching. Argon milling, on the other hand, uses only physical etching and in our case is performed under an incident angle of 45° to avoid redeposition on the sample.

Resist stripping

In a last step, the resist mask has to be removed to obtain the final structures. If the metal has been deposited on top of the resist (lift-off process), the resist and the metal on top of the resist are removed. For an etching process, the resist mask protecting the structures is simply removed. In both cases, this is achieved in a bath with organic solvents. The solubility of the resist and the efficiency of resist removal can be enhanced by increasing the solvent temperature on a heat plate or by mechanical assistance such as ultrasonication, bubbling with a pipette, or shaking the chip in the solvent.

4.3. Fabrication of normal conducting circuit chips

The design of the normal conducting circuit chips is illustrated in figure 4.3 and the fabrication contains four lithographies. This section only gives an overview of the processes; details can be found in the appendix B.2.

1. Deposition of large DC lines and markers:
   As mentioned in the basic design considerations, these large parts remain largely unmodified and are therefore patterned with optical lithography. We also pattern markers, which are required to align the following lithographies with respect to each other. We use gold because of its high electrical conductance, chemical stability as noble metal, and high contrast in electron microscopy.
2. Deposition of local gates:
   The local gates as part of the nanocircuits are patterned with e-beam lithography in a lift-off process. Due to their thickness of about 20 nm, it is more convenient to

---

[4] Sentech Plasma Etcher SI220, SENTECH Instruments GmbH, Schwarzschildstraße 2, 12489 Berlin

[5] Kaufman KDC 40 Ion Source, Kaufman & Robinson Inc., 1330 Blue Spruce Dr, Fort Collins, CO 80524, USA

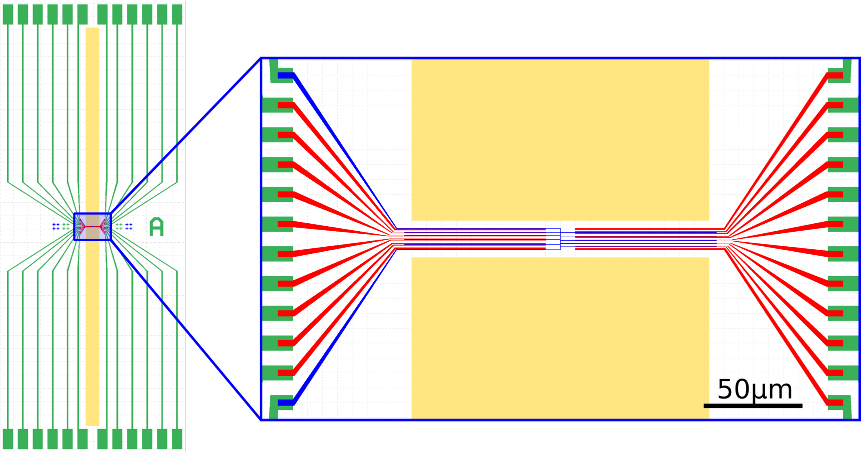

Figure 4.3.: Layout of a single normal conducting electrode circuit chip. Chip size 7.2 mm × 3.2 mm. Right: zoom into the nanocircuits. Green: DC lines and markers, red: contacts, blue: gates, yellow: trenches.

fabricate them before the thicker contact electrodes. A double layer resist stack is used to facilitate the lift-off.

3. Deposition of contact electrodes:
The contact electrodes are fabricated in a similar way with a lift-off process and e-beam lithography. The thickness measures about 100 nm, and likewise a double layer resist stack is used.

4. Trench etching:
In order to etch 10-15 µm deep trenches into the substrate, first the 290 nm thick SiO_2 layer has to be etched with RIE and then pure silicon. After an optical lithography the SiO_2 is etched using CHF_3 gas, which only barely attacks the about 2 µm thick S1818 resist. A high aspect ratio, i.e. vertical trench walls are targeted. In semiconductor industries a so-called Bosch process [156] with fluorine gases in an inductively-coupled plasma (ICP) machine is commonly used. The Bosch-process consists of multiple cycles of two steps, an etching step and a passivation step. First, a high bias is applied and the SF_6 ions physically etch the silicon at the bottom with high anisotropy and chemically in a more isotrope process. A cycle follows where the SF_6 is replaced by C_4F_8 at lower bias, leading to an almost purely chemical passivation of the trench, including the side walls. When SF_6 enters the vacuum chamber again, the physical etching will remove the passivation layer on the bottom first and during the chemical etching the trench bottom is primarily attacked, while the side walls are still protected. In principle, it is possible to achieve almost vertical sidewalls [157], but at the NSL we could only use an ordinary RIE machine with less anisotropy resulting in less vertical walls.

4.4. Fabrication of superconducting circuit chips

The need for new fabrication schemes

Initially for superconducting circuits, we followed the same lift-off process as for normal conducting circuits in section 4.3 and only replaced the core of the normal conducting contact electrode by a superconductor, such as niobium or aluminum. However, it turned out that aluminum is not compatible with the contact improvement technique of radiative thermal annealing in chapter 5, and all other available superconductors, such as niobium, require high evaporation temperature and heat up the resist by thermal radiation from the crucible heating or deposition of hot atoms. This might not be an issue for large electrodes or on unpatterned substrates where we could achieve a critical temperature of close to 9 K of 100 nm thick niobium films. If the electrode width is on the order of 1 µm or smaller, the resist can degas in the vicinity of the contact electrodes and deteriorate the quality of the metal [158]. For instance, niobium contacts of 400 nm width fabricated with a lift-off did not show a superconducting transition down to 2 K (end of the measurement range of the PPMS[6]).

The solution to this problem is the metal deposition on a plain substrate without resist and the risk of degassing, either via thermal evaporation or sputtering and then patterning the circuits in an etching process at comparably low temperatures.

4.4.1. Molybdenum-rhenium as superconductor

The etching process is also compatible with sputtering and opens up the use of new materials that cannot be easily evaporated. In this work, the type II superconductor alloy molybdenum-rhenium (MoRe) is used as source of superconductivity.

Material properties

$\mathrm{Mo}_{1-x}\mathrm{Re}_x$ has been investigated since the 1960's [159] and possesses different properties depending on the substrate temperature during deposition and the atomic ratio x which is usually chosen between 0.25 and 0.62 to yield a high critical temperature [160]. Critical temperatures ranging from 10-13 K are commonly observed [161, 162, 159, 163] and even for 2-10 nm thick films critical temperatures of $5.6\,\mathrm{K} < T_\mathrm{c} < 9.7\,\mathrm{K}$ have been reported [164]. In many studies, this high critical temperature is related to the formation of a metastable A15 phase for thin films [165, 160]. Critical fields as high as $H_{\mathrm{c}2}(0) = 8.5\,\mathrm{T}$ could be measured [162]. The residual resistance ratio RRR $\approx$ 1.1-1.7 [162, 160] indicates the large degree of disorder in the superconductor. Due to the low solubility of elements, such as oxygen, in interstitial sites and the observation that superconductivity is largely unaffected [163], the

---

[6] Physical-Property-Measurement-System, Quantum Design, 10307 Pacific Center Court San Diego, CA 92121 USA

superconductor has been suggested for microwave resonators. Internal quality factors of 23 700 [166] and even 700 000 [167] have been measured in $\lambda/4$ coplanar waveguide resonators, both limited by coupling to two-level systems in the substrate.

Applications of molybdenum-rhenium in hybrid nanostructures

In the field of hybrid nanostructures MoRe has been used to proximitize InAs nanowires [168], induce supercurrent in graphene [169] or single-molecule magnets in electromigrated gold junctions [170] and even nano-SQUIDs with nanoconstrictions made out of MoRe have been reported [171].

With respect to CNTs, MoRe has been tested in the frame of the top growth process [166, 167] due to its resilience against the harsh CVD conditions. In particular, MoRe has already been used to successfully fabricate superconducting CNT circuits with the top growth process [31, 122] at the elevated growth temperatures of 800-900 °C. In another work [172], synthesized CNTs are distributed over circuits and after an annealing at high temperatures of 900 °C transparent CNT metal contacts are formed, which can carry supercurrents up to 50 nA. The authors link these transparent contacts to the formation of molybdenum carbides, but could also measure a yet much smaller supercurrent of 350 pA in a MoRe+Pd material stack annealed at 220 °C. Driven by these promising results which should also be applicable to our nanoassembly technique (with the restriction of low annealing temperature) and the extraordinary properties of $\mathrm{Mo}_{1-x}\mathrm{Re}_x$, we decided to use this material in the same atomic percentage ratio of $x = 0.4$ as a source of superconductivity in our circuits.

4.4.2. Fabrication scheme for MoRe based circuit chips

An overview of the fabrication process is given in table 4.1, details can be found in the appendix B.3. A characterization of the superconducting properties of the MoRe films is presented in the appendix A.3.

Metal deposition

Prior to sputtering, the chip is heated in the vacuum chamber to 200 °C for 15 min to desorb water and organic residues. The area of the holder with the heating unit restricts the maximum chip size to 15 mm × 15 mm hosting up to 6 devices. First a layer of 15 nm molybdenum is sputtered onto the circuit chip and then a second sputter gun with a rhenium target is turned on to sputter simultaneously from two sources (co-sputter) the 41 nm thick MoRe alloy film at a rate of 0.5 nm/s. The ratio of the sputtering powers is set to result in an approximate atomic percentage ratio of Mo(60)Re(40). Once the MoRe has been deposited, the top layer (palladium or platinum) is sputtered from another sputter gun in the same vacuum chamber. Performing the MoRe and Pd/Pt deposition in the same

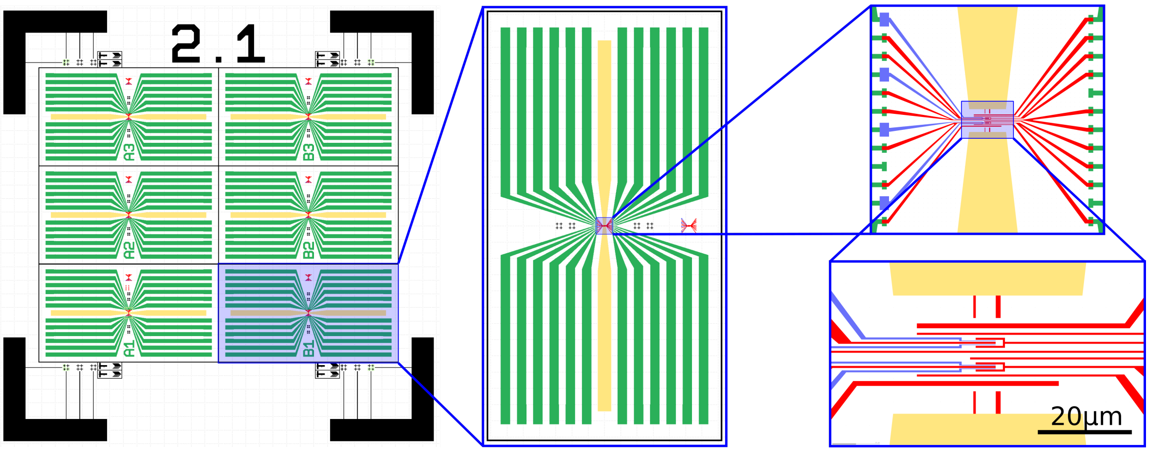

Figure 4.4.: Layout of the superconducting circuit chip. The full chip of 15 mm × 15 mm contains 6 circuit chips (3.6 mm × 6.6 mm). Black: alignment markers, green: DC lines (optical lithography part of the contacts), red: e-beam parts of the contacts (fabricated in one step with the DC lines), blue: gates and yellow: trenches. The blue electrodes cover the green electrodes in all directions to ensure gate continuity.

Table 4.1.: Overview of the different fabrication steps for the superconducting circuit chips. Details see text.

step	process	material
metal deposition	sputtering	15 nm Mo, 41 nm MoRe 11-13 nm Pd or Pt
alignment markers	optical lithography lift-off process	5 nm Ti, 40 nm Au
contact electrodes	e-beam lithography optical lithography etching process	Ar milling: −13 nm Pd/Pt RIE ($SF_6/Ar/O_2$): −41 nm MoRe −15 nm Mo RIE (CHF_3): −150 nm SiO_2
gate electrodes	e-beam lithography lift-off process	20 nm Ti, 25 nm Pt
trenches	optical lithography etching process	RIE (CHF_3): − rest of SiO_2 Bosch process: −15µm Si

vacuum chamber and keeping the time between the two depositions as short as possible ensures a clean MoRe-Pd/Pt interface. The final stack is depicted in figure 4.5.

Alignment markers

Similar to the fabrication of normal conducting electrodes alignment markers are used to align different lithography steps with respect to each other. Gold also has a sufficiently large e-beam contrast to MoRe+Pd/Pt to be easily used in e-beam lithography.

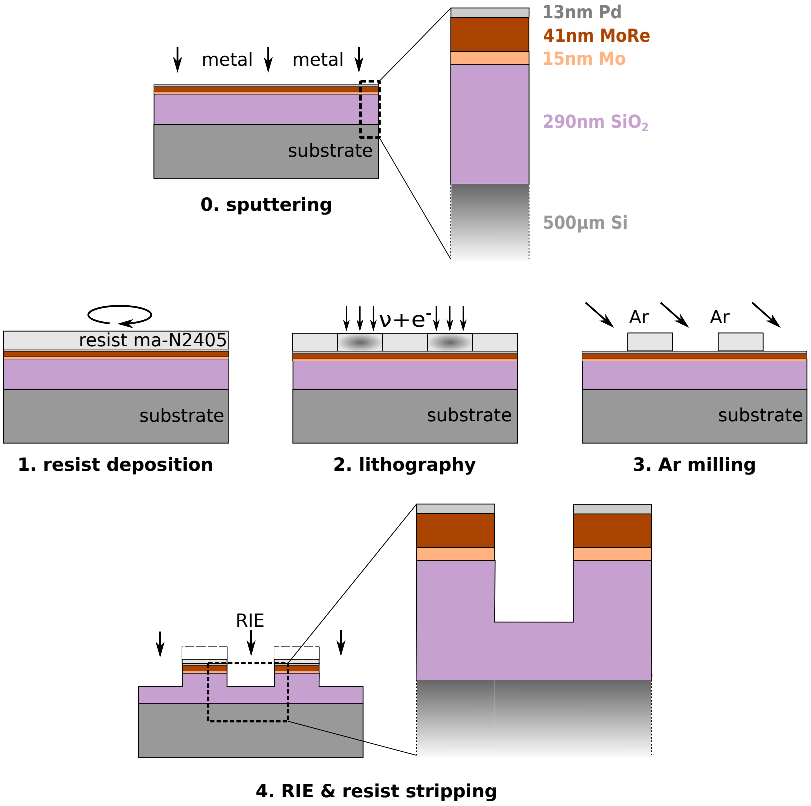

Figure 4.5.: Overview of the sputtered material stack and the process of negative contact electrode lithography. 0. The metal is sputtered on top of the substrate. **1.** The resist ma-N2405 is spin coated on the substrate. **2.** The resist is exposed using optical and ebeam lithography followed by a single development process. **3.** Argon milling is performed under angle indicated by the arrows, removing the Pd/Pt top layer. **4.** Reactive ion etching (RIE) etches the MoRe and part of the SiO_2 resulting in self-aligned trenches in the SiO_2 after resist stripping.

Negative contact electrode lithography

This step is the most delicate one in the whole fabrication process and illustrated in figure 4.5. The key is to use a negative resist (ma-N2405[7]) which is highly sensitive to electrons and photons allowing to perform e-beam lithography followed by optical lithography and only one development. The large DC lines and the contact electrodes of the nanocircuit can then be etched at the same time. Since palladium or platinum are hard to etch chemically with RIE, they are physically removed with argon milling under an angle. Then in the RIE-machine the MoRe is etched using a combination of SF_6 for chemical etching and Ar for physical etching, improving the anisotropy of the etching which leads to more vertical sidewalls. A small amount of oxygen was added to the plasma to potentially yield a cleaner result. After a minimum overetch into the SiO_2 we etch about 150 nm further into the SiO_2 with CHF_3, Ar and O_2. This step allows to embed the gate electrodes well below the contact electrodes to ensure suspended CNTs and to keep the contact electrode thickness to a minimum.

---

[7] micro resist technology GmbH, Köpenicker Str. 325, 12555 Berlin

Comments on the process:

- Compared to the target design, the final structures possess a tail of 1 µm length which is due to application of argon milling under angle (cf. figure 4.1). Argon milling perpendicular to resist walls results in a protective effect from the resist walls and an incomplete Pd/Pt milling. In the following RIE process this remaining Pd/Pt serves as etch mask and this part remains as a tail.
- After the process the surface roughness is increased which is due to pillars covering in particular large areas. For the nanocircuits and smaller etching area these features do not appear. This points towards area dependent etching dynamics but the origin of these pillars is still unclear. A possible cause could be re-deposition of palladium which serves as an etch mask during subsequent RIE. Since the important CNT transfer area of the nanocircuits is almost unaffected, these pillars are not a drawback.

Gate lithography

The gates are deposited in a similar lift-off process as in the case of normal conducting circuits. However, there are a few changes to ensure gate continuity. First, the etching of the chip surface results in large surface roughness, and therefore, we increase the thickness to 20 nm of titanium adhesion layer and 25 nm of platinum gate electrode. Second, the gates need to be connected to the large DC lines outside the nanocircuits. To achieve a reliable electrical contact, the gates have to climb up the insulating silicon oxide until they reach the conducting MoRe+Pd/Pt. Therefore, the gate evaporation is performed under an angle of 25°.

Trenches

The removal of about 150 nm of SiO_2 does not impact the trench etching. The same recipe as for the normal conducting electrodes can be used. We decreased the trench widths from 200 µm to 40 µm to decrease the length of the nanocircuit and to reduce the risk of fabrication failures.

4.4.3. Fabrication challenges of MoRe electrodes

The fabrication process for MoRe electrodes had to be developed from scratch and many difficulties arose during fabrication tests. These are dealt with in this section.

A common feature is the appearance of crystallites ranging from few 100 nm to few µm which are homogeneously distributed over the sample and can impede the sensitive fabrication process of the contacts (cf. figure 4.6a). They occur also on pure rhenium and are most likely related to the formation of rhenium oxides (ReO_3) [173] and also observed for films deposited with atomic layer deposition [174]. The sensitivity to oxygen exposure is nicely demonstrated by applying oxygen plasma to MoRe or Re surfaces, leading to a

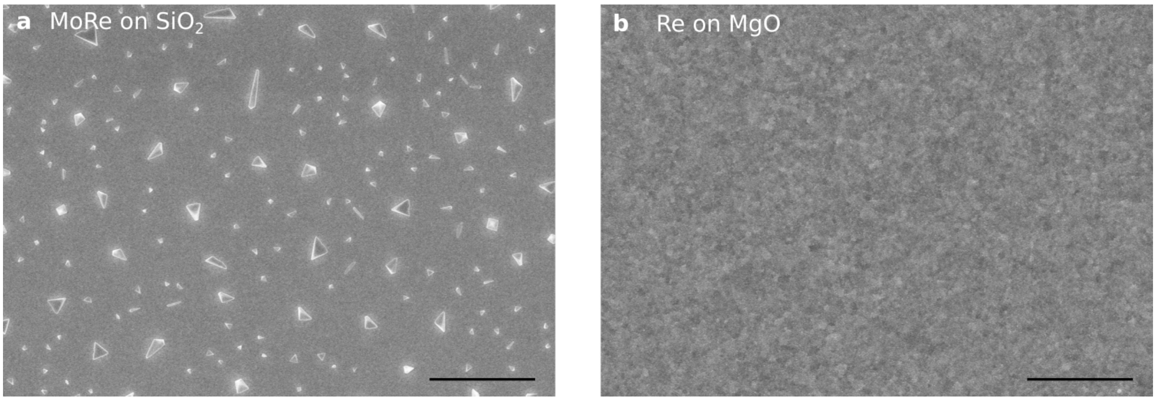

Figure 4.6.: Scanning electron micrograph of crystallites. **a** Surface of a 60 nm thick Mo(60% at.)Re(40% at.) co-sputtered film on a SiO$_2$-substrate showing the formation of crystallites. Similar crystallites could be observed on 50 nm thick Re films. **b** Surface of a 50 nm thick Re film on a chip with MgO surface with absence of crystallites. Black: scale bars 2 µm.

significant increase of these crystallites, or by adding oxygen to the deposition process [173]. The Re^{6+} cation in ReO$_3$ is unstable and the oxide decomposes to Re$_2$O$_7$ and ReO$_2$ above 400 °C [175]. While Re$_2$O$_7$ sublimes at around 300 °C, the ReO$_2$ decomposes at a temperature of 850 °C [175], a temperature we cannot reach with our heating setup. The main aim lies therefore in the reduction of possible oxygen contamination on the chip and in the vacuum chamber of the sputterer. Interestingly, the crystallites do not occur on an MgO surface (cf. figure 4.6b), pointing towards a reaction with the Re and the silicon oxide surface. Several measures have been taken to reduce the number of crystallites:

- Heating the chip at 200 °C prior to sputtering in the vacuum chamber to desorb water and other potentially oxygen containing species.
- Sputtering a molybdenum layer of 15 nm first to isolate the Re from the silicon oxide.
- Minimizing the air exposure time of the chips and storing them in vacuum (10^{-1}-1 mbar).
- Covering the chip with inert metal. Adding a Pd/Pt layer of 10 nm before exposing to air makes the MoRe film more resilient to air exposure. Luckily this layer is required for our application anyway.

During further processing several rules must be obeyed:

- O$_2$ plasma must not be applied at any time after the MoRe is deposited.
- Organic solvents such as NEP or DMSO attack the film and only acetone, IPA, water and TMAH containing developer (such as MF-319[8], AZ726MF[9] with 3-5 % TMAH) have been successfully tested. Even ma-N2405 resist reacts with the MoRe+Pd/Pt when exposed to air for more than two days.

---

[8] micro resist technology GmbH, Köpenicker Str. 325, 12555 Berlin

[9] MicroChemicals GmbH, Nicolaus-Otto-Str. 39, 89079 Ulm

5. Integrating CNTs into electrical circuits by nanoassembly

In the last two chapters, we have discussed how suspended CNTs are grown on cantilever chips and how the electric circuits on the circuit chips are fabricated. The next step is the core of the sample fabrication, the integration of suspended CNTs into the electric circuits on the circuit chip. In the introduction, we reviewed the three main integration techniques: post-growth fabrication, post-fabrication top growth, and nanoassembly, and explained why nanoassembly is our first choice. In this chapter, we will first highlight how our nanoassembly technique differs from other nanoassembly techniques and explain our nanoassembly technique in detail. The second part of the chapter is then dedicated to the improvement techniques of the CNT metal contact, which allowed us to reach the open quantum dot regime and proximity-induced superconductivity in nanoassembled CNT devices. Part of the results have been published in [37], where we demonstrate our ability to reliably reach the open-quantum dot regime with our nanoassembly technique.

5.1. Introduction to CNT nanoassembly

In this section, we will give an overview of the state-of-the-art nanoassembly techniques and explain the differences in our approach.

5.1.1. Overview of nanoassembly techniques

An overview of different nanoassembly techniques is given in figure 5.1. All techniques have in common that their circuit chip has some elevated area/mesa structure ("bridge"), where the electrodes are patterned onto which the CNT is transferred. Likewise, the separate chip on which CNTs are grown consists of some cantilevers or a mesa-like structure to be able to transfer the suspended CNTs.

Zhong’s group was the first to report the mechanical transfer of CNTs [176]. They used a quartz chip with nanopillars as growth chip and a mask aligner for the alignment of suspended CNTs and the mechanical transfer. A similar approach has been implemented in the Kouwenhoven group [180] and in the Laird group [181, 83]. This approach has the advantage of allowing multiple CNTs to be transferred simultaneously. A different approach has been realized by the Ilani group [177] where instead of using a mask aligner,

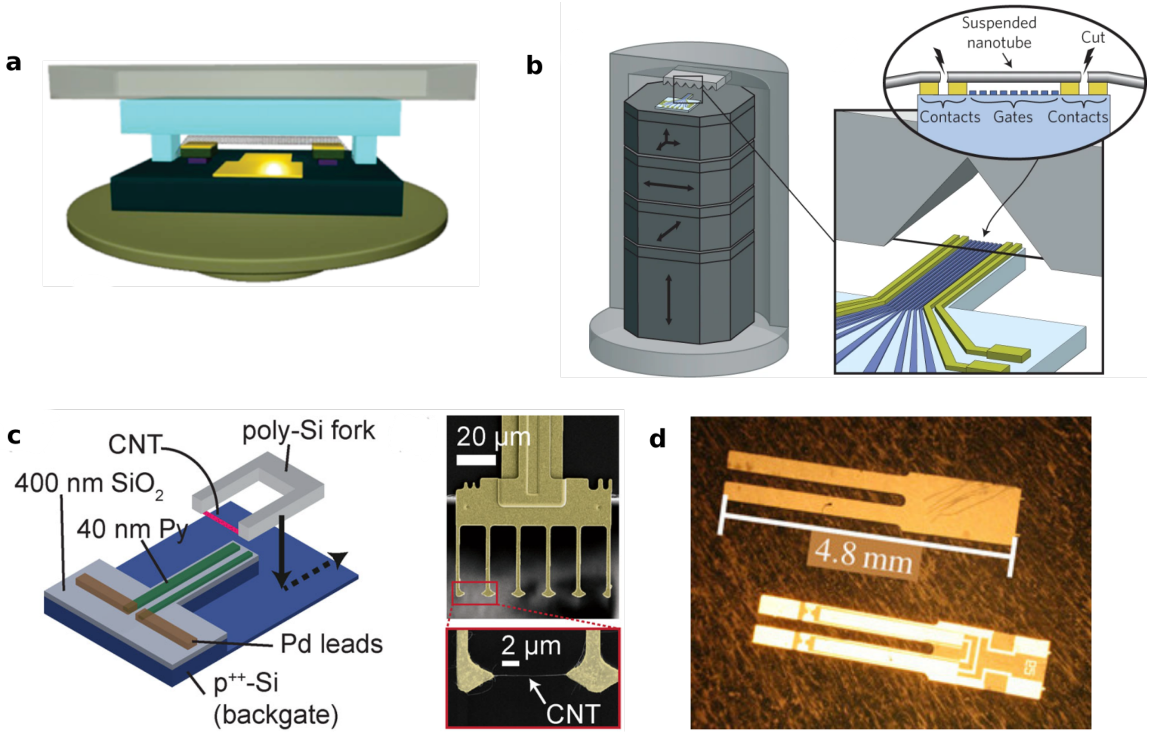

Figure 5.1.: Selection of different CNT transfer techniques. **a** Technique with mask aligner [176], **b** technique with transfer in optical microscope [177], **c** technique with cantilever chips from [178] and **d** cantilever chip layout from [179].

a micromanipulator is used for the alignment in a dedicated setup. This comes with the benefit that the circuit chip can already be electrically connected to the sample holder, giving rise to a more precise control of the transfer process compared to a purely mechanical approach. During the approach, a bias voltage is applied between two electrodes, and once the CNT is in mechanical contact, the contact can be detected electrically by measuring a current through the CNT. Moreover, the ability to electrically monitor the transfer process can give a more detailed understanding of the room-temperature transport properties of the CNTs and the CNT metal contact. For instance, when a CNT is cut by applying a too high voltage, a single cut is expected for a single-walled CNT, and multiple cuts indicate bundles or multi-walled CNTs. Similar approaches have been implemented in the Schönenberger group, where they used cantilevers instead of a mesa growth structure [178]. This approach has been further developed by the Hierold group [182, 61]. The design of cantilevers varies between the different groups. For instance, the Hüttel group uses commercially available quartz forks with only two cantilevers [179]. Our approach is based on the works in the Kontos group [183] and has been implemented and further developed by Tino Cubaynes at KIT. The most recent developments in the field include the foundation of start-ups, such as Chiral Nano[1] or C12[2], specialized in the nanoassembly technique with the aim of commercializing CNT based devices.

---

[1] Chiral Nano AG, Überlandstrasse 129, 8600 Dübendorf, Switzerland

[2] C12 Quantum Technologies, 26 rue des Fossés Saint-Jacques, 75005 Paris, France

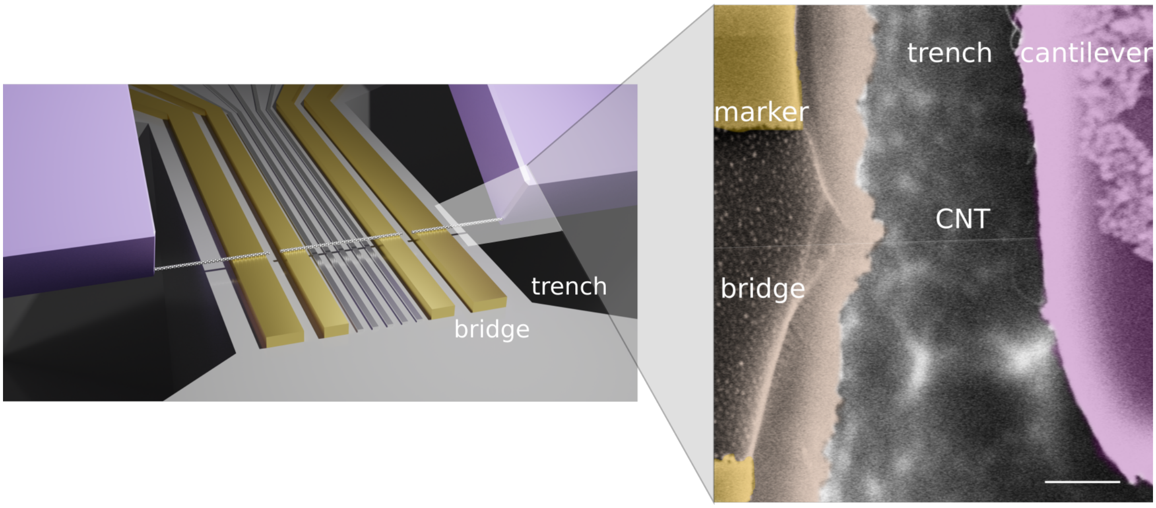

Figure 5.2.: CNT transfer in vacuum chamber of scanning electron microscope (SEM). The CNT can be precisely aligned with the help of markers (not shown in the left schematics) and e-beam imaging. The distance between CNT and the "bridge" of the circuit chip can be monitored throughout the whole transfer without exposing the relevant section of the CNT. Scale bar: 1 µm.

This also demonstrates the superiority of the nanoassembly technique compared to other fabrication techniques with respect to the potential for industrial fabrication. Compared with our fundamental research where we prioritize quality over quantity, the industrial implementation of the nanoassembly technique has a huge potential to be automated, boosting the fabrication efficiency towards mass fabrication.

5.1.2. Our nanoassembly approach

Our nanoassembly approach stands out from the other approaches in several aspects, which we will highlight in the following.

Scanning electron microscope (SEM)

Instead of using a mask aligner at ambient pressure or micromanipulators in combination with an optical microscope under vacuum, our approach is based on transferring the CNTs inside the vacuum chamber of a dedicated scanning electron microscope with the ability to apply voltages and measure currents in situ on 24 individual lines (cf. figure 5.2). This comes with multiple benefits:

1. Complete monitoring of the transfer process: With SEM, the CNT position can be tracked during the entire transfer process. To avoid e-beam induced contamination, the SEM observation is done far from the sections implemented in devices (cf. figure 5.2b). The difference in working distance between the focal plane of the CNT and the focal plane of the substrate allows the distance between the CNT and the electrodes to be measured with a precision of a few µm at any time. The contact is then detected

electrically by applying a bias voltage between two electrodes and measuring the current.

2. Easy investigation of circuit problems: The SEM contrast is proportional to the detection rate of secondary electrons. The application of a voltage on an electrode of the circuit chip results in a local electric field that modifies the secondary electron emission, which appears as a contrast change in imaging. By applying a bias voltage to the electrodes on the circuit chip and their connections can be checked in situ. In particular, in the case of some fabrication error in the circuit chip or a broken CNT, SEM in combination with the application of a DC bias voltage on any of the electrodes is a powerful tool, allowing for a quick and easy investigation of the problem.
3. Alignment: The custom piezostage allows us to align the cantilever chip with respect to the circuit chip laterally with a minimum step of 10 nm. As seen in figure 5.3, we can perfectly center the CNT on electrodes of only 800 nm width and conservatively estimate the positioning accuracy by ±200 nm [37].
4. CNT observation: As shown in chapter 3, we can quickly localize CNTs with scanning electron microscopy on cantilever chips and reliably pre-characterize them based on SEM contrast, while potential e-beam induced contamination is negligible. In contrast to [184] with only a single pair of cantilevers, we use cantilever chips with at least 44 cantilevers to increase the chance of having single suspended CNTs (cf. figure 3.2).

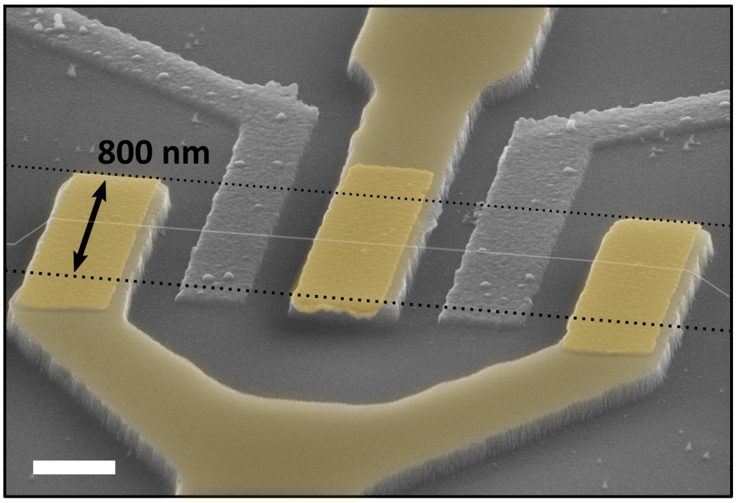

Figure 5.3.: Scanning electron micrograph of a CNT-SQUID. The CNT is perfectly centered and the positioning accuracy is estimated to ±200 nm. Scale bar: 500 nm. Fabricated by Tino Cubaynes (from [37]).

Full vacuum process

Another unique feature of our approach is that the CNT is never exposed to air, minimizing the potential contamination of the CNT. For this purpose, we have implemented the following process flow:

1. CVD growth of CNTs and storage under vacuum (10^{-2} mbar) in the CVD chamber
2. Transfer of the cantilever chip with a custom vacuum transfer arm into the vacuum chamber of the SEM ($< 5 \times 10^{-2}$ mbar)
3. Nanoassembly in the vacuum chamber of the SEM ($\sim 2.5 \times 10^{-6}$ mbar)
4. Transfer into the vacuum pumped cryostat ($< 10^{-5}$ mbar) using another custom vacuum transfer arm ($< 5 \times 10^{-2}$ mbar)

5.2. Setup and transfer process

Before detailing the CNT transfer process, we will describe the setup used for the transfer, including sample holders, transfer arms, and the custom SEM setup.

5.2.1. Sample holders and transfer arms

For the nanoassembly, two different types of chips are used, the cantilever chip with the CNTs and the circuit chip to transfer the CNTs onto. Each type of chip has its own holder, as shown in figure 5.4. We refer to them as cantilever holder (for the cantilever chip) and sample holder (for the circuit chip). Each holder is compatible with one custom vacuum transfer arm (cantilever vacuum transfer arm or sample holder vacuum transfer arm, respectively).

The sample holder has to fulfill several requirements since it must be compatible with the setup in the SEM, cryostat, and vacuum transfer arm. This includes the DC and RF connection lines, good thermalization at mK temperatures, filtering, such as RC filters for the DC lines or bias-Tees for the RF lines, and easy connectivity to the different setups.

The core of the sample holder (cf. figure 5.4a) is the custom PCB that hosts the circuit chip and makes the electrical connection to the chip via microbonded[3] 25 µm diameter aluminum wires. The circuit chip is glued with PMMA close to the tip of the PCB. This has the advantage that the chip is easily accessible when transferring CNTs and that the chip can be placed inside the 3D vector coils in the cryostat. In total, there are 24 DC lines made from gold-plated copper, with 12 lines on each side of the sample. To mechanically excite the CNT and apply RF, there are three coplanar waveguides on the side that is further away from the tip. At the rectangular base of the PCB, a custom RC filter stage

---

[3] West Bond 7476E, WEST BOND Inc., 1551 South Harris Court, Anaheim, CA 92806-5932

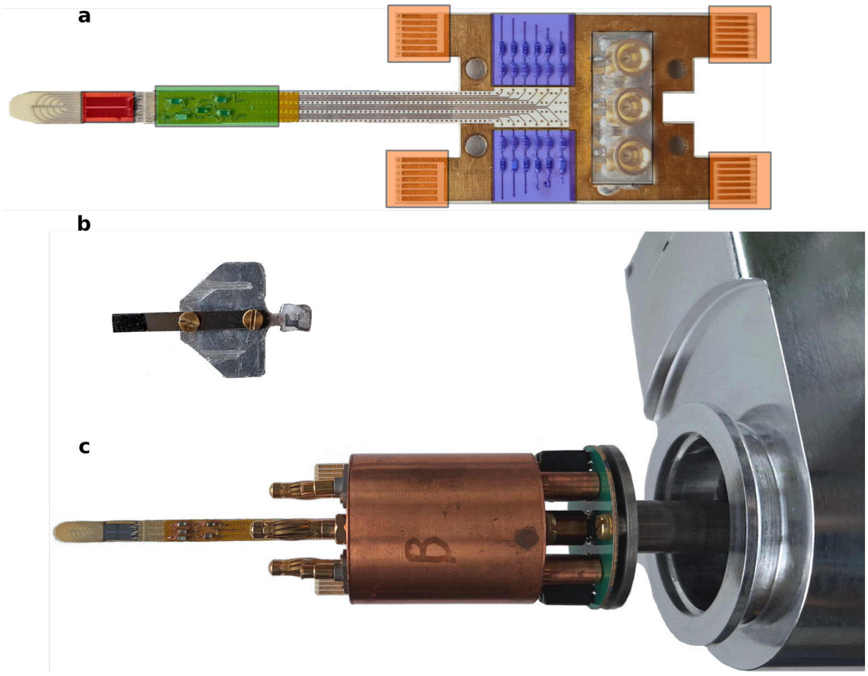

Figure 5.4.: Overview of sample holder, cantilever holder and transfer arm. **a** PCB with 24 DC lines and 3 RF lines (representation inspired by [64]). Red: Position to glue and microbond the circuit chip, orange: PCI connectors to electrically connect the PCB to SEM and cryostat setup, blue: RC-filter stage, green: Resistors in the DC line as part of the bias-Tees to block RF and grey: RF connectors and inline capacitors as second part of the bias-Tees to block DC in the RF line. **b** Cantilever holder with connector on the right to be inserted into the cantilever transfer arm (not shown) and front with black carbon tape to pick up the cantilever chip. **c** PCB inserted into full sample holder with banana plugs and SMP connectors. The sample holder is screwed to the sample holder vacuum transfer arm. Green: PCB of vacuum transfer arm to ground the DC lines during transfer.

can be implemented by choosing suitable SMD capacitors and resistors. We typically choose $C = 1\,\mathrm{nF}$ and $R = 1\text{-}100\,\mathrm{k\Omega}$ which results in a RC-time constant of 1-100 µs. To decouple DC and RF, bias-Tees have been implemented. They consist of a capacitor in the RF line to block all DC components and a resistor in the DC line that sufficiently attenuates RF signals. For more details on the bias-Tees see [64]. The DC electrical connections to the cryostat, SEM, or transfer arm are made via PCI plugs, and the PCB contains special connectors on each side of the rectangular base. Each connector has 6 lines on the top side and 6 lines on the bottom side. The connectors on the front part of the PCB and the rear part connect to the same lines. The sample holder is plugged to the transfer stage in the SEM and the mK stage in the cryostat with the front connectors of the PCB, while the rear connectors allow for grounding of the PCB during transfers between the SEM and the cryostat to avoid electrostatic discharge issues. For this purpose, the transfer arm contains PCI plugs that are grounded via 500 kΩ resistors. For RF connectivity, SMP connectors are used, which are only plugged in the cryostat, and each sample holder is equipped with coaxial cables, linking these connectors with the PCB. The whole PCB is mounted inside a copper barrel, which is equipped with banana plugs on the front side to be able to plug the sample holder into the transfer stage of the SEM or the cryostat. In addition to mechanical support, they also ensure proper grounding of the sample holder and thermalization at mK temperatures. The rear side of the sample holder contains a threading that is required to screw the rod of the vacuum transfer arm to the sample holder for the transfer between the different setups.

5.2.2. Custom SEM for nanoassembly

The scanning electron microscope is a Zeiss Sigma 300[4] and is operated using the InLens secondary electron detector at an acceleration voltage of 8 kV during transfer to limit hydrocarbon deposition (cf. chapter 3).

Custom SEM stage

Instead of using a standard sample holder, the SEM is equipped with a custom CNT transfer stage (cf. figure 5.5) providing a plugging mechanism for the cantilever holder and the sample holder. The cantilever holder is plugged to a connector that is mounted on top of a piezostage[5] that combines x, y, z-motions and the two angles Θ_x, Θ_z around the x-axis to tilt and around the z-axis to rotate the cantilever holder. The transfer stage is mounted on top of the SEM stage, which can move and rotate the transfer stage as a whole. The independent local movement of the cantilever holder with the piezostage and the global movement with the SEM stage allow us to align the cantilever chip with the circuit chip with electron microscopy precision. The electrical connections to the piezomotors and the 24 DC lines come in the form of cables connected to plugs mounted at the door of the SEM chamber. For this reason, displacements and rotations have to be performed carefully to avoid pinching of the cables. The DC lines end in a breakout box which allows us to connect individual DC lines to BNC cables, while each line comes with a switch to change the potential of the line between floating, ground or ground via a resistor of 470 Ω[6]. To give rise to radiative thermal annealing, which is a method we use to improve the CNT metal contact after the transfer, a 70 W halogen lamp has been installed on the side of the e-beam column. The lamp is surrounded by a tantalum shield and has two electrical connections that are connected to a voltage source controlling the heating power.

Measurement electronics

The in-situ measurement of contact resistances and application of voltage to induce a current through the CNT junctions are performed with an ADwin Gold II[7] which is a computer-controlled real-time data acquisition system. It features 8 analog outputs and 16 analog inputs, which can be controlled by a computer that is connected to the ADwin

---

[4] Carl Zeiss AG, Carl-Zeiss-Straße 22, 73447 Oberkochen

[5] SmarAct GmbH, Schuette-Lanz-Strasse 9, 26135 Oldenburg

[6] Due to a confusion, resistors of 470 Ω were accidentally implemented instead of the targeted 470 kΩ, without any negative impact

[7] Jäger Computergesteuerte Meßtechnik GmbH, Rheinstraße 2, 64653 Lorsch

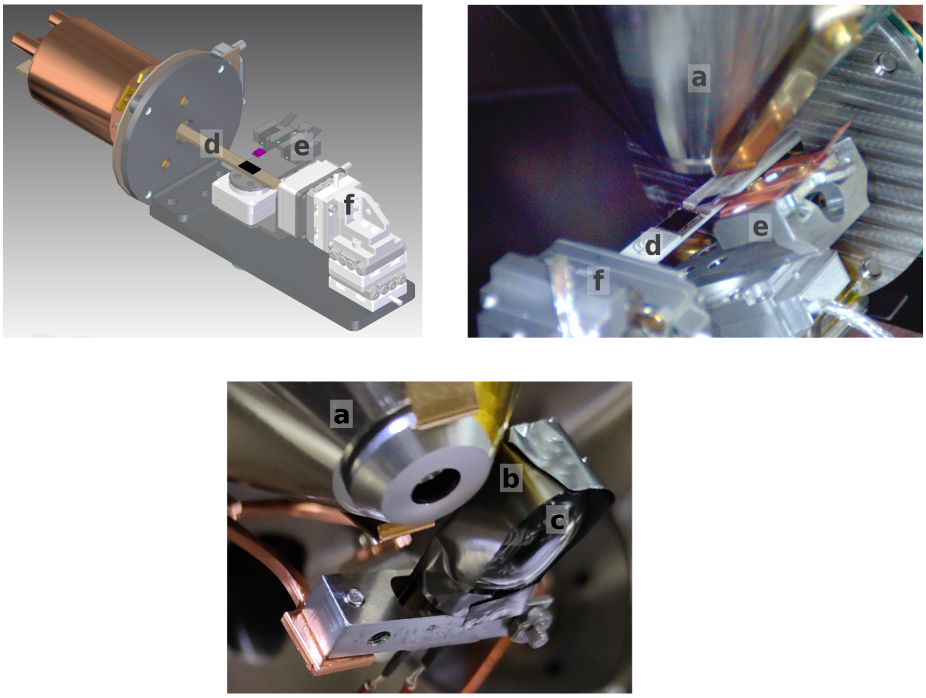

Figure 5.5.: Overview of the setup in the SEM. Left Custom transfer stage designed by Tino Cubaynes. **Right** Cantilever chip tilted during transfer. **Bottom** Heater setup (from [37]). Legend: a) E-beam column, b) Tantalum shield, c) Halogen lamp, d) PCB with circuit chip (dark), e) Cantilever holder with cantilever chip (pink), f) Piezostage.

via an ethernet connection. Each port comes with a voltage range from -10 V to 10 V. The output ports have a resolution of 16 bits that determine the minimum voltage step to $20\,\mathrm{V}/2^{16}$=305 µV, while the input ports have a resolution of 18 bits with a minimum voltage step of $20\,\mathrm{V}/2^{18}$=76 µV, respectively.

For in-situ CNT transport measurements, we typically use one output port and a resistor in series to protect the CNT and connect to a DC line that leads to a CNT junction. On the other side of the junction we connect a transimpedance amplifier[8]. The purpose of the transimpedance amplifier is to convert and amplify the current flowing through the junction into a voltage, which can then be measured at an input port of the ADwin. Eventually, another output port is used to control a gate electrode or a set of gate electrodes.

On the software side, the nanoqt framework is used. It was developed at the Néel Institute in Grenoble by Edgar Bonet, and designed for low-frequency real-time electronic transport measurements with the ADwin system. It is JavaScript-based and offers some built-in filtering options and a lock-in. The basic program used for CNT transfer and contact characterization measures the current as a function of time and consists of three different modules. (i) Monitoring: Measuring the current as a function of time at constant V_{sd} and V_{g}, (ii) ramping V_{sd}: Measuring the current as a function of time while ramping the

---

[8] Low Noise High Stability I to V Converter SP983c IF3602, Basel Precision Instruments GmbH, Mülhauserstrasse 113, 4056 Basel, Switzerland. Gain used: 10^5

bias voltage for a constant gate voltage and (iii) ramping V_g: Measuring the current as a function of time while ramping the gate voltage V_g for a constant bias voltage V_{sd}.

5.2.3. Transfer process workflow

In this section we will show how we transfer the CNTs and discuss the nanoassembly workflow. During the PhD project, several parts of the process have been modified and improved, which we will discuss in detail in the later sections. Here, we restrict ourselves to the final workflow, including the contact improvement techniques.

1. ***Preparation of cantilever chip:***
   a) Growth of CNTs on cantilever chips following section 3.1.2.
   b) Transfer of a cantilever chip into the SEM vacuum chamber with a vacuum transfer arm.
   c) Localization of CNTs: Cantilever imaging to check for single CNTs with low SEM contrast at the tip of the cantilevers. If there is no suitable CNT, another cantilever is loaded.
2. ***Preparation of the circuit chip:***
   a) An individual circuit chip is freshly cleaned up or taken from a storage vacuum flow box.
   b) The circuit chip is glued with PMMA to the PCB of the sample holder and microbonded.
   c) Argon milling is performed to remove oxygen-containing species and organic residues removing the top few nanometers of the electrode surface.
   d) The sample holder is mounted to the transfer arm, the transfer arm connected to the SEM, pumped, and the sample holder transferred to the SEM. Air exposure is restricted to a minimum, usually around one minute.
   e) The connectivity of the electrical lines is controlled by applying a bias voltage on each line and checking for a SEM contrast change.
3. ***CNT transfer:***
   a) Alignment of the cantilever pair with respect to the selected suspended CNT and the transfer position on the circuit chip. The cantilever chip is tilted by 25-35° to lower the cantilevers into the trench.
   b) A bias voltage of 4 V is applied at the two outermost electrodes and the current to the next inner electrodes is measured. This biasing scheme allows for contact detection regardless of which side the CNT touches first.

   c) Approaching the cantilever chip with the CNT to the circuit chip. The distance between the focal plane of the CNT and the focal plane of the substrate on the circuit chip can be tracked with the SEM on a section of the CNT that is far away from the final devices. The electrical contact between the CNT and the contacts manifests itself as an onset in current through the outermost CNT junctions.

   d) First contact improvement by current annealing: With a 1 MΩ resistor in series, the voltage is ramped to the maximum voltage of 10 V without cutting the CNT. The contact is checked and the current is ramped to ±10 V on each junction.

   e) Cutting the CNT on the outermost cutting sections: A high current is driven through the outermost cutting sections, which is sufficient to break the CNT by Joule heating. The cantilever chip is then retracted.

4. ***Contact characterization and current-induced annealing:***

   a) Isolating CNT junctions: The CNT still connects different junctions that need to be isolated. A high current is driven through the junctions, and the CNT metal contact is carefully improved (current-induced annealing) before cutting the respective CNT junctions.

   b) Careful current-induced annealing of the important junctions.

   c) Characterization of the room-temperature gate voltage dependence of the junctions.

5. ***Radiative-thermal annealing (RTA):***

   a) Further improvement of the contact resistance by heating the circuit chip globally with the halogen lamp at two different powers.

   b) Measurement of the resistance and gate voltage dependence between the heating steps.

   c) If the room-temperature resistance of a SQUID is less than 25 kΩ (single-junction resistance less than 50 kΩ) and the gate voltage dependence is consistent with a single CNT, the sample is worth being measured in the cryostat.

5.2.4. Current-voltage characteristics of suspended CNTs

The current-voltage characteristic is key to evaluate the CNT metal contact and to gain an understanding of the electronic transport through the CNT.

First contact

A typical current trace of the first contact is shown in figure 5.6a when we transfer a CNT and apply a bias voltage of 4 V. A mechanical contact results in a current step. The height of the current jump already gives some first indication on the quality of the contact. When the electrode is contaminated, the height of the jump is drastically reduced (cf. figure 5.6b). An increase in the voltage and a sweep to negative voltages give us information on the low bias voltage transport (cf. figure 5.6c). Ideally we would like to obtain perfect ohmic behavior (i.e. a linear I-V characteristic). However, depending on the contact barrier height, we observe either a small change in slope or a plateau with negligible current, which can extend up to a few volts. The origin of the contact barrier has been discussed in chapter 2.2.2 and is mainly determined by the Schottky barrier due to mismatch in work function, surface contamination serving as an insulating barrier, or insufficient metal wetting of the CNT. Differentiating between the individual contributions is rather difficult, and the objective was to reduce the contact barrier globally.

Cutting CNTs

When we increase the applied bias voltage and drive a higher current through a suspended CNT junction, at some point its maximum current is exceeded and the CNT breaks, manifesting itself as a current drop to zero. The CNT junctions are cut mainly in the center, which is the thermally most isolated part. This would point towards Joule heating as the dominant cutting mechanism. The number of distinct cuts gives information on the number of individual CNTs. If there is more than one cut, the CNT is likely to be a bundle or multi-walled (cf. figure 5.6e). However, the current measured during cutting depends on the ramping speed of the voltage. When ramping the voltage very slowly (rate of 0.1 V/10 s or slower) or waiting at the cutting voltage, the current usually does not decrease in a single step, but rather in a continuous evolution (cf. figure 5.6f), indicating that the CNT does not break abruptly. The microscopic origin is unclear, but it could be related to defects in the sp^2-lattice structure that affect the room-temperature electrical and mechanical properties.

A particular feature of the I-V characteristic is the current saturation and negative differential conductance shortly before the CNT breaks. The maximum current depends on the length of the CNT junction. The shorter the CNT, the better the central part is coupled to the contacts and the higher the maximum current it can sustain. For multiple junctions made of the same CNT with an identical suspension length, the maximum current is approximately the same.

The origin of the negative differential conductance has been attributed to the scattering with phonons [185, 186]. This was supported by experiments where suspended CNTs are exposed to gas atmosphere and heat can dissipate more easily, resulting in a higher saturation current with increasing gas pressure [187]. An even stronger dissipation can occur when the CNTs touch the substrate and in this case a negative differential conductance is not observed at all. The negative differential conductance has been modeled

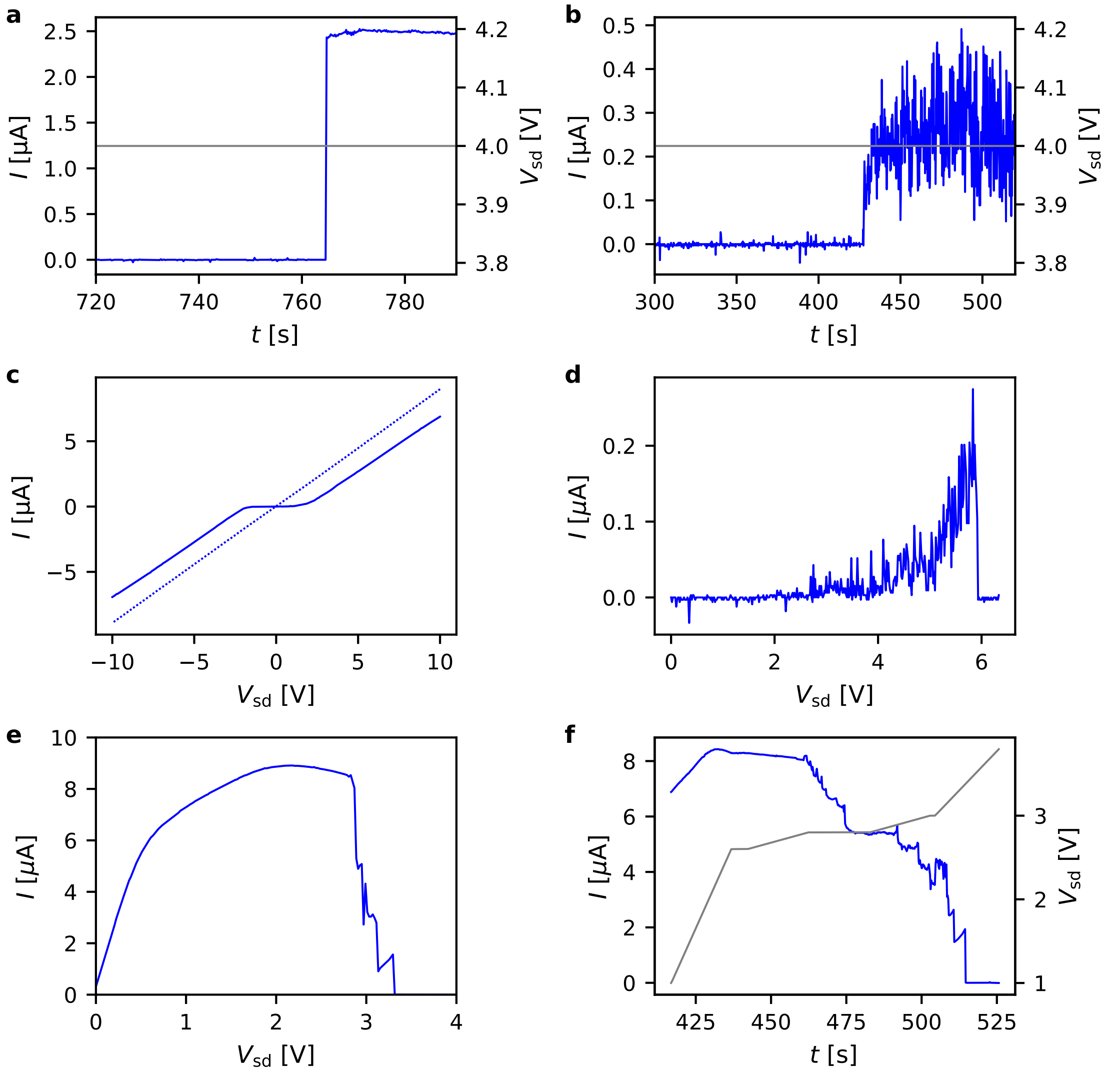

Figure 5.6.: Current-voltage characteristics of transferred CNTs (**a**-**d** with 1 MΩ resistor in series, **e**,**f** with 1 kΩ resistor in series). **a** Establishing the CNT metal contact. A constant voltage is applied (grey) and the contact is visible as a jump in current (blue). **b** Contact formation for a bad contact. The contact jump is lower and the current fluctuates. **c** *I*-*V* characteristic of an ohmic contact (dashed) and a high contact resistance around zero bias voltage, visible as a plateau of negligible current. **d** Contact formation with polluted circuit chip surface. The current fluctuates and the CNT cuts well below 1 µA. **e** Cutting a well-coupled CNT. The current first saturates and then develops a negative differential conductance before cutting in multiple steps. Note that the small offset at 0 V from the transimpedance amplifier has not been removed. **f** Time evolution of the CNT cutting. The cutting is performed more slowly than for **e** and the conductance degradation is more continuous.

in [188] where they assume a scattering with non-equilibrium, high-temperature optical phonons at high bias voltage. The optical branches involved in scattering with electrons possess a small DOS and their population can build up quickly if dissipation into other modes or the substrate is limited, as is the case for suspended CNTs.

However, the observation of negative differential conductance requires sufficiently well-connected CNTs. For a bad contact, when the contact resistance is high, the CNT breaks before reaching the negative differential conductance. A possible explanation could be that the large contact barrier for electrons also implies a very weak thermal coupling for phonons between the CNT and the contact electrodes. Because dissipation into the contacts is negligible, the phonon population builds up too quickly to be able to measure it before the CNT is cut.

In the case of very bad contacts, the CNT contact is very switchy, and the CNT cuts well before we can drive some high current through the CNT to improve the contact. For example, this occurred repeatedly when there was some organic contamination in our vacuum storage box (cf. figure 5.6d). We believe that in these cases the contact could improve suddenly, resulting in an abrupt increase in current through the CNT. This increase would lead to a strong non-equilibrium electron-phonon scattering cutting the CNT directly on a time scale that is not resolvable with our measurement setup (50 Hz acquisition rate).

5.3. Contact improvement techniques - Overview

A low CNT metal contact resistance is essential to enable electronic transport at low bias voltage, and thus a key requirement for proximity-induced supercurrent. The *I*-*V* curves of transferred CNTs commonly feature a plateau with negligible current and very high contact resistance beyond 1 MΩ around zero bias voltage, making any superconducting measurement impossible. Current-induced annealing can improve the contact. At a higher bias voltage of 1 V though, the resistance can already reach a good value between 150-250 kΩ. However, this is still far beyond the device resistance (contact and channel resistance) of $\sim$ 30-50 kΩ required for observing a supercurrent through CNTs. Therefore, one of the key challenges of this PhD project was the reduction of the contact resistance. Since it is not possible to isolate the contact resistance from the channel resistance in resistance measurements, we always compare the total device resistances. In this section, we first want to motivate all the different contact improvement strategies that have been tested in our subgroup, before discussing in detail the ones we continued to pursue.

Surface treatment

It is obvious that the surface should be as clean as possible, since any contamination would result in an additional tunnel barrier at the CNT metal contact. The contact material was mainly palladium. However, even for clean palladium surfaces, the adsorption of oxygen-containing species or oxidation can occur with the result of a modification of the work function and an increase in contact resistance. The interaction between a palladium surface and oxygen from air has been investigated in [61] by X-ray photoelectron spectroscopy combined with argon milling as surface preparation. Within a few seconds, carbon compounds adsorb on the palladium surface, while oxygen-containing species can be

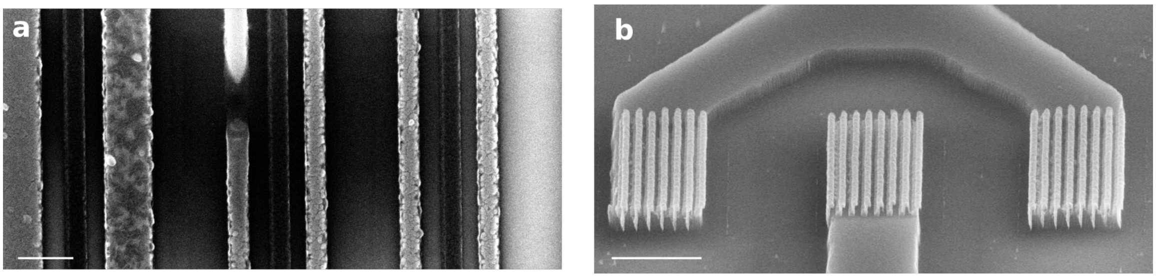

Figure 5.7.: Scanning electron micrograph of two contact improvement techniques. a Heating by current driving. The aluminum electrode could be cut with a molten range of 1 µm as becomes visible by the roughness change. However, there was no easy control of this range. Scale bar: 300 nm. **b** Engineered artificial fences fabricated by Tino Cubaynes, scale bar: 600 nm.

detected within minutes on the surface. The chemical oxidation processes occur on a longer time scale beyond one hour with the formation of C-O bonds and palladium oxidation. Moreover, the oxygen concentration was only detected within the top 3-4 nm which is ideal for removing the top layer by argon milling. The only drawback is the increase in surface roughness, which did not result in a worse contact resistance for us even for 8 nm etching. Therefore, we implemented the argon milling process successfully.

Circuit design

The design offers flexibility in electrode width and electrode shape which can be exploited to thermally decouple the transfer section more efficiently. This would potentially allow for higher temperatures when driving a high current through the CNT to anneal the contact. For this purpose, we tested electrodes of different widths ranging from 50 nm to 800 nm before introducing the argon milling step, but could not find clear evidence for contact improvement for smaller widths. A more innovative approach resulted in the fabrication of dedicated fences on top of the electrodes, but likewise we did not measure a significant reduction of the contact resistance for these chips compared to flat electrodes (cf. figure 5.7b). For the final contact improvement process on flat electrodes, a lower contact resistance was found for electrodes of a width of 800 nm than for 400 nm wide electrodes. Overall, we can conclude that there might be a small influence of the contact width on the contact resistance which can assist in reducing the contact resistance but the effect is too weak to reach a low contact resistance on its own.

Post-transfer heating

With the argon milling we could obtain a contact resistance of about 100-250 kΩ at a low voltage of 0.1 V, which is still too high and requires further improvement. Our main ideas were inspired by the post-fabrication top growth [31] and the post-growth fabricated samples [189, 32], where a high supercurrent could be achieved by establishing the CNT metal contact in a hot environment (evaporating hot metal on CNTs or growing CNTs on metal at CVD temperatures). In contrast to these methods, nanoassembly is performed at room temperature and the current on the order of µA that can be driven through a CNT lets us assume that the contact temperature is well below these temperatures. Therefore, a post-transfer heating was pursued. In combination with palladium as a top electrode material, the authors in [61, 172] could show that a mild heating at 220-250 °C already led to a significant contact improvement. Several techniques have been tried, which are listed below:

1. Heating by current driving: In principle, the contact electrodes could be heated by driving a high current (~ mA) through them, much higher than it would be possible through the CNT, and by designing a constriction close to the transfer position the contact area could be heated locally. As shown in figure 5.7a, electrodes could be cut, but the cutting and melting lack reproducibility and the technique was discarded.
2. Laser heating: Another approach was based on heating the circuit chip with a laser as tested in [190]. However, also this method was not easy to control and lacked reproducibility.
3. Radiative thermal annealing (RTA): We implemented a halogen lamp inside our SEM to heat the chip globally. This technique was controllable and successfully implemented.

Variation of the contact material

As discussed in section 2.2.2, it is essential that the work function of the metal is comparable to the work function of the CNT. We mainly used palladium, but we also tried gold and platinum as noble metals with high work function. Gold was only quickly tested at the beginning (before introducing the argon milling and radiative thermal annealing) and was found to give slightly worse contact resistance than palladium which could be due to inferior wetting, but it was not investigated in detail. Platinum was only tested at the end and gave contact resistances comparable to palladium (cf. section 5.4.5).

The direct use of a superconductor without an additional top contact material would increase the proximity-induced supercurrent, which motivated us to try molybdenum and molybdenum rhenium without an additional top layer. Molybdenum is known to form carbides with CNTs at elevated temperatures with low contact resistance [48]. The problem with molybdenum-based electrodes is the surface oxide that can lead to an additional insulating tunnel barrier or change the metal work function, which results in a large work function mismatch, both deteriorating the CNT metal contact with too high contact resistance at low bias voltage. We did not observe a substantial resistance decrease with our final annealing techniques. Argon milling could not improve the high initial contact resistance. Current annealing did not provide sufficiently high temperatures of $\sim$ 800 °C to induce carbide formation, also when globally heating the circuit chip with the halogen lamp in the SEM at moderate temperatures of $\lesssim$ 300 °C. Heating at $\sim$ 800 °C would not be compatible with our sample holder and would have required the sample to be removed, heated, and rebonded after heating, which would be too dangerous for the transferred CNT. Likewise, it would require air exposure and interrupt the full vacuum process.

Overall, our nanoassembly technique requires a top contact material with high work function, where palladium and later platinum worked best and were used as top contact materials in the devices measured in this thesis.

5.4. Final contact improvement process

Our final contact improvement strategy presented in [37] comprises surface pre-treatment with argon milling and a two-step annealing process in the SEM vacuum chamber at $\sim 10^{-6}$ mbar. The first step is current-induced annealing by driving a high current through the CNT, and the second step is radiative thermal annealing (RTA), where the circuit chip is globally heated with the thermal radiation of a halogen lamp.

5.4.1. Argon-milling surface pretreatment

After cleaning the circuit chip, we perform an argon milling using a Kaufman source[9] at a low beam voltage of 200 V to remove the top 5-8 nm of palladium or platinum. As shown in [61], 4 nm would have been sufficient to remove the oxygen-containing palladium top layer, but a higher etch depth did not result in worse contact resistance. A variation of the etch depth is even beneficial in tuning the final Pd/Pt thickness to potentially increase the superconducting proximity effect. The effect of argon milling on the contact resistance of palladium contacts at a bias voltage of 1 V is shown in figure 5.8. We can conclude that argon milling is a successful pretreatment to lower the contact resistance. The effect is even more drastic at a low bias voltage of 0.1 V where we could rarely measure a resistance below 1 MΩ without argon milling but around 200 kΩ with argon milling (resistance values after current annealing).

5.4.2. Current-induced annealing

The current annealing is shown in figure 5.9. When contacting a junction for the first time with a resistor of 1 MΩ in series and the CNT is not yet electrically connected, a certain bias voltage is required to measure a current. With an increasing bias voltage, the current can fluctuate, indicating a modification of the CNT metal interface which could be related to diffusion processes, local rearrangements of the atoms, or a change in CNT wetting. These processes are most likely thermally activated and usually occur at a higher bias voltage. Sometimes, a further modification is visible if we just wait at a high bias voltage, as shown in the inset. On the decreasing voltage ramp, the slope, in particular at low bias voltage, has improved, and the first current annealing has reduced the contact resistance.

---

[9] Kaufman KDC 40 Ion Source, Kaufman & Robinson Inc., 1330 Blue Spruce Dr, Fort Collins, CO 80524, USA

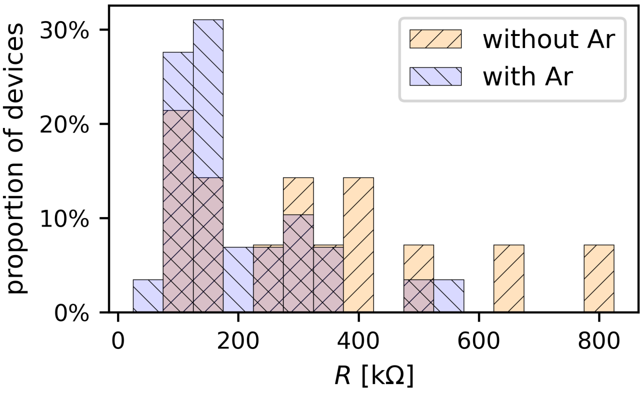

Figure 5.8.: Influence of argon-milling pre-treatment on palladium electrodes. Device resistance distribution of samples with and without argon milling (Device resistances averaged per sample, comprising only samples with device resistances of $R < 1\,\mathrm{M\Omega}$ measured at 1 V bias voltage, in total 14 samples without and 29 samples with argon milling). Figure from [37]).

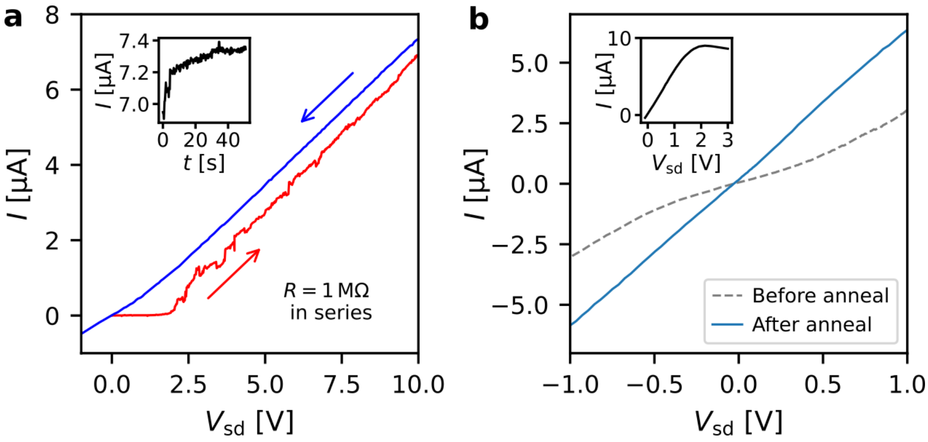

Figure 5.9.: Current-induced annealing. (replotted from [37]) **a** Trace-retrace cycle during the first current-induced annealing step with $1\,\mathrm{M\Omega}$ in series. The inset shows the time evolution of the current between the trace and the retrace. **b** I-V curves measured before and after the second current-induced annealing step. The current measured during this annealing step is shown in the inset.

For further improvement, the $1\,\mathrm{M\Omega}$ resistor is removed and the CNT is driven into the negative differential conductance. However, this is risky as the CNT might get cut, and therefore, we only go beyond the maximum current for cutting sections. We find that the contact resistance decreases most significantly after annealing in the negative differential conductance region (cf. figure 5.10). Following the argument with the phonon scattering, the CNT lattice should have the highest temperature in this regime, which would boost the local diffusion processes.

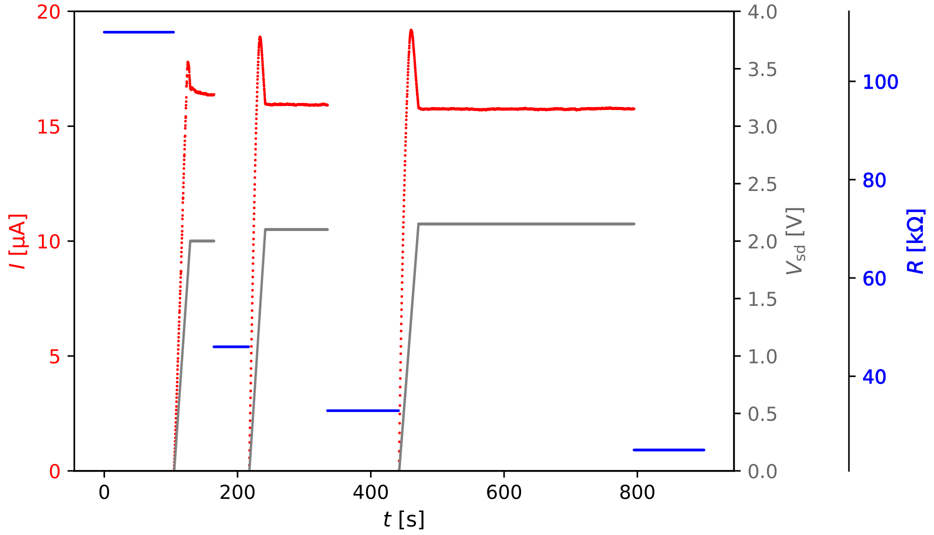

Figure 5.10.: Current-induced annealing of an ancillary junction with particular low device resistance. The annealing is performed by repeatedly driving strongly into the negative differential conductance and waiting for some time. For each iteration, the junction bias voltage is slightly increased and the CNT more strongly driven into negative differential conductance. Red color indicates the current measured, grey color the applied voltage and blue color the resistance measured between the annealing steps.

5.4.3. Radiative thermal annealing (RTA)

After the current-induced annealing of the individual junctions, we heat the circuit chip globally with the thermal radiation of a 70 W halogen lamp at a distance of 5 mm.

Heating procedure

The heating procedure has been calibrated by monitoring the current flow through an ancillary junction during the heating. This allowed for an in-situ measurement of the contact resistance. The final RTA process consists of two distinct heating steps at a lamp power of 5.6 W and 11 W. Heating beyond 11 W did not further improve the contact and a device exhibited increased disorder at low temperatures. Different heating durations between 5 min and 45 min have been tested. Usually, the pressure of the vacuum chamber starts to increase after $\sim$ 5 min and there is only small change in resistance below 5 min. This indicates that the circuit chip takes some time to heat up. The in-situ current measurement on ancillary junctions allows us to track the temperature change (cf. figure 5.11). In these measurements, we observe a current saturation for a heating time beyond 30 min, and therefore, we conclude that 30-45 min should be sufficient. The current change is a superposition of the contact improvement and a current that depends on temperature and diminuishes when the circuit chip cools down. We associate this current with some thermoelectric effect occurring at metal junctions in the circuit, which is supported by the fact that the sign and magnitude of the thermocurrent depend on the electrode materials of the circuit chip. In contrast to current-induced annealing, the contact improvement occurs

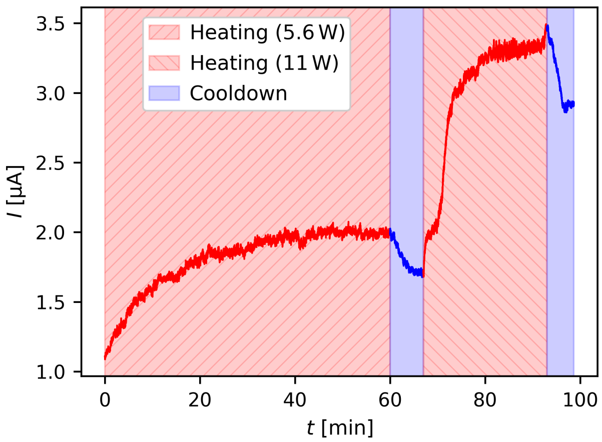

Figure 5.11.: Monitoring a junction during RTA. Current measured in an ancillary CNT junction during the two steps of RTA at a bias voltage of 0.1 V (replotted from [37]).

in a more continuous process, suggesting a slow modification of the contact interface. We measure the room-temperature resistance and gate voltage dependence before and after each heating step when the circuit chip has cooled again to evaluate the contact improvement.

Estimation of temperature

A temperature measurement at the circuit chip surface is not straightforward. One might think of using a thermocouple, but this simple measurement does not take into account the thermal dissipation through the substrate of the circuit chip and the sample holder. We therefore rely on the melting temperature of aluminum bond wires to get an upper bound for the substrate temperature. As illustrated in figure 5.12, heating tests have been performed on bond wires at a pressure in the low 10^{-5} mbar range for different lamp powers for 30 min each. RTA at 26.2 W leaves the wires almost unchanged and only the surface is partially molten, while RTA at 29.5 W is sufficient to completely melt the wires. These heating powers must be set in reference with the melting temperature of bulk aluminum of 660 °C. If we assumed a linear relationship between the heating power and the surface temperature of the circuit chip, a heating power of 11 W would correspond to 200-300 °C and 5.6 W to 100-150 °C. For CNTs transferred onto palladium and annealed in an oven with comparable temperature ranges, a significant contact improvement has been reported [61, 172]. However, it should be noted that our temperature ranges are rough estimates, and the exact surface temperature strongly depends on the metal and circuit design. Nonetheless, these temperatures are well below the temperatures involved in the CNT post-fabrication top growth technique of 800-900 °C [36] or the temperatures of 800 °C required to form CNT metal covalent bonds (MoC [48], or TiC formations [49, 50]). RTA does not impose high temperature resilience on superconducting circuit materials, making it a versatile technique compatible with quantum technologies. However, we found that

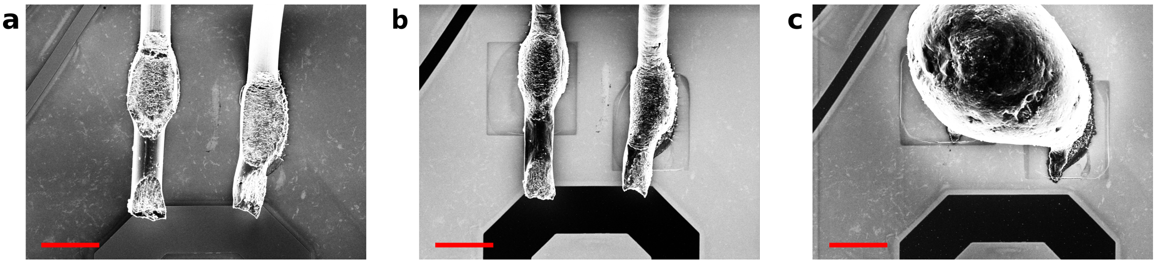

Figure 5.12.: RTA temperature calibration. SEM image of a circuit chip with aluminum bond wires. **a** Before RTA, **b** After RTA at 26.2 W, **c** After RTA at 29.5 W. Scale bar: 50 µm. From [191]

the standard two-step RTA process is not compatible with aluminum as a contact electrode material for CNT devices (cf. appendix A.2).

Resulting device resistances

A summary of the device resistances is shown in figure 5.13 for 27 samples before RTA and after RTA at 5.6 W and 11 W. The devices have been current annealed prior to heating. RTA reduces the device resistance substantially. The median resistance before RTA is 210 kΩ, after the first step it decreases to 92 kΩ, and reaches a value of 49 kΩ after the final heating step. There are even three samples with an average device resistance below 30 kΩ. We further find that RTA is more effective when the I-V characteristic exhibits ohmic behavior after current-induced annealing. If we observe a plateau of negligible current or a strong change in slope at low bias voltage and a resistance greater than 1 MΩ at 0.1 V, the effect of RTA is limited, and therefore, these samples were excluded from the data in figure 5.13.

Overall, this highlights that the combination of argon milling, current-induced annealing, and RTA is necessary to reach low resistance values. For devices with different electrode widths fabricated from the same CNT, we find that the effect of RTA is influenced by the electrode width. As expected for 800 nm electrode width, we observed slightly lower device resistance (about 25 %) than for 400 nm wide electrodes in the two samples where the electrode width was varied.

5.4.4. Gate voltage dependence

The transport properties of the CNT devices can be further investigated at room temperature by tuning the gate voltage, which affects the chemical potential in the CNT. At room temperature, the thermal energy can be large enough to overcome the charging energy and the quantum level spacing, and sharp current features are smeared out. Nonetheless, the band gap of CNTs can be probed and we can differentiate between quasi-metallic CNTs with no dip in conductance, narrow gap CNTs with a dip, and true semiconducting CNTs where the conduction is true zero in the band gap, as shown in figure 5.14. If the gate voltage dependence shows additional dips or several kinks, the gate voltage dependence

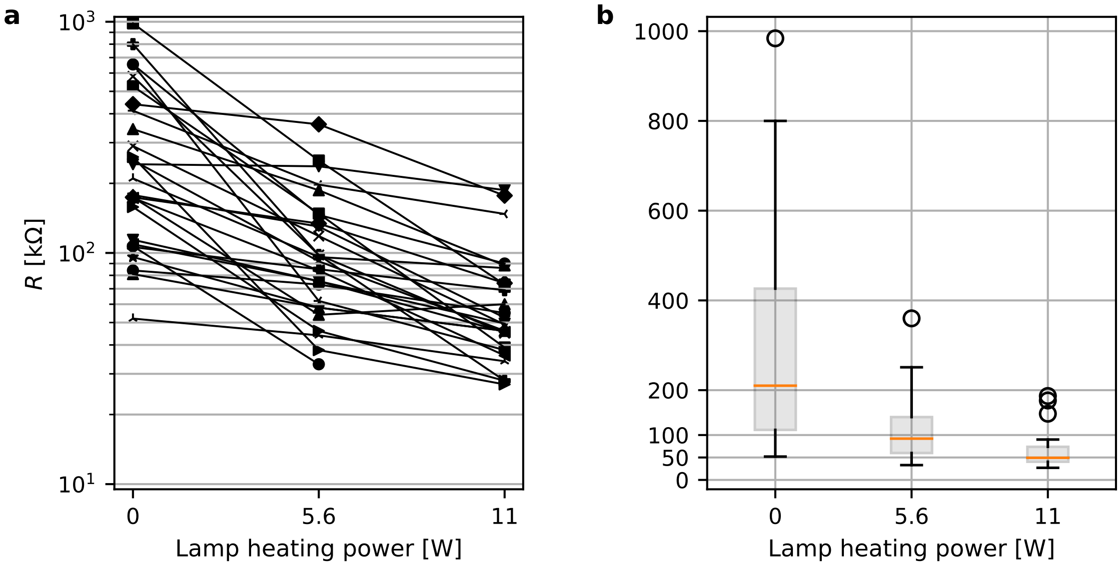

Figure 5.13.: Evolution of the device resistance during the RTA process. 27 samples with palladium top layer are characterized at a bias voltage of 0.1 V (only for samples with initial device resistance less than 1 MΩ, device resistance averaged per sample, including contact and CNT conductance channel resistance). **a** Traces for individual devices. Note, that some devices have only been heated at low power. **b** Boxplot of the device resistance. The box shows the interquartile range, the line the median, the whiskers 1.5 times the interquartile range and circles outliers.

cannot be explained by a single CNT and it is likely that there are multiple CNTs suspended over a junction [30]. These can be bundles or multi-walled CNTs and the total current can be approximated by the sum of the individual CNTs. For obvious big bundles, we often observe a flat gate voltage dependence, ressembling that of single metallic CNTs. We find the lowest contact resistance and cleanest low-temperature transport spectra in CNTs with narrow-gap gate voltage dependence and target those for the superconducting devices.

Another parameter that can be inferred from the gate voltage dependence is potential contamination. For this purpose, we sweep up and down the gate voltage and look for hysteresis that can be induced by potential contamination, such as adsorption of gaseous species [30]. With our nanoassembly technique, strong hysteresis has never been observed, which is another indicator of the cleanliness of our devices.

Most of our nanoassembled CNT devices show ambipolar or weak *p*-type transport behavior after current-induced annealing, characterized by a minimum around zero gate voltage and comparable electron (*n*-type) and hole (*p*-type) transport. This is in contrast to the other non-vacuum fabrication techniques [31], where *p*-type transport behavior is much stronger. Thermal annealing is found to modify the gate voltage dependence. For all palladium devices, we observe a transition of the CNT transport behavior from ambipolar to unipolar *n*-type. In addition, the center of the semiconducting gap shifts towards negative gate voltages for some devices.

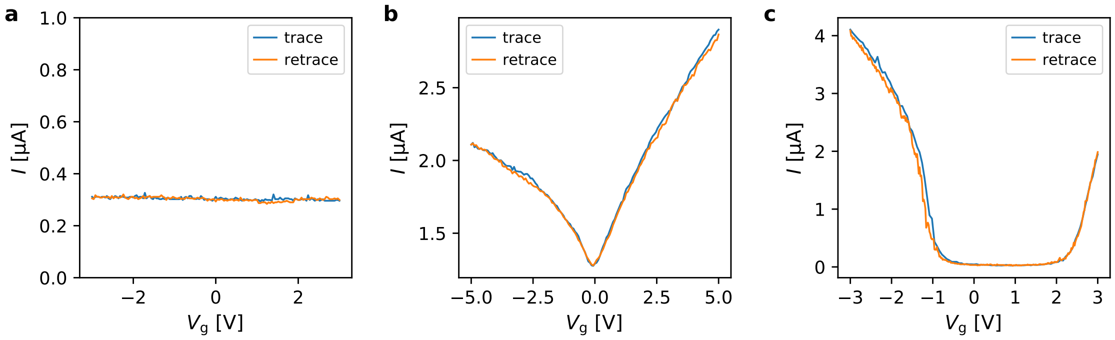

Figure 5.14.: Different examples of the room-temperature gate voltage dependence. In all examples, the trace (upward sweep of V_g) and retrace (downward sweep of V_g) overlap, no hysteresis can be measured as typical for our nanoassembled CNT devices. **a** Flat gate voltage dependence as typical for metallic CNTs or a superposition of many CNT channels ($V_{sd} = 0.1\,\text{V}$). **b** Narrow gap gate voltage dependence with a pronounced dip ($V_{sd} = 0.1\,\text{V}$). **c** Gate voltage dependence of a semiconducting tube ($V_{sd} = 2\,\text{V}$)

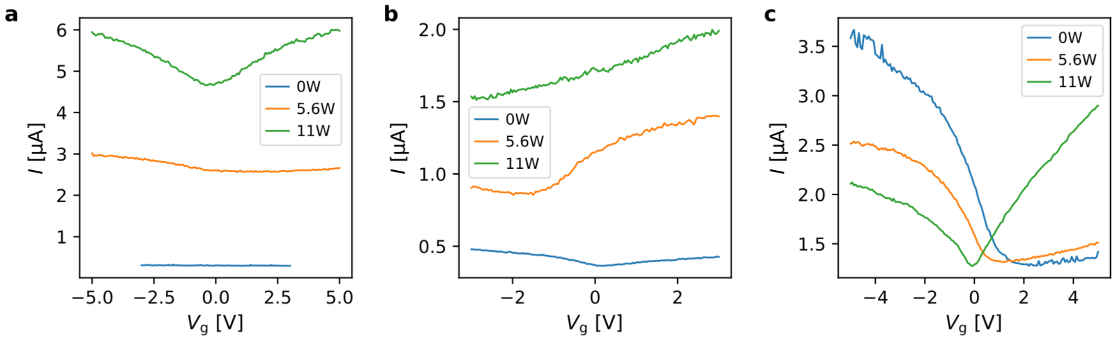

Figure 5.15.: Gate voltage dependence evolution at the different radiative thermal annealing steps. The devices were measured at 0.1 V with 3 kΩ in series. **a** Device from sample SC3, **b** Device from sample DQD-EA1 replotted from [37], **c** Device from sample MoRePd9B2 with particular high *p*-type transport before RTA.

The change in gate voltage dependence during RTA can be due to doping [192, 193] or a modification of the work function mismatch between the top electrode material (palladium or platinum) and the CNT during the heating process. The situation in both cases is represented in figure 5.16. We start with the situation 5.16a and assume the metal work function to be slightly higher than the work function in the semiconducting CNT.

When the contact between the CNT and the metal is made, there will be an additional barrier for electrons at the contact interface, while the barrier for holes is reduced. This manifests itself as a higher current on the hole side and a lower current on the electron side. Assuming that the metal work function is reduced during RTA (or the work function in the CNT increased), as shown in 5.16b, electron transport can be favored with respect to hole transport at the interface with the result of a higher electron current compared to hole current. Since the situation in the center is drawn at zero gate voltage, the energy levels of the quantum dot above the conduction band and below the valence band are

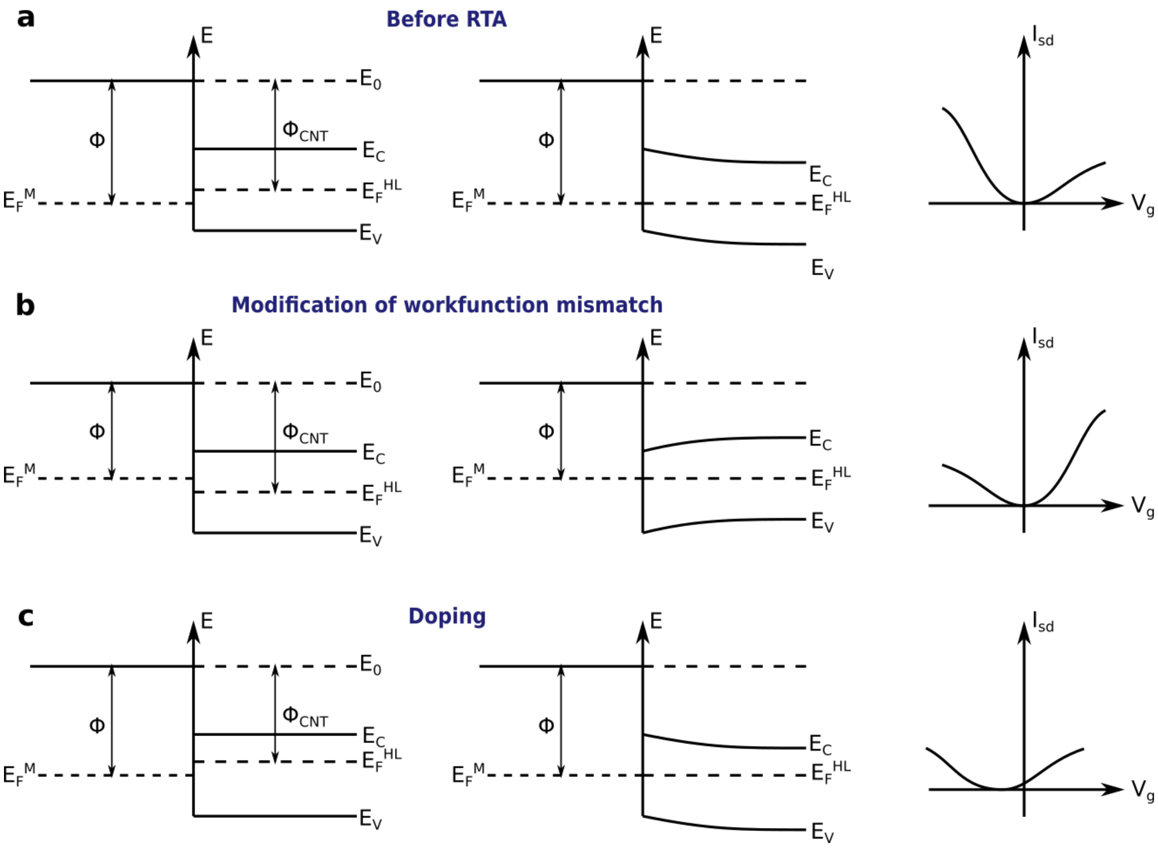

Figure 5.16.: Schematics to explain the change of the gate voltage dependence during RTA. Left: before contact, center: contact, right: I_{sd}-V_g characteristic at constant V_{sd}. **a** Initial situation with the metal work function larger than the work function of the CNT ($\Phi > \Phi_{CNT}$). **b** Situation when the RTA decreases the metal work function. **c** Situation when pure doping (no work function mismatch without doping) is involved. Shown only for *n*-doping, *p*-doping would lead to a minimum shift in the other direction.

symmetric around zero gate voltage and the current minimum is around zero gate voltage. The situation is fundamentally different for pure doping of the CNT. In case of *n*-doping (cf. figure 5.16c), the electrons and holes face the same contact barrier and the current increase is symmetric around the minimum. However, this minimum is shifted towards positive gate voltage since the Fermi level needs to be pulled down to be centered between the valence and conduction bands.

Nonetheless, a distinction between the two mechanisms doping and modification of the work function mismatch is not always straightforward. In particular, for narrow-gap CNTs at room temperature, electron and hole conduction cannot be completely separated, and the minimum can also be shifted when work function modification is involved. It is also possible that the two processes are involved at the same time.

The change in the work function mismatch could be related to adsorption or desorption of gaseous species on the contact material (palladium, platinum) or the CNT itself. In fact, the transition from *p*- to *n*-conduction is consistent with a decrease in the metal work function during thermal annealing. Common gaseous species could be oxygen that is removed during argon milling but can re-adsorb during the transfer of the circuit chip to the SEM vacuum chamber (minimum time $t \gtrsim 1\,\mathrm{min}$) and desorb during RTA, or hydrogen that could cover the CNT after the growth. Both oxygen and hydrogen are known to modify the work functions of palladium and platinum. Oxygen adsorption increases the work function of both platinum and palladium [194, 195]. For palladium, an increase in the work function of 0.18 eV is reported for hydrogen exposure, while the increase in work function for oxygen is estimated to be at least 3 times higher [196]. The situation for hydrogen in platinum is less clear, as at room temperature most of the adsorbed hydrogen already desorbs and the work function does not show any change beyond 320 K [197, 198]. As both oxygen and hydrogen can modify the work function in the same direction, it is hard to distinguish between the two, and a detailed study would require a full vacuum transfer of the circuit chip after argon milling.

Particular insight in the modification of the gate voltage dependence could be gained from the last sample measured in this thesis with a platinum top layer. The platinum sample was characterized before the transfer to the cryostat (cf. figure 5.17a,c) and had to be warmed up due to technical issues with the cryostat. It was remeasured in the SEM setup after air exposure and another set of annealing was performed (cf. figure 5.17b). The air exposure shifted the minimum of the gate voltage dependence and the device is slightly p-type transport dominated after air exposure (cf. figure 5.17b,d).

It is very interesting that the gate voltage dependence of the two SQUIDs with SQUID800 (800 nm electrode width, 500 nm CNT suspension length, figure 5.17b) and SQUID400 (400 nm electrode width, 350 nm CNT suspension length, figure 5.17d) was affected differently after air exposure. The two SQUIDs have only slightly different CNT suspension lengths but differ by a factor of two in electrode width, which makes it likely that the different behavior after air exposure has its origin in the contact and not the CNT. Independent of the initial gate voltage dependence, heating shifts the minimum to negative gate voltages and enhances n-type transport. At the end of the RTA process, we could even recover the initial minimum position before air exposure. During exposure to air, oxygen could adsorb on the CNT or the contacts and the change in gate voltage dependence during RTA could be explained by oxygen desorption from the CNT itself, changing the doping or its work function [199] or the contacts, modifying the metal work function. Again, on the basis of the data, it is hard to conclude which of the processes dominates.

At the end of the second annealing process, we could not only restore the minimum of the gate voltage dependence, but we could even achieve a device resistance slightly lower than that obtained after the first annealing process. This could be partially due to the longer heating time at 11 W. Nevertheless, it shows that RTA can potentially help reset CNTs and to degaz adsorbates, which is very interesting in the future when we plan to put single-molecule magnets on CNT-SQUIDs because it allows us to potentially recycle CNT-SQUIDs. In particular, with the non-deterministic evaporation of molecules on CNTs, this could become a very powerful tool.

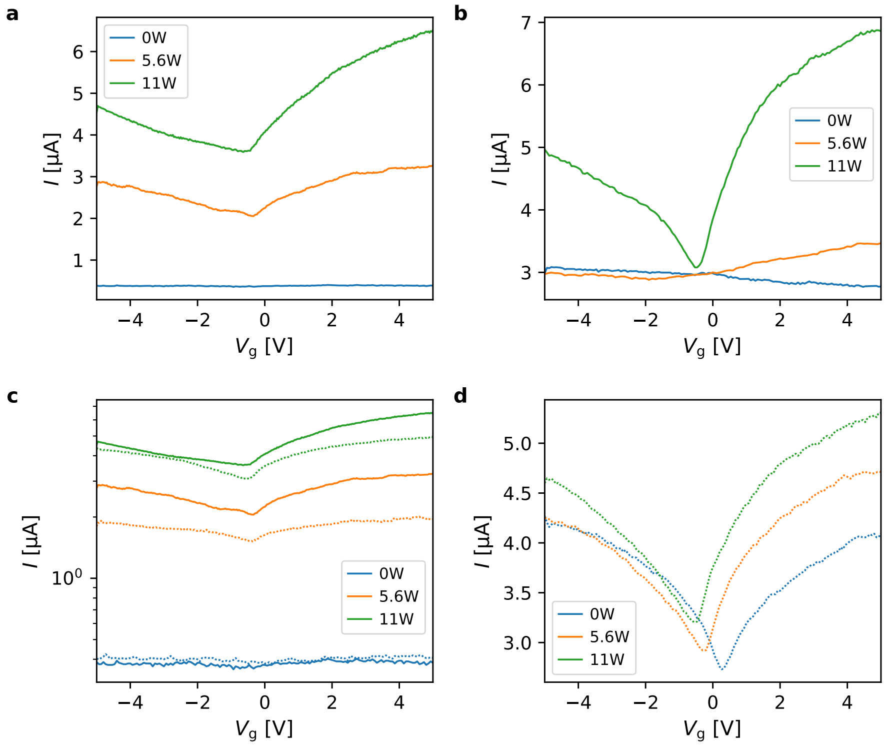

Figure 5.17.: Gate voltage dependence evolution during RTA of devices with platinum top layer (sample SC5). **a** First RTA cycle before cooldown (45 min at 5.6 W and 45 min at 11 W, SQUID800). **b** Second RTA cycle (40 min at 5.6 W and 60 min at 11 W, SQUID800) after the warmup of the sample before re-cooldown. **c** Comparison between the two SQUIDs before cooldown (800 nm wide electrodes, solid line and 400 nm wide electrodes, dashed line). **d** Second RTA cycle (40 min at 5.6 W and 60 min at 11 W, SQUID400) after the warmup of the sample before re-cooldown.

5.4.5. Comparison of platinum and palladium as contact material

So far we have only discussed the statistics of devices with palladium top material (unless indicated otherwise). The last sample measured during this thesis was fabricated with platinum as a top layer and included the device with the highest supercurrent measured (of 3-4 nA). The RTA statistics of this sample are compared with palladium in table 5.1 and plotted in figure 5.17c. Current annealing was slightly more effective for the device SQUID400 (400 nm electrode width, 350 nm CNT suspension length) than for the device SQUID800 (800 nm electrode width, 500 nm CNT suspension length). However, RTA is significantly more effective for the device SQUID800 with wider contact electrodes.

The *I*-*V* characteristic exhibits almost perfect ohmic behavior as rarely observed for palladium, but the resistance at 0.1 V after current annealing was still relatively high with an average value of 356 kΩ for the two measured junctions. The final room temperature resistance after RTA of a single junction was 32 kΩ and 42 kΩ for 800 nm wide electrodes and 400 nm wide electrodes, respectively. This shows that RTA (in particular at 11 W) is also very efficient for platinum, while current annealing might be less effective for platinum.

Table 5.1.: Comparison of the median device resistance. Measured before (0 W) and after the RTA steps at 5.6 W and 11 W at a bias voltage of 0.1 V for palladium contact top material (27 samples) and platinum contact top material (1 sample)

	0 W	5.6 W	11 W
Pd (27 samples)	210 kΩ	92 kΩ	49 kΩ
Pt (1 sample)	356 kΩ	97 kΩ	37 kΩ

To better understand the modification of the gate voltage dependence in platinum, we also measured the evolution of the gate voltage dependence with RTA. As shown in figure 5.17, the minimum of the gate voltage dependence is at constant gate voltage, and the device transitions from ambipolar to *n*-type transport, as well, which is consistent with the explanations above. In chapter 2.2.2, we have discussed the different wetting properties of platinum and palladium. With the samples fabricated so far, both materials seem to be equally well suited for achieving low contact resistance. However, with respect to proximity-induced superconductivity, it might be favorable to choose platinum over palladium due to its lower magnetic susceptibility [200].

6. Cryogenic measurements

For the observation of low-energy physics phenomena, it is essential that the energy scale governing the underlying physics dominates the thermal energy, which requires cooling down the sample to mK-temperatures using a dilution cryostat. Otherwise, thermal excitations would mask the effects we are interested in, which in this work are charge quantization, determined by the charging energy $E_C \sim$ meV, the quantization of wave functions determined by the quantum level spacing $\Delta E \sim$ meV and superconductivity determined by the superconducting gap $\Delta \sim 0.1$meV and eventually the thermal occupation of mechanical modes in the CNT determined by its resonance frequency $\hbar\omega \sim$ μeV. In this chapter, we will first give an introduction to the cryogenic measurement setup before discussing low-temperature CNT electronic transport measurements with normal conducting and superconducting electrodes.

6.1. Cryogenic measurement setup

In this section, we explain the basic working principle of a dilution cryostat and focus on the custom components and special features of our cryostat, including the DC and RF measurement setup and the software used for cryogenic measurements.

6.1.1. Dilution cryostat

We use a homemade dilution cryostat of "Sionludi"-type with a base temperature of 40 mK (newer versions of comparable build-type are available at Qinu[1]). In contrast to the majority of cryostats, the order of the different cooling stages is inverted with respect to the temperatures, with the coldest stage at the top where the sample is connected to. It comes in a convenient table-top implementation and can reach fast cooling times below 100 mK of about three to four hours with the current installations inside.

The general cooling mechanism of a dilution cryostat makes use of two circuits, a liquid ^{4}He circuit to cool down to 4.2 K (evaporation temperature of liquid ^{4}He) and a closed cooling cycle with a mixture of ^{4}He and ^{3}He. While pumping on ^{4}He can decrease the temperature to around 1.5 K, the lower temperatures are reached with a mixture of ^{3}He/^{4}He.

---

[1] Qinu GmbH, Windeckstrasse 8, 76135 Karlsruhe, Germany

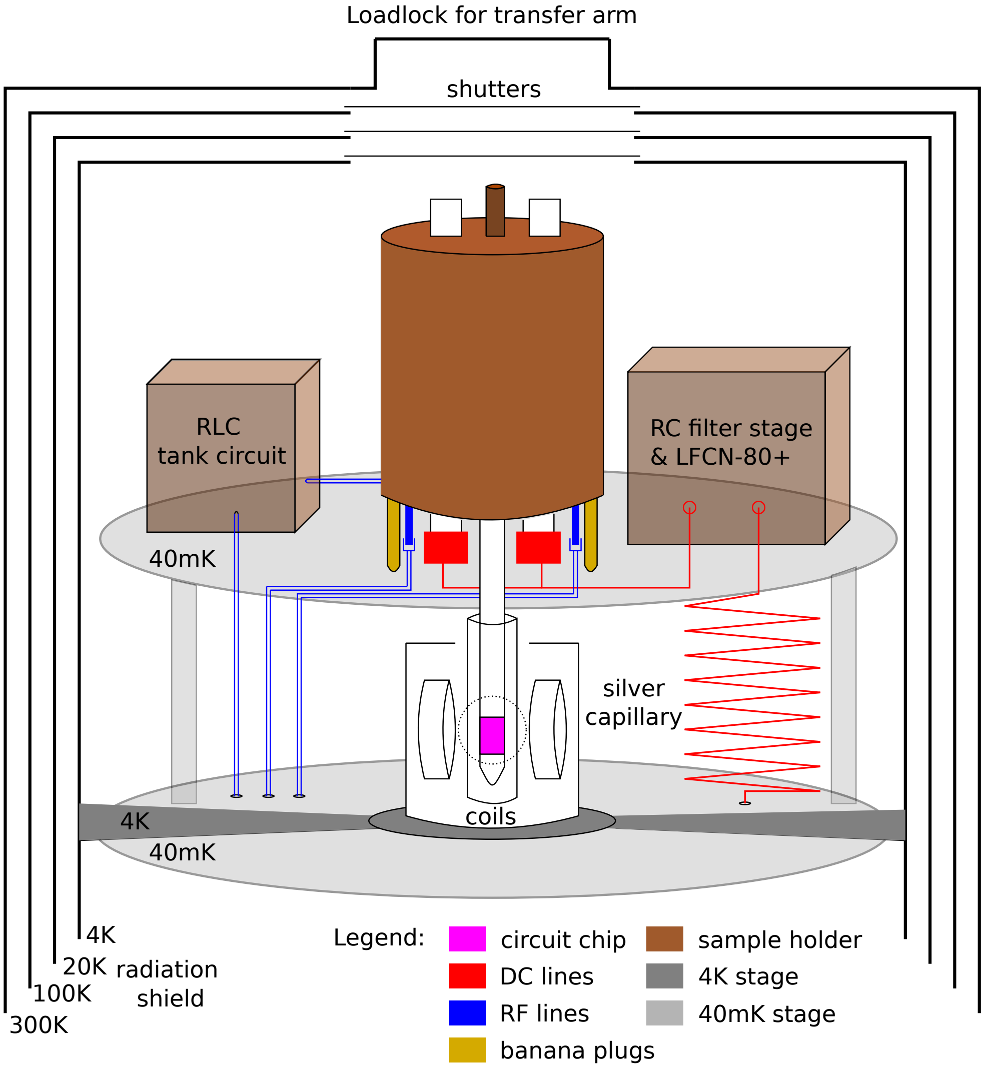

Figure 6.1.: Sketch of the mK stage of the cryostat with all added components. The mK stage consists of two plates leaving room for the coils thermalized at 4 K. Only part of the 4 K-stage is drawn, the rest and the other stages would follow below the sketch. The DC lines are split in two blocks each containing 12 DC lines. Here only one block is shown for simplicity.

Below 850 mK and for a ^{3}He concentration above 6.5% the mixture is separated into two phases, an almost pure phase of ^{3}He and a phase of ^{4}He with a temperature dependent percentage of ^{3}He. The pure phase has a lower entropy, and the mixed phase has a higher entropy. By continuously removing ^{3}He from the mixed phase, e.g. by pumping, ^{3}He from the pure phase is diluted in the mixed phase, thereby locally decreasing the entropy in the mixing chamber where the dilution takes place and generating a cooling power $\Delta Q = T\Delta S$. For a detailed description of the working principle of the Sionludi cryostat see e.g. [201]. We will now focus on the custom setup shown in figure 6.1.

The cryostat is equipped with a "quickswap" system, allowing for a simple sample exchange, maintaining the CNT device under vacuum throughout the transfer into the already cold cryostat. For this purpose, each thermal radiation shield is equipped with a shutter with magnet that can be conveniently opened and closed by applying a strong magnetic field with another magnet from outside the cryostat. The vacuum transfer arm with the sample holder can be plugged to the loadlock on the top of the cryostat and connected to the vacuum of the cryostat and the sample holder inserted. The ^{3}He/^{4}He mixture circulation is interrupted since temperatures of up to 50-60 K can be reached at the mK stage when the sample holder is connected, which is still at room temperature. After restarting the cooldown, the mK-stage reaches its base temperature in about one hour. This saves a significant amount of time that would be required to completely warmup to room temperature and recooldown.

For the application of magnetic fields, the cryostat is equipped with a 3D vector magnet consisting of three sets of superconducting coils made out of Nb-Ti wire, a cylindrical coil in z-direction ($B_z^{\max} = 1.6\,\mathrm{T}$) that fits around the PCB tip of the sample holder (cf. chapter 5.2.1) and two pairs of Helmholtz coils surrounding the z-coil for magnetic field application in x-direction ($B_x^{\max} = 0.395\,\mathrm{T}$) and y-direction ($B_y^{\max} = 0.24\,\mathrm{T}$)[2]. The coils are thermalized at the 4 K stage due to the higher cooling power at 4 K and to avoid excessive heating of the sample in case of quenching or fast magnetic field ramps.

6.1.2. DC measurement setup

The wiring of the DC setup is shown in figure 6.2. A switch box mounted outside the cryostat allows us to individually address each of the 24 DC lines and to connect BNC cables to their corresponding port. Similarly to the SEM setup, there are 3 different terminations for each port: Ground, ground via a resistor of 470 kΩ or floating to apply a current or voltage.

Filtering of the DC lines

To reduce high-frequency noise over a wide range from tens of kHz to GHz, several filter stages are implemented at the mK stage. For filtering noise starting from the kHz range, two RC low-pass filter stages are used, one mounted inside the cryostat ($R = 1\,\mathrm{k\Omega}$ and $C = 25\,\mathrm{nF}$) and another one at the PCB ($R = 1\,\mathrm{k\Omega}$ for contacts and $R = 100\,\mathrm{k\Omega}$ for the gates, $C = 1\,\mathrm{nF}$), as mentioned in chapter 5.2.1. Noise from $\sim 100\,\mathrm{MHz}$ to $\sim 5\,\mathrm{GHz}$ is efficiently filtered with commercial LFCN-80+ filters[3]. For filtering higher GHz noise, Eccosorb[4] filters are used, consisting of two one meter long silver capillaries filled with Eccosorb which contain 12 DC lines each. This filter has been added to the setup at a later stage and was used to measure the samples SC2-SC5 which will be discussed in section 6.3.

---

[2] The maximum B-field is determined by the current that can be sent through the wire before quenching and the current-to-field ratio from simulations, cf. [64]

[3] LTCC Low Pass Filter, DC, 80 MHz, 50Ω, Mini-Circuits, 13 Neptune Ave, Brooklyn, NY 11235

[4] Eccosorb CRS 117 PTA-Absorber, Laird Performance Materials, 8 Pengfeng Rd, Songjiang Qu, Shanghai Shi, China

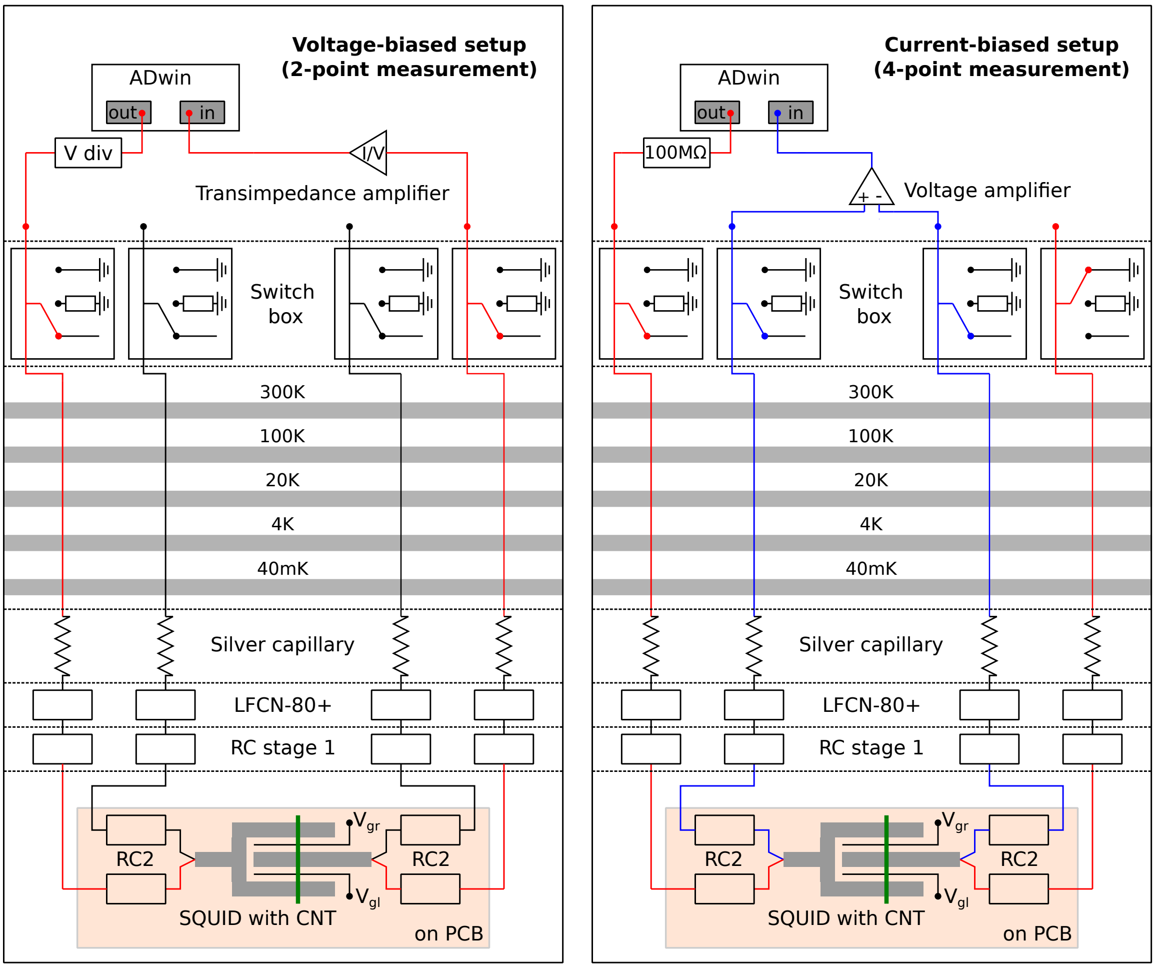

Figure 6.2.: DC measurement setup. Schematically shown for a SQUID but the filtering in the cryostat is the same for all 24 DC lines. Temperatures indicate the thermalization stages in the cryostat. Filtering via a silver capillary filled with Eccosorb (for GHz filtering), a commercial LFCN-80+ low pass filter (cutoff 145 MHz), and RC filter stage 1 ($R = 1\,\text{k}\Omega$, $C = 25\,\text{nF}$). The second RC filter stage is implemented on the PCB in light orange ($R = 1\,\text{k}\Omega$ for source and drain and $100\,\text{k}\Omega$ for gates, $C = 1\,\text{nF}$). **Left:** Voltage-biased setup with current flowing through the red line and converted into a voltage in a transimpedance amplifier. **Right:** Current-biased setup with current flowing through the red line and voltage drop measured via the blue lines with a differential voltage amplifier. Inspired by [64].

Voltage-biased setup

For superconducting samples including SQUIDs, two different measurement setups are used in this thesis, as shown in figure 6.2. In both cases, an ADwin Gold II is used, which is a computer-controlled real-time data acquisition system, and has been already introduced for the SEM setup in chapter 5.2.2.

A voltage-biased setup (2-point measurement, cf. figure 6.2 left) is used to measure the current or differential conductance through a SQUID device. The output voltage of the ADwin is applied directly to the sample. A voltage divider might be inserted between the ADwin and the switch box to decrease the voltage resolution below the minimum step size of the ADwin. Only two of the four SQUID ports are used, one at the source and one at the drain, and the other ports are floating and disconnected. The electrostatic potential in the CNT can be adjusted by two gate electrodes, denoted as the left and right gate electrode with applied gate voltage V_{gl} or V_{gr}, respectively. The signal passes through the device and after exiting the switch box, the current is converted to a voltage and amplified with a transimpedance amplifier[5], whose output is connected to the ADwin input port.

Current-biased setup

A current-biased setup (4-point measurement, cf. figure 6.2 right) is used to extract the supercurrent. A bias current is sent between two ports of the SQUID, and the voltage drop across the SQUID is measured via the other two ports. For current biasing, a resistor of 100 MΩ is placed between the ADwin and the switch box. The resistance value must be a few orders of magnitude larger than the internal device resistance to reach the largest voltage drop at the resistor and to set the current through the device. The voltage drop across the SQUID is amplified with a differential voltage amplifier[6] whose output is connected to the ADwin where the voltage drop is measured. The voltage can be numerically differentiated to obtain the differential resistance.

6.1.3. RF measurement setup

The full RF wiring of the cryostat is shown in figure 6.3 and allows in principle to perform experiments where the CNT is employed as a frequency mixer. For these experiments, an RF signal can be applied at the source and at the gate simultaneously, and the mixed signal is detected via an output RF line. For more details on this setup, see [64]. In this thesis, RF was only applied locally at a gate electrode or via a microbonded RF antenna using port 6 in the schematics in figure 6.3. Note that the attenuation of -60 dB has been modified for some measurements. For the application of RF, two different sources have been used. An SMA100A from Rohde&Schwarz[7] and an APULN20 from Anapico[8]

6.1.4. Measurement software

Two measurement softwares are used, the first one, NanoQt, has already been introduced in chapter 5.2.2 in the frame of the SEM setup. It is written to integrate perfectly with the

---

[5] Low Noise High Stability I to V Converter SP983c LSK389A, Basel Precision Instruments GmbH, Mülhauserstrasse 113, 4056 Basel, Switzerland. Gain used: 10^6 to 10^8

[6] ANS EPC1-D, ANS instruments Celians, SPHEREL Systèmes, 10 bis route d'Ax, 31120 Portet sur Garonne, France

[7] Rohde & Schwarz GmbH & Co. KG, Mühldorfstraße 15, 81671 München

[8] AnaPico AG, Feldeggstrasse 5, 8152 Opfikon, Switzerland

[9] Cryo Amp A5-1 by CRYOHEMT, 6 Boulevard Dubreuil, 91400 Orsay, France. Range: 1-7 MHz, gain: 13 dB

[10] LNF-LNC0.3-14A by Low Noise Factory, Nellickevägen 24, 412 63 Göteborg, Sweden. Range: 0.3-14 GHz

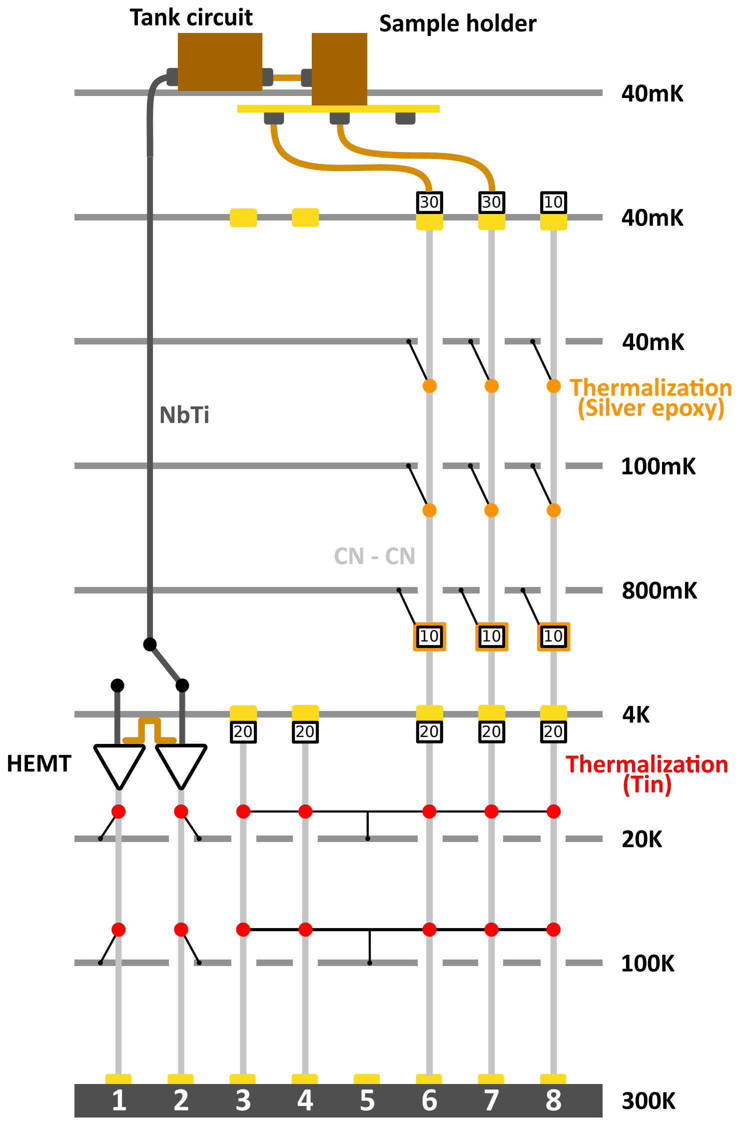

Figure 6.3.: Full RF wiring of the cryostat. Boxes: Numbers indicate attenuation in dB, Red/orange circles: Thermalization made from tin or silver epoxy, yellow: Feedthrough connectors with additional thermalization, CN: Cupronickel. In this thesis only line 6 was used to excite RF at a local gate or via an antenna. RF line 7 is used for the mixing setup to apply RF at the source. The RF readout line is connected via the RLC tank circuit and two HEMT amplifiers[9][10]to the output 1 or 2. Figure adapted from [64].

ADwin setup and acquire data at the maximum sampling rate of the ADwin, but lacks the flexibility to easily integrate new instruments such as RF sources. Due to its higher speed, it is commonly used for quick overview characterizations of the quantum dots.

For all other measurements, we use the python package qkit[11] that has been developed at KIT in the group of Hannes Rotzinger. The documentation of the specific measurement modules can be found in [202]. It is designed to integrate easily with other devices, but it is currently not optimized for the ADwin.

---

[11] https://github.com/qkitgroup/qkit

For voltage-biased measurements, lock-in techniques are used, which have been implemented in both softwares directly on the ADwin. The lock-in operates at a low frequency of $\sim$ 91 Hz with a lock-in amplitude down to 5 µV.

6.2. Electronic transport measurements with normal conducting electrodes

In the last chapter, we discussed the CNT transfer and contact improvement technique to reach a low device resistance. However, in order to fully evaluate the capabilities of the nanoassembly technique, low-temperature electronic transport measurements are crucial. Before measuring CNTs transferred on superconducting contacts, first CNT transport measurements were performed on normal conducting electrodes. The contact electrode core material of the devices presented in the following consists of niobium or molybdenum, which, fabricated with a lift-off process, was not superconducting (cf. chapter 4.4). The top electrode material is palladium or platinum with a final thickness greater than 4 nm. We will present measurements ranging from the weak coupling regime to the intermediate coupling regime and open-quantum dot regime.

6.2.1. Transport without applying contact improvement techniques

Before introducing the contact improvement technique, four samples have been measured in the cryostat (neither treated with argon milling nor RTA) that had a room-temperature device resistance of about 250 kΩ at a bias of $V_{\mathrm{sd}} = 1\,\mathrm{V}$ (the resistance at $V_{\mathrm{sd}} = 0.1\,\mathrm{V}$ was not measured, but it is expected to be higher than at $V_{\mathrm{sd}} = 1\,\mathrm{V}$). The charge stability diagram of one of the best early devices is shown in figure 6.4. It consists of two 500 nm wide electrodes and a CNT suspended over a single gate electrode to form a simple quantum dot. In the center of the diagram in figure 6.4a the semiconducting gap of the CNT on the order of 200 meV can be recognized, followed by a decreasing envelope on the electron side due to the soft confinement (cf. figure 2.7) and a region where the constant-interaction model is a good approximation.

A zoom in this region is represented in figure 6.4b, where it is difficult to identify individual Coulomb diamonds, pointing to large disorder (cf. figure 2.6). Electronic transport is strongly suppressed for $|V_{\mathrm{sd}}| < 15\,\mathrm{mV}$ and a closing of the Coulomb diamonds at $V_{\mathrm{sd}} = 0\,\mathrm{V}$ is not visible. Overall, the differential conductance is well below $4e^2/h$ which indicates very weak coupling, consistent with the high room-temperature resistance. Such a reduction in transport could be explained by surface contamination. A weak oxygen plasma was performed on this circuit chip to remove organic solvents which resulted in lower room-temperature resistance, but this might have come at the cost of an insulating oxide layer inhibiting low bias transport.

On the basis of these first measurements, it becomes immediately clear that contact improvement is a key requirement for any superconducting experiment with nanoassembled

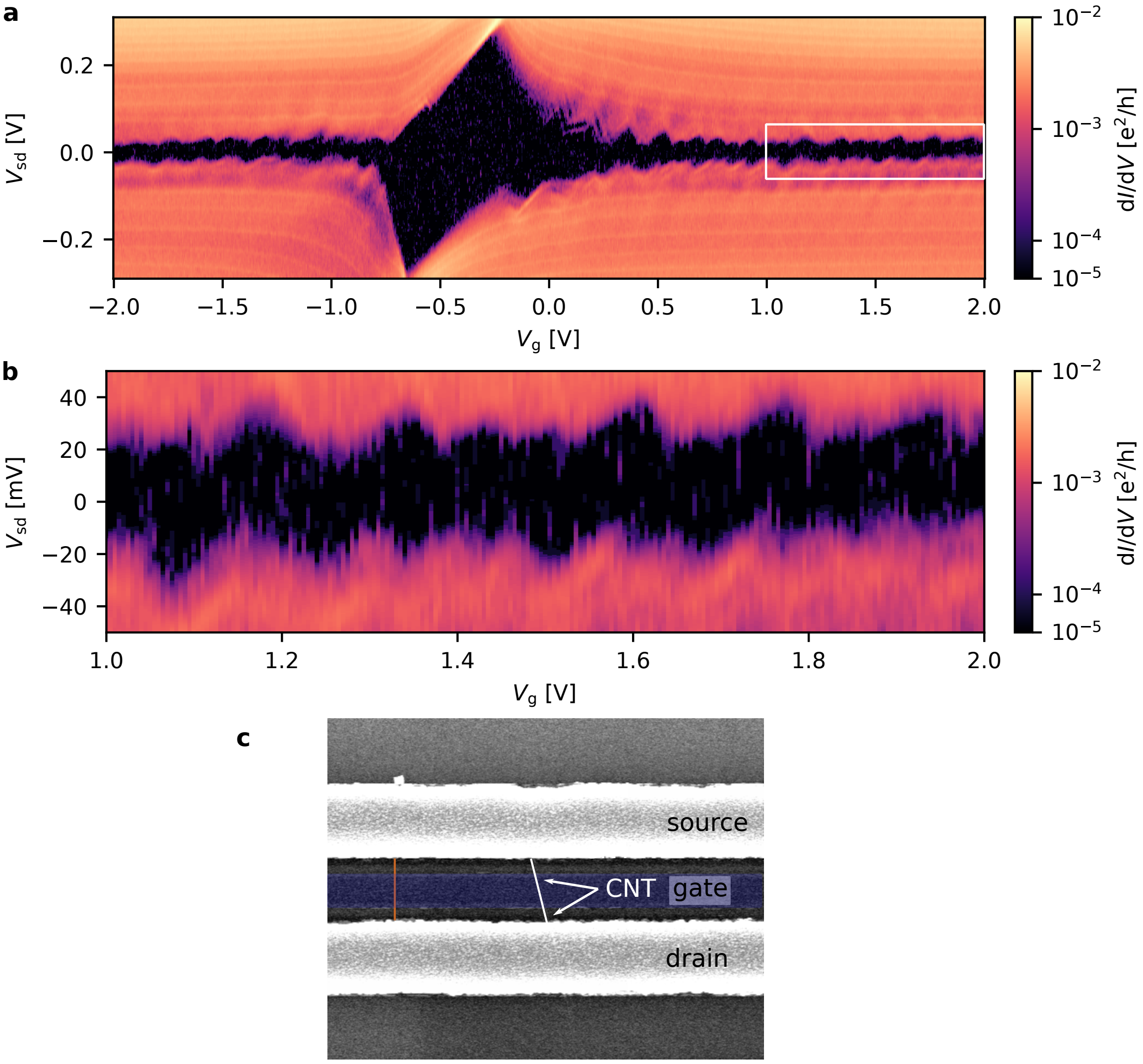

Figure 6.4.: Charge stability diagram of a junction of one of the first devices (sample NC1). Without argon milling and RTA. **a** Large overview. **b** Zoom into the electron side and low bias range (white frame). **c** Scanning electron micrograph showing the CNT quantum dot. The orange scale bar shows the suspension length of 400 nm.

CNTs. All samples presented henceforth have been fabricated following the full contact improvement process detailed in chapter 5.4 and show substantially higher conductance and cleaner transport spectra in low temperature measurements.

6.2.2. Transport in the weak coupling regime

In this section we will discuss measurements of CNT quantum dots in the weak coupling or Coulomb blockade regime in sample NC2, consisting of a single CNT transferred onto molybdenum electrodes of 80 nm thickness and a top contact layer of 5-8 nm of palladium. The focus will be on two junctions with comparable dimensions fabricated from the

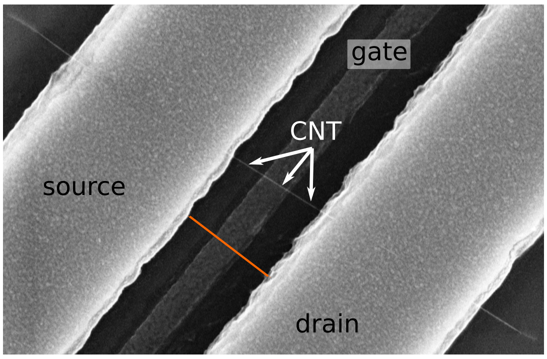

Figure 6.5.: Scanning electron micrograph showing the suspended CNT forming the second quantum dot of sample NC2. (cf. figure 6.6c,d). The orange scale bar shows the suspension length of 400 nm. The first quantum dot in figure 6.6a,b has the same dimensions.

same CNT. For each junction, the CNT is suspended $\sim 70\,\text{nm}$ above a single central gate electrode (cf. figure 6.5). The charge stability diagrams for the first junction are shown in figure 6.6a,b and for the second junction in figure 6.6c,d. The room temperature resistance of the individual junctions at $V_{\text{sd}} = 0.1\,\text{V}$ was about $150\,\text{k}\Omega$ which is the highest of all devices presented in the following and already indicates a weak coupling between CNT and contacts. The CNT does not show any conduction for a gate voltage between -2 V and 0 V and can be considered semiconducting. Here, the focus will be on the electron side with a higher differential conductance reaching up to 10 µS. In contrast to the device from sample NC1 in the last section 6.2.1, a regular series of Coulomb diamonds can be recognized that touch at zero bias, owing to the contact improvement techniques. The transport behavior is consistent with the theory presented in chapter 2.2.3.

The main device properties can be calculated from the charge stability diagram. The height of the diamonds is equal to the addition energy and results in $E_{\text{add}} = 16\,\text{meV}$ for the first quantum dot at a gate voltage $V_{\text{g}} = 0.93\,\text{V}$ and $E_{\text{add}} = 29\,\text{meV}$ for the second quantum dot at a gate voltage $V_{\text{g}} = 1.2\,\text{V}$. A quantum level spacing of $\Delta E = 4\,\text{meV}$ is expected for a 400 nm long suspended CNT but in the charge stability diagram, fourfold degeneracy is absent, and the addition energy is dominated by the charging energy. The charge stability diagram allows us to extract the capacitances, lever arm, and tunnel coupling. The data are summarized in table 6.1. The low separation between the CNT and the gate of only 70 nm leads to a high lever arm of $\alpha = 0.15$ for the first dot and $\alpha = 0.26$ for the second dot. Already in figure 6.6 the tunnel coupling is asymmetric and Breit-Wigner lineshapes can be fitted [203] to the last three Coulomb peaks to extract the tunnel coupling Γ_{s} and Γ_{d}

$$\frac{\mathrm{d}I}{\mathrm{d}V} = 4\frac{e^2}{h}\frac{4\Gamma_{\text{s}}\Gamma_{\text{d}}}{(\Gamma_{\text{s}}+\Gamma_{\text{d}})^2 + (2\alpha e(V_{\text{g}} - V_{\text{g}}^{\text{CP}}))^2} \tag{6.1}$$

where the term V_{g}^{CP} is the gate voltage at a Coulomb peak[12]. For the two dots, the ratio $\Gamma_{\text{s}}/\Gamma_{\text{d}} > 1000$ (cf. table 6.1) indicates a very strong coupling asymmetry.

---

[12] This formula is only valid in the regime $\Gamma \gg k_{\text{B}}T$, otherwise finite-temperature effects broadening the Coulomb peaks must be taken into account [204]. Despite the low value of Γ_{d}, the sum $\Gamma = \Gamma_{\text{s}} + \Gamma_{\text{d}}$ is well above the thermal energy at 40 mK of 3 µV.

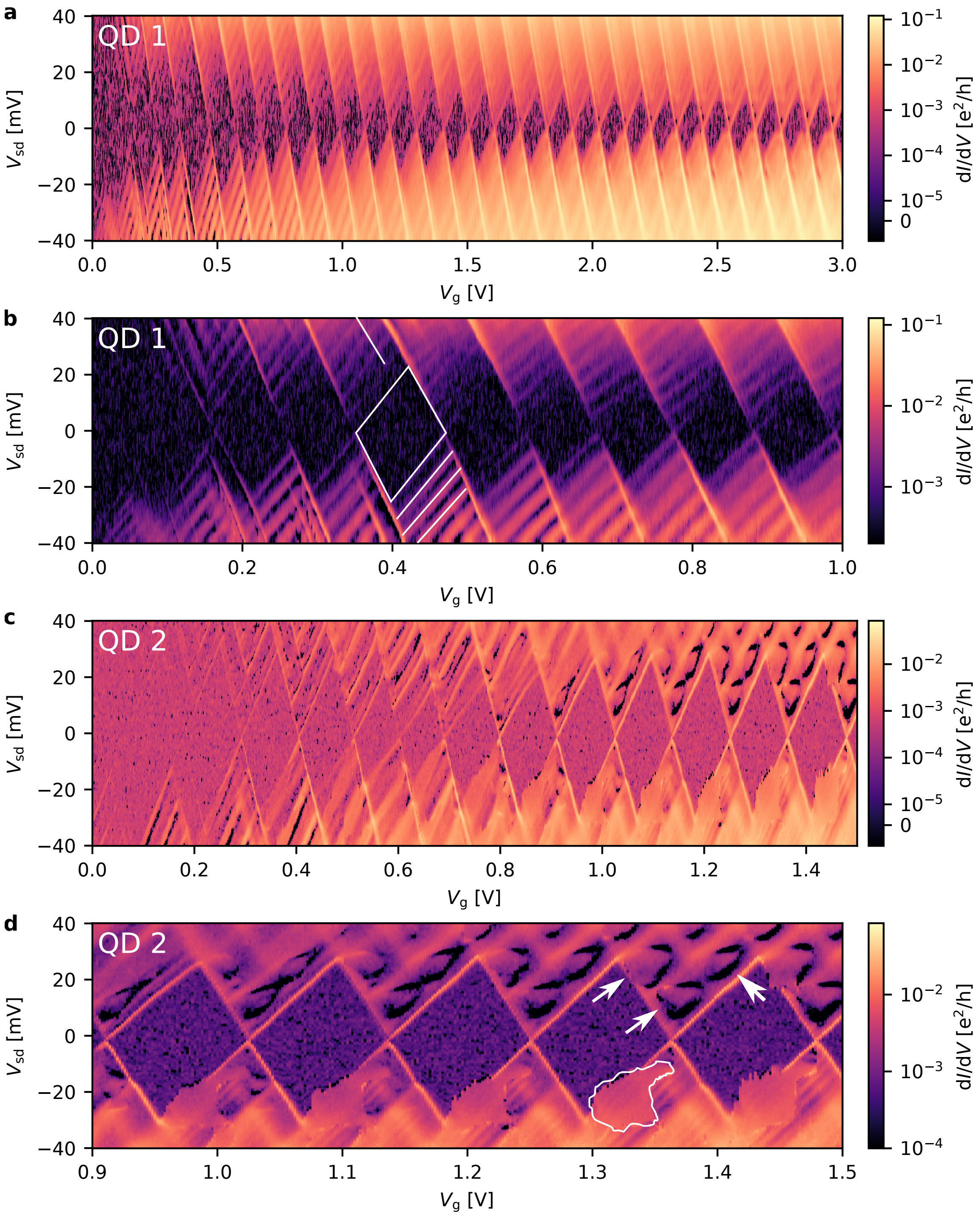

Figure 6.6.: Charge stability diagram of sample NC2. a,b First quantum dot (QD1). **b** shows a zoom into **a** with an adapted colorbar to highlight the lines running parallel to the Coulomb diamond edges (white). **c,d** Second quantum dot (QD2). **d** shows a zoom into **c** with an adjusted colorbar to highlight the areas with negative differential conductance in **c** marked by the arrows and regions with mechanical bistabilities encircled with white color.

Table 6.1.: Calculated parameters for the two quantum dots from figure 6.6. The quantum level spacing ΔE is not visible in the diagrams and it is assumed that the charging energy is equal to the addition energy in the calculation. $\Gamma_{\mathrm{s,d}}$ has been averaged over the last 3 diamonds in figure 6.6a,c.

Parameter	Dot 1	Dot 2
E_{add} [meV]	16 ($V_{\mathrm{g}} = 0.93\,\mathrm{V}$)	29 ($V_{\mathrm{g}} = 1.2\,\mathrm{V}$)
α	0.15	0.26
C_{g} [aF]	0.74	0.71
C_{s} [aF]	1.19	1.05
C_{d} [aF]	2.05	1.01
Γ_{s} [meV]	1.3	0.9
Γ_{d} [meV]	0.0006	0.0006
$\Gamma_{\mathrm{s}}/\Gamma_{\mathrm{d}}$	2070	1479

In figure 6.6a and highlighted in 6.6b, we can distinguish parallel lines running inside the Coulomb diamonds that are due to excited states (cf. figure 2.8 in chapter 2.2.3). The excited states could be of electronic or mechanical origin. To estimate the energy scale, the energy spacing between the lines along the y-axis in figure 6.6b can be calculated to (9.33 ± 0.25) meV. In the following, we will compare this energy scale with the energy scales for electronic and mechanical excitations.

For electronic excitations, this scale has to be compared to the quantum level spacing $\Delta E = hv_{\mathrm{F}}/2L \approx 4\,\mathrm{meV}$ for $L = 400\,\mathrm{nm}$, which is approximately half as much. Under the assumption of a local confinement in the CNT, an effective dot length of 177 nm would match with the energy scale. For instance, this local confinement could occur if the confinement potential extends over the contact barrier into the suspended section of the CNT due to the gate width being shorter than the length of the CNT. However, there are two indications that contradict this assumption. First, the quantum level spacing of $\sim 9\,\mathrm{meV}$ should be well visible in the charge stability diagram, and second, the excited electronic states cannot explain the suppression of conductance at low bias.

Regarding a mechanical origin, there are several indications that would be consistent with a coupling to longitudinal stretching modes [67]. First, the parallel lines have a reduced differential conductance closer to the edges of the diamonds, and the edges are very weakly conducting. In particular, at low bias, there is a partial suppression of conductance. This would point towards a strong electron-vibron coupling, which will shift the vibron potential and reduce the probability for ground state to ground state transitions as reported in [67]. In addition, assuming a strong vibrational relaxation from the excited state to the ground state as in [67], each tunneling starts from the vibrational ground state. A significant overlap is only achieved with higher vibronic states, thereby increasing the conductance of their corresponding lines. Second, negative differential conductance can be observed between some of the lines, which has been observed for a coupling to longitudinal stretching modes [67, 43]. Lastly, the spacing of the lines is not gate-voltage dependent, and therefore independent of the electronic structure of the dot.

However, the energy scale is an order of magnitude higher than the 0.8 meV reported in [67] for excited states due to electron-vibron coupling with longitudinal stretching modes in a 240 nm long CNT quantum dot or for longer suspension lengths in [43]. Assuming an electron-vibron coupling for longitudinal stretching modes, the vibron length can be calculated from the energy spacing $\Delta E_{\mathrm{vib}} = \hbar v_{\mathrm{ph}} n\pi/L$ for the vibron mode n in a doubly clamped beam and the group velocity of the longitudinal stretching mode $v_{\mathrm{ph}} \approx 2.4\times10^4$ m/s [67]. This calculation would result in a vibron size for the fundamental mode of only 5.3 nm, well below the CNT suspension length.

Whereas this seems to contradict a coupling between single-electron tunneling and longitudinal stretching modes at first glance, the situation may be more complex, as detailed in [205]. The vibrons are coupled not only to the total charge of the quantum dot but also to fluctuations of the electron density. In particular, in combination with high barrier asymmetry, the Franck-Condon factors can become position-dependent. In fact, the parallel lines in figure 6.6b are more dominant for positive slope when the dot level is aligned with the source and only some weak lines can be distinguished for decreasing slope when the dot is aligned with the drain. In contrast to the parallel lines, the edges of the diamonds exhibit a higher differential conductance for the decreasing slope. These findings are consistent with position-dependent Franck-Condon factors, where stronger electron-vibron coupling is observed near the source electrode, leading to a suppression of ground state to ground state transitions, while the electron-vibron coupling is reduced in the vicinity of the drain, increasing the probability for ground state to ground state transitions.

In [67], the authors also mention a potential strong electron-phonon coupling to radial breathing modes (RBMs) which could be excited by electron tunneling and provide an alternative explanation of the parallel lines. The energy scale of RBMs is higher than for the longitudinal stretching modes and even higher than for the electronic excitations (cf. figure 2.3). The expected Raman shift can be calculated using the formula $E_{\mathrm{RBM}} = hc\omega_{\mathrm{RBM}}$ yielding a Raman shift of 75 cm^{-1} that would correspond to a CNT diameter of 3 nm (using eq. 3.1). Although the CNT diameter was not measured, a diameter of 3 nm would be consistent with the Raman and TEM characterization in chapter 3. The coupling between single-electron tunneling and RBMs has been observed for example in [206],r and could also explain the parallel lines.

Further evidence for the coupling between nanomechanics and single-electron tunneling is found for the second quantum dot (cf. figure 6.6c,d). Again, there are lines running parallel to the edges of the Coulomb diamonds which we have discussed in detail for the first quantum dot. For a gate voltage higher than $\sim$ 1 V one can distinguish areas with high negative differential conductance mainly for positive bias. A zoom in these features is shown in figure 6.6d (note that the colorbar has been adjusted to positive values to highlight all the features). The negative differential conductance features marked by the white arrows repeat for several diamonds. Another intriguing feature is highlighted by the white area. Here, for several diamonds, a region with homogeneous differential conductance can be observed that also extends into the diamonds. Similar features have been discussed in [83, 207, 208, 209, 210] and have been associated with self-driven oscillations due to electromechanical feedback. When the voltage bias exceeds a critical threshold, electron tunneling may drive mechanical oscillations in the CNT, which impact the electronic transport through the CNT. While the authors in [83] could mainly observe negative differential conductance features outside the diamonds as marked by the arrows in figure 6.6d, the authors in [207] could also observe regions with conductance in Coulomb diamonds. They attribute these regions to a widening of the Coulomb peak owing to rectification when the oscillations in the CNT are driven.

Unfortunately, in this sample NC2, mechanical resonances could not be detected with current rectification when driving via a wire-bonded RF antenna. Nonetheless, the sample NC2 clearly demonstrates the strong coupling between nanomechanical motion in the CNT and single-electron tunneling in the weak coupling regime.

6.2.3. Transport in the intermediate and open quantum dot regime

When increasing the tunnel coupling by decreasing the device resistance below $\sim 50\,\mathrm{k\Omega}$, the intermediate or for even higher coupling the open quantum dot regime is typically accessed. In this section, the cleanest device of sample NC3 will be discussed which was also presented in our publication [37] and is one of the devices where we could demonstrate reaching the open quantum dot regime in nanoassembled CNT devices.

Basic characterization

Figure 6.7a represents the charge stability diagram of the SQUID in figure 6.7b with a suspension length of 700 nm. It consists of a CNT transferred onto a SQUID structure of 90 nm niobium with a top contact layer of 4 nm palladium. The gate crosstalk is negligible and the two parallel dots formed by the same CNT can be considered independent, as expected for gates that are separated by a central contact electrode. The charge stability diagram is split into four regions, a higher conducting region in the upper right corner where both SQUID junctions are n-type conducting, a lower conducting region in the lower left corner (both junctions p-type conducting) and two regions with intermediate conductance (upper left, lower right) where one junction is p-type and the other junction n-type conducting. The dark region around $V_{\mathrm{gl,gr}} = -0.5\,\mathrm{V}$ indicates the narrow gap of the CNT. From the charge stability diagram, it can be inferred that the left dot has a higher differential conductance than the right dot. In the following, we will discuss only the left dot while the right dot is turned off (V_{gr} tuned to the narrow gap).

Figure 6.8a shows an overview of electronic transport through the left dot, where all three transport regimes can be accessed, as described in chapter 2.2.3. By increasing the gate voltage V_{gl} the conductance can be tuned from the intermediate transport regime at $V_{\mathrm{gl}} = -3\,\mathrm{V}$ to the weak coupling regime on the hole side. Once the narrow band gap is overcome at $V_{\mathrm{gl}} = -0.4\,\mathrm{V}$, the electron conductance is high, characteristic for the open quantum dot regime. From the height of the neutral diamond of about 60 meV (not shown)

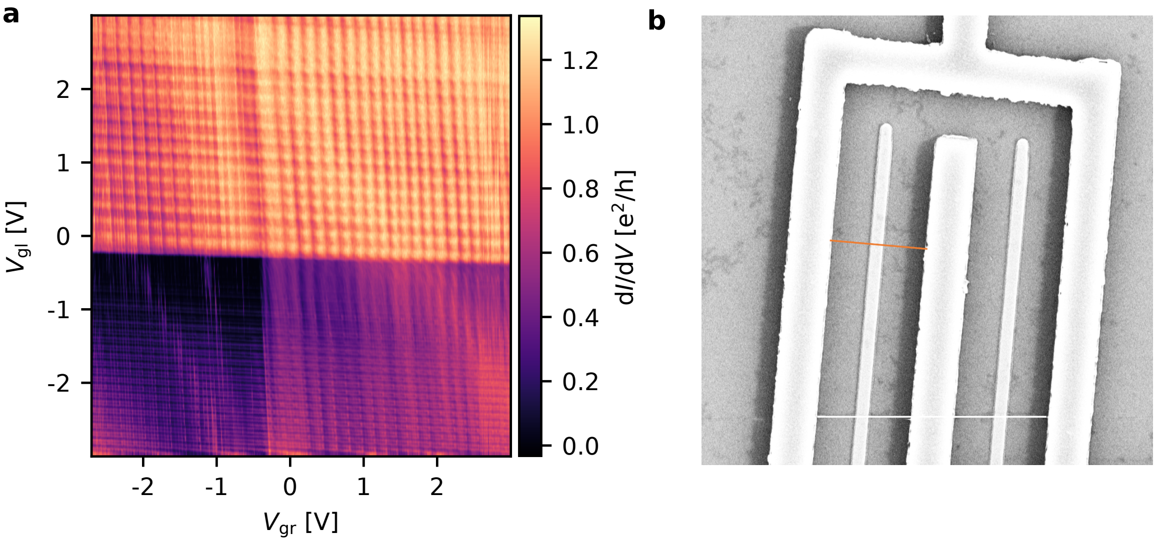

Figure 6.7.: Device overview of sample NC3. a Charge stability diagram at $V_{\mathrm{sd}} = 0\,\mathrm{V}$. **b** Scanning electron micrograph of a SQUID from sample NC3 with a suspended CNT highlighted in white and a scale bar in orange indicating the suspension length of 700 nm.

and the addition energy $E_{\mathrm{add}} \approx 25\,\mathrm{meV}$ of the first diamond on the hole side, the band gap can be calculated to $E_{\mathrm{G}} \approx 35\,\mathrm{meV}$.

Open quantum dot regime

In the following the different transport regimes will be discussed in detail, starting with the open quantum dot regime in figure 6.8b (cf. chapter 2.2.6). There exists a region with an almost homogeneous, high differential conductance which is patterned with a checkerboard pattern due to Fabry-Pérot oscillations as reported in [47]. The height of the lines, as indicated by the white arrows, allows us to extract the quantum level spacing $\Delta E = hv_{\mathrm{F}}/2L$ when the charging energy is negligible. The length of the quantum dot can be calculated to 490 nm, which is less than the actual suspension length of the CNT of 700 nm. However, taking a look at the actual SQUID in figure 6.7, it becomes apparent that the gate is only around 100 nm wide. Hence, it is likely that the size of the quantum dot is not defined by the hard boundaries at the contact interface but by the local potential inside the CNT which can differ from the suspension length. Similar results for the dot size have been obtained for devices from other samples in the Fabry-Pérot regime with gate widths much smaller than the suspension length.

Intermediate coupling regime

The zoom in the p-type conduction is shown in figure 6.8c. One can see a series of Coulomb diamonds with particularly high conductance around zero bias, as it is typical for elastic cotunneling mediated by Kondo resonances in the intermediate regime (cf. chapter 2.2.5). Around $V_{\mathrm{gl}} = -3\,\mathrm{V}$ the line at zero bias links three diamonds in a sequence, characteristic

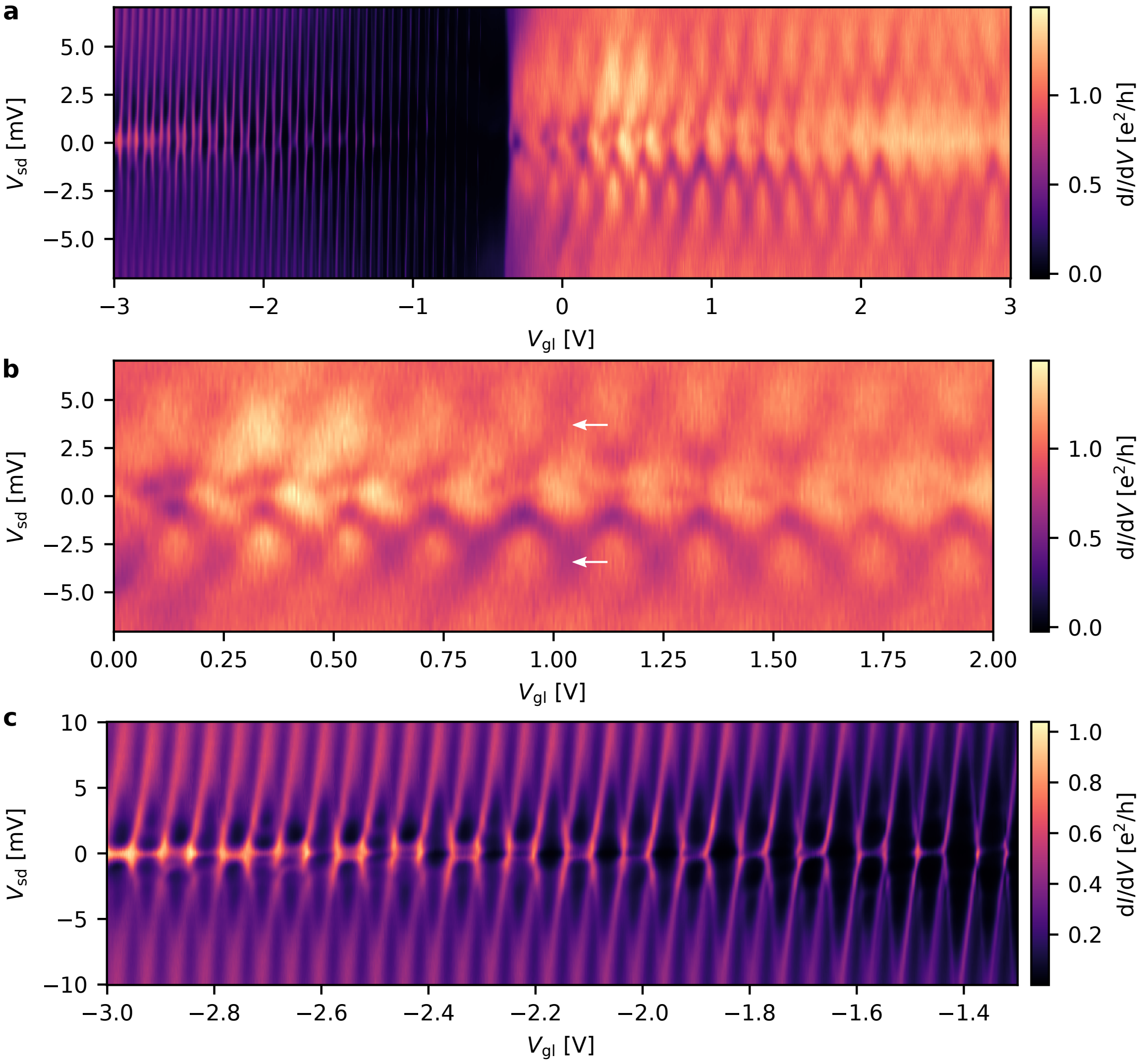

Figure 6.8.: Charge stability diagram of the left dot (right dot "off", $V_{gr} = -0.5$ V). **a** Overview, **b** Zoom into the high conducting electron side with Fabry-Pérot oscillations. The spacing between the white arrows allows to calculate the quantum level spacing. **c** Zoom into the hole side showing Kondo ridges with high differential conductance at zero bias voltage.

for the SU(4)-Kondo effect for spin and valley degeneracy, whereas towards the CNT band gap the tunnel coupling is reduced and the Kondo ridges only occur every odd diamond, characteristic for the SU(2)-Kondo effect.

For $V_{gl} > -1.4$ V, the ridges disappear and the device approaches the weak coupling regime where cotunneling processes are suppressed. However, in contrast to the standard spin 1/2 Kondo effect explained in chapter 2.2.5 where only a single zero bias line is expected, the zero bias line splits into two lines for certain gate voltage ranges. An example is marked by the arrow in figure 6.10a. The splitting vanishes for higher tunnel coupling and is absent where the SU(4)-Kondo effect is observable (white box). The effects can be explained by the interplay between the Kondo effect and spin-orbit coupling [73, 211], as we shall see in the following.

Interplay between Kondo effect and spin-orbit coupling

In general, there are two contributions to zero field splitting, disorder-induced orbital mixing $\Delta_{KK'}$ and spin-orbit coupling Δ_{SO}. The two contributions can be separated by applying a parallel magnetic field along the CNT axis (cf. figure 6.9). In contrast to a perpendicular field which only affects the spin degree of freedom, a magnetic field applied along the CNT axis also affects the two valley degrees of freedom K, K' which can be conceived as clockwise and counterclockwise rotating electron states around the CNT circumference. The orbital magnetic moment of this motion around the CNT couples to the parallel magnetic field with a magnitude given by the orbital g-factor g_{orb}, splitting a fourfold degenerate state at zero field into two doublets with different valley numbers at $B_{||} \neq 0$. Each doublet is further split by a smaller degree due to the weaker Zeeman splitting of the electron spins ($g_s < g_{\mathrm{orb}}$, cf. figure 6.9a).

Although $\Delta_{KK'}$ and Δ_{SO} can both lead to a splitting already at zero field, the nature and magnetic field dependence is fundamentally different [212]. Orbital mixing results in an avoided level crossing at zero field between two doublets with the same valley quantum number, as shown in figure 6.9b. Spin-orbit coupling, in a simple picture, arises from an effective radial electrical field due to the curvature of the CNT.

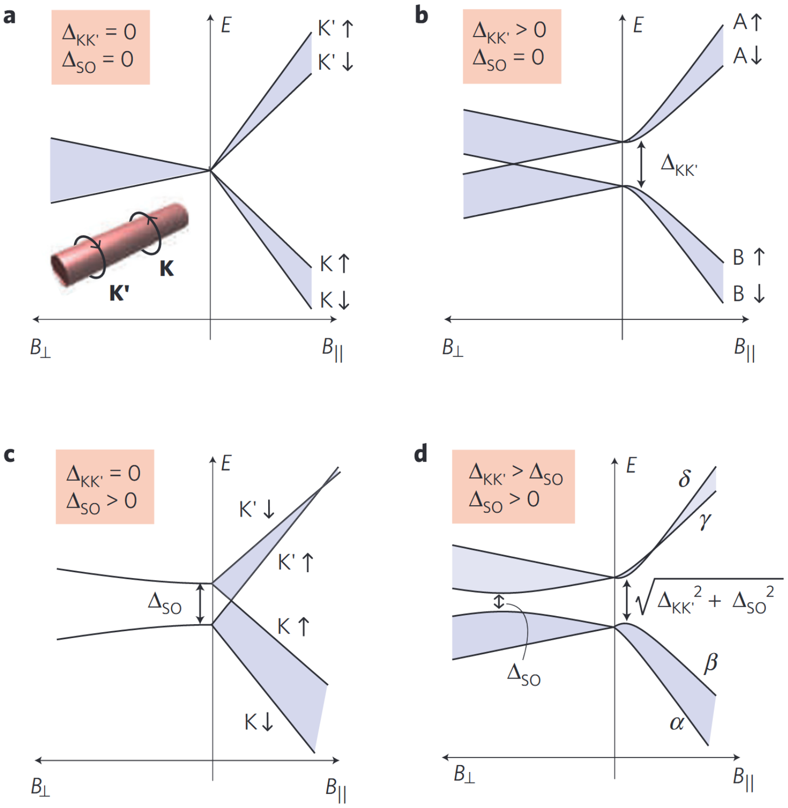

Figure 6.9.: Spin-orbit coupling. Spin-orbit coupling (Δ_{SO}) and orbital mixing ($\Delta_{KK'}$) as a function of magnetic field along the CNT axis $B_{||}$ and perpendicular $B_\perp$ for different ratios of Δ_{SO} and $\Delta_{KK'}$. Figure from [212].

Together with the circumferential motion of the K, K' states, this results in an effective magnetic field along the CNT axis ($\mathbf{B}_{\mathrm{SO}} = -(\mathbf{v} \times \mathbf{E})/c^2$), polarizing the spins along the CNT axis [212]. The effect can be described by a spin-orbit coupling Hamiltonian $H_{\mathrm{SO}} = \Delta_{\mathrm{SO}} \mathbf{L} \cdot \mathbf{S}$ coupling the spin and valley degrees of freedom. At zero magnetic field the coupling results in two degenerate Kramers doublets $(K\uparrow, K'\downarrow)$ and $(K\downarrow, K'\uparrow)$, split by an energy Δ_{SO}. In contrast to orbital mixing, the magnetic field dependence of the Kramers doublets leads to a crossing at finite $B_{||}$ (cf. figure 6.9c). The combination of the two effects is sketched in figure 6.9d.

Having discussed the underlying physics, one can estimate the spin-orbit coupling in a similar way as in [73]. The estimation was performed for the fifth hole (cf. figure 6.11), which corresponds to the situation of the first hole in the fourfold shell. Figure 6.11a is consistent with a dominant spin-orbit coupling. The two lines with slope $|\alpha|$ seem to cross at a magnetic field $B_{||} \geq 1.4\,\mathrm{T}$, there is no avoided level crossing visible and we therefore assume to be in the limit $\Delta_{\mathrm{SO}} \gg \Delta_{KK'}$. The extrapolation of the two lines with slope $|\alpha|$ gives an estimate of the spin-orbit coupling of about $\Delta_{\mathrm{SO}} = 1.3\,\mathrm{meV}$ which is high compared to the few hundreds of microvolts in [212, 73, 213] but less than the record high spin-orbit coupling of 3.4 meV in [214].

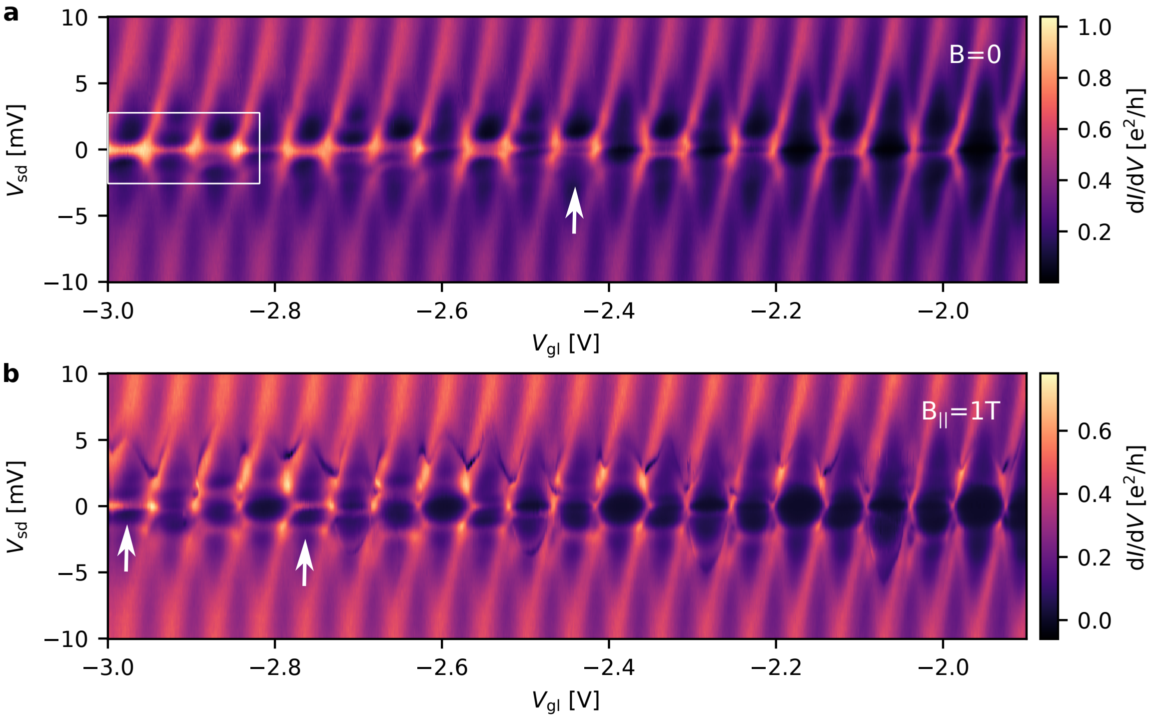

Figure 6.10.: Zoom in the Kondo resonances around zero bias voltage. a No magnetic field is applied. The zero bias line is split as indicated by the arrow, except where the tunnel coupling is higher, e.g. in the white box where a SU(4)-Kondo ridge is highlighted. **b** A magnetic field $B_{||} = B_z = 1\,\mathrm{T}$ is applied along the axis of the CNT. Most of the Kondo resonances vanish at zero bias except the ones marked by the white arrows.

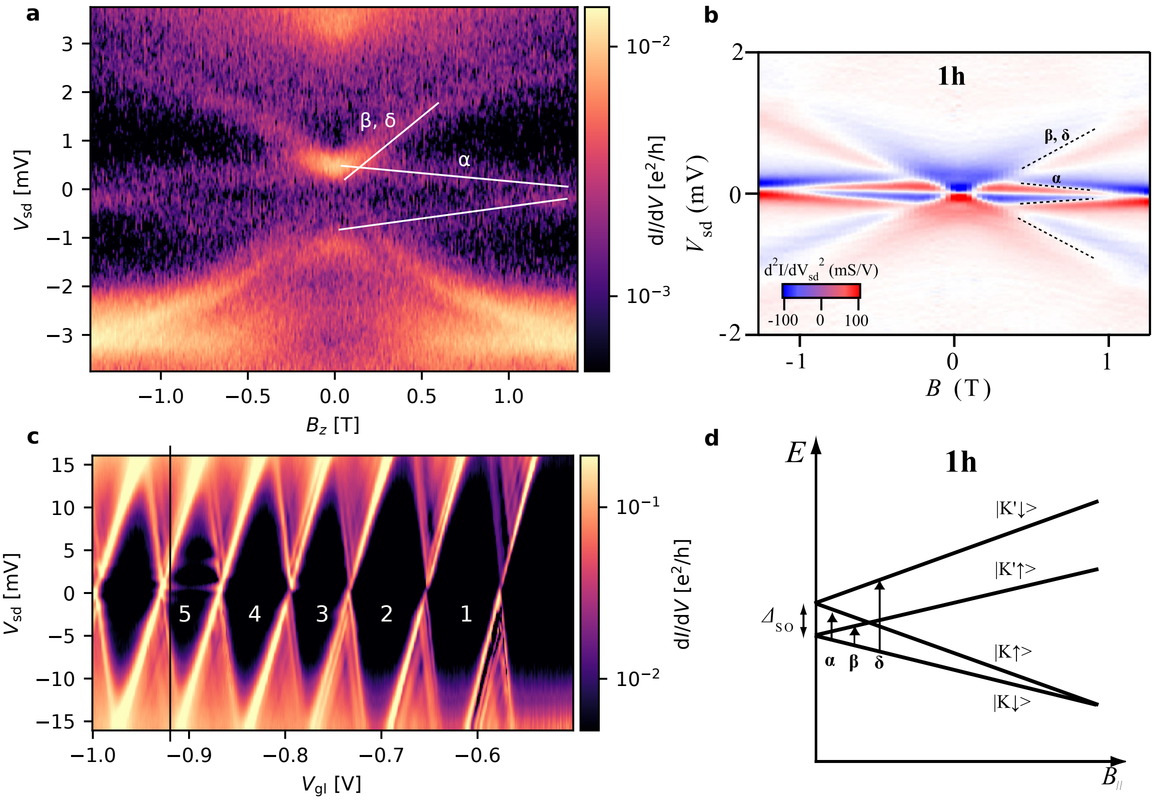

Figure 6.11.: Extraction of spin-orbit coupling. For the fifth hole marked by the black line in **c**. **a** Differential conductance as a function of magnetic field along the CNT axis ($B_z = B_{||}$) allowing for the extraction of spin-orbit coupling by extrapolating the lines with α to zero. **b** Similar situation in [73]. Here the second derivative is plotted to enhance visibility. **c** First six holes with tuning point for **a** (black line). **d** Schematic spin-orbit level dependence on $B_{||}$ for the first hole of a fourfold shell (from [73])

We can now better understand the charge stability diagram in figure 6.10. The more negative V_{gl}, the higher the tunnel coupling, and the more likely is the probability of cotunneling processes. This also affects the Kondo temperature, which decreases with increasing V_{gl}. As observed in other experiments [73] and theoretically explained in [211], the decrease in Kondo temperature $T_K^{SU(4)}$ with increasing V_{gl} leads to a crossover around $V_{gl} = -2.6$ V, where the energy scale associated with spin-orbit coupling Δ_{SO} dominates and a transition to the SU(2) Kondo effect occurs (with the two degrees of freedom originating from Kramers doublets).

At a parallel magnetic field $B_{||} = 1$ T most of the spin-orbit split Kondo ridges have disappeared around zero bias because the magnetic field splits the Kramers doublets. This is nicely visualized by the white arrow in figure 6.10a where the two ridges have vanished at a finite magnetic field in 6.10b. The parallel magnetic field should, in principle, completely lift the fourfold degeneracy for the SU(4) Kondo effect visualized for a shell in the white box. However, a single Kondo ridge still exists for the third diamond, as marked by the arrows in figure 6.10b. Similar observations are reported in [215] and theoretically derived in [211]. It is possible that $B_{||} = 1$ T corresponds exactly to the energy scale required for a level crossing at zero bias.

In conclusion, we have demonstrated that our normal conducting devices fabricated with the nanoassembly technique can access all three transport regimes and we were able to explore interesting phenomena, such as the Franck-Condon blockade or the interplay between SU(4) Kondo physics and spin-orbit coupling. In particular, the latter phenomenon requires ultraclean CNTs [213, 212] to reach the regime where $\Delta_{\mathrm{SO}} \gg \Delta_{KK'}$. In addition to the high cleanliness of our nanoassembled CNT device, we could also report reaching the open quantum dot regime [37] which indicates transparent contacts that are essential for superconductivity experiments in CNTs, which will be discussed in the next section.

6.3. Electronic transport measurements with superconducting electrodes

In this section we present cryogenic CNT transport measurements with molybdenum rhenium as source of superconductivity and palladium or platinum as contact material. The total stack comprises 15 nm Mo, 41 nm MoRe and 4-7 nm Pd/Pt[13] (cf. chapter 4). In total, five superconducting samples (SC1-SC5) have been measured and we will focus on the three samples with highest supercurrent in this chapter. The physics phenomena observed in these devices are addressed in individual subchapters.

6.3.1. Pre-characterization of the superconducting samples

Similarly to the normal conducting devices, a short overview of the device characteristics is presented including charge stability diagrams and differential resistance measurements to characterize the superconductivity. The key properties of the samples are summarized in table 6.2.

Table 6.2.: Overview of the five superconducting samples. R_{SQUID} is the room temperature device resistance for the whole SQUID with both gates tuned to lowest resistance. For sample SC1 this value has not been measured and the maximum switching current $I_{\mathrm{sw}}^{\mathrm{max}}$ is a lower bound.

Device	Contact material	R_{SQUID} [kΩ] at 300 K	$I_{\mathrm{sw}}^{\mathrm{max}}$ [nA]
SC1 SQUID400	Pd	-	~2
SC2 SQUID400	Pd	14	1-2
SC3 SQUID400	Pd	20	0.1-0.2
SC4 SQUID400	Pd	14	0.1
SC5 SQUID800	Pt	16	3-4
SC5 SQUID400	Pt	21	0.1

---

[13] The final contact layer thickness is determined by argon milling as part of the contact improvement and can slightly vary.

First superconducting sample (SC1)

A SQUID of the first superconducting sample (SC1) with palladium contact material is shown in figure 6.12b with a CNT suspension length of about 300 nm, as indicated by the orange scale bar. The charge stability diagram is depicted in figure 6.12a. Similar to all other devices, it shows a higher conductance for electrons than holes. The gate crosstalk is negligible and the two parallel quantum dots can be considered as independent.

The left dot features a higher differential conductance, and therefore, we mainly focus on this dot, while the right dot is turned off by tuning its gate voltage into the narrow gap. The charge stability diagram of the left dot is represented in figure 6.12c. Apart from the low bias conductance, it resembles the device from sample NC3 where the transport regimes have been discussed in detail. For the electron side, Fabry-Pérot oscillations can be recognized, indicating the open quantum dot regime, whereas for holes low conductance is measured as typical in the Coulomb blockade regime. By decreasing the gate voltage, the intermediate coupling regime can be approached, marked by the onset of cotunneling for $V_{\mathrm{gl}} < -2\,\mathrm{V}$.

While all measurements so far have been performed in a voltage-biased setup (two-terminal measurements, with lock-in), the measurement of the switching current requires current-biasing four-point measurements without lock-in techniques (cf. figure 6.2). Such a measurement is shown in grayscale in figure 6.12d where the current through the CNT quantum dot is controlled and the voltage drop across the junction is measured. The differential resistance can be calculated by numerical differentiation. Figure 6.12d shows only the electron side where a higher switching current is expected due to the higher differential conductance in figure 6.12c. The differential resistance is modulated with the gate voltage and current bias. The modulation period with the gate voltage fits to the modulation of the differential conductance in figure 6.12c. One can distinguish pockets with homogeneous, particularly low resistance around zero current, e.g. at $V_{\mathrm{gl}} = 1.25,\ 1.75\,\mathrm{V}$. These pockets can be associated with supercurrent. The transition between the low-resistive regions and the regions with higher resistance defines the switching current where the CNT junction turns into the finite-voltage state. In regions where the differential conductance is low, the pockets close, and the supercurrent vanishes entirely.

For this device, due to a connection issue, the four-point measurement could not be carried out properly and we expect an additional inline resistance of 5-7 kΩ, which explains the non-zero differential resistance. When the superconducting pockets are well defined, e.g. at $V_{\mathrm{gl}} = 1.25\,\mathrm{V}$, it is easy to calculate the switching current. Unfortunately, this is not the case for all pockets and the maximum switching current is not clearly visible, and the transition between superconducting and the finite-voltage state is smeared out. This behavior is typical for the overdamped junction regime in the framework of the RCSJ model (cf. chapter 2.4.4). One way to distinguish between the overdamped and underdamped junction regime in the experiment is to record trace-retrace measurements (increasing and decreasing I_{sd}) and investigate hysteresis. We only show the trace (increasing I_{sd}-ramp) in this section, but the quantum dot exhibits negligible hysteresis, indicating that the junction operates in the overdamped regime. Beyond the transition to the normal conducting state,

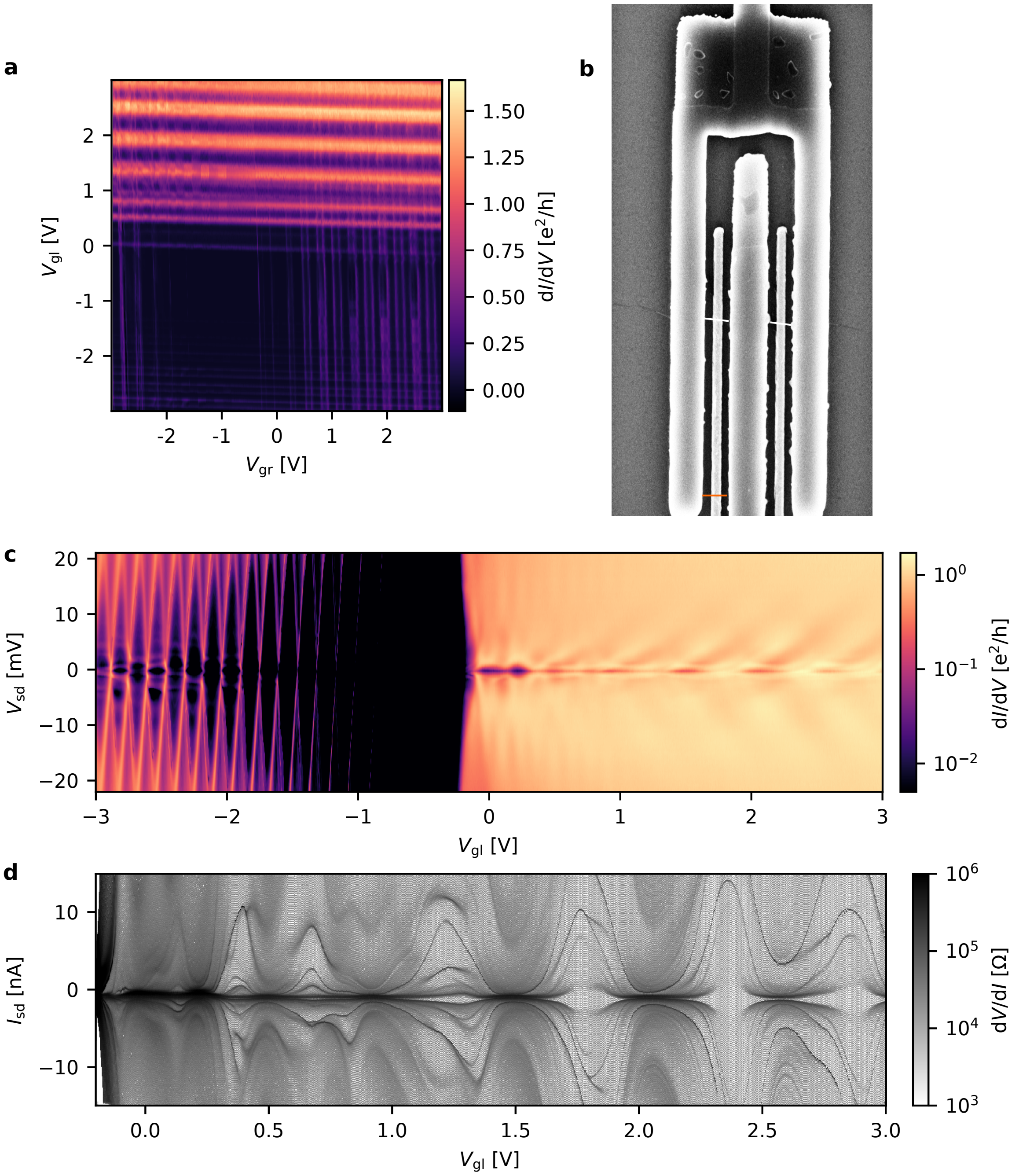

Figure 6.12.: Overview of the device from SC1. **a** Charge stability diagram. **b** Scanning electron micrograph with the CNT highlighted in white. The scale bar in orange indicates the suspension length of 300 nm. **c** Charge stability diagram of the left dot. **d** Differential resistance map in current-biased setup.

one can recognize several darker lines similar to [189] which can be attributed to multiple Andreev reflections at finite bias voltage V_{sd}.

A key parameter to evaluate proximity-induced superconductivity is the proximity-induced superconducting gap Δ. For $V_{\mathrm{sd}} > 2\Delta$, quasiparticle tunneling is allowed, and due to the van-Hove singularities in the DOS (cf. figure 2.15) a sudden increase in differential conductance

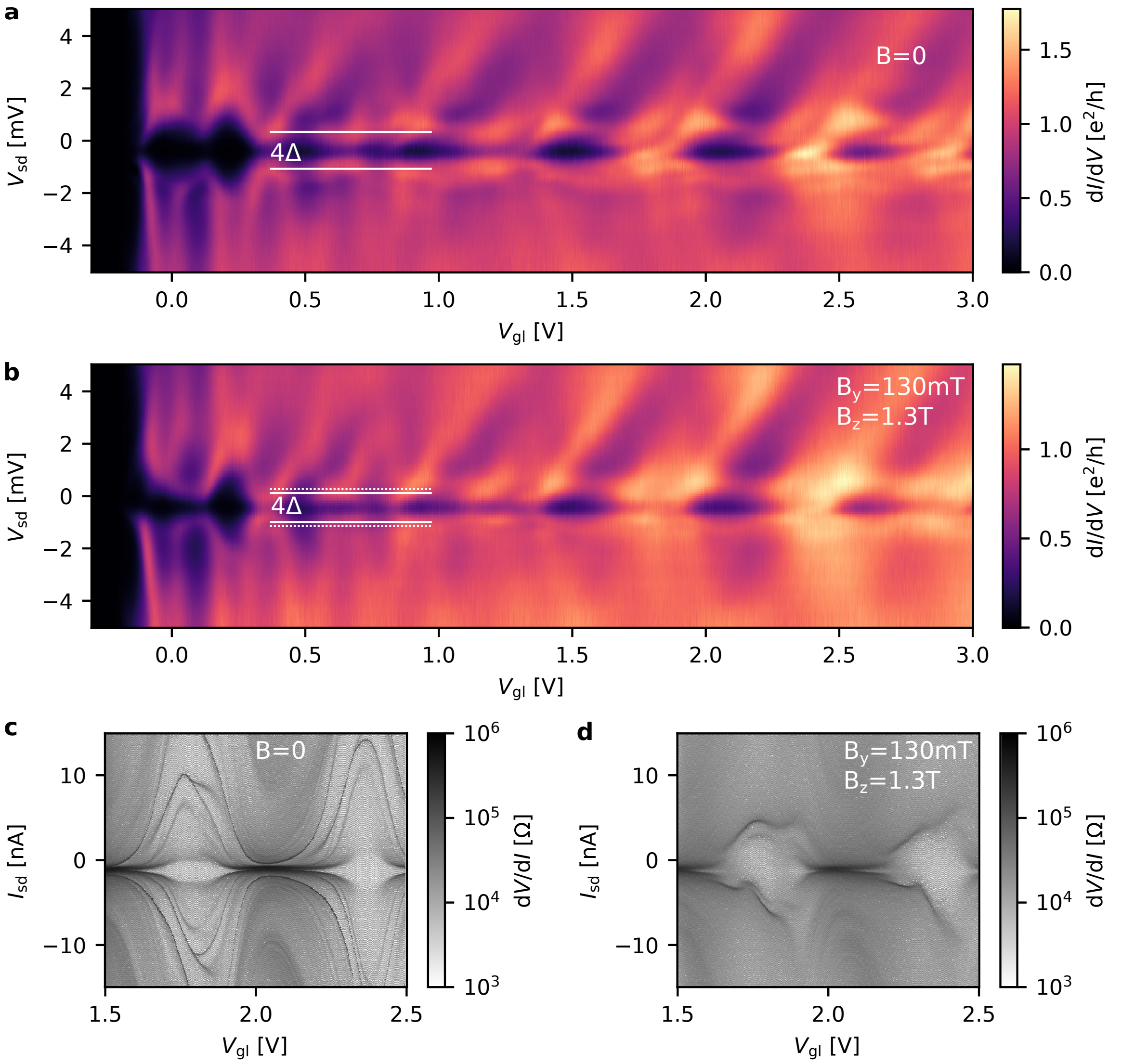

Figure 6.13.: Application of magnetic field. Applied along the CNT ($B_z = B_{||}$) and perpendicular to the SQUID loop ($B_y = B_\perp$). **a**, **c** Without magnetic field. **b**, **d** With magnetic field. The assumed proximity-induced superconducting gap Δ can be calculated from the two parallel lines in **a** to 1.4/4 meV.

is expected. In figure 6.13a the location of the proximity-induced superconducting gap is indicated at the center of the ridges with high differential conductance. The extraction from figure 6.13a results in $\Delta = 1.4\,\text{meV}/4 = 0.35\,\text{meV}$ which would correspond to $T_c = 2.3\,\text{K}$ and is below the critical temperature of the superconducting film of 8-10 K due to the proximity effect. This temperature can be compared with that reported for similar experiments. Because there are no values for the proximity-induced gap with MoRe-based samples that have not been exposed to CVD conditions, we have to compare the temperature with materials with a similar critical temperature. For instance, it is higher than the 1.7 K reported for niobium as a source of superconductivity in [101] with a similarly thick palladium layer for devices fabricated with post-growth fabrication. The authors attribute this low critical temperature to the formation of oxides of NbO or contamination. In our fabrication process, the palladium or platinum film is sputtered directly on top of the MoRe without air exposure, which could lead to a much cleaner interface and higher proximity-induced superconductivity.

To verify that these ridges indicate the proximity-induced superconducting gap, superconductivity can be suppressed. In general, there are two options to turn the junction to the normal conducting state. First, increasing the temperature beyond the critical temperature, and second, applying a magnetic field larger than the critical field. In contrast to superconductors with a low critical temperature, such as aluminum, the molybdenum rhenium film has a high critical temperature of 8-10 K. Even though, a lower critical temperature is expected for proximity-induced superconductivity, a heating to $\gtrsim 2.5$ K would be required, as estimated above. Since this could lead to potential contamination of the CNT, we chose the second method and applied a magnetic field. Indeed, as shown in figure 6.13b, the application of a magnetic field reduces the spacing between the high conductance ridges, which can be associated with the proximity-induced superconducting gap. The reduction is small despite the magnitude of the magnetic field close to the maximum possible with the coils, which is expected for high critical magnetic fields of the superconducting film (cf. chapter A.3).

Another visible effect of magnetic field application is the reduction of the maximum differential conductance which was reached in the regions around zero bias, e.g. at $V_{\mathrm{gl}} = 2.5\,\mathrm{V}$. This high conductance at $V_{\mathrm{sd}} = 0$ is caused by a supercurrent which is suppressed by applying magnetic fields. Indeed, in figure 6.13c,d, the application of the magnetic field destroys the superconducting pockets. Likewise, most of the multiple Andreev reflections vanish which could be due to magnetic field induced decoherence of electron and hole pairs in the CNT which are required for Andreev processes.

Second superconducting sample (SC2)

A scanning electron micrograph of a SQUID of the second superconducting sample (SC2) with palladium contact material is shown in figure 6.14b with a CNT suspension length of about 350 nm, as indicated by the orange scale bar. The charge stability diagram is represented in figure 6.12a. It looks fundamentally different from the charge stability diagram for the SQUID of the first superconducting sample SC1.

One can again identify four regions separated roughly at $V_{\mathrm{gl}}, V_{\mathrm{gr}} = -0.5\,\mathrm{V}$ despite the absence of a clear band gap. The maxima of conductance are aligned parallel to the V_{gl}- and V_{gr}-axis, indicating negligible crosstalk between a gate and the opposite quantum dot. However, avoided level crossings appear and additional lines running at a 45°-angle. This indicates that the two dots are not independent but capacitively coupled to each other, which might point towards a CNT bundle. For a bundle, the capacitive coupling could be mediated via a CNT that is only weakly coupled to other CNTs from the bundle and weakly coupled to the central drain electrode.

The charge stability diagram of the right dot is shown in figure 6.14c and also exhibits two broadened highly conducting ridges around $V_{\mathrm{sd}} \approx \pm 0.75\,\mathrm{mV}$ that have been identified with

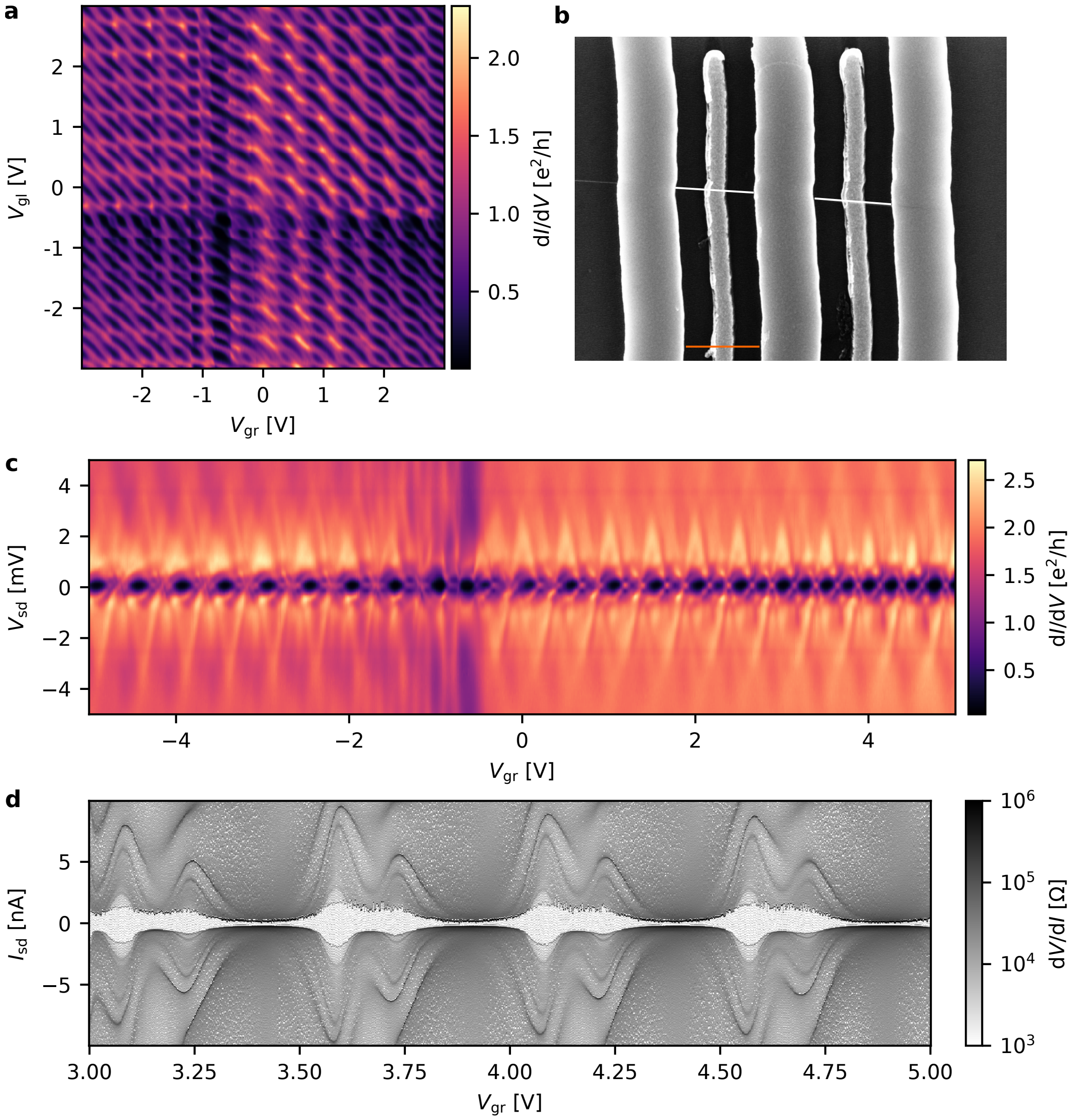

Figure 6.14.: Overview of the device from sample SC2. **a** Charge stability diagram at $V_{sd} = 0$ V. **b** Scanning electron micrograph with the CNT highlighted in white. The scale bar in orange indicates the suspension length of 350 nm. **c** Charge stability diagram of the right dot ($V_{gl} = -0.66$ V). **d** Differential resistance map in current-biased setup after current annealing.

the proximity-induced superconducting gap for the sample NC1. The electronic transport shows high differential conductance beyond 2.5 e^2/h but the open quantum dot regime is not reached, and we can recognize a pattern of mostly regularly spaced high conductance areas at zero bias. Outside the superconducting gap, overlapping diamonds are visible, which could be another indicator of a CNT bundle. The SQUID of NC2 has a switching current of about 1-2 nA, as shown in figure 6.14d for a zoom into the highest switching current region. The superconducting pockets are well defined, and few multiple Andreev reflections are also visible.

Fifth superconducting sample (SC5)

The fifth superconducting sample was the first and only sample with platinum contact material instead of palladium. The room temperature transport of this sample has been analyzed in figure 5.17. On this sample, two SQUIDs have been measured at cryogenic temperatures, the first one ("SQUID800") with 800 nm wide contact electrodes and 500 nm CNT suspension length and the second one ("SQUID400") with 400 nm wide electrodes and a suspension length of 350 nm similar to the other superconducting samples. Due to technical issues with the cryostat, the sample had to be warmed up and another current-induced annealing and radiative thermal annealing was performed in the scanning electron microscope before cooling down the sample for a second time. Unless mentioned otherwise, data of SQUID800 have been acquired during the first cooldown, while SQUID400 has only been analyzed during the second cooldown.

The low-temperature transport of SQUID800 is shown in figure 6.15. The left and right dot exhibit Fabry-Pérot oscillations for the electron conduction and Coulomb blockade for the hole side. Unfortunately, the right gate has been connected to ground, forming an effective voltage divider of 1/20, and thereby limiting the accessible gate voltage range. For the left dot for negative gate voltage, one can recognize Coulomb diamonds packed into series of four consecutive lines, indicating fourfold periodicity in figure 6.15a. Again, gate-independent high conductance ridges can be distinguished around $V_{\mathrm{sd}} \approx \pm 1$ meV. Although a precise estimation of 4Δ remains difficult due to the broadening of the quasiparticle tunneling onset, the spacing of the ridges is of the same order as for the other superconducting samples. From the differential resistance maps in figure 6.15c,d the switching current can be extracted. Since the right dot has not been completely turned off in figure 6.15c and the current through the SQUID is a superposition of the two parallel quantum dots, the switching current of the right dot must be subtracted to obtain the true switching current of the left dot. The switching current of the left dot can be estimated to $I_{\mathrm{sw}} = 3\text{-}4$ nA, which is the highest observed in all superconducting devices. The switching current is modulated by the gate voltage, but in contrast to the other superconducting samples, the superconducting pockets do not close and form one big pocket for the better conducting electron side. Inside the big pocket, one can recognize a pattern of periodic lines, which are probably signatures of 50 Hz noise in our setup, and become well visible in switching current measurements that are performed without lock-in techniques.

The transport through SQUID400 could only be measured after the second cooldown of the sample. The charge stability diagrams displayed in figure 6.16 show a perfect fourfold periodicity of Coulomb diamonds, as visible by the series of four parallel lines running along the V_{sd}-axis. Similarly to SQUID800, there are gate-independent high conductance ridges around $V_{\mathrm{sd}} \approx \pm 1$ meV with the spacing of 4Δ. The left dot does not exhibit a particularly high conductance at zero bias and the superconducting pockets shown in figure 6.16c,d are difficult to see. They are highlighted in the region of the white arrow in figure 6.16c. The right dot shows high conductance at zero bias and the superconducting pockets are larger, as becomes apparent in the highlighted region marked by the white arrow in figure 6.16d. However, the maximum supercurrent does not exceed 100 pA.

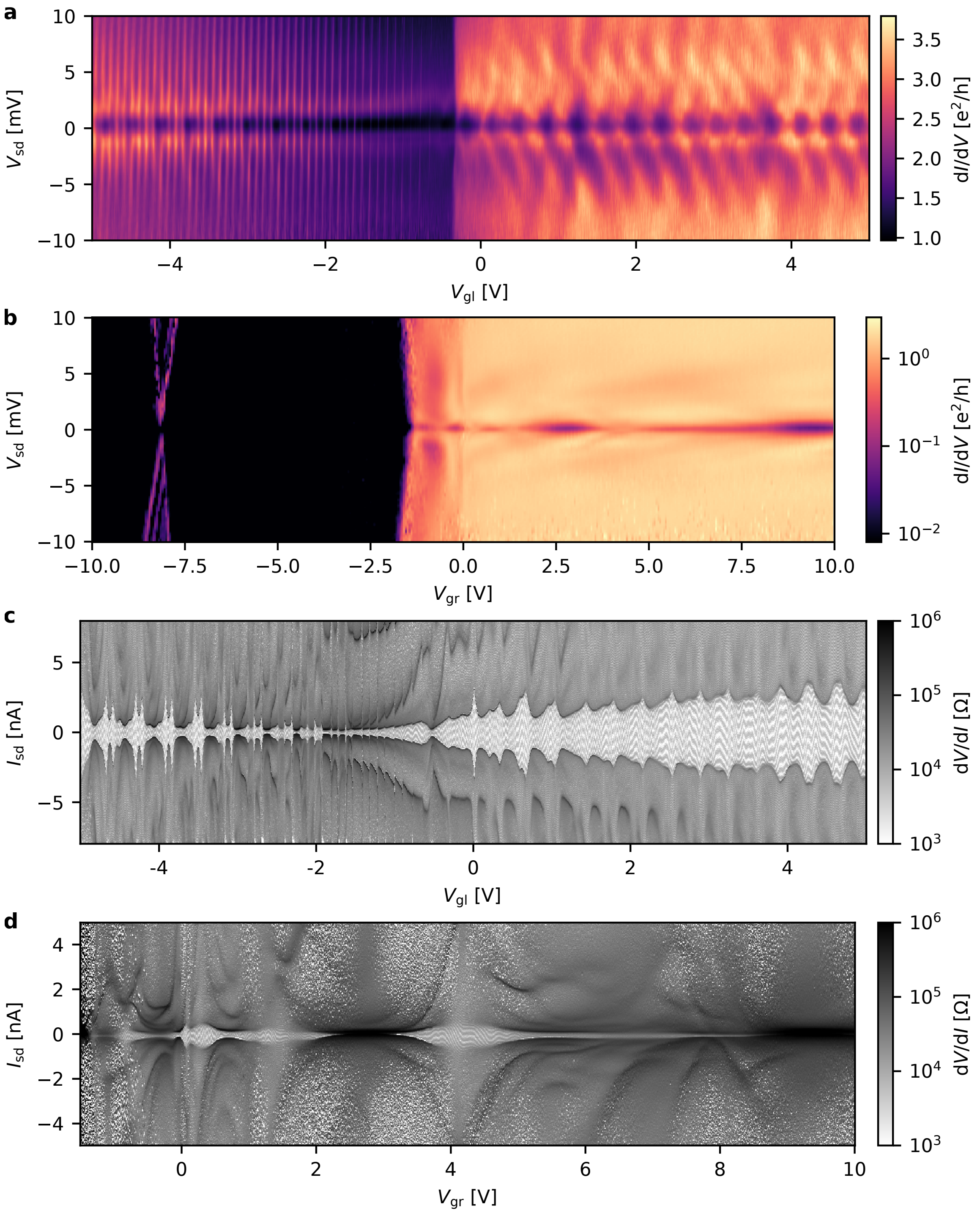

Figure 6.15.: Overview of device SQUID800 from sample SC5. **a** Charge stability diagram of left dot ($V_{gr} = 0\,\mathrm{V}$, not in the off state). **b** Charge stability diagram of right dot ($V_{gl} = -0.4\,\mathrm{V}$, in the off state). Due to a default the right dot is connected to ground with an effective voltage divider of $\sim 1/20$. **c** Differential resistance map of the left dot in current-biased setup ($V_{gr} = 0\,\mathrm{V}$). **d** Differential resistance map of right dot in current-biased setup ($V_{gl} = -0.4\,\mathrm{V}$).

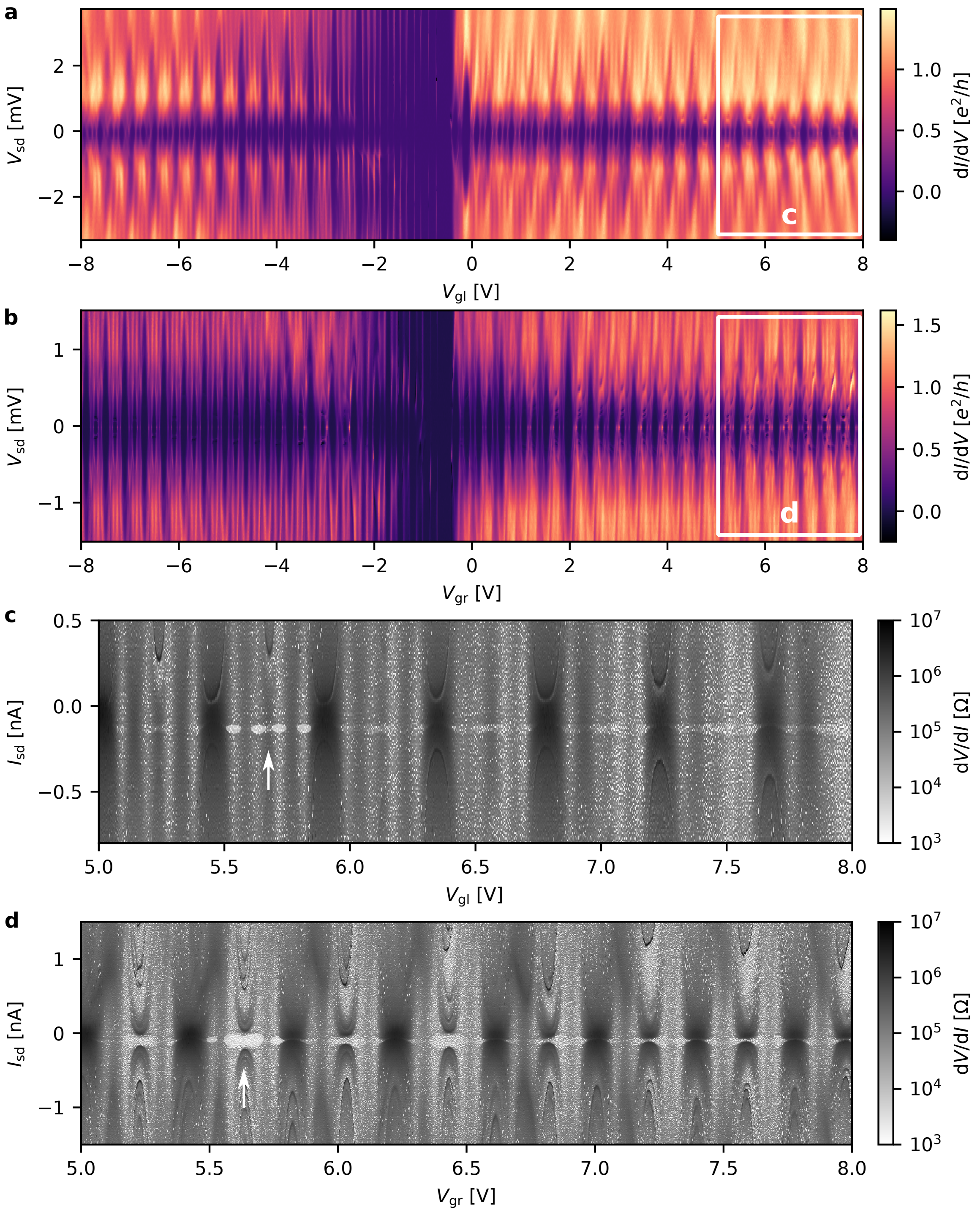

Figure 6.16.: Overview of device SQUID400 from sample SC5. Data taken during the second cooldown. **a**, **b** Charge stability diagrams of left/right dot with the other dot turned off ($V_{gr} = -0.5\,\mathrm{V}/V_{gl} = -0.6\,\mathrm{V}$). **c**, **d** Differential resistance map of left/right dot in current-biased setup with the other dot turned off ($V_{gr} = -0.5\,\mathrm{V}/V_{gl} = -0.6\,\mathrm{V}$). The weak superconducting pockets are highlighted in the regions marked by the arrows.

Overall, the superconductivity in device SQUID400 is significantly weaker than in device SQUID800. A possible explanation could be the lower efficiency of the radiative thermal annealing for 400 nm wide electrodes resulting in a higher device resistance for device SQUID400 already at room temperature (for a comparison see figure 5.17).

6.3.2. Investigation of subgap transport

In this section we present more resolved differential conductance measurements centered in a small bias range around $V_{\mathrm{sd}} = 0$ to explore the subgap conductance features. Below 2Δ one expects to observe high conductance at zero bias for non-resistive supercurrent and multiple Andreev reflections at finite bias. The supercurrent is mediated by Andreev bound states that can also be investigated at finite bias using one electrode as a probe [108]. The subgap spectrum has been analyzed for sample NC5, SQUID800 for the first and second cooldown. In the following, we will focus on the subgap transport measured during the second cooldown, where individual features could be separated more easily.

The conductance measurement zoomed into the low bias range (figure 6.17a) reveals a high conductance at zero bias as expected, but instead of a clean well-distinguishable subgap transport, the expected features are superposed, making a detailed investigation almost impossible. This is likely due to the high tunnel coupling smoothing the van-Hove singularity of the quasiparticle DOS which is used as a probe for multiple Andreev reflections and signatures of Andreev bound states. In the weak coupling regime, the proximity-induced superconducting gap can be identified more easily as indicated in figure 6.17a,b. Under the assumption that the bright ridges in figure 6.17a mark the onset of quasiparticle tunneling and that all conductance features inside the Coulomb diamonds in 6.17b are due to subgap transport, the proximity-induced gap can be estimated to $4\Delta \approx 1.6\,\mathrm{meV}$ which is slightly higher than for samples with palladium contact material. In contrast to a normal metal, where the DOS is constant, a CNT quantum dot has a discrete DOS and the subgap transport can change depending on the location of the chemical potential of the dot. When the energy level of the dot matches the energy of a charge carrier in an Andreev process, the Andreev process is enhanced compared to the off-resonant case. This makes it extremely difficult to identify the individual multiple Andreev reflections or the dispersion of Andreev bound states.

In an attempt to identify possible multiple Andreev reflections, vertical cuts were taken along V_{sd}, as indicated by the white arrows in figure 6.17b,c. At these gate values the conductance is still comparably weak and the quantum dot is in the "on" state since an energy level of the dot is aligned to the drain. Depending on the gate voltage, different multiple Andreev reflections can be identified. The cut at $V_{\mathrm{gl}} = -2.48\,\mathrm{V}$ in figure 6.17d shows two broadened peaks at around $\pm 0.8\,\mathrm{meV}$ which are expected for the location of the induced gap at $eV_{\mathrm{sd}} = 2\Delta$ and in addition, two smaller peaks which would match $eV_{\mathrm{sd}} = 2\Delta/2 = \Delta$ and could correspond to the Andreev reflection of second order $n = 2$. For the gate voltage of $V_{\mathrm{gl}} = 0.075\,\mathrm{V}$ on the electron side, many potential multiple Andreev reflections can be identified, as indicated in figure 6.17e, while the proximity-induced superconducting gap is less pronounced at $eV_{\mathrm{sd}} = 2\Delta$.

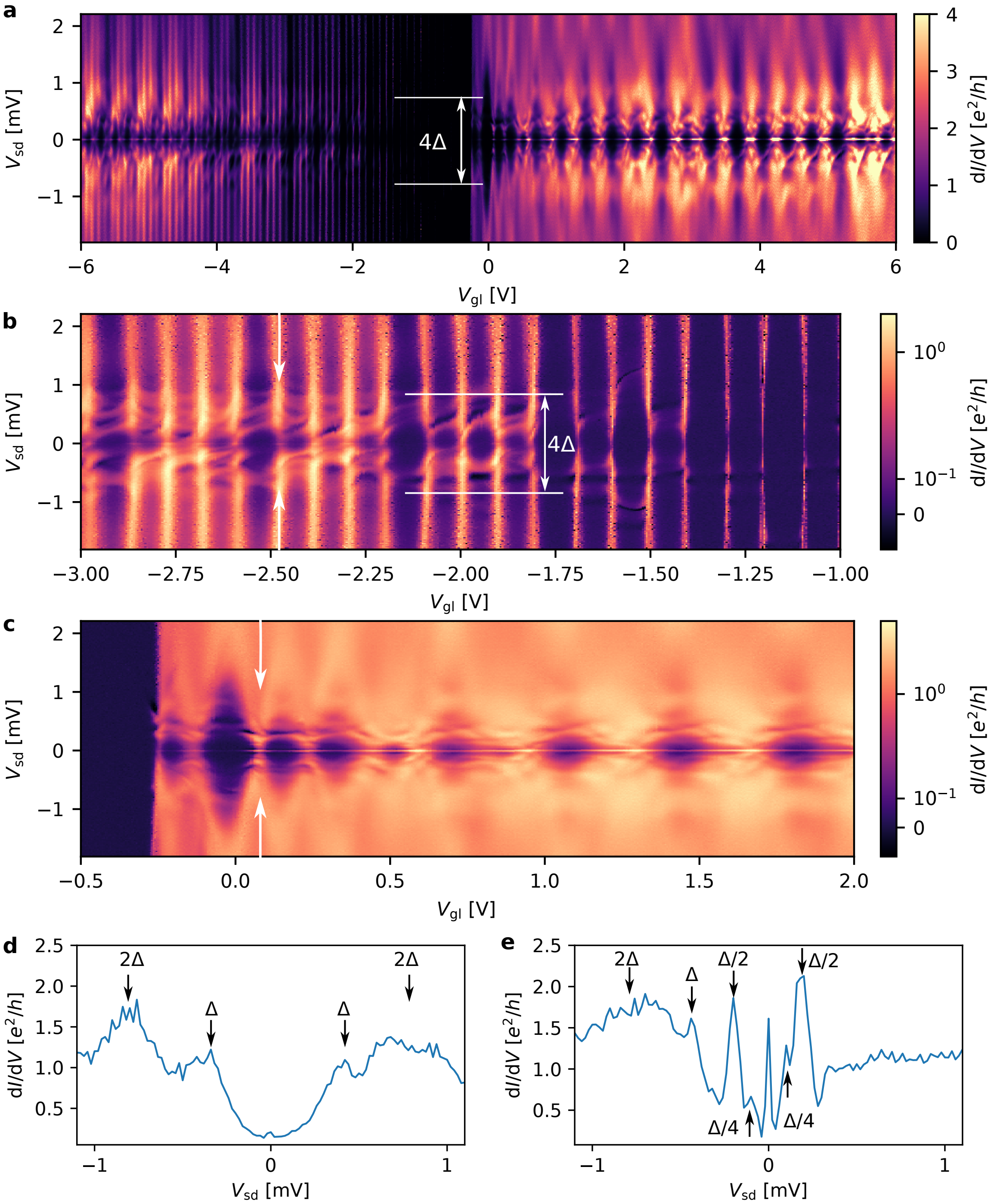

Figure 6.17.: Resolved conductance measurement around $V_{sd} = 0$. Data from device SC5, SQUID800, second cooldown, $V_{gr} = -5$ V. **a** Overview of the differential conductance with adaptation of the colorbar to highlight the subgap features below 4Δ. **b** Zoom into the weak coupling regime in the hole side with indication of the possible proximity-induced superconducting gap 4Δ. **c** Zoom into the stronger conducting electron side. **d** Cut at $V_{gl} = -2.48$ V along the arrows shown in **b**. Potential multiple Andreev reflections are marked by the arrows. **e** Cut at $V_{gl} = 0.075$ V along the arrows shown in **c** with potential MARs.

This could be related to the higher supercurrent for electrons than for holes which is visible as a peak at $V_{\mathrm{sd}} = 0$. In figure 6.17e, there is an asymmetry between positive and negative V_{sd} and for positive bias, the peaks at Δ and 2Δ are absent. The reason for this is unknown and it is crucial to note that even though the peaks in figures 6.17d,e match nicely with the MAR resonances, we do not have any further evidence that these peaks originate from MAR resonances. In general, subgap transport can be complex as it becomes visible for gate voltages different from the two selected in figure 6.17d,e.

6.3.3. Impact of out-of-plane magnetic field on superconductivity

For the operation of a DC-SQUID, it is essential to apply a magnetic field perpendicular to the SQUID loop. The applied magnetic field should only result in a temporary, reversible modification of the supercurrent. However, molybdenum rhenium is a type II superconductor which can host vortices that could be generated by the magnetic field perpendicular to the SQUID loop. Vortices close to the CNT could alter the superconducting properties of the CNT-SQUIDs even when the magnetic field is turned off. Therefore, we will discuss the effect of the magnetic field on supercurrent in the following.

Initially, before any magnetic field was applied, the differential resistance map in figure 6.19a was measured, showing a sharply defined transition from the superconducting to the normal conducting state at a maximum switching current of $I_{\mathrm{sw}} \gtrsim 3\,\mathrm{nA}$. After ramping the out-of-plane magnetic field to $B_y = 200\,\mathrm{mT}$ and returning to $B_y = 0$ the supercurrent has completely vanished.

The disappearance of superconducting transport through the CNT could be due to some residual magnetic field in the superconductor caused by vortices close to the CNT or due to a global change of the tunnel coupling caused by a contact deterioration. A global change of conductance was excluded by measuring the differential conductance and sweeping V_{sd} above the superconducting gap (cf. figure 6.18). The differential conductance above the superconducting gap is unchanged in contrast to the subgap conductance which implies that only the superconducting transport properties have been affected.

Aiming to restore superconductivity, two different approaches have been tested. The first approach was current annealing of the CNT which was performed at a high current of $18.5\,\mu\mathrm{A}$ for 90 min. Figure 6.19b shows the differential resistance after current annealing in the cryostat. Superconducting pockets reemerge but with a much lower switching current of only 1 nA. In addition, the transition from the superconducting state to the normal conducting state is broadened whenever the switching current is high. This reminds us of the transport through the left dot of the SQUID of the first superconducting sample SC1 which was in the overdamped regime. A possible explanation for the observed phenomena could be the creation of vortices in molybdenum rhenium by an out-of-plane magnetic field which remain when the magnetic field is turned off. Some of the vortices could form close to the CNT impacting the superconducting transport. By driving a high current through the CNT, the vortices could move in the superconducting film, with the result of

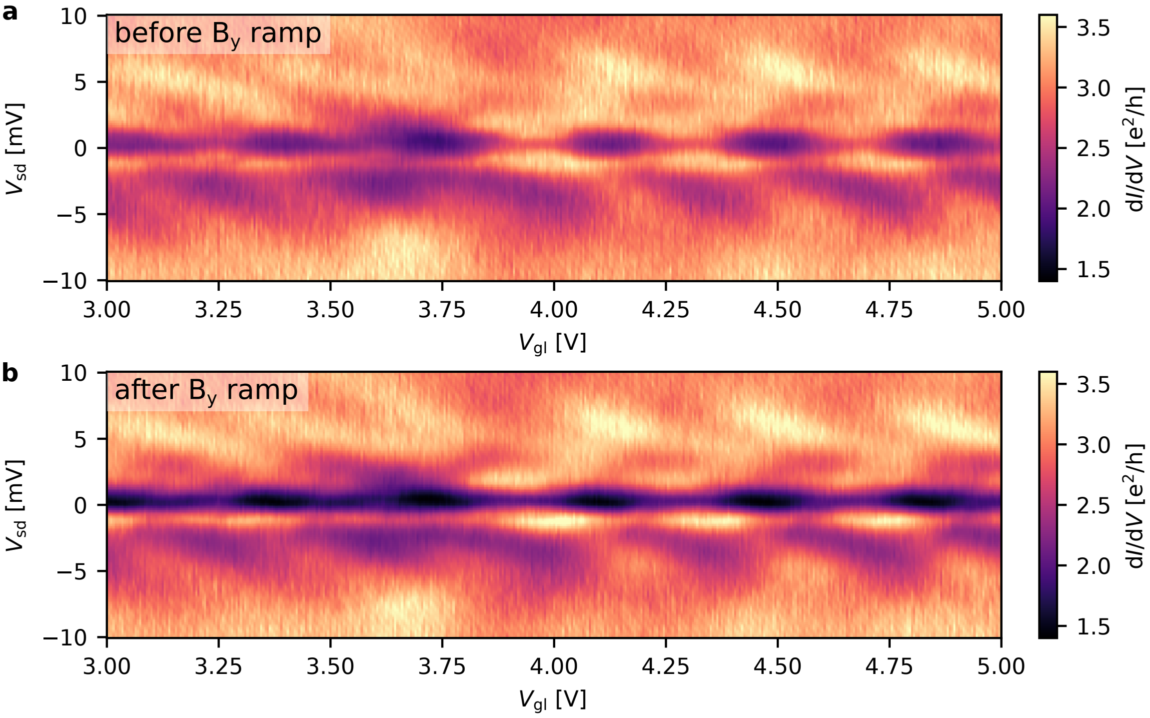

Figure 6.18.: Differential conductance before and after out-of-plane magnetic field application. Data from device SC5 SQUID800, $B_\perp = B_y$, $V_{gr} = 0\,\mathrm{V}$ **a** Before magnetic field application. **b** After ramping the out-of-plane magnetic field to $B_y = 200\,\mathrm{mT}$ and back to zero.

a reduction of vortices in the vicinity of the CNT metal contact and a partial restoration of the supercurrent.

A natural option to remove the vortices could be heating beyond the critical temperature of the superconducting molybdenum rhenium film at ~ 10 K. Due to potential contamination of the CNT during heating, this option was discarded. A second approach, which does not require a temperature increase, relies on affecting the vortices by magnetic field ramps. By periodically ramping up and down the out-of-plane magnetic field while slowly converging to zero, as shown in figure 6.19d, a high switching current could be restored. Likewise, the sharp transition between the superconducting and resistive state as shown in figure 6.19c could be reproduced, although the shape and size of the superconducting pockets remained partially modified. The exact physical mechanism is unknown, but one could think of averaging the residual flux generated by the vortices to zero. Under the application of a magnetic field, the majority of the flux through the vortices aligns with the magnetic field direction. By periodically ramping up and down the out-of-plane magnetic field while slowly converging to zero as shown in figure 6.19d the net flux of the vortices could be averaged to zero.

For a further investigation of the effects occurring during the magnetic field ramps, the switching current has been recorded in detail for another measurement shown in figure 6.19e. Instead of a smooth change of the switching current, several abrupt jumps become visible, which can lead to a higher or lower switching current.

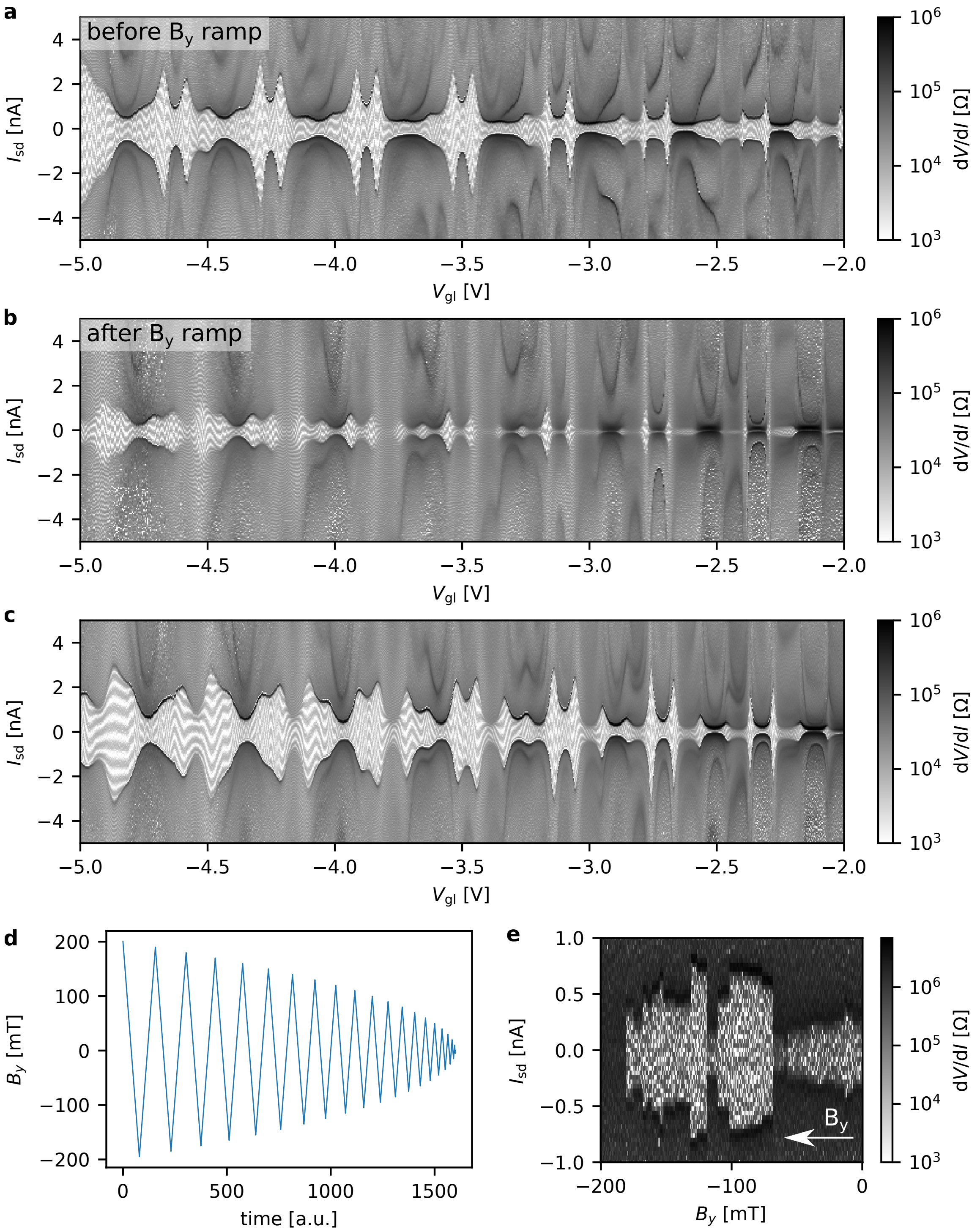

Figure 6.19.: Investigation of out-of-plane magnetic field dependence. Data from device SC5 SQUID800, $B_\perp = B_y$, $V_{\mathrm{gr}} = 0\,\mathrm{V}$. **a** Differential resistance before magnetic field application. **b** After magnetic field ramps to $B_y = 200\,\mathrm{mT}$ and current annealing of the CNT. Part of the supercurrent is restored. **c** Differential resistance after periodically ramping the magnetic field as in **d**. **d** Ramping of magnetic field converging to zero ("demagnetization sweep"). **e** Change of switching current when ramping the magnetic field.

This highlights that the generation of vortices in the vicinity of the CNT is difficult to control. The most efficient way to avoid the creation of vortices is to apply only weak out-of-plane magnetic fields when possible. For this reason, only the SQUID800 has been investigated in detail with respect to a high out-of-plane magnetic field. It is unclear if the effects mentioned in this subsection apply only to electrodes with large widths or if electrodes of standard width of 400 nm show a similar reduction of superconductivity when a high out-of-plane magnetic field is applied.

6.3.4. SQUID measurements

Having investigated the impact of the out-of-plane magnetic field on the switching current of a single junction, this subsection presents SQUID measurements where the two parallel junctions of the DC-SQUID are turned in the "on" state to enable a current to flow through the superconducting loop. SQUID measurements have been performed on three of the five superconducting samples. Here, we present the measurements performed on SQUID800 of sample SC5, which featured the highest supercurrent and a sharp transition between the superconducting state and the normal conducting state. A well-defined switching current is essential if the switching current is measured as a function of the external magnetic field or flux penetrating the SQUID loop, respectively. The theory of SQUIDs has been described in chapter 2.4.6, and we recall the dependence of the critical current and the lower experimentally observed switching current as a function of the external flux from eq. 2.79 (including a possible flux offset Φ_{off})

$$I_{\text{sw}} = \sqrt{(I_{\text{sw1}} - I_{\text{sw2}})^2 + 4 I_{\text{sw1}} I_{\text{sw2}} \cos^2(\pi(\Phi_{\text{ext}} - \Phi_{\text{off}})/\Phi_0)}. \tag{6.2}$$

Since for this device, the Josephson junctions operate in the underdamped, hysteretic regime, both trace and retrace measurements are shown as a function of the out-of-plane magnetic field B_y in figure 6.20a,b. Both differential resistance measurements show clear periodic SQUID oscillations with magnetic field. The oscillations of the switching current are in good agreement with the theoretical prediction from eq. 6.2 as indicated by the red curve in figure 6.20a. For the selected gate tuning point ($V_{\text{gl}} = -7.8\,\text{V}$, $V_{\text{gr}} = 5\,\text{V}$), a switching current of $I_{\text{sw1}} = 0.96\,\text{nA}$ can be extracted for the left dot and $I_{\text{sw2}} = 0.46\,\text{nA}$ for the right dot.

The periodicity of the SQUID oscillations is determined by the flux quantum $\Phi_0 = B_y \cdot A$ and allows us to calculate the SQUID area A. One can extract a periodicity of $\Phi_0/A = 0.465\,\text{mT}$ and an offset of $\Phi_{\text{off}}/A = -0.097\,\text{mT}$, which could, for example, originate from an offset of the coils, the magnets of the shutters from the thermal radiation shields, or partially from the earth's magnetic field ($B = 40\,\mu\text{T}$). From other SQUID measurements we know that the actual magnetic field at the position of the SQUID is lower than the externally applied magnetic field due to some misalignment of the y-coil with the CNT position. Unfortunately, the SQUID area could not be verified by SEM since the sample is still measured when this chapter is written.

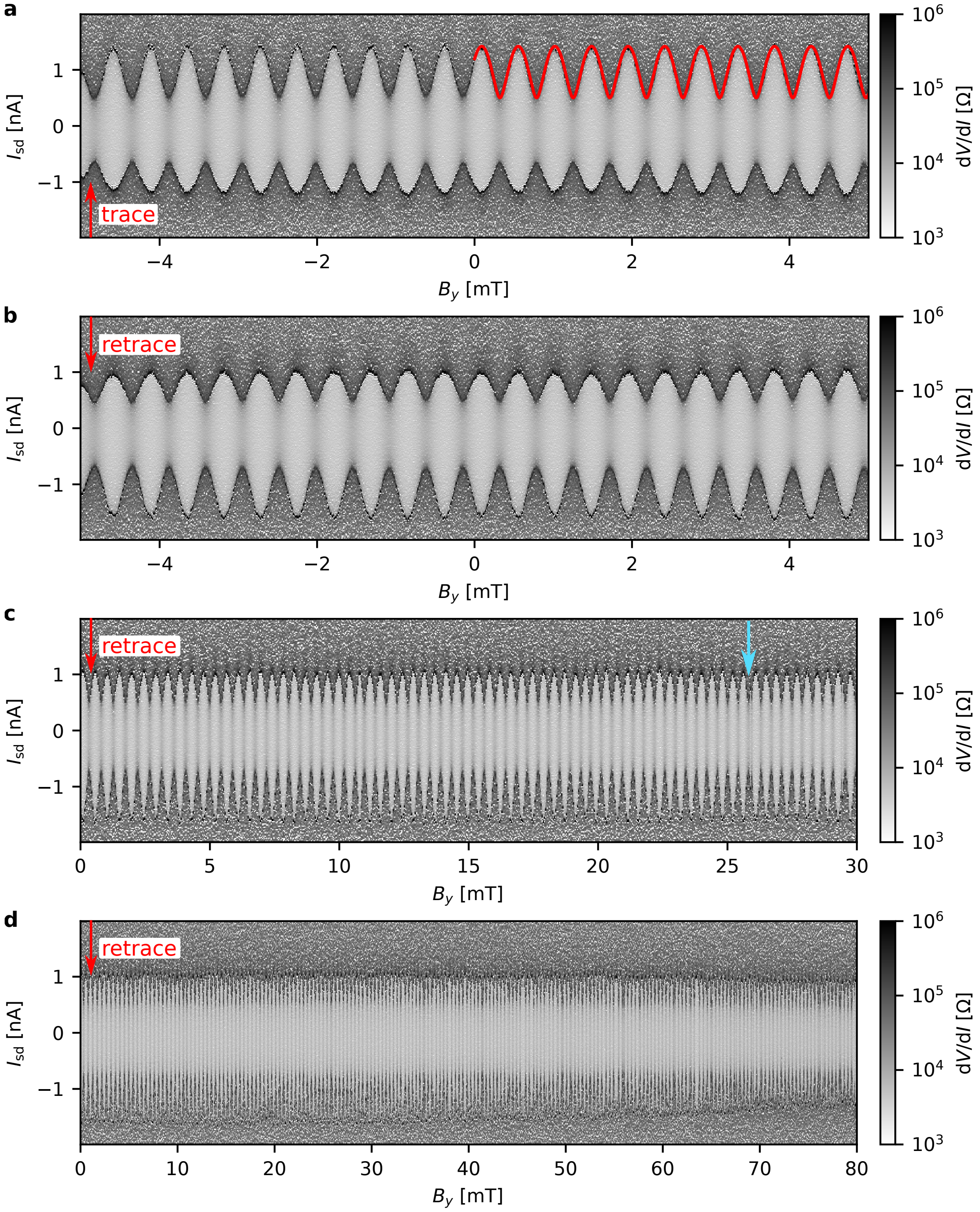

Figure 6.20.: SQUID measurements. Data from device SC5, SQUID800 at $V_{gl} = -7.8$ V, $V_{gr} = 5$ V. **a** Trace (sweeping the current from - to +). The red curve shows the theoretical prediction from equation 6.2 with $I_{sw1} = 0.96$ nA, $I_{sw2} = 0.46$ nA, field to flux conversion of Φ_0[Vs] = 0.465[mT]/A and a flux offset of −0.097[mT]/A with the SQUID area A. **b** Retrace (sweeping the current from + to -). **c** Retrace for larger magnetic field range. The first flux jump occurs at 26 mT (blue arrow). **d** Retrace for extended magnetic field range. The amplitude of the oscillation does not decrease significantly up to 80 mT but there are more magnetic flux jumps.

Taking into account the correction factor of $B_y^{\mathrm{corr}} = 0.529 B_y^{\mathrm{applied}}$ from another SQUID measurement of a previous device, the SQUID area can be estimated to $A = 8.1\,\mu\mathrm{m}^2$. With a lateral dimension of 2.6 µm this would correspond to a CNT position of 3.1 µm measured from the center of the splitting of the source electrode, which seems plausible.

Larger magnetic field ranges are shown in figure 6.20c,d. The SQUID oscillations persist at least up to 80 mT without a significant decrease in the maximum switching current which is due to the strong proximity-induced superconductivity by molybdenum rhenium. This magnetic field range is much higher than reported in [32] for aluminum as a source of superconductivity where a decay is already visible for the second SQUID oscillation at few mT. However, with respect to the vortex discussion in the last subsection, starting from 26 mT, the periodicity is partially broken by irregular jumps in flux. Such flux jumps by non-integer values of Φ_0 could be due to vortex creation or vortex motion in the vicinity of the CNT-SQUID.

6.3.5. Measurements of Shapiro steps

The operation of the device from sample SC1 in the overdamped junction regime is ideal for the observation of non-hysteretic Shapiro steps. The corresponding theory has been treated in chapter 2.4.5. We only probe the transport through the left dot in these measurements, while the right dot is turned "off" ($V_{\mathrm{gr}} = -1\,\mathrm{V}$). To be able to observe the switching current, the voltage of the left gate was tuned to $V_{\mathrm{gl}} = 1.3\,\mathrm{V}$ in the superconducting pocket that shows the sharpest transition from the superconducting to the normal conducting state (cf. figure 6.21a). The external microwaves were applied via the left gate electrode locally below the suspended CNT and a power dependence at different microwave frequencies was measured, shown in figure 6.21b-f.

For weak RF drive power V_{AC}, the switching current is constant and the current plateau of the zeroth Shapiro step coincides with the switching current. The power dependence is determined by the Bessel functions drawn in figure 2.24. The argument of the Bessel functions is $2eV_{\mathrm{AC}}/(\hbar\omega_{\mathrm{AC}})$, and therefore, with higher RF power, the contribution of higher-order Shapiro steps increases. By increasing the frequency from 2 to 6 GHz, as shown in figure 6.21b-f, the argument of the Bessel functions is reduced. As a result, the higher-order Shapiro steps are observed at a higher RF drive power for higher RF frequencies, as visible in figure 6.21b-f.

The height of a voltage step is given by $V_{\mathrm{DC}} = \hbar\omega_{\mathrm{AC}}/2e$, and thus the voltage steps do not depend on the RF drive power but only on the RF frequency. Therefore, it is expected that the measured voltage drop across the junction increases with higher frequency ω_{AC}. In the differential resistance measurements, this results in a higher differential resistance and a higher contrast of the voltage steps, as is visible in figure 6.21b-f. Overall, our measurements are qualitatively consistent with [115] and the theory explained in chapter 2.4.5.

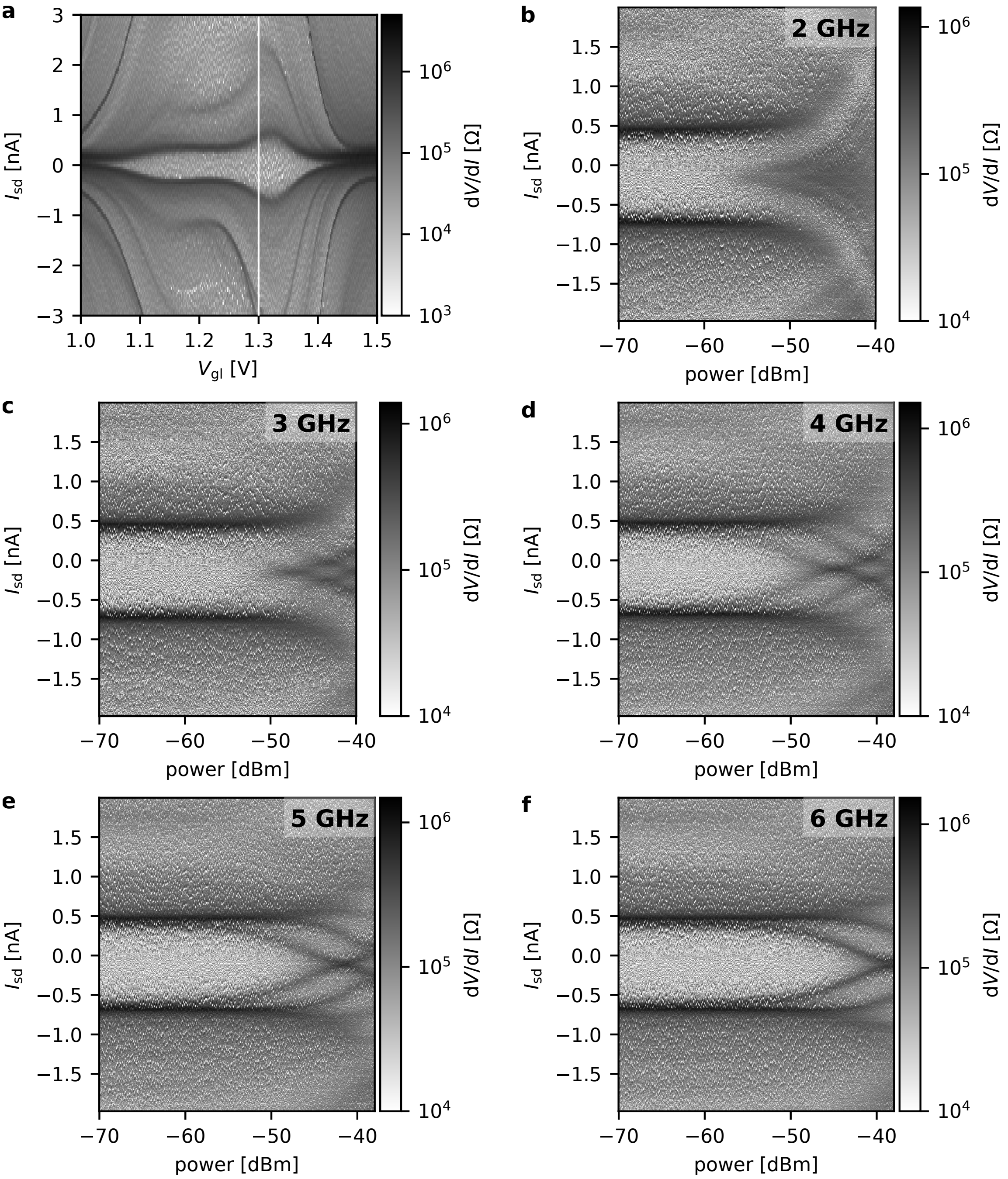

Figure 6.21.: Shapiro step measurements on device SC1. a Tuning point for measurements ($V_{gl} = 1.3$ V, right dot off: $V_{gr} = -1$ V). **b**-**f** Power dependence of the switching current for different RF drive frequencies applied to the left gate.

6.3.6. Impact of air exposure on electronic transport

For future experiments, single-molecule magnets might be evaporated on CNT-SQUIDs. Evaporation is a non-deterministic method that requires a warmup of the samples for each evaporation and possibly a few iterations to find a molecule that adsorbs on the CNT and couples strongly to the flux through the SQUID loop. Therefore, in order to be able to recycle CNT-SQUIDs, it is crucial to check if their transport properties are affected by warmups and if they can be restored for a next cooldown. Two of the five superconducting samples (SC1 and SC5) have been warmed up after the first measurements and cooled down again. For the warmup, they have been transferred into the transfer arm, exposed to helium gas, and heated with a heat gun before exposure to air.

The differential conductance of sample SC1 during the first cooldown and during the second cooldown after current annealing is shown in figure 6.22. In the second cooldown, the Fabry-Pérot oscillations have disappeared, the band gap position and size are modified, and the conductance of electron and hole transport becomes comparable. The shift in the band gap can be explained by p-doping of the CNT due to oxygen adsorption [216] during air exposure, as also discussed in chapter 5.4.4, while the ratio of electron and hole conduction could be related to a modification of the workfunction of the contacts or CNT during air exposure. The modification in the size of the band gap could be due to a change in the gate lever arm. However, as can be seen in the negative gate voltage range, the gate lever arm has not changed. Another option could be a strain-induced modification of the CNT band gap. A current annealing in the cryostat could not restore the original position of the band gap. Nonetheless, we could measure supercurrent in the device from sample SC1 during the second cooldown.

The situation is fundamentally different for the SQUID800 from sample SC5 shown in figure 6.22. Between the two cooldowns, a current-induced annealing was performed in the scanning electron microscope, followed by radiative thermal annealing, as detailed in chapter 5.4.4. At the end of the annealing process, the device recovered the characteristic room-temperature gate voltage dependence of our nanoassembled devices with higher electron than hole conductance. After vacuum transfer, in the second cooldown, the Fabry-Pérot oscillations could not be recovered, but the electron conductance remains higher than the hole conductance. In both measurements zero-bias conductance peaks can be distinguished, indicating supercurrent. The size of the narrow gap E_{G}^{*} has decreased, which could be strain-induced. The center of the gap does not change between the two measurements, which indicates that there is no difference in doping. The measurement in figure 6.22 even shows an earlier onset of fourfold periodicity close to the band gap, a sign of high cleanliness. Overall, we can conclude that the impact of air exposure on electronic transport (doping and modification of the CNT or metal workfunction) is reversible. The low-temperature transport properties can be restored by using the full annealing process in the SEM (in particular, the radiative thermal annealing) and the vacuum sample transfer, allowing the potential recycling of CNT-SQUIDs.

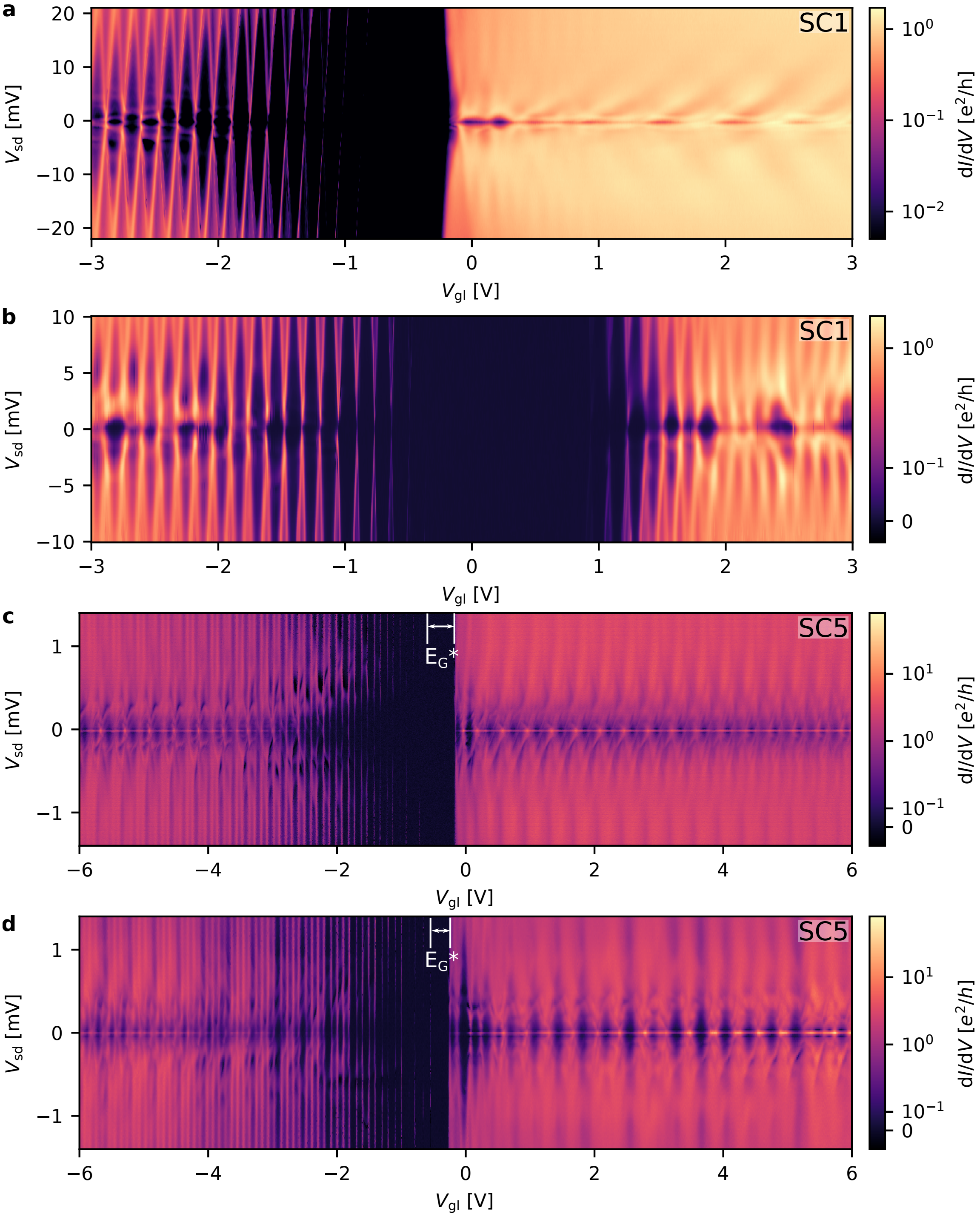

Figure 6.22.: Impact of air exposure on electronic transport and reset with RTA. a First cooldown of sample SC1 (left dot). **b** Second cooldown of sample SC1 after air exposure and storage in a vacuum flow box ($p \sim$ 1mbar) for about a month. Device cooled down without RTA and measured after performing a current annealing at 40 mK in the cryostat at 14 µA. **c** First cooldown of device SC5 SQUID800 (left dot). The width of the zeroth diamond is indicated by E^*_G/e and is proportional to the band gap. The value E^*_G is neither corrected by E_C nor ΔE and neglects the lever arm which is unchanged in the two measurements. **c** Second cooldown after air exposure for one hour and full annealing process in SEM (current-induced annealing and radiative thermal annealing for 45 min at 5.6 W and 60 min at 11 W). Measured without current annealing in the cryostat.

6.4. Nanomechanics of proximitized superconducting CNT quantum dots

Nanoassembled CNT devices have the benefit that the CNT is directly suspended and the coupling between the mechanical degrees of freedom and the electronic transport can be studied. In this thesis, we investigated the nanomechanics by exciting motion in the CNT with a local gate electrode (sample SC1) or a wirebond RF antenna bonded over the circuit chip (sample SC5, SQUID400). As explained in chapter 2.3, in this configuration the highest coupling to the AC electric field is expected for transverse bending modes.

6.4.1. Basic characterization of the nanomechanics of the device from sample SC1

The electronic transport of the device from sample SC1 has been shown in figure 6.12 as a reference. As explained in chapter 2.3, mechanical resonances are detected via current rectification. This technique requires a non-zero local curvature of the differential conductance $\mathrm{d}I/\mathrm{d}V$ or of the current I. For this reason, a gate voltage with maximum curvature is targeted when searching for mechanical resonances which is typically found on the slope of a Coulomb diamond.

The device showed many resonances in the Coulomb blockade regime which have been tracked at different Coulomb diamonds for a bias voltage beyond the superconducting gap. A frequency sweep at $V_{\mathrm{gl}} = -2.87\,\mathrm{V}$ reveals all different resonances marked by the arrows in figure 6.23a. Mechanical resonances can be distinguished from other resonances by their bifurcating Duffing oscillator lineshape already at low power owing to the high mechanical nonlinearity of CNT bending modes. The two broad resonances between 250 MHz and 300 MHz do not exhibit a bifurcation and are not due to mechanical origin and probably electrical resonances related to the setup. In total, we could identify seven distinct mechanical resonances up to 800 MHz. In figure 6.23b the gate voltage dependence of the resonance frequencies is shown. For positive gate voltage in the Fabry-Pérot regime, measurements were performed at $V_{\mathrm{sd}} = 0$ where the strongest conductance modulations occurred. Some resonances can only be tracked within a limited range of gate voltages, whereas two resonances are well coupled to electronic transport and could be tracked over a wide range of gate voltage and also in the Fabry-Pérot regime for positive gate voltage.

The two resonances are close in frequency and probably due to different polarizations of the fundamental transverse bending mode. Similarly to [217], it could be possible that these modes are the fundamental modes for in-plane oscillation like a swing (S-mode, blue) and out-of-plane oscillation like a trampoline (T-mode, red), as shown in figure 6.23b. The S-mode also exhibits partial out-of-plane motion and is not completely orthogonal to the T-mode. This is crucial for its detection by current rectification, which is based on modulation of the gate capacitance. The two resonances follow a quadratic gate voltage dependence, as expected for transverse bending modes in the bending limit.

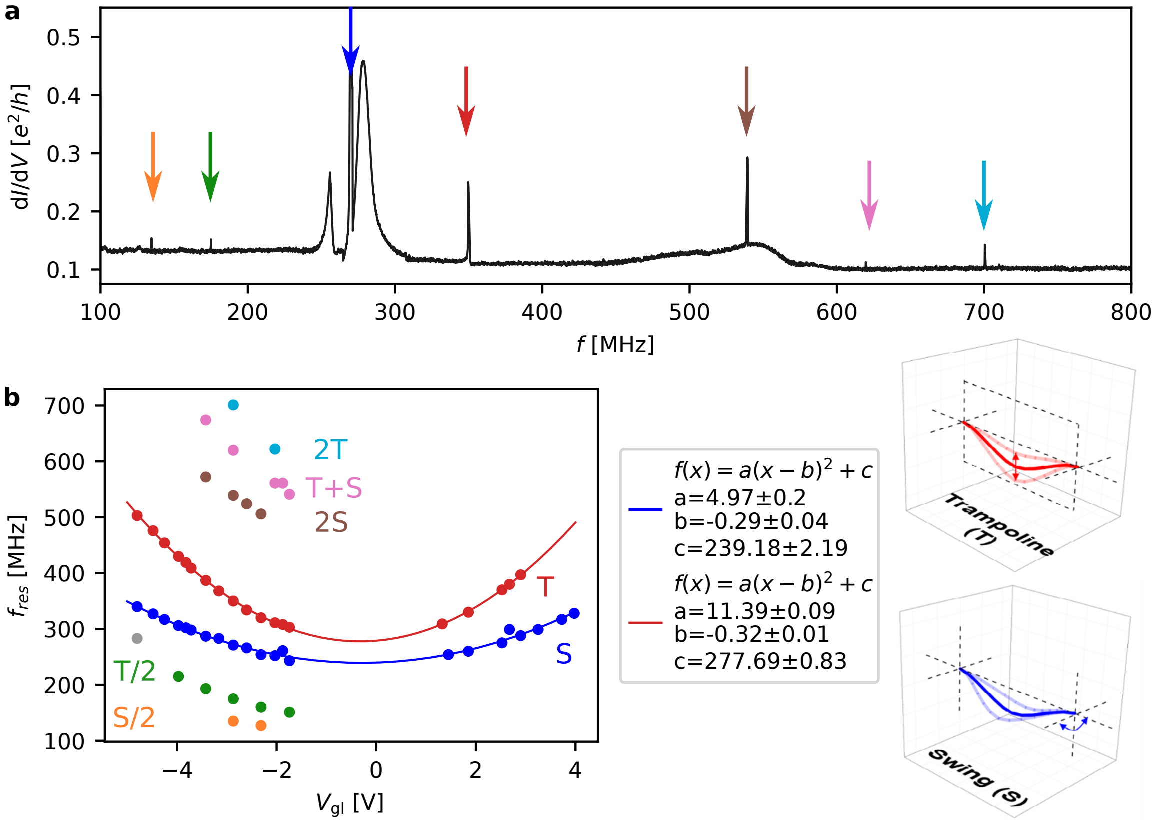

Figure 6.23.: Overview of mechanical resonances for the device from SC1. RF at power $P = -50\,\mathrm{dBm}$ applied at the left gate, $V_{gr} = -1\,\mathrm{V}$, $V_{sd} = -1.5\,\mathrm{mV}$. **a** At $V_{gl} = -2.87\,\mathrm{V}$ seven distinct bifurcating mechanical resonances could be detected. **b** Tracking of resonances over a large gate voltage range including quadratic fit for two resonances, which are probably the trampoline (T) and swing mode (S) as illustrated (subfigure from [217]). Modes matching combinations and fractions of T and S modes are indicated. The grey data points do not match any of the modes.

The center of the parabolas is not located at $V_{gl} = 0\,\mathrm{V}$, but matches the center of the band gap where the tension in the CNT is minimum. The gate-induced tension breaks the symmetry between in-plane and out-of-plane polarization, and thus affects the S- and T-mode differently, which can explain the different slopes of the parabolas.

The other five mechanical modes are also consistent with this hypothesis. The three modes higher in frequency denoted 2T, T+S and 2S match the corresponding linear combinations of the T- and S-mode. These linear combinations (subharmonic resonances) can be actuated when a quadratic nonlinearity occurs in the equation of motion [218]. Lastly, the two low-frequency modes T/2 and S/2 will be addressed. The resonances occur at exactly half the frequency of the T- or S-mode and show a much weaker peak in the differential conductance (cf. figure 6.23a). The origin of these superharmonic resonances could be related to two-phonon driving enabled by the quadratic nonlinearity [218].

The resonances can also be monitored along a single Coulomb peak, and a spring softening dip is expected (cf. chapter 2.3). This softening is visible for many Coulomb diamonds in figure 6.24a and shown for a single diamond in figure 6.24b. The measurements are

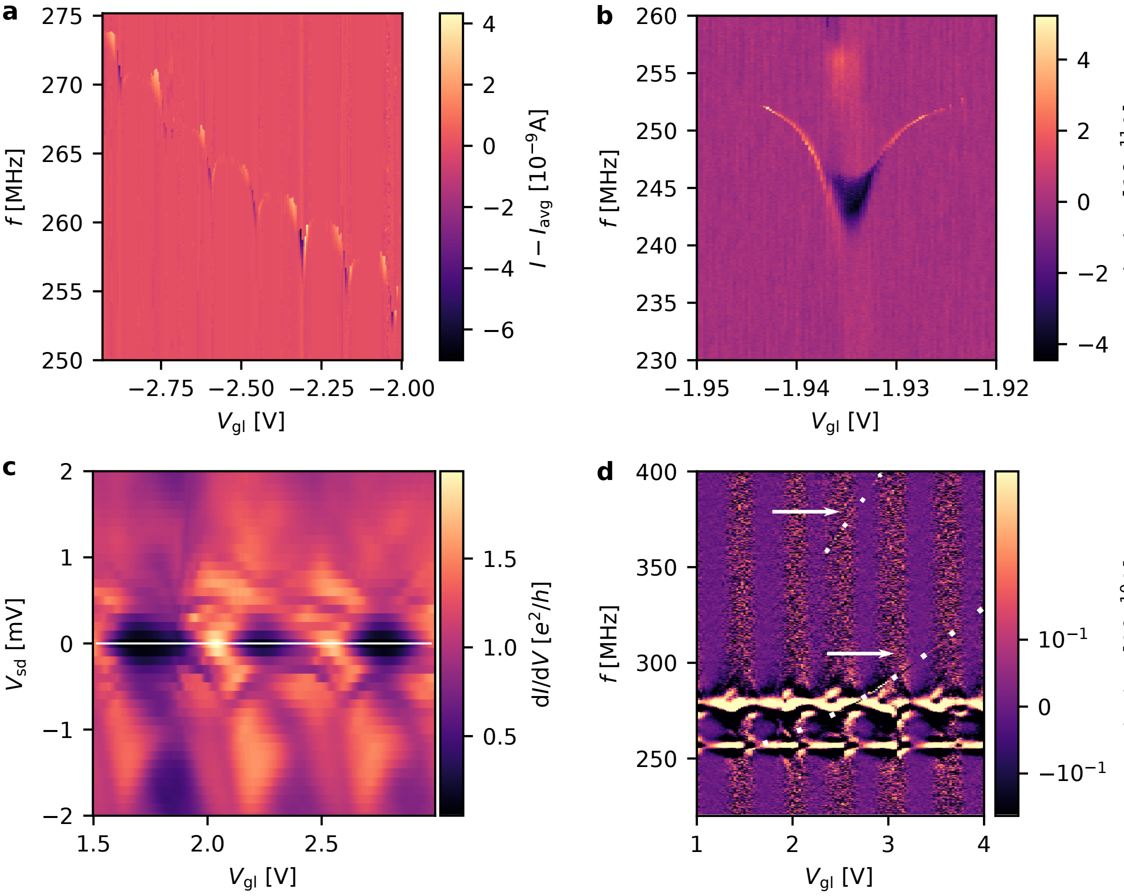

Figure 6.24.: Gate voltage dependence of mechanical resonances for the device from SC1. Average current has been subtracted, RF applied at power $P = -50$ dBm at the left gate, $V_{gr} = -1$ V. **a** Tracking of resonances in the Coulomb blockade regime with clearly visible softening of the spring constant at each diamond ($V_{sd} = 5.5$ mV). **b** Softening of the spring constant for a single Coulomb diamond with clearly visible sign change of the Duffing parameter α. **c** Tuning point $V_{sd} = 0$ V with highest conductance modulation for the measurement in **d**. **d** Tracking of mechanical resonances in the Fabry-Pérot regime, with the two resonances highlighted by the arrows and white dots.

consistent with the measurement in [11] shown in figure 2.14 and also exhibit a change of sign at the inflection points of the Coulomb peak which is related to a change of sign of the Duffing parameter α.

In the Fabry-Pérot regime, the curvature $\partial^2 I/\partial V_g^2$ is much weaker compared to the Coulomb blockade regime, which naturally makes it difficult to detect mechanical resonances with rectification. However, the subgap conductance features shown in figure 6.24c exhibit a strong conductance modulation with gate voltage. Two resonances can be identified in figure 6.24d at $V_{sd} = 0$ V, marked by the white line in figure 6.24c, where the highest modulation with gate voltage and the strongest rectification signal could be reached. The bright features at 260 MHz and 280 MHz are due to the parasitic broad resonances which are also visible in figure 6.23a. Since these bright conductance peaks at zero bias are due to supercurrent, this implies that the rectification of supercurrent has been used in this measurement.

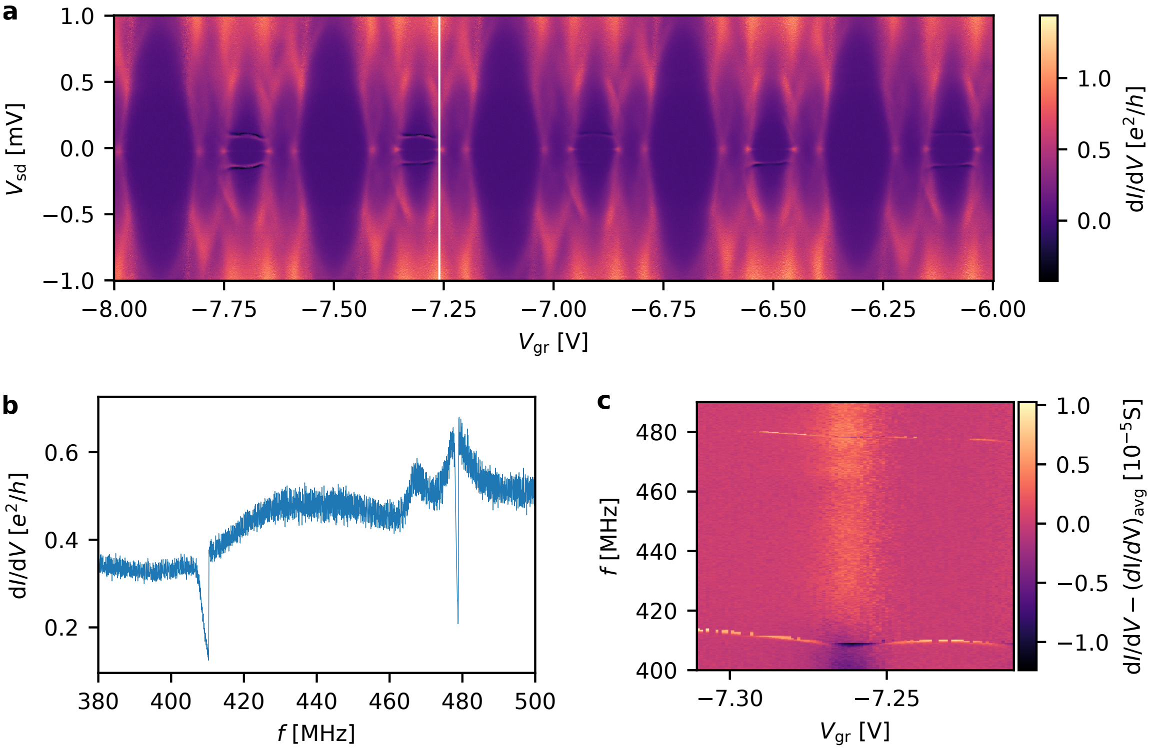

Figure 6.25.: Overview of mechanical resonances for SQUID400 from sample SC5. Data taken during the second cooldown with the left dot off ($V_{gl} = -0.6$ V), RF power $P = -50$ dBm. **a** Charge stability diagram with gate tuning point for the further measurements. **b** Frequency dependence of the mechanical resonances showing two resonances at 410 MHz and 480 MHz ($V_{gr} = -7.27$ V, $V_{sd} = 0$ V). **c** Gate voltage dependence of the mechanical resonances showing weak softening of the spring constant ($V_{sd} = 0$ V).

6.4.2. Basic characterization of the nanomechanics of device SQUID400 from sample SC5

A similar mechanical characterization to the device from SC1 has also been carried out on the SQUID400 of sample SC5 during the second cooldown. Figure 6.25a shows the gate voltage selected for the mechanical resonance measurements in figure 6.25b,c where pronounced dips in the differential conductance occur for two resonances around 410 MHz and 480 MHz. Similarly to the device from SC1, these two resonances are close in frequency and could be the swing and trampoline mode. The softening of the spring constant over a small gate voltage range is shown in figure 6.25c providing further evidence that these bifurcating resonances are of mechanical origin. In analogy to the detection in the Fabry-Pérot regime for the device on SC1, we also rely on the rectification of supercurrent at the zero bias peak for the detection of the mechanical resonance since this is the feature with highest contrast in figure 6.25a.

6.4.3. Investigation of the interplay between nanomechanics and superconductivity

The fact that current rectification was successful in the detection of mechanical resonances at zero bias already points towards an interplay between nanomechanics and superconducting transport in suspended CNTs. In order to obtain a better understanding, current-biased measurements need to be performed while applying microwaves at the mechanical resonance. In this subsection, we will address these measurements, which have been performed on the right dot of SQUID400 from sample SC5. This section aims to provide an overview of the preliminary results.

A particularly intriguing gate voltage region for the resonance measurements was found around $V_{\mathrm{gr}} = -7.7\,\mathrm{V}$ and $V_{\mathrm{gr}} = -7.3\,\mathrm{V}$, as shown in figure 6.26. The maximum supercurrent at this gate voltage is rather low at around 50-100 pA. However, there exists an unexpected region with particularly low differential resistance. Instead of highly resistive plateaus, irregular regions with a differential resistance close to zero can be observed, similar to the superconducting pockets. The origin of these plateaus is unclear, but they resemble the mechanical bistabilities observed in the device from sample NC2 (cf. section 6.2.2). The plateaus depend on the sweep direction of the current bias and occur only at a positive current bias for the trace and at a negative current bias for the retrace. Taking a look at the differential conductance in figure 6.25a, it becomes apparent that these regions seem to coincide with the two parallel cotunneling lines on the second diamond. These cotunneling lines are accompanied by high negative differential conductance. Cotunneling lines with negative differential conductance have been observed in [101] for the first diamond with only a single electron in a shell and are attributed to the interaction between the spin and the superconducting leads [219]. Here for the second diamond, the situation is difficult to explain as the two spins can interact with each other and couple both to the leads.

As discussed, the low resistive plateaus for trace and retrace in figure 6.26 occur only for one bias polarity. Comparing the current-biased measurements with figure 6.25a, it seems that a requirement for the observation of low resistive plateaus is a transition from high positive differential conductance to negative differential conductance when the bias voltage is swept across a cotunneling line. This is supported by the absence of low resistive plateaus for $V_{\mathrm{gr}} = -6.5\,\mathrm{V}$ where negative differential conductance is also absent for positive bias in figure 6.25a.

For an investigation of the interplay between superconductivity and nanomechanics, an RF drive was applied via the wire bond antenna around the resonance frequency of 479 MHz, as shown in figure 6.27. Figure 6.27c,d shows a zoom in the low current range to visualize the superconducting pocket. The RF drive has little effect except close to the resonance. At resonance, the superconducting pocket widens for both trace and retrace, as expected. The switching current depends on the gate voltage and the gate capacitance is modulated when the CNT oscillates. At the selected gate tuning point with finite curvature, the increase in switching current can be explained by current rectification similar to the current in the voltage-biased measurements.

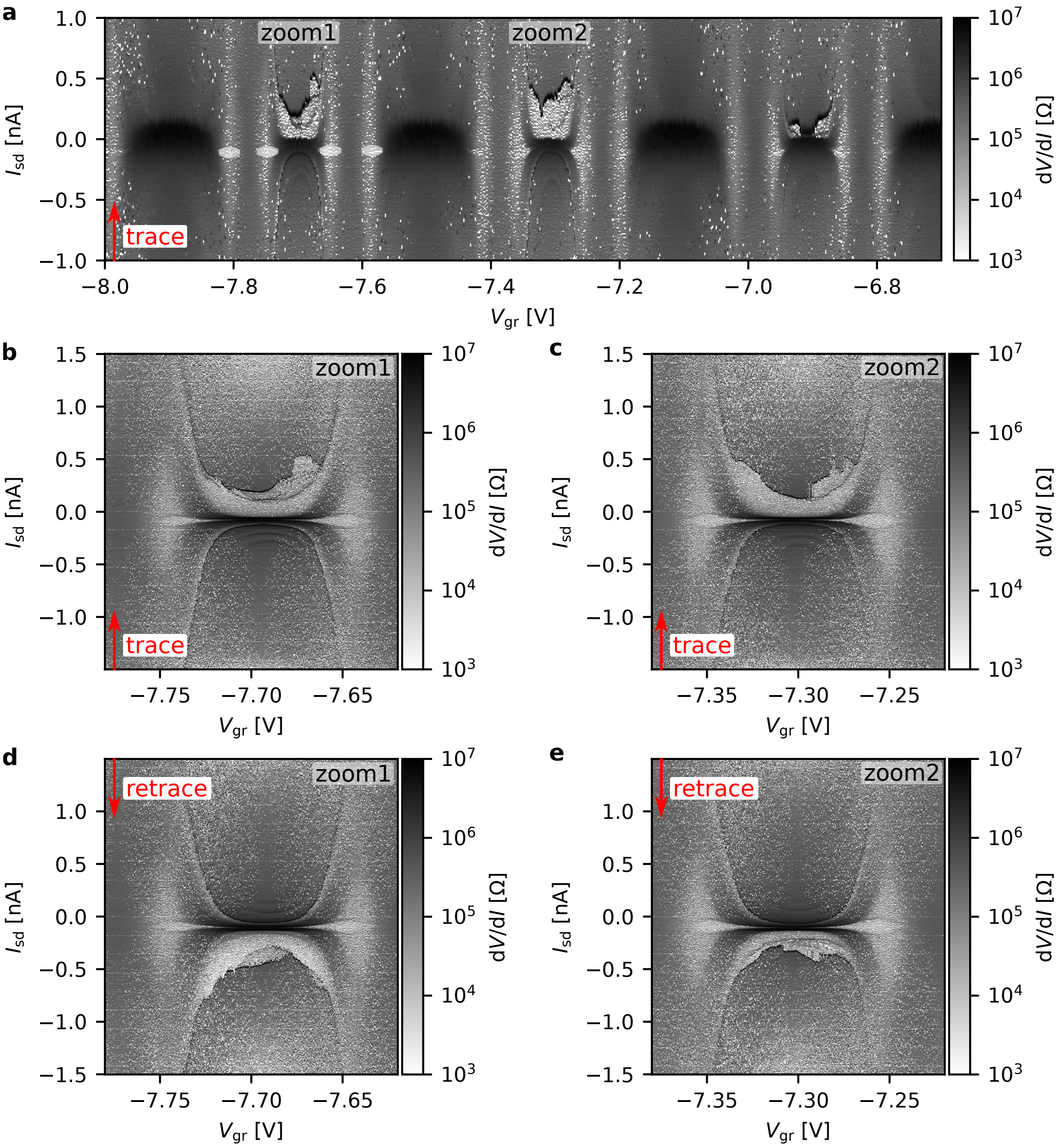

Figure 6.26.: Current-biased measurements of the right dot from SQUID400, sample SC5. Data taken during the second cooldown with the left dot is "off" ($V_{gl} = -0.6\,\mathrm{V}$). **a** Overview with highlighted superconducting pockets in the region of zoom 1. **b**, **d** Zoom into the first pocket with trace and retrace. **c**, **e** Zoom into the second pocket with trace and retrace.

The difference in the maximum switching current between trace and retrace could be attributed to a small change in the gate voltage between the two measurements. Another intriguing feature in figure 6.27d is the series of vertical lines for frequencies beyond the widening of the superconducting pocket. These jumps could simply be an artifact of a non-continuous phase of the microwaves when the frequency is stepped, which results in a frequency spectrum including further high frequency components that lead to jumps between the two bistable states of the Duffing oscillator.

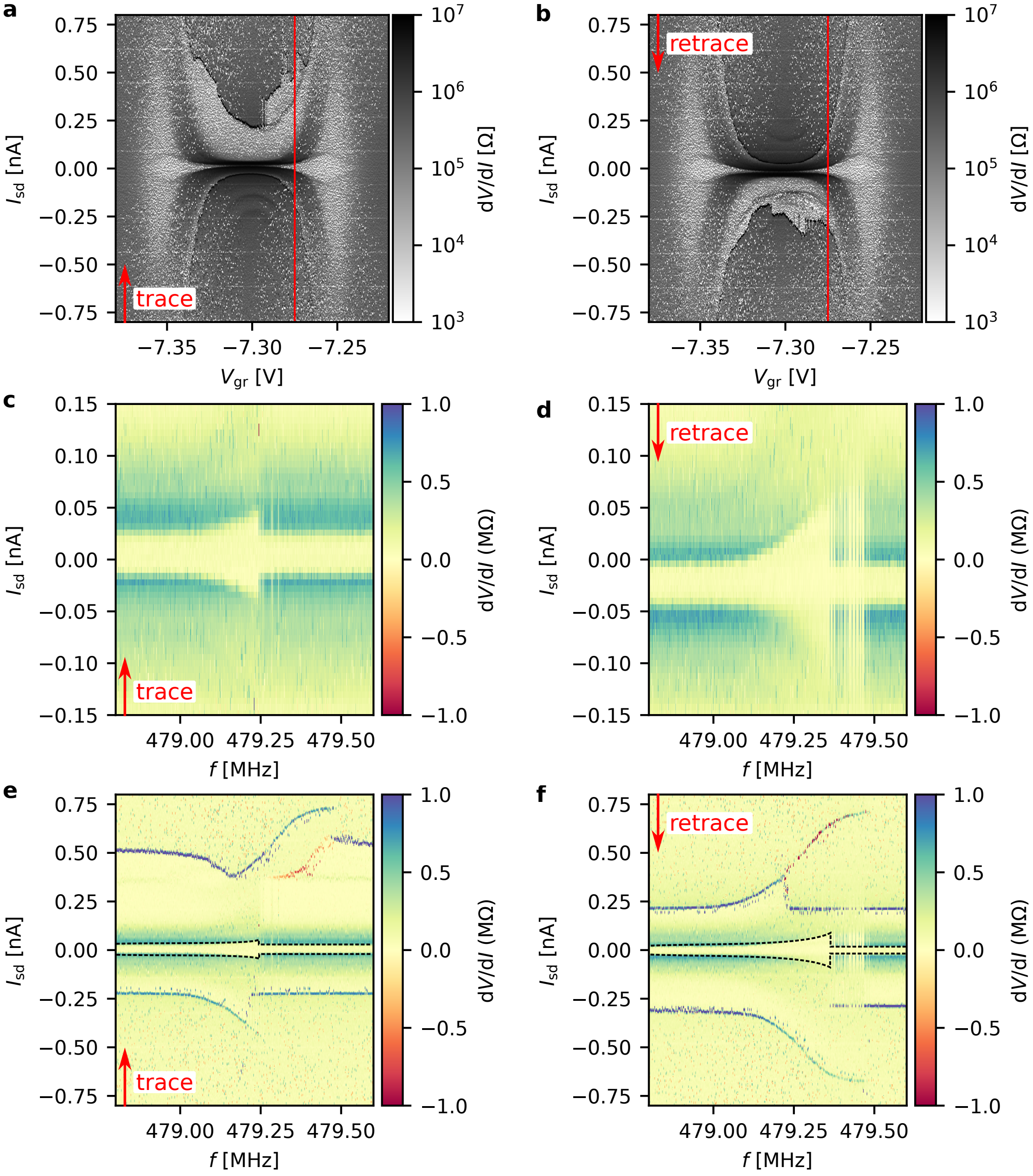

Figure 6.27.: Investigating the interplay between nanomechanics and superconductivity. On the right dot of SQUID400, sample SC5, $V_{gl} = -0.6$ V, RF power $P = -50$ dBm, second cooldown. **a**, **b** Gate voltage dependence of the differential resistance (zoom 1, with gate tuning point for the following measurements). **c**, **d** Differential resistance as function of RF frequency (power −50 dBm) with zoom on the superconducting pocket. **e**, **f** Zoom out on larger current bias with **c**, **d** marked by the dashed area.

We now discuss the frequency dependence of the highly resistive lines confining the low resistive plateaus, which is shown in figure 6.27e,f. One would expect to observe a behavior comparable to the superconducting pockets marked in dashed black, but the highly resistive lines exhibit a very intriguing frequency dependence. Again, far away from the mechanical resonance, the effect of the RF drive is negligible, as expected. At the resonance, there is a very strong frequency dependence in contrast to the switching current, which could be due to the higher curvature. However, the splitting of the highly resistive lines in two branches with positive and negative differential resistance is not understood at the moment. The splitting occurs only for positive current but for the trace and the retrace. Beyond that, the bifurcation occurs at a higher frequency than for the switching current, which could imply that, in the finite-voltage state, additional energy is pumped into the mechanical resonator. Although the origin of these two effects is unclear, they demonstrate a strong interaction between the highly resistive lines confining the low resistive plateaus and the mechanical motion driven in the CNT. In conclusion, these preliminary measurements show that transport through superconducting CNT junctions couples to nanomechanics, but a detailed explanation is complicated and requires more investigation.

7. Conclusion

The main goal of this thesis was to build a suspended CNT-SQUID with potential applications ranging from a platform to study fundamental condensed matter physics phenomena, such as the interplay between proximity-induced superconducting transport and nanomechanics in the suspended CNT, to a magnetometer for single-molecule magnets. While a suspended CNT-SQUID has already been built with the post-fabrication top growth method [31], where CNTs are grown on the circuit chip electrodes, the approach in this thesis is based on the nanoassembly technique.

Nanoassembly technique

Nanoassembly is one of the most advanced techniques for the precise and well-controlled integration of CNTs into electrical devices. Here, the CNTs are CVD-grown on a separate cantilever chip and mechanically transferred onto the circuit chip. For this purpose, we developed a custom CNT transfer setup inside a scanning electron microscope. CNTs on a cantilever chip are pre-characterized with SEM imaging. With the help of piezomotors, a selected CNT can be aligned with respect to the circuit chip. An alignment precision below ± 200 nm is demonstrated, which can still be improved by using narrower alignment markers and is ultimately limited by the minimum step size of the piezomotors. Beyond that, the setup allows for a simultaneous scanning electron microscopy (SEM) observation and current measurement between contacts of the circuit chip, well suited to study the formation of the electrical contact between CNT and circuit electrodes. From their growth to their measurement in the cryostat, the CNTs are never exposed to air and are transported in vacuum transfer arms, resulting in ultraclean CNT devices.

However, first CNT devices exhibited high contact resistance on the order of MΩ at low bias ($V_{\mathrm{sd}} = 0.1\,\mathrm{V}$) making them unsuitable for superconducting transport measurements. These high contact resistances arise from poor wetting of the CNT and work function mismatch due to oxygen concentration in the contact metal or surface oxides. One of the key challenges that has been overcome in this PhD is the reduction of the contact resistance. For this purpose, we use a combination of argon milling to remove a few nanometers of contact material to achieve a pristine surface before the transfer and a two-step annealing process after the CNT transfer. First, a high current close to the maximum current is driven through the CNT junction. In the I-V characteristics, discrete modifications in the resistance can be observed, pointing towards a local atomic rearrangement at the CNT metal interface. Second, we use a technique called radiative thermal annealing (RTA), where the circuit chip with the integrated CNT is globally heated with the thermal radiation of a halogen lamp installed inside the vacuum chamber of the SEM at temperatures below 300 °C. With these contact improvement techniques, the median device resistance could be reduced to 50 kΩ at a bias voltage of 0.1 V. The key results of the contact improvement technique have been published in [37], while the study within this thesis has a more comprehensive scope, including the CNT growth characterization, circuit chip fabrication, nanoassembly setup, the workflow of the nanoassembly process, and an extensive room-temperature transport characterization of the CNT devices. We also discussed in detail the development of the contact improvement techniques and different approaches that have been unsuccessful.

Nanoassembled CNT quantum dots reaching the open quantum dot regime

Samples with clean room temperature transport and low contact resistance have been measured in a dilution cryostat at 40 mK. The devices exhibited ultraclean electronic transport behavior, as demonstrated by the observation of fourfold degeneracy extending over a wide range of gate voltage in the majority of devices. In devices with normal conducting electrodes in the Coulomb blockade regime, we could show strong electron-phonon coupling in the suspended CNT junctions. This could be demonstrated by mechanical bistabilities and the observation of Franck-Condon sidebands, which could arise from a coupling between single-electron tunneling and longitudinal stretching modes. With the contact improvement techniques, the limitation of the nanoassembly technique to the closed quantum dot regime could be overcome. In multiple CNT devices with room-temperature resistance below 50 kΩ, Fabry-Pérot oscillations were measured, indicating an operation in the open quantum dot regime. In the intermediate coupling regime, we could study the SU(4) Kondo effect and its interplay with spin-orbit coupling, providing further evidence for the ultraclean electronic transport in the nanoassembled devices.

Having overcome the limitation of opaque metal nanotube interfaces within the nanoassembly technique by using the contact improvement techniques developed in this thesis, all transport regimes are accessible from the closed to the open quantum dot regime. This allows to envisage many experiments with nanoassembled CNT devices.

The precision of the nanoassembly technique could be used to fabricate devices with multiple CNTs close to each other. For instance, in the case of two CNTs close to each other, one could be employed as a charge sensor for the charge in the quantum dot formed in the adjacent CNT. Another option could be based on using the nanometer diameter CNT as the gate electrode to modulate electronic transport in 2D materials, such as graphene, similar to [220].

As 1D ballistic conductors, CNTs have a low number of transport channels. In addition, for suspended CNTs, the phononic density of states is low and charge noise is limited due to the absence of dielectrics in the vicinity of the CNT. These factors significantly reduce the number of decoherence channels, making suspended CNTs well suited for qubit implementations, such as valley spin-qubits [221] or potentially even nanomechanical qubits [222].

Proximity-induced superconductivity in nanoassembled CNT quantum dots

A clean fabrication process based on sputtering and reactive ion etching was developed to replace the normal metal with the superconductor molybdenum rhenium in combination with a thin palladium or platinum top layer. Using SQUID designs, proximity-induced superconductivity could be explored in five samples. A maximum switching current of $\sim 4\,\mathrm{nA}$ could be reached, probably limited by the remaining thickness of the platinum contact layer between the CNT and the superconductor. Periodic switching current modulations were measured as a function of the applied magnetic field perpendicular to the SQUID loop, demonstrating the successful operation of the suspended CNT-SQUID. The magnetic field dependence has been investigated in detail, also with respect to vortex formation in the type II superconductor molybdenum rhenium.

In a CNT Josephson junction, a gatemon qubit might be directly implemented. The gate voltage dependence of the supercurrent corresponds to a gate-dependent nonlinear inductance, and by embedding the CNT Josephson junction into a superconducting cavity, the qubit state could be readout similarly to [223]. Although, a gatemon qubit does not require suspended CNTs, the decoherence channels should be significantly reduced for a suspended CNT, as explained above.

Coupling superconducting transport and nanomechanics

The suspended nature of the CNT allowed for probing the mechanical degree of freedom and for investigating the coupling between mechanical motion and superconducting electronic transport. Strong coupling was demonstrated in the Coulomb blockade regime, as indicated by the pronounced softening of the spring constant in the differential conductance. In addition, a modulation of the switching current was observed at the mechanical resonance.

In this direction, there are still some open questions. First, the interplay between multiple Andreev reflections and mechanical motion at resonance remains to be explained. Second, in chapter 2.5 we discussed a capacitive coupling approach between superconducting transport and nanomechanics [33]. This approach leads to a Josephson force proportional to the gradient of the Josephson energy that depends on the superconducting phase difference across a CNT Josephson junction. In contrast to [224], a SQUID would allow for the control of the superconducting phase difference across a Josephson junction and for a distinction between the Josephson force and the simple capacitive gate force. In a device with a sufficiently high and well-defined supercurrent, this Josephson force might be detected. The coupling between superconducting transport and the mechanical degree of freedom could also be exploited to cool the nanomechanical resonator by vibration-assisted Andreev reflection [34].

CNT-SQUID as magnetometer

The CNT-SQUIDs fabricated in this thesis are functional and in the future single-molecule magnets could be evaporated on a CNT-SQUID. In general, the deposition of molecules is non-deterministic. Although the small CNT surface and suspension reduce the number of molecules attaching to the CNT, the key challenge lies in the grafting of a single molecular magnet that exhibits large coupling to the flux through the SQUID loop, requiring multiple iterations of evaporation and cooldown cycles. In this case, the sample quickswap system integrated in the cryostat reduces the time consumption significantly. Nonetheless, each warmup can alter the electronic transport properties of the suspended CNT. In this work, we were able to successfully reset the electronic transport properties and recycle a CNT device by applying another RTA cycle after the warmup and air exposure of a sample. A similar reset effect is expected for organic contamination by molecules, and it is likely that a SQUID can be reused many times by applying RTA. A functional CNT-SQUID would allow for a direct measurement of the magnetization reversal of molecular magnets as detailed in chapter 2.4.6.

CNT-SQUID for optomechanical coupling

Instead of the application as magnetometer, the suspended CNT-SQUID can also be used for detecting mechanical motion. The area of the SQUID loop can be altered by the mechanical motion of the CNT resonator, and therefore, the CNT-SQUID can be considered as a position-dependent inductor. This would allow for an alternative readout scheme of the mechanical resonator based on flux-mediated optomechanical coupling with higher single-photon coupling rates than those for capacitive optomechanical coupling schemes [225]. For this purpose, the CNT-SQUID can be implemented as a position-dependent inductor in a microwave cavity similar to SQUIDs based on suspended aluminum beams [225]. The single-photon coupling rate is proportional to the magnetic flux fluctuations, which in turn depend on the mechanical zero-point fluctuations. Due to its low mass, high zero-point fluctuations (~ pm) are expected for a CNT nanomechanical resonator, and the single-photon coupling can be estimated to $g_0 \sim 1\,\mathrm{MHz}$ [191], which is sufficient to reach the strong coupling regime.

Bibliography

[1] National Oceanic and Atmospheric Administration. *2024 was the world's warmest year on record.* `https://www.noaa.gov/news/2024-was-worlds-warmest-year-on-record` [Accessed: 03.03.25]. 2025.

[2] S. Iijima. "Helical microtubules of graphitic carbon". In: *nature* 354.6348 (1991), pp. 56–58.

[3] L. X. Zheng et al. "Ultralong single-wall carbon nanotubes". In: *Nature Materials* 3.10 (2004), pp. 673–676.

[4] A. K. Hüttel et al. "Carbon nanotubes as ultrahigh quality factor mechanical resonators". In: *Nano Letters* 9.7 (2009), pp. 2547–2552.

[5] M. M. J. Treacy, T. W. Ebbesen, and J. M. Gibson. "Exceptionally high Young's modulus observed for individual carbon nanotubes". In: *nature* 381.6584 (1996), pp. 678–680.

[6] O. Lourie and H. D. Wagner. "Evaluation of Young's modulus of carbon nanotubes by micro-Raman spectroscopy". In: *Journal of Materials Research* 13.9 (1998), pp. 2418–2422.

[7] Y. I. Jhon et al. "Tensile characterization of single-walled carbon nanotubes with helical structural defects". In: *Scientific reports* 6.1 (2016), p. 20324.

[8] M.-F. Yu et al. "Tensile loading of ropes of single wall carbon nanotubes and their mechanical properties". In: *Physical review letters* 84.24 (2000), p. 5552.

[9] MatWeb Material Property Data. *2800 Maraging Steel.* `https://www.matweb.com/search/DataSheet.aspx?MatGUID=de22e04486ff4598a26027abc48e6382` [Accessed: 04.04.25]. 2025.

[10] K. L. Ekinci and M. L. Roukes. "Nanoelectromechanical systems". In: *Review of scientific instruments* 76.6 (2005).

[11] G. A. Steele et al. "Strong coupling between single-electron tunneling and nanomechanical motion". In: *Science* 325.5944 (2009), pp. 1103–1107.

[12] J. Svensson and E. E. B. Campbell. "Schottky barriers in carbon nanotube-metal contacts". In: *Journal of Applied Physics* 110.11 (2011).

[13] B. Lassagne et al. "Coupling Mechanics to Charge Transport in Carbon Nanotube Mechanical Resonators". In: *Science* 325.5944 (2009), pp. 1107–1110.

[14] K. Jensen, K. Kim, and A. Zettl. "An atomic-resolution nanomechanical mass sensor". In: *Nature nanotechnology* 3.9 (2008), pp. 533–537.

[15] B. Lassagne et al. “Ultrasensitive mass sensing with a nanotube electromechanical resonator”. In: *Nano letters* 8.11 (2008), pp. 3735–3738.

[16] H.-Y. Chiu et al. “Atomic-scale mass sensing using carbon nanotube resonators”. In: *Nano letters* 8.12 (2008), pp. 4342–4346.

[17] D. A. Garanin and E. M. Chudnovsky. “Quantum entanglement of a tunneling spin with mechanical modes of a torsional resonator”. In: *Physical Review X* 1.1 (2011), p. 011005.

[18] B. Lassagne, D. Ugnati, and M. Respaud. “Ultrasensitive magnetometers based on carbon-nanotube mechanical resonators”. In: *Physical Review Letters* 107.13 (2011), p. 130801.

[19] M. Ganzhorn et al. “Strong spin–phonon coupling between a single-molecule magnet and a carbon nanotube nanoelectromechanical system”. In: *Nature nanotechnology* 8.3 (2013), pp. 165–169.

[20] M. Ganzhorn et al. “Quantum Einstein-de haas effect”. In: *Nature Communications* 7.1 (2016), p. 11443.

[21] S. Thiele et al. “Electrically driven nuclear spin resonance in single-molecule magnets”. In: *Science* 344.6188 (2014), pp. 1135–1138.

[22] C. Godfrin et al. “Operating quantum states in single magnetic molecules: implementation of Grover’s quantum algorithm”. In: *Physical review letters* 119.18 (2017), p. 187702.

[23] S. J. Bartolome, F. Luis, and J. F. Fernández. *Molecular magnets*. Springer, 2016.

[24] J. Kong et al. “Quantum interference and ballistic transmission in nanotube electron waveguides”. In: *Physical review letters* 87.10 (2001), p. 106801.

[25] M. Urdampilleta et al. “Supramolecular spin valves”. In: *Nature materials* 10.7 (2011), pp. 502–506.

[26] M. Urdampilleta et al. “Landau-Zener tunneling of a single Tb 3+ magnetic moment allowing the electronic read-out of a nuclear spin”. In: *Physical Review B—Condensed Matter and Materials Physics* 87.19 (2013), p. 195412.

[27] M. Urdampilleta et al. “Magnetic interaction between a radical spin and a single-molecule magnet in a molecular spin-valve”. In: *ACS nano* 9.4 (2015), pp. 4458–4464.

[28] A. Einstein. “Experimenteller nachweis der ampereschen molekularströme”. In: *Naturwissenschaften* 3.19 (1915), pp. 237–238.

[29] M. Urdampilleta. “Spintronique moléculaire de la vanne de spin à la détection d’un spin unique”. PhD thesis. Université de Grenoble, 2012.

[30] M. Ganzhorn. “Coupling Magnetism and Mechanics at a molecular scale”. PhD thesis. Université de Grenoble, 2013.

[31] B. H. Schneider et al. “Coupling carbon nanotube mechanics to a superconducting circuit”. In: *Scientific Reports* 2 (2012).

[32] J. P. Cleuziou et al. “Carbon nanotube superconducting quantum interference device”. In: *Nature Nanotechnology* 1.1 (2006), pp. 53–59.

[33] C. Padurariu, C. J. H. Keijzers, and Yu V. Nazarov. “Effect of mechanical resonance on Josephson dynamics”. In: *Physical Review B - Condensed Matter and Materials Physics* 86.15 (2012), pp. 1–18.

[34] P. Stadler, W. Belzig, and G. Rastelli. “Ground-state cooling of a mechanical oscillator by interference in Andreev reflection”. In: *Physical Review Letters* 117.19 (2016), p. 197202.

[35] A. Bachtold et al. “Aharonov–Bohm oscillations in carbon nanotubes”. In: *Nature* 397.6721 (1999), pp. 673–675.

[36] J. Cao, Q. Wang, and H. Dai. “Electron transport in very clean, as-grown suspended carbon nanotubes”. In: *Nature materials* 4.10 (2005), pp. 745–749.

[37] T. Althuon et al. “Nano-assembled open quantum dot nanotube devices”. In: *Commun Mater* 5.1 (2024), p. 5.

[38] E. A. Laird et al. “Quantum transport in carbon nanotubes”. In: *Reviews of Modern Physics* 87.3 (2015), pp. 703–764.

[39] A. H. Castro Neto et al. “The electronic properties of graphene”. In: *Reviews of Modern Physics* 81.1 (2009), pp. 109–162.

[40] J.-C. Charlier, X. Blase, and S. Roche. “Electronic and transport properties of nanotubes”. In: *Rev. Mod. Phys.* 79.2 (2007), pp. 677–732.

[41] A. Baydin et al. “Carbon Nanotube Devices for Quantum Technology”. In: *Materials* 15.4 (2022), p. 1535.

[42] M. S. Dresselhaus et al. “Raman spectroscopy of carbon nanotubes”. In: *Physics Reports* 409.2 (2005), pp. 47–99.

[43] S. Sapmaz et al. “Tunneling in suspended carbon nanotubes assisted by longitudinal phonons”. In: *Physical Review Letters* 96.2 (2006), pp. 1–4.

[44] R. Landauer. “Electrical resistance of disordered one-dimensional lattices”. In: *Philosophical magazine* 21.172 (1970), pp. 863–867.

[45] Y. V. Nazarov and Y. M. Blanter. *Quantum transport: introduction to nanoscience.* Cambridge University Press, 2009.

[46] P. L. McEuen and J.-Y. Park. “Electron transport in single-walled carbon nanotubes”. In: *MRS bulletin* 29.4 (2004), pp. 272–275.

[47] W. Liang et al. “Fabry - Perot interference in a nanotube electron waveguide”. In: *Nature* 411.6838 (2001), pp. 665–669.

[48] Q. Cao et al. “End-bonded contacts for carbon nanotube transistors with low, size-independent resistance”. In: *Science* 350.6256 (2015), pp. 68–72.

[49] Y. Zhang et al. “Heterostructures of single-walled carbon nanotubes and carbide nanorods”. In: *Science* 285.5434 (1999), pp. 1719–1722.

[50] H. Maki, M. Suzuki, and K. Ishibashi. “Local change of carbon nanotube-metal contacts by current flow through electrodes”. In: *Japanese journal of applied physics* 43.4S (2004), p. 2027.

[51] F. Banhart. “Interactions between metals and carbon nanotubes: At the interface between old and new materials”. In: *Nanoscale* 1.2 (2009), pp. 201–213.

[52] Y. Zhang et al. “Metal coating on suspended carbon nanotubes and its implication to metal–tube interaction”. In: *Chemical Physics Letters* 331.1 (2000), pp. 35–41.

[53] S. Lee, S. J. Kahng, and Y. Kuk. “Nano-level wettings of platinum and palladium on single-walled carbon nanotubes”. In: *Chemical Physics Letters* 500.1-3 (2010), pp. 82–85.

[54] A. Maiti and A. Ricca. “Metal–nanotube interactions–binding energies and wetting properties”. In: *Chemical Physics Letters* 395.1-3 (2004), pp. 7–11.

[55] M. Shiraishi and M. Ata. “Work function of carbon nanotubes”. In: *Carbon* 39.12 (2001), pp. 1913–1917.

[56] J. P. Sun et al. “Work function of single-walled carbon nanotubes determined by field emission microscopy”. In: *Applied Physics A* 75 (2002), pp. 479–483.

[57] S. Suzuki et al. “Work functions and valence band states of pristine and Cs-intercalated single-walled carbon nanotube bundles”. In: *Applied Physics Letters* 76.26 (2000), pp. 4007–4009.

[58] W. Kim et al. “Electrical contacts to carbon nanotubes down to 1nm in diameter”. In: *Applied Physics Letters* 87.17 (2005).

[59] F. Léonard and J. Tersoff. “Role of Fermi-level pinning in nanotube Schottky diodes”. In: *Physical Review Letters* 84.20 (2000), p. 4693.

[60] W. Liu, C. Hierold, and M. Haluska. “Electrical contacts to individual SWCNTs: A review”. In: *Beilstein J. Nanotechnol.* 5 (2014), pp. 2202–2215.

[61] S. Jung et al. “Understanding and improving carbon nanotube-electrode contact in bottom-contacted nanotube gas sensors”. In: *Sensors and Actuators, B: Chemical* 331 (2021), p. 129406.

[62] J. M. Thijssen and H. S. J. Van Der Zant. “Charge transport and single-electron effects in nanoscale systems”. In: *Physica Status Solidi (B) Basic Research* 245.8 (2008), pp. 1455–1470.

[63] C. Schönenberger. “Charge and spin transport in carbon nanotubes”. In: *Semiconductor science and technology* 21.11 (2006), S1.

[64] A. Auer. “Interfacing nanomechanics with multi-gated suspended carbon nanotube quantum circuits”. PhD thesis. Karlsruher Institut für Technologie, PHI, 2024.

[65] R. Hanson et al. “Spins in few-electron quantum dots”. In: *Rev. Mod. Phys.* 79.4 (2007), pp. 1217–1265.

[66] B. Babić, T. Kontos, and C. Schönenberger. “Kondo effect in carbon nanotubes at half filling”. In: *Phys. Rev. B* 70.23 (2004), p. 235419.

[67] R. Leturcq et al. “Franck-Condon blockade in suspended carbon nanotube quantum dots”. In: *Nature Physics* 5.5 (2009), pp. 327–331.

[68] M. Laber. “Carbon Nanotube SQUIDs Exploring Superconductor Quantum Dot Junctions”. Master’s Thesis. Karlsruher Institut für Technologie, PHI, 2020.

[69] J. Kondo. “Resistance minimum in dilute magnetic alloys”. In: *Progress of theoretical physics* 32.1 (1964), pp. 37–49.

[70] J. Nygård, D. H. Cobden, and P. E. Lindelof. “Kondo physics in carbon nanotubes”. In: *Nature* 408.6810 (2000), pp. 342–346.

[71] L. Kouwenhoven and L. Glazman. “Revival of the Kondo effect”. In: *Phys. World* 14.1 (2001), pp. 33–38.

[72] J. S. Lim et al. “Kondo effects in carbon nanotubes: From SU (4) to SU (2) symmetry”. In: *Physical Review B—Condensed Matter and Materials Physics* 74.20 (2006), p. 205119.

[73] J. P. Cleuziou et al. “Interplay of the kondo effect and strong spin-orbit coupling in multihole ultraclean carbon nanotubes”. In: *Physical Review Letters* 111.13 (2013), pp. 1–5.

[74] P. Jarillo-Herrero et al. “Orbital Kondo effect in carbon nanotubes”. In: *Nature* 434.7032 (2005), pp. 484–488.

[75] S. L. De Bonis et al. “Ultrasensitive Displacement Noise Measurement of Carbon Nanotube Mechanical Resonators”. In: *Nano Lett.* 18.8 (2018), pp. 5324–5328.

[76] M. Poot and H. S.J. van der Zant. “Mechanical systems in the quantum regime”. In: *Physics Reports* 511.5 (2012), pp. 273–335.

[77] R. Lifshitz and M. C. Cross. “Nonlinear Dynamics of Nanomechanical and Micromechanical Resonators”. In: *Reviews of Nonlinear Dynamics and Complexity.* Ed. by H. G. Schuster. 1st ed. Wiley, 2008, pp. 1–52.

[78] V. Sazonova. “A Tunable Carbon Nanotube Resonator”. PhD thesis. Cornell University, 2006.

[79] S. Sapmaz et al. “Carbon nanotubes as nanoelectromechanical systems”. In: *Physical Review B* 67.23 (2003), p. 235414.

[80] H. W. Ch. Postma et al. “Dynamic range of nanotube- and nanowire-based electromechanical systems”. In: *Applied Physics Letters* 86.22 (2005), p. 223105.

[81] G. M. Moatimid. “Stability analysis of a parametric Duffing oscillator”. In: *Journal of Engineering Mechanics* 146.5 (2020), p. 05020001.

[82] W. Wawrzynski. “The origin point of the unstable solution area of a forced softening Duffing oscillator”. In: *Scientific Reports* 12.1 (2022), p. 4518.

[83] Y. Wen et al. “A coherent nanomechanical oscillator driven by single-electron tunnelling”. In: *Nature physics* 16.1 (2020), pp. 75–82.

[84] C. Urgell et al. “Cooling and self-oscillation in a nanotube electromechanical resonator”. In: *Nature Physics* 16.1 (2020), pp. 32–37.

[85] M. Kociak et al. “Superconductivity in ropes of single-walled carbon nanotubes”. In: *Physical review letters* 86.11 (2001), p. 2416.

[86] J. Bardeen, L. N. Cooper, and J. R. Schrieffer. “Theory of superconductivity”. In: *Physical review* 108.5 (1957), p. 1175.

[87] H. Fröhlich. “Theory of the superconducting state. I. The ground state at the absolute zero of temperature”. In: *Physical Review* 79.5 (1950), p. 845.

[88] M. Tinkham. *Introduction to superconductivity*. 2nd ed. New York: McGraw Hill, 1996.

[89] P. Mangin and R. Kahn. *Superconductivity: an introduction*. Springer, 2016.

[90] A. K. Karnad. *Study of Josephson Junction. II: Simulations and analysis*. `https://ashwinschronicles.github.io/josephson-junction-simulation-and-analysis` [Accessed: 07.02.25]. 2022.

[91] B. D. Josephson. “Possible new effects in superconductive tunnelling”. In: *Physics letters* 1.7 (1962), pp. 251–253.

[92] A. A. Golubov, M. Y. Kupriyanov, and E. Il’ichev. “The current-phase relation in Josephson junctions”. In: *Rev. Mod. Phys.* 76.2 (2004), pp. 411–469.

[93] V. Ambegaokar and A. Baratoff. “Tunneling between superconductors”. In: *Physical review letters* 10.11 (1963), p. 486.

[94] I. V. Borzenets et al. “Ballistic graphene Josephson junctions from the short to the long junction regimes”. In: *Physical review letters* 117.23 (2016), p. 237002.

[95] P. Dubos et al. “Josephson critical current in a long mesoscopic SNS junction”. In: *Physical Review B* 63.6 (2001), p. 064502.

[96] T. T. Heikkilä. *The physics of nanoelectronics: transport and fluctuation phenomena at low temperatures*. Oxford University Press, 2013.

[97] J. D. Pillet et al. “Andreev bound states in supercurrent-carrying carbon nanotubes revealed”. In: *Nature Physics* 6.12 (2010), pp. 965–969.

[98] T. M. Klapwijk, G. E. Blonder, and M. Tinkham. “Explanation of subharmonic energy gap structure in superconducting contacts”. In: *Physica B+ C* 109 (1982), pp. 1657–1664.

[99] M. R. Buitelaar et al. “Multiple Andreev Reflections in a Carbon Nanotube Quantum Dot”. In: *Phys. Rev. Lett.* 91.5 (2003), p. 057005.

[100] S. De Franceschi et al. “Hybrid superconductor-quantum dot devices”. In: *Nature Nanotechnology* 5.10 (2010), pp. 703–711.

[101] K. Grove-Rasmussen et al. “Superconductivity-enhanced bias spectroscopy in carbon nanotube quantum dots”. In: *Phys. Rev. B* 79.13 (2009), p. 134518.

[102] R. Delagrange. “Josephson effect and high frequency emission in a carbon nanotube in the Kondo regime”. PhD thesis. Université Paris-Saclay, 2016.

[103] R. Maurand et al. "First-order 0-pi quantum phase transition in the kondo regime of a superconducting carbon-nanotube quantum dot". In: *Physical Review X* 2.1 (2012), pp. 1–11.

[104] H. I. Jørgensen et al. "Critical Current 0-pi Transition in Designed Josephson Quantum Dot Junctions". In: *Nano Lett.* 7.8 (2007), pp. 2441–2445.

[105] A. Eichler et al. "Even-Odd Effect in Andreev Transport through a Carbon Nanotube Quantum Dot". In: *Phys. Rev. Lett.* 99.12 (2007), p. 126602.

[106] H. I. Jørgensen et al. "Electron Transport in Single-Wall Carbon Nanotube Weak Links in the Fabry-Perot Regime". In: *Phys. Rev. Lett.* 96.20 (2006), p. 207003.

[107] R. Delagrange et al. "0-pi quantum transition in a carbon nanotube Josephson junction: Universal phase dependence and orbital degeneracy". In: *Phys. Rev. B* 93.19 (2016), p. 195437.

[108] B.-K. Kim et al. "Transport Measurement of Andreev Bound States in a Kondo-Correlated Quantum Dot". In: *Phys. Rev. Lett.* 110.7 (2013), p. 076803.

[109] C. W. J. Beenakker and H. van Houten. "Resonant Josephson current through a quantum dot". In: *Single-Electron Tunneling and Mesoscopic Devices: Proceedings of the 4th International Conference SQUID'91.* arXiv:cond-mat/0111505. Springer. 1992, pp. 175–179.

[110] R. Gross and A. Marx. *Applied Superconductivity - Josephson Effect and Superconducting Electronics.* `https://www.wmi.badw.de/fileadmin/WMI/Lecturenotes/Applied_Superconductivity/AS_Chapter3.pdf` [Accessed: 20.01.25]. 2005.

[111] W. C. Stewart. "Current-voltage characteristics of Josephson junctions". In: *Applied physics letters* 12.8 (1968), pp. 277–280.

[112] D. E. McCumber. "Effect of ac impedance on dc voltage-current characteristics of superconductor weak-link junctions". In: *Journal of Applied Physics* 39.7 (1968), pp. 3113–3118.

[113] T. McDermott et al. "Strong mechanically induced effects in DC current-biased suspended Josephson junctions". In: *Phys. Rev. B* 97.1 (2018), p. 014526.

[114] S. Shapiro. "Josephson currents in superconducting tunneling: The effect of microwaves and other observations". In: *Physical Review Letters* 11.2 (1963), p. 80.

[115] J. P. Cleuziou et al. "Gate-tuned high frequency response of carbon nanotube josephson junctions". In: *Physical Review Letters* 99.11 (2007), pp. 1–4.

[116] J. Heintze. *Lehrbuch zur Experimentalphysik Band 5: Quantenphysik: Wellen, Teilchen und Atome.* Springer-Verlag, 2019.

[117] C. A. Hamilton. "Josephson voltage standards". In: *Review of scientific instruments* 71.10 (2000), pp. 3611–3623.

[118] W. Wernsdorfer. "From micro-to nano-SQUIDs: Applications to nanomagnetism". In: *Superconductor Science and Technology* 22.6 (2009), p. 064013.

[119] R. Gross and A. Marx. *Applied Superconductivity - Josephson Effect and Superconducting Electronics.* `https://www.wmi.badw.de/fileadmin/WMI/Lecturenotes/Applied_Superconductivity/AS_Chapter4.pdf` [Accessed: 20.01.25]. 2005.

[120] T. Q. Yang and K. Enpuku. "SQUID magnetometer utilizing normal pickup coil and resonant-type coupling circuit". In: *Physica C: Superconductivity* 392 (2003), pp. 1396–1400.

[121] S. Etaki et al. "Motion detection of a micromechanical resonator embedded in a d.c. SQUID". In: *Nature Physics* 4.10 (2008), pp. 785–788.

[122] C. J. H. Keijzers. "Josephson effects in carbon nanotube mechanical resonators and graphene". PhD thesis. 2012.

[123] G. Sonne et al. "Superconducting pumping of nanomechanical vibrations". In: *Phys. Rev. B* 78.14 (2008), p. 144501.

[124] G. Sonne et al. "Cooling of a Suspended Nanowire by an ac Josephson Current Flow". In: *Phys. Rev. Lett.* 104.22 (2010), p. 226802.

[125] Thomas McDermott. "Theory of Josephson Junction Resonators". PhD thesis. University of Exeter, 2019.

[126] J. M. Le Signe. "Probing Mechanics in Quantum Mechanics: Josephson Nano-Resonator Metamaterials". PhD thesis. University of Exeter, 2022.

[127] W. Krätschmer et al. "Solid C60: a new form of carbon". In: *Nature* 347.6291 (1990), pp. 354–358.

[128] S. Farhat and C. D. Scott. "Review of the arc process modeling for fullerene and nanotube production". In: *Journal of nanoscience and nanotechnology* 6.5 (2006), pp. 1189–1210.

[129] T. Guo et al. "Catalytic growth of single-walled manotubes by laser vaporization". In: *Chemical physics letters* 243.1-2 (1995), pp. 49–54.

[130] A. Thess et al. "Crystalline ropes of metallic carbon nanotubes". In: *science* 273.5274 (1996), pp. 483–487.

[131] M. Kumar and Y. Ando. "Chemical vapor deposition of carbon nanotubes: A review on growth mechanism and mass production". In: *Journal of Nanoscience and Nanotechnology* 10.6 (2010), pp. 3739–3758.

[132] J. P. Tessonnier and D. S. Su. "Recent progress on the growth mechanism of carbon nanotubes: A review". In: *ChemSusChem* 4.7 (2011), pp. 824–847.

[133] R. T. K. Baker et al. "Nucleation and growth of carbon deposits from the nickel catalyzed decomposition of acetylene". In: *Journal of catalysis* 26.1 (1972), pp. 51–62.

[134] R. T. K. Baker et al. "Formation of filamentous carbon from iron, cobalt and chromium catalyzed decomposition of acetylene". In: *Journal of catalysis* 30.1 (1973), pp. 86–95.

[135] Y. Chen et al. "State of the Art of Single-Walled Carbon Nanotube Synthesis on Surfaces". In: *Advanced Materials* 26.34 (2014), pp. 5898–5922.

[136] Z. Jin et al. “Ultralow feeding gas flow guiding growth of large-scale horizontally aligned single-walled carbon nanotube arrays”. In: *Nano Letters* 7.7 (2007), pp. 2073–2079.

[137] M. Hofmann et al. “In-situ sample rotation as a tool to understand chemical vapor deposition growth of long aligned carbon nanotubes”. In: *Nano Letters* 8.12 (2008), pp. 4122–4127.

[138] X. Wang et al. “Fabrication of ultralong and electrically uniform single-walled carbon nanotubes on clean substrates”. In: *Nano Letters* 9.9 (2009), pp. 3137–3141.

[139] I. R. Hamdani et al. “Thermocatalytic decomposition of methane: a review on carbon-based catalysts”. In: *ACS omega* 8.32 (2023), pp. 28945–28967.

[140] C. T. Wirth, S. Hofmann, and J. Robertson. “State of the catalyst during carbon nanotube growth”. In: *Diamond and Related Materials* 18.5-8 (2009), pp. 940–945.

[141] A. M. Cassell et al. “Large Scale CVD Synthesis of Single-Walled Carbon Nanotubes”. In: *J. Phys. Chem. B* 103.31 (1999), pp. 6484–6492.

[142] Y. Li et al. “How catalysts affect the growth of single-walled carbon nanotubes on substrates”. In: *Advanced Materials* 22.13 (2010), pp. 1508–1515.

[143] M. H. Rümmeli et al. “Synthesis of carbon nanotubes with and without catalyst particles”. In: *Nanoscale Research Letters* 6.1 (2011), pp. 1–9.

[144] T. Tsuji et al. “Role of hydrogen in catalyst activation for plasma-based synthesis of carbon nanotubes”. In: *ACS omega* 6.29 (2021), pp. 18763–18769.

[145] N. V. Nguyen. “Synthèse et transport électronique dans des nanotubes de carbone ultrapropres”. PhD thesis. Université de Grenoble, 2012.

[146] S. Bellucci et al. “Atomic Force Microscopy Characterization of Carbon Nanotubes”. In: *J. Phys.: Conf. Ser.* 61 (2007), pp. 99–104.

[147] S. Sandoval et al. “Determination of the length of single-walled carbon nanotubes by scanning electron microscopy”. In: *MethodsX* 5 (2018), pp. 1465–1472.

[148] N. Martin. “Growth and analysis of carbon nanotubes”. Bachelor’s Thesis. Karlsruher Institut für Technologie, PHI, 2022.

[149] A. Jorio and R. Saito. “Raman spectroscopy for carbon nanotube applications”. In: *Journal of Applied Physics* 129.2 (2021).

[150] K. Liu et al. “Intrinsic radial breathing oscillation in suspended single-walled carbon nanotubes”. In: *Physical Review B - Condensed Matter and Materials Physics* 83.11 (2011), pp. 1–4.

[151] B. W. Smith and D. E. Luzzi. “Electron irradiation effects in single wall carbon nanotubes”. In: *Journal of Applied Physics* 90.7 (2001), pp. 3509–3515.

[152] C. Kübel et al. “Recent Advances in Electron Tomography: TEM and HAADF-STEM Tomography for Materials Science and Semiconductor Applications”. In: *Microsc Microanal* 11.5 (2005), pp. 378–400.

[153] M. Hugenschmidt et al. “Electron-Beam-Induced Carbon Contamination in STEM-in-SEM: Quantification and Mitigation”. In: *Microscopy and Microanalysis* 29.1 (2023), pp. 219–234.

[154] D. J. Burbridge et al. “Strategies for the immobilization of nanoparticles using electron beam induced deposition”. In: *Nanotechnology* 19.44 (2008), p. 445302.

[155] M. Todeschini et al. “Influence of Ti and Cr adhesion layers on ultrathin Au films”. In: *ACS applied materials & interfaces* 9.42 (2017), pp. 37374–37385.

[156] F. Laermer. “Method of anisotropically etching silicon”. In: *United States Patent 5,501,893* (1996).

[157] H. V. Jansen et al. “Black silicon method: X. A review on high speed and selective plasma etching of silicon with profile control: an in-depth comparison between Bosch and cryostat DRIE processes as a roadmap to next generation equipment”. In: *J. Micromech. Microeng.* 19.3 (2009), p. 033001.

[158] T. Hoss, C. Strunk, and C. Schönenberger. “Nonorganic evaporation mask for superconducting nanodevices”. In: *Microelectronic Engineering* 46.1 (1999), pp. 149–152.

[159] E. Lerner, J. G. Daunt, and E. Maxwell. “Magnetic Properties of Superconducting Mo-Re Alloys”. In: *Phys. Rev.* 153.2 (1967), pp. 487–492.

[160] S. M. Deambrosis et al. “A15 superconductors: An alternative to niobium for RF cavities”. In: *Physica C: Superconductivity* 441.1-2 (2006), pp. 108–113.

[161] J. Talvacchio, M. A. Janocko, and J. Greggi. “Properties of evaporated Mo-Re thin-film superconductors”. In: *J Low Temp Phys* 64.5-6 (1986), pp. 395–408.

[162] S. Sundar et al. “Electrical transport and magnetic properties of superconducting Mo 52 Re 48 alloy”. In: *AIP Conference Proceedings*. Vol. 1512. 1. American Institute of Physics. 2013, pp. 1092–1093.

[163] A. Andreone et al. “Mo-Re superconducting thin films by single target magnetron sputtering”. In: *IEEE Trans. Magn.* 25.2 (1989), pp. 1972–1975.

[164] V. A. Seleznev et al. “Deposition and characterization of few-nanometers-thick superconducting Mo–Re films”. In: *Supercond. Sci. Technol.* 21.11 (2008), p. 115006.

[165] J. R. Gavaler, M. A. Janocko, and C. K. Jones. “A-15 structure Mo–Re superconductor”. In: *Applied Physics Letters* 21.4 (1972), pp. 179–180.

[166] K. J. G. Götz et al. “Co-sputtered MoRe thin films for carbon nanotube growth-compatible superconducting coplanar resonators”. In: *Nanotechnology* 27.13 (2016).

[167] V. Singh et al. “Molybdenum-rhenium alloy based high-Q superconducting microwave resonators”. In: *Applied Physics Letters* 105.22 (2014).

[168] B. Kousar et al. “InAs/MoRe Hybrid Semiconductor/Superconductor Nanowire Devices”. In: *Nano Letters* 22.22 (2022), pp. 8845–8851.

[169] F. Amet et al. “Supercurrent in the quantum Hall regime”. In: *Science* 352.6288 (2016), pp. 966–969.

[170] R. Gaudenzi et al. “Superconducting molybdenum-rhenium electrodes for single-molecule transport studies”. In: *Applied Physics Letters* 106.22 (2015).

[171] A. G. Shishkin et al. “Planar MoRe-based direct current nanoSQUID”. In: *Superconductor Science and Technology* 33.6 (2020).

[172] J. P. Kaikkonen et al. “Suspended superconducting weak links from aerosol-synthesized single-walled carbon nanotubes”. In: *Nano Research* 13.12 (2020), pp. 3433–3438.

[173] A. G. Bagmut et al. “Crystallization and natural aging of thin films produced by pulsed laser evaporation of rhenium”. In: *Functional Materials* 20.2 (2013), pp. 180–185.

[174] J. Hämäläinen et al. “Rhenium Metal and Rhenium Nitride Thin Films Grown by Atomic Layer Deposition”. In: *Angewandte Chemie - International Edition* 57.44 (2018), pp. 14538–14542.

[175] M. T. Greiner et al. “The oxidation of rhenium and identification of rhenium oxides during catalytic partial oxidation of ethylene: An in-situ xps study”. In: *Zeitschrift fur Physikalische Chemie* 228.4-5 (2014), pp. 521–541.

[176] C. C. Wu, C. H. Liu, and Z. Zhong. “One-step direct transfer of pristine single-walled carbon nanotubes for functional nanoelectronics”. In: *Nano letters* 10.3 (2010), pp. 1032–1036.

[177] J. Waissman et al. “Realization of pristine and locally tunable one-dimensional electron systems in carbon nanotubes”. In: *Nature Nanotech* 8.8 (2013), pp. 569–574.

[178] J. Gramich et al. “Fork stamping of pristine carbon nanotubes onto ferromagnetic contacts for spin-valve devices”. In: *physica status solidi (b)* 252.11 (2015), pp. 2496–2502.

[179] S. Blien et al. “Quartz Tuning-Fork Based Carbon Nanotube Transfer into Quantum Device Geometries”. In: *physica status solidi (b)* 255.12 (2018), p. 1800118.

[180] F. Pei et al. “Valley–spin blockade and spin resonance in carbon nanotubes”. In: *Nature nanotechnology* 7.10 (2012), pp. 630–634.

[181] N. Ares et al. “Resonant optomechanics with a vibrating carbon nanotube and a radio-frequency cavity”. In: *Physical Review Letters* 117.17 (2016), p. 170801.

[182] S. Jung. “Fabrication and Operation of Fast, Ultra-low-power Gas Sensors with Carbon Nanotubes”. PhD thesis. ETH Zurich, 2024.

[183] T. Cubaynes et al. “Nanoassembly technique of carbon nanotubes for hybrid circuit-QED”. In: *Applied Physics Letters* 117.11 (2020).

[184] S. Blien et al. “Towards carbon nanotube growth into superconducting microwave resonator geometries”. In: *Physica Status Solidi (B) Basic Research* 253.12 (2016), pp. 2385–2390.

[185] Z. Yao, C. L. Kane, and C. Dekker. “High-field electrical transport in single-wall carbon nanotubes”. In: *Physical Review Letters* 84.13 (2000), p. 2941.

[186] V. Perebeinos, J. Tersoff, and P. Avouris. “Electron-phonon interaction and transport in semiconducting carbon nanotubes”. In: *Physical review letters* 94.8 (2005), p. 086802.

[187] D. Mann et al. “Thermally and Molecularly Stimulated Relaxation of Hot Phonons in Suspended Carbon Nanotubes”. In: *J. Phys. Chem. B* 110.4 (2006), pp. 1502–1505.

[188] E. Pop et al. “Negative differential conductance and hot phonons in suspended nanotube molecular wires”. In: *Physical Review Letters* 95.15 (2005), pp. 1–4.

[189] P. Jarillo-Herrero, J. A. Van Dam, and L. P. Kouwenhoven. “Quantum supercurrent transistors in carbon nanotubes”. In: *Nature* 439.7079 (2006), pp. 953–956.

[190] S. Müller. “Fabrication and Characterisation of Carbon Nanotube Based Nanoelectromechanical Systems”. Master’s Thesis. Karlsruher Institut für Technologie, PHI, 2022.

[191] T. Althuon et al. “Supplementary information: Nano-assembled open quantum dot nanotube devices”. In: *Commun Mater* 5.1 (2024), p. 5.

[192] V. Derycke et al. “Carbon nanotube inter-and intramolecular logic gates”. In: *Nano letters* 1.9 (2001), pp. 453–456.

[193] V. Derycke et al. “Controlling doping and carrier injection in carbon nanotube transistors”. In: *Applied Physics Letters* 80.15 (2002), pp. 2773–2775.

[194] D. Yamashita and A. Ishizaki. “In situ measurements of change in work function of Pt, Pd and Au surfaces during desorption of oxygen by using photoemission yield spectrometer in air”. In: *Applied Surface Science* 363 (2016), pp. 240–244.

[195] C. W. Oatley. “The adsorption of oxygen and hydrogen on platinum and the removal of these gases by positive-ion bombardment”. In: *Proceedings of the Physical Society* 51.2 (1939), p. 318.

[196] R. Jaeckel and B. Wagner. “Photo-electric measurement of the work function of metals and its alteration after gas adsorption”. In: *Vacuum* 13.12 (1963), pp. 509–511.

[197] P. R. Norton and J. W. Goodale. “Hydrogen on Pt(111) studied by dynamic measurements of the work function”. In: *Solid State Communications* 31.4 (1979), pp. 223–227.

[198] R. Lewis and R. Gomer. “Adsorption of hydrogen on platinum”. In: *Surface Science* 17.2 (1969), pp. 333–345.

[199] Y.-F. Chen and M. S. Fuhrer. “Tuning from thermionic emission to ohmic tunnel contacts via doping in Schottky-barrier nanotube transistors”. In: *Nano letters* 6.9 (2006), pp. 2158–2162.

[200] U. V. Rao, ed. *Platinum Group Metals and Compounds.* Vol. 98. Advances in Chemistry. Washington, D. C.: American Chemical Society, 1971.

[201] A. Zilz. “Investigation of the Rarefied Gas Flow in the Pumping Tube of a 3He/4He Dilution Refrigerator”. Master’s Thesis. Karlsruher Institut für Technologie, PHI, 2022.

[202] J. Ferrero. “Development of a cryogenic platform with fast-turnaround in-situ characterization of semiconductor circuits for qubit applications”. PhD thesis. Karlsruher Institut für Technologie, PHI, 2024.

[203] C. W. J. Beenakker. “Theory of Coulomb-blockade oscillations in the conductance of a quantum dot”. In: *Physical Review B* 44.4 (1991), pp. 1646–1656.

[204] L. P. Kouwenhoven et al. “Electron transport in quantum dots”. In: *Mesoscopic electron transport* (1997), pp. 105–214.

[205] F. Cavaliere et al. “Asymmetric Franck-Condon factors in suspended carbon nanotube quantum dots”. In: *Phys. Rev. B* 81.20 (2010), p. 201303.

[206] B. J. LeRoy et al. “Electrical generation and absorption of phonons in carbon nanotubes”. In: *Nature* 432.7015 (2004), pp. 371–374.

[207] K. Willick and J. Baugh. “Self-driven oscillation in Coulomb blockaded suspended carbon nanotubes”. In: *Phys. Rev. Research* 2.3 (2020), p. 033040.

[208] D. R. Schmid et al. “Liquid-induced damping of mechanical feedback effects in single electron tunneling through a suspended carbon nanotube”. In: *Applied Physics Letters* 107.12 (2015), p. 123110.

[209] D. R. Schmid et al. “Magnetic damping of a carbon nanotube nano-electromechanical resonator”. In: *New J. Phys.* 14.8 (2012), p. 083024.

[210] O. Usmani, Y. M. Blanter, and Y. V. Nazarov. “Strong feedback and current noise in nanoelectromechanical systems”. In: *Phys. Rev. B* 75.19 (2007), p. 195312.

[211] M. R. Galpin et al. “Interplay between Kondo physics and spin-orbit coupling in carbon nanotube quantum dots”. In: *Physical Review B—Condensed Matter and Materials Physics* 81.7 (2010), p. 075437.

[212] T. S. Jespersen et al. “Gate-dependent orbital magnetic moments in carbon nanotubes”. In: *Physical Review Letters* 107.18 (2011), p. 186802.

[213] F. Kuemmeth et al. “Coupling of spin and orbital motion of electrons in carbon nanotubes”. In: *Nature* 452.7186 (2008), pp. 448–452.

[214] G. A. Steele et al. “Large spin-orbit coupling in carbon nanotubes”. In: *Nature communications* 4.1 (2013), p. 1573.

[215] A. Makarovski et al. “SU (2) and SU (4) Kondo effects in carbon nanotube quantum dots”. In: *Physical Review B—Condensed Matter and Materials Physics* 75.24 (2007), p. 241407.

[216] D. Kang et al. “Oxygen-induced p-type doping of a long individual single-walled carbon nanotube”. In: *Nanotechnology* 16.8 (2005), p. 1048.

[217] X. Wang et al. “Visualizing nonlinear resonance in nanomechanical systems via single-electron tunneling”. In: *Nano Research* 14 (2021), pp. 1156–1161.

[218] A. H. Nayfeh and D. T. Mook. *Nonlinear oscillations.* John Wiley & Sons, 1995.

[219] B. M. Andersen et al. “Nonequilibrium transport through a spinful quantum dot with superconducting leads”. In: *Physical review letters* 107.25 (2011), p. 256802.

[220] A. Cheng et al. “Guiding Dirac fermions in graphene with a carbon nanotube”. In: *Physical Review Letters* 123.21 (2019), p. 216804.

[221] E. A. Laird, F. Pei, and L. P. Kouwenhoven. “A valley–spin qubit in a carbon nanotube”. In: *Nature nanotechnology* 8.8 (2013), pp. 565–568.

[222] F. Pistolesi, A. N. Cleland, and A. Bachtold. “Proposal for a nanomechanical qubit”. In: *Physical Review X* 11.3 (2021), p. 031027.

[223] H. Riechert et al. “Superconducting qubit based on a single molecule: the carbon nanotube gatemon”. In: *arXiv preprint arXiv:2503.01978* (2025).

[224] C. J. H. Keijzers. “Josephson effects in carbon nanotube mechanical resonators and graphene”. PhD thesis. University of Delft, 2012.

[225] I. C. Rodrigues, D. Bothner, and G. A. Steele. “Coupling microwave photons to a mechanical resonator using quantum interference”. In: *Nature communications* 10.1 (2019), p. 5359.

[226] L. J. van der Pauw. “A method of measuring the resistivity and Hall coefficient on lamellae of arbitrary shape”. In: *Philips technical review* 20 (1958), pp. 220–224.

[227] L. L. Chang and B. C. Giessen. *Synthetic modulated structures*. Academic Press Inc., 1985.

[228] D. Neerinck et al. “Crossover in the critical field of Pb/Ge multilayers: From single-film to coupled behavior”. In: *Physical Review B* 43.10 (1991), p. 8676.

A. Appendix (I) - Additional Data

A.1. Device overview

An overview of all relevant sample parameters of the devices analyzed in chapter 6 is given in table A.1.

Table A.1.: Overview of samples included in chapter 6. With argon milling duration t_{Ar} either done on the circuit chip before bonding ("flat") or for a circuit chip mounted on a sample holder (custom holder, "c.h."). The rates fluctuated and the final thickness is about 4-6 nm of Pt/Pd. The air exposure time after argon milling is denoted t_{air} and the heating times at 5.6 W and 11 W are denoted $t_{\mathrm{heat1,2}}$. Remarks: *For this chip oxygen plasma was applied and no Ar, **Low discharge current on the Kaufman source, etch rate unknown.

sample	electrode material	t_{Ar} [s]	t_{air} [min]	t_{heat1} [min]	t_{heat2} [min]
NC1 (A12)	Ti, Nb, Pd 5nm, 90nm, 5nm	120* (flat)	>60	-	-
NC2 (MoPdB1)	Ti, Mo, Pd 5nm, 80nm, 10nm	210** (flat)	22	51	30
NC3 (SQUID5B2)	Ti, Nb, Pd 5nm, 90nm, 8nm	90 (flat)	42	30	5.5
SC1 (MoRePd7B1)	Mo, MoRe, Pd 15nm, 41nm, 13nm	70 (c.h.)	1.5	41	30
SC2 (MoRePd8A3)	Mo, MoRe, Pd 15nm, 41nm, 13nm	80 (c.h.)	2	30	45
SC3 (MoRePd8B1)	Mo, MoRe, Pd 15nm, 41nm, 13nm	85 (c.h.)	1.33	45	45
SC4 (MoRePd15A1)	Mo, MoRe, Pd 15nm, 41nm, 13nm	85 (c.h.)	1.1	45	-
SC5 (MoRePt6A3)	Mo, MoRe, Pt 15nm, 41nm, 11nm	105 (c.h.)	3.75	45	45

A.2. Compatibility of RTA with aluminum electrodes

The contact improvement tests have been developed mainly on pure palladium contact electrodes or on niobium electrodes with palladium top layer. For superconducting devices molybdenum rhenium was used as a source of superconductivity. Another promising superconducting material is aluminum, which has also been tested as a contact electrode material. However, it is not compatible with radiative thermal annealing. Despite heating temperatures estimated well below the melting temperature of aluminum bond wires of 25 µm diameter (cf. chapter 5.4.3), the heating clearly affected 400 nm wide aluminum contact electrodes. To test the RTA on aluminum, the lamp heating was performed for several powers for a duration of 30 min each. The dependence of resistance on the lamp

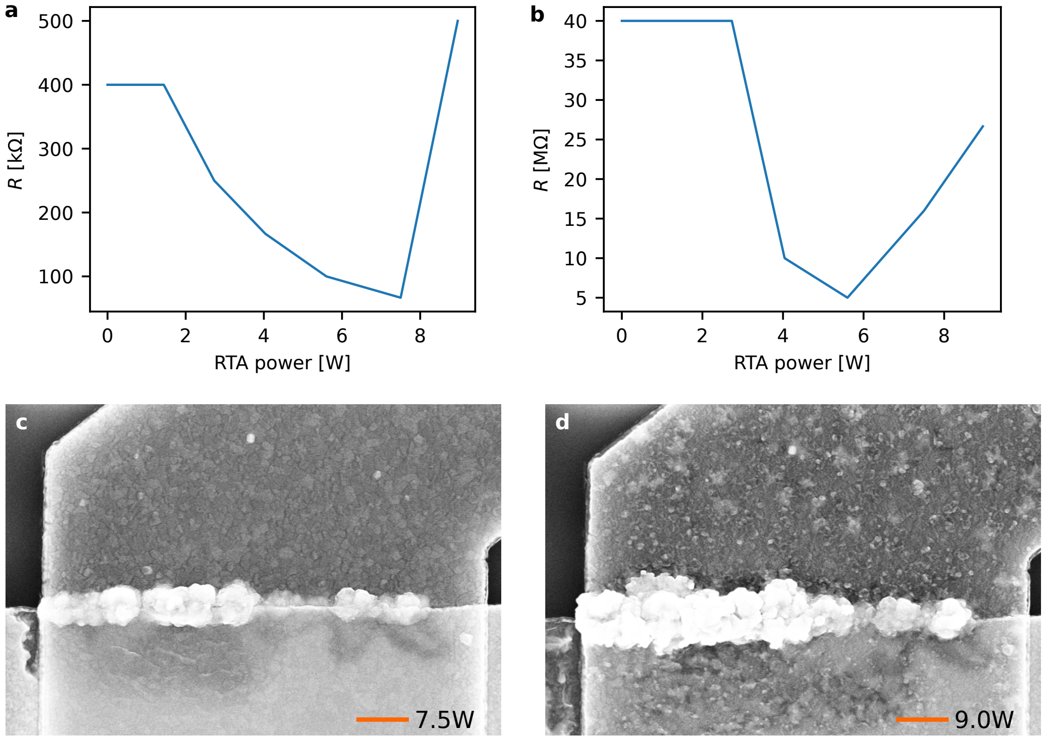

Figure A.1.: Radiative thermal annealing on sample SQUID6A1. With 5 nm Ti, 100 nm Al, 8 nm Pd, 90 *s* Ar milling before microbonding without the custom holder. **a** Device with high device resistance ($V_{\mathrm{sd}} = 1\,\mathrm{V}$). **b** Device with particular high device resistance ($V_{\mathrm{sd}} = 4\,\mathrm{V}$). **c** Scanning electron micrograph of transition from DC lines to nanorcircuits after heating at 7.5 W, orange scale bar: 500 nm. **d** Same region after heating at 9 W.

power was measured after each heating step and is shown in figure A.1a,b. The sample had rather high contact resistances after current-induced annealing which could be decreased by a factor of four with RTA. In contrast to niobium or molybdenum rhenium electrodes, a significant contact improvement could already be observed at a power below 5.6 W. However, heating at powers higher than ∼ 6 W led to a contact deterioration. In the scanning electron micrographs in figure A.1c,d, we can see that the contact deterioration is accompanied by a change in the surface texture of the film. Around a power of 5.6 W, the interface between the gold DC lines and the nanocircuit is modified, and grains start to grow. Between 7.5 W and 9 W the grain size increases but the heating also affects the texture of the surface far from this interface and in the vicinity of the CNT (not shown). It is unclear if the aluminum partially melts or if the texture change is related to diffusion processes of palladium on aluminum or the aluminum itself. In conclusion, the contact deterioration restricts the use of RTA to low heating powers, and therefore, aluminum was discarded as contact electrode material.

A.3. Characterization of MoRe films

In this section we want to present a quick characterization of the superconducting molybdenum rhenium films used in circuit chips. The characterization was performed on a 15 mm × 15 mm chip with the same film thickness as the circuit chip of sample SC5 (transport measurement in chapter 6.3). It consists of 15 nm Mo, 41 nm MoRe, 11 nm Pt on a 500 µm thick silicon substrate covered with 290 nm silicon oxide. The characterization was performed with the van der Pauw method [226] in the PPMS system[1] with a base temperature of 2 K (cf. figure A.2). At 2 K the MoRe film is superconducting and the molybdenum and platinum layers are normal conducting.

The critical temperature of the film is characterized by the resistance drop to zero in figure A.2a and can be extracted to $T_\mathrm{c} = 8.8\,\mathrm{K}$. The angular dependence of the critical magnetic field at 2 K is shown in figure A.2b, where an angle of $\sim 0\,^\circ$ corresponds to a magnetic field parallel to the film and an angle of $90\,^\circ$ corresponds to a magnetic field perpendicular to the film. In general, the dependence of the critical magnetic field on the angle is weak, as expected for thick films. The critical magnetic field parallel to the film is 6.13 T. The critical magnetic field perpendicular to the film has not been measured at 2 K. In the data in figure A.2b we can already see a significant decrease in slope for moderate angles around $30\,^\circ$ and we conservatively estimate the out-of-plane critical magnetic field higher than 5.5 T. Overall, the critical temperature and the critical magnetic field match well with the literature values for pure MoRe films (cf. section 4.4.1).

For an estimation of the superconducting coherence length ξ_0 and to compare it with the thickness of the film, the temperature dependence of the critical magnetic field has been investigated for parallel and perpendicular magnetic field orientation, as shown in figure A.2c. The perpendicular critical magnetic field exhibits a linear temperature dependence. The temperature dependence of the parallel magnetic field cannot be described by a linear relationship that would be expected for a 3D film with thickness d, i.e. the coherence length $\xi_0 \ll d$, and is consistent with the 2D limit ($\xi_0 \gtrsim d$).

In an attempt to estimate the superconducting coherence length, we can fit the slopes and extract the superconducting coherence length based on equations from the Ginzburg-Landau theory [227, 228] with the film thickness d, superconducting coherence length ξ_0, flux quantum Φ_0 and critical temperature T_c

$$B_{\mathrm{c2}\perp} = \frac{\Phi_0}{2\pi\xi_0^2}\left(1 - \frac{T}{T_\mathrm{c}}\right) \tag{A.1}$$

$$B_{\mathrm{c2}||} = \frac{\Phi_0\sqrt{12}}{2\pi\xi_0 d}\sqrt{1 - \frac{T}{T_\mathrm{c}}}. \tag{A.2}$$

---

[1] Physical-Property-Measurement-System, Quantum Design, 10307 Pacific Center Court San Diego, CA 92121 USA

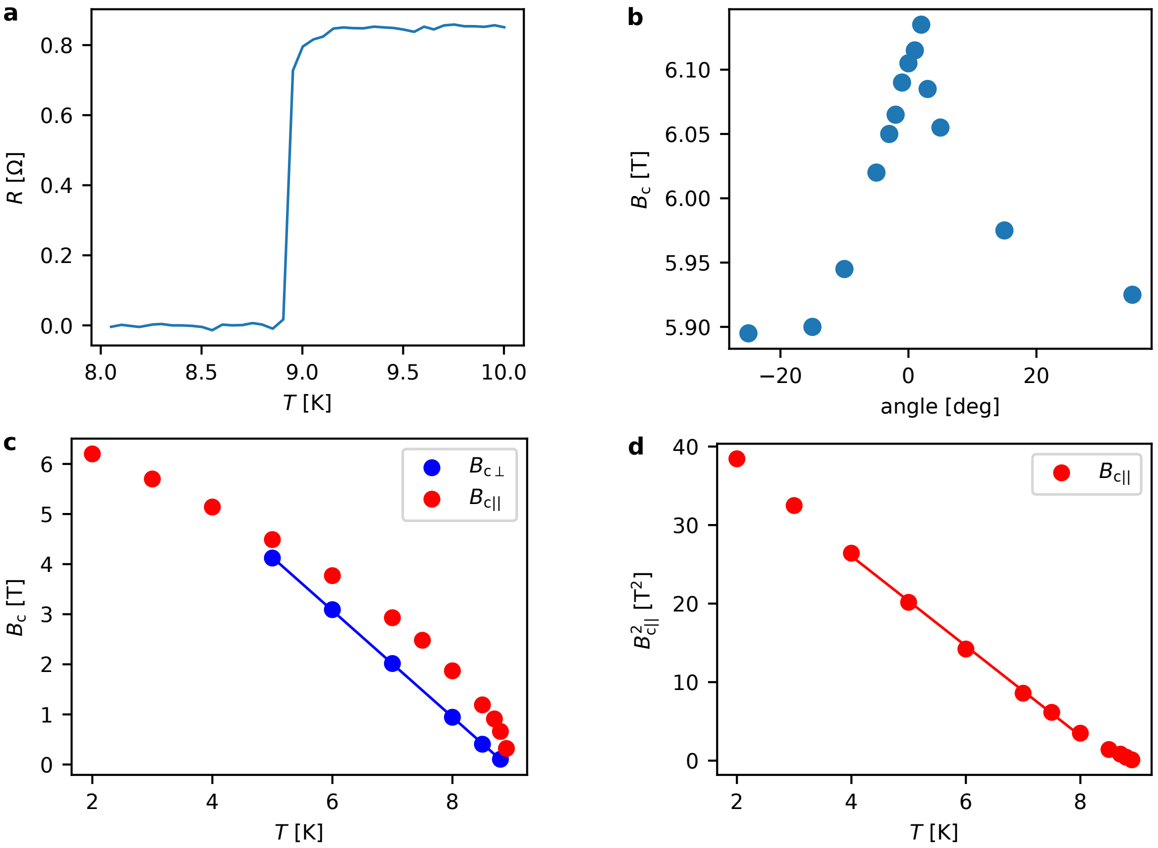

Figure A.2.: Characterization of superconductivity for a Mo+MoRe+Pt film. **a** Critical temperature. **b** Angular dependence of critical magnetic field at 2 K. The magnetic field is parallel to the film at ~ 2 °. **c** Temperature dependence of the critical magnetic field in plane ($B_{c||}$) and out-of-plane ($B_{c_\perp}$) with linear fit for $B_{c\perp}$ (slope: -1.06 ± 0.004 T/K). **d** Linear fit of $(B_{c||})^2$ in the range where 2D film behavior is dominant (slope: -5.72 ± 0.11 T^2/K)

From the fit in figure A.2c with equation A.1 we can calculate the superconducting coherence length for the perpendicular magnetic field to $\xi_0 = 5.8$ nm, which is well below the film thickness of 41 nm.

At this point, it is important to emphasize that the interpretation of the data obtained from the fits is only a rough estimate, since we only considered the simple equations A.1 and A.2. In general, the equations are for a single superconductor and not for a superconducting film sandwiched between two normal conductors. In addition, we neglect a possible anisotropy in the film.

B. Appendix (II) - Fabrication recipes

B.1. CNT growth recipe

Catalyst preparation:

- composition: 352.7 mg $Fe(NO_3)_3 \cdot 9H_2O$, 9.7 mg MoO_2, 192 mg Alumina (Al_2O_3) as catalyst support and 180 ml IPA as solvent
- sonication until the black MoO_2 powder is not visible anymore and storage on a stirring plate

Catalyst deposition: Different techniques have been tested, the most promising will be detailed in following.

- dilute the catalyst in IPA (ratio: 1:8 - 1:16)
- dip and move cantilever chip in the dilution for 10s
- dip in pure IPA for 5s (to make the distribution more homogeneous)
- blow dry with N_2 under an angle of 30 ° to the chip surface
- repeat a few times depending on the desired density

Growth process:

- vent the oven with Ar (0.625 l/min)
- load cantilever chips, pump to $< 10^{-2}$ mbar, stop pumping
- flush the oven with Ar (0.625 l/min) until ambient pressure
- purge lines (Ar 0.625 l/min, CH_4 300 sccm, H_2 300 sccm) for 10 minutes
- pump to $< 10^{-2}$ mbar, stop pumping
- vent oven with Ar (0.625 l/min)
- heat the oven with Ar atmosphere for 30 minutes to 880 °C
- turn off the Ar and flush with H_2 only for 5 minutes
- growth: change the H_2-flow to 50 sccm and turn on the methane flow to 75 sccm (standard recipe, low flow), stop 15 min
- add Ar flow (0.625 l/min), stop CH_4 flow after 15 min, change H_2 flow to 200 sccm, turn off the heater
- open oven at 350 °C, turn off H_2 at 200 °C, stop Ar flow at 90 °C and pump the oven

B.2. Fabrication of normal conducting circuit chips

Marker deposition

Chip preparation

- A 4 inch Si wafer is spin coated with S1818 at 4000 rpm for 60 s and diced with a wafer saw into 20 mm × 20 mm chips.
- cleaning of an individual 20 mm × 20 mm chip
  - resist lifting in acetone (90 °C, 10 min on a hot plate, then ultrasonication power 9, 2 min)
  - changing to a beaker with cold acetone (ultrasonication power 9, 2 min)
  - dip in a beaker with IPA, short rinse for 10 s
  - changing to a new beaker with IPA (ultrasonication power 9, 2 min)
  - blow dry with nitrogen

- oxygen plasma (10 min, 240 W, 25 sccm), Diener low pressure plasma cleaner

Optical lithography

- spin coating (degazing on hotplate at T>100 °C, spin coat AZ5214E at 6000 rpm for 1 min, bake out at 110 °C for 90 s)
- optical exposure through mask (365 nm, 13 mW/cm^2, hard contact, gap 50 µm, 5 s) chip placement with the clamp shadow on the bottom
- development (30 s in AZ MIF726, stop bath 40 s DI Water)

Evaporation

- Kaufman cleaning in Kaufman source (90 s descum at 40 V, 200 V beam voltage, 9 sccm Ar, 1 sccm O_2)
- evaporate 5 nm Ti, 40 nm Au at 0.2 nm/s in the Prevac e-beam evaporator

Lift-off

- lift-off in acetone (90 °C, 10 min on a hot plate, then bubble with a plastic pipette, shake the chip and use the acetone rinsing bottle before moving to the next beaker)
- changing to a beaker with cold acetone (ultrasonication power 9, 2 min, shake the chip for 10 s)
- dip in a beaker with IPA, short rinse for 10 s
- changing to a new beaker with IPA (ultrasonication power 9, 2 min)
- blow dry with nitrogen

Gate lithography

E-beam lithography

- bakeout chip at 185 °C for 3 min
- spin coating: MMA/PMMA copolymer 33%, 4000 rpm, 60 s (for 355 nm thickness) or 6000 rpm, 60 s (for 210 nm thickness), bakeout 3 min, 185 °C
- spin coating: PMMA600K, 4000 rpm, 60 s (for 150-200 nm) or 6000 rpm, 60 s (for 90 nm), bakeout 3 min, 185 °C
- e-beam lithography (dose 500 µC/cm^2, 50 kV)
- development (90 s in Ar600.56, stop bath: 45 s in IPA)

Evaporation

- Kaufman cleaning in Kaufman source (90 s descum at 40 V, 200 V beam voltage, 9 sccm Ar, 1 sccm O_2)
- evaporate 5 nm Ti at 0.2 nm/s, 5 nm Al at 0.2 nm/s, 7 nm AlOx at 0.1 nm/s

Lift-off

- lift-off in acetone (90 °C, 12 min on a hot plate, then bubble with a plastic pipette, shake the chip and use the acetone rinsing bottle before moving to the next beaker)
- changing to a beaker with cold acetone (ultrasonication power 3, 2 min, shake the chip for 10 s)
- changing to a new beaker with IPA (ultrasonication power 3, 2 min)
- blow dry with nitrogen

Contact electrode lithography

E-beam lithography

- bakeout chip at >150 °C for 1 min
- spin coating: MMA/PMMA copolymer 33%, 4000 rpm, 60 s (for 355 nm thickness) or 6000 rpm, 60 s (for 210 nm thickness), bakeout 3 min, 185 °C
- spin coating: PMMA600K, 4000 rpm, 60 s (for 150-200 nm) or 6000 rpm, 60 s (for 90 nm), bakeout 3 min, 185 °C
- e-beam lithography (dose 420 $\mu C/cm^2$, 50 kV)
- development (90 s in Ar600.56, stop bath: 45 s in IPA)

Lift-off

- lift-off in hot NEP overnight (90 °C, then bubble with a plastic pipette, shake the chip and use the acetone rinsing bottle before moving to the next beaker)
- changing to a beaker with hot acetone (90 °C, 10 min, bubble with a pipette)
- changing to a beaker with cold acetone (ultrasonication power 3, 2 min, shake the chip for 10 s)
- changing to a new beaker with IPA (ultrasonication power 3, 2 min)
- blow dry with nitrogen

Trench etching

Optical lithography

- spin coat S1818 at 4000 rpm for 60 s
- bakeout at 115 °C for 60 s
- optical exposure through mask (365 nm, 13 mW/cm^2, hard contact, gap 50 µm, 7 s), pattern: MoRe pattern trench, chip placement with the clamp shadow on the bottom
- development (30 s AZ MIF726, stop bath 30 s Di water), long blow dry from different directions to get rid of all the water

Trench etching

- Reactive ion etching
  - always make sure the chamber pressure p<5e-5 mbar before starting a process
  - 30 min O_2 conditioning to have the Baratron warm up, always adjust the pressure screw before each process
  - SiO_2 etching with CHF_3 (70 W, 18 min, 6 Pa, 50 sccm)
  - 5 min O_2 conditioning
  - SiO_2 etching with CHF_3 (70 W, 18 min, 6 Pa, 50 sccm)
  - conditioning for Bosch process 10 cycles, 25 sccm, 8 Pa (100 W bias for C_4F_8, 200 W bias for SF_6, each step for 20 s)
  - Si trench etching: Bosch process 25 cycles, 25 sccm, 8 Pa (100 W bias for C_4F_8, 200 W bias for SF_6, each step for 20 s)
  - total etch depth about 12-15 µm
- resist stripping
  - lift-off in acetone (90 °C, 20 min on a hot plate), insert the chip in warm acetone beaker, that feels hot when touching and shake it heavily for 30 s before dropping it

  - intense pipette bubbling in hot acetone
  - ultrasonication power 2, 2 min, shake and bubble again
  - rinse with the acetone rinsing bottle
  - change to beaker with cold acetone, ultrasonication power 2, 2 min
  - rinse with acetone rinsing bottle
  - dip in a beaker with IPA, short rinse for 10 s
  - changing to a new beaker with IPA, ultrasonication power 2, 2 min
  - blow dry with nitrogen

Chip dicing

- protective spin coating S1818 at 6000 rpm for 60 s
- bakeout at 80 °C for 5 min
- dicing into 10 small chips per 20 mm × 20 mm chip

Cleanup of individual chips

- clean in acetone (90 °C, 10 min on a hot plate), insert the chip in warm acetone beaker, that feels hot when touching
- ultrasonication power 2, 2 min, shake chip
- rinse with the acetone rinsing bottle
- change to beaker with cold acetone, ultrasonication power 2, 2 min
- dip in a beaker with IPA, short rinse for 10 s
- changing to a new beaker with IPA, ultrasonication power 2, 2 min
- blow dry with nitrogen

Ar milling

- microbond the chip
- Ar milling to remove top few nm in Kaufman source (70 s at 40 V discharge voltage, 200 V beam voltage, 9 sccm Ar, removing 6 nm of Pd, or 90 s for 5 nm of Pt)
- shortest air exposure possible before transfer to SEM vacuum chamber for nanoassembly

B.3. Fabrication of MoRePd/MoRePt circuit chips

MoRePd/Pt sputtering

Chip preparation

- A 4 inch Si wafer is spin coated with S1818 at 4000 rpm for 60 s and diced with a wafer saw into 15 mm × 15 mm chips.
- cleaning of an individual 15 mm × 15 mm chip
  - resist lifting in acetone (90 °C, 10 min on a hot plate, then ultrasonication power 9, 2 min)
  - changing to a beaker with cold acetone (ultrasonication power 9, 2 min)
  - dip in a beaker with IPA, short rinse for 10 s
  - changing to a new beaker with IPA (ultrasonication power 9, 2 min)
  - blow dry with nitrogen
- oxygen plasma (10 min, 240 W, 25 sccm), Diener low pressure plasma cleaner

Sputtering

- transfer chip to homemade sputterer, pumping with primary pump to low 1e-2 mbar, then connect to main chamber
- preheat the chip in the main chamber at 200 °C for 15 min (ramp for 4 min to reach 200 °C (6 A at the current source), reduce to 2.7 A at 180 °C, start timer at 190 °C)
- cooldown below 100 °C perform a presputtering for 2 min with the final powers, then wait for pressure $p<1.5e\text{-}6$ mbar,
- Ar atmosphere for sputtering, flow 7.5 sccm and pressure 0.007 mbar
- sputter 13-15 nm Mo (151 W, 49 s), exact thickness has to be calibrated after each target exchange at the sputter gun
- cosputter 41 nm MoRe for 90 s, Mo (151 W), Re (111 W)
- sputter 13 nm Pd (with RF gun, 75 W forward power, 38 s) or 11 nm Pt (with DC gun, 75 W, increase pressure to 0.0082 mbar before, 37 s Pt)
- cooldown below 70 °C
- storage in vacuum never expose to NEP or DMSO or oxygen plasma again

Marker deposition

Optical lithography

- spin coating (degazing on hotplate at T>100 °C, spin coat S1818 at 6000 rpm for 1 min, bake out at 115 °C for 1 min 15 s)
- optical exposure through mask (365 nm, 13 mW/cm^2, hard contact, gap 40 µm, 7 s), pattern: mask Mo-Re, pattern 2.1, chip placement with the clamp shadow on the bottom
- development (35 s in AZ MIF726, stop bath 30 s DI Water)

Evaporation

- Kaufman cleaning in Kaufman source (60 s descum at 40 V, 200 V beam voltage, 9 sccm Ar, 1 sccm O_2)
- evaporate 5 nm Ti, 40 nm Au at 0.2 nm/s in the Prevac e-beam evaporator

Lift-off

- lift-off in acetone (90 °C, 10 min on a hot plate, then bubble with a plastic pipette, shake the chip and use the acetone rinsing bottle before moving to the next beaker)
- changing to a beaker with cold acetone (ultrasonication power 9, 5 min, shake the chip for 10 s)
- dip in a beaker with IPA, short rinse for 10 s
- changing to a new beaker with IPA (ultrasonication power 9, 2 min)
- blow dry with nitrogen

Negative contact lithography

Optical and e-beam lithography

- bakeout chip at 200 °C for 8 min, 1 min cooldown (to get better resist sticking)
- spin coat ma-N2405 directly afterwards at 3000 rpm for 60 s
- bakeout at 90 °C for 60 s
- e-beam lithography (dose 125 μC/cm^2, 50 kV)
- optical exposure through mask (250 nm filter, 375 W, 0.73 mW/cm^2, constant power (CP-mode), hard contact, gap 40 μm, 20 s), pattern: mask Mo-Re, pattern 2.2, chip placement with the clamp shadow on the bottom
- development (50 s MIF319, moving the chip gently around (this can have an influence on the development), stop bath 50 s DI water), long blow dry from different directions to get rid of all the water
- post exposure bakeout (80 °C for 10 min, after development)

Contact etching

- Ar milling of Pd/Pt (13 nm or more)
  - chip orientation matters: number bottom (away from plasma) or clamp on top facing the plasma
  - Ar milling in Kaufman source (90 s, 50 V discharge, 500 V beam, high discharge current, 10 sccm Ar), angle 45° to the substrate
- Reactive ion etching
  - always make sure the chamber pressure p<5e-5 mbar before starting a process
  - 30 min O_2 conditioning to have the Baratron warm up, always adjust the pressure screw before each process
  - 10 min conditioning: SF_6 15 sccm, Ar 5 sccm, O_2 1 sccm; 2 Pa, 200 W, expect -550 V bias
  - MoRe etching (30 s): SF_6 15 sccm, Ar 5 sccm, O_2 1 sccm; 2 Pa, 200 W, expect -550 V bias
  - 10 min conditioning: O_2 (plasma should change color, yellow to blue-white)
  - 210 s conditioning: 25 sccm CHF_3, 23 sccm Ar, 2 sccm O_2; 150 W, 6 Pa (expect -450 V bias)
  - SiO_2 etching (210 s): 25 sccm CHF_3, 23 sccm Ar, 2 sccm O_2; 150 W, 6 Pa (expect -450 V bias)
  - total etch depth about 220 nm
- resist stripping
  - This step might appear a little exaggerated but it is crucial, as only acetone can be used and the resist does not get removed easily.
  - lift-off in acetone (90 °C, 20 min on a hot plate), insert the chip in warm acetone beaker, that feels hot when touching and shake it heavily for 30 s before dropping it
  - intense pipette bubbling in hot acetone
  - ultrasonication power 9, 6 min, power 5, 2 min and power 2, 2 min, shake and bubble again
  - rinse with the acetone rinsing bottle
  - change to beaker with cold acetone, ultrasonication power 9, 2 min
  - rinse with acetone rinsing bottle
  - dip in a beaker with IPA, short rinse for 10 s
  - changing to a new beaker with IPA (ultrasonication power 9, 2 min)
  - blow dry with nitrogen

Gate lithography

E-beam lithography

- bakeout chip at 185 °C for 5 min
- spin coating: PMMA600K at 2000 rpm, bakeout 3 min, 185 °C
- spin coating: PMMA950K at 6000 rpm, bakeout 3 min, 185 °C
- e-beam lithography (dose 500 μC/cm^2, 50 kV)
- development (60 s in Ar600.56, stop bath: 1 min in IPA)

Evaporation

- Kaufman cleaning in Kaufman source (60 s descum at 40 V, 200 V beam voltage, 9 sccm Ar, 1 sccm O_2)
- load chip at -25° angle and with same chip orientation as for Ar milling
- evaporate 20 nm Ti at 0.2 nm/s and 25 nm Pt at 0.1 nm/s

Lift-off

- lift-off in acetone (90 °C, 20 min on a hot plate, then bubble with a plastic pipette, shake the chip and use the acetone rinsing bottle before moving to the next beaker)
- changing to a beaker with cold acetone (ultrasonication power 5, 2 min, shake the chip for 10 s)
- dip in a beaker with IPA, short rinse for 10 s
- changing to a new beaker with IPA (ultrasonication power 5, 2 min)
- blow dry with nitrogen
- higher sonication power destroys the gates

Trench etching

Optical lithography

- spin coat S1818 at 4000 rpm for 60 s
- bakeout at 115 °C for 60 s
- optical exposure through mask (365 nm, 13 mW/cm^2, hard contact, gap 50 μm, 7 s), pattern: MoRe pattern trench, chip placement with the clamp shadow on the bottom
- development (30 s AZ MIF726, stop bath 30 s DI water), long blow dry from different directions to get rid of all the water

Trench etching

- Reactive ion etching
  - always make sure the chamber pressure $p <$ 5e-5mbar before starting a process
  - 30 min O_2 conditioning to have the Baratron warm up, always adjust the pressure screw before each process
  - SiO_2 etching with CHF_3 (70 W, 18 min, 6 Pa, 50 sccm)
  - 5 min O_2 conditioning
  - SiO_2 etching with CHF_3 (70 W, 18 min, 6 Pa, 50 sccm)
  - Conditioning for Bosch process 10 cycles, 25 sccm, 8 Pa (100 W bias for C_4F_8, 200 W bias for SF_6, each step for 20 s)
  - Si trench etching: Bosch process 25 cycles, 25 sccm, 8 Pa (100 W bias for C_4F_8, 200 W bias for SF_6, each step for 20 s)

    - total etch depth about 12-15 µm
- Resist stripping
    - lift-off in acetone (90 °C, 20 min on a hot plate), insert the chip in warm acetone beaker, that feels hot when touching and shake it heavily for 30 s before dropping it
    - intense pipette bubbling in hot acetone
    - ultrasonication power 2, 2 min, shake and bubble again
    - rinse with the acetone rinsing bottle
    - change to beaker with cold acetone, ultrasonication power 2, 2 min
    - rinse with acetone rinsing bottle
    - dip in a beaker with IPA, short rinse for 10 s
    - changing to a new beaker with IPA, ultrasonication power 2, 2 min
    - blow dry with nitrogen

Chip dicing

- protective spin coating S1818 at 6000 rpm for 60 s
- bakeout at 80 °C for 5 min
- dicing into 6 small chips per 15 mm × 15 mm chip

Cleanup of individual chips

- clean in acetone (90 °C, 10 min on a hot plate), insert the chip in warm acetone beaker, that feels hot when touching
- ultrasonication power 2, 2 min, shake chip
- rinse with the acetone rinsing bottle
- change to beaker with cold acetone, ultrasonication power 2, 2 min
- dip in a beaker with IPA, short rinse for 10 s
- changing to a new beaker with IPA (ultrasonication power 2, 2 min)
- blow dry with nitrogen

Ar milling

- microbond the chip
- Ar milling to remove top few nm in Kaufman source (70 s at 40 V discharge voltage, 200 V beam voltage, 9 sccm Ar, removing 6 nm of Pd, or 90 s for 5 nm of Pt)
- shortest air exposure possible before transfer to SEM vacuum chamber for nanoassembly

C. Acknowledgements

This thesis would not have been possible without the help, guidance, and encouragement of many people at the KIT and outside. As my PhD journey is slowly coming to an end, I would like to take a moment to thank everyone who contributed to this work and made it a fulfilling and unforgettable experience in my life. Special thanks go to:

- Wolfgang Wernsdorfer: Für deine offene, ehrliche und bodenständige Art, die Unterstützung während meiner Zeit in Grenoble und die Möglichkeit den PhD in deiner Gruppe durchführen zu können. Als Doktorvater liegt dir viel an dem Wohl deiner Studenten und trotz der großen Gruppe findet sich immer Zeit, wenn es was zu besprechen gibt. Beeindruckend ist dabei der einfache, intuitive Blick auf die physikalischen Probleme und die experimentelle Intuition.
- Ralph Krupke: Für den tollen wissenschaftlichen Austausch und das Interesse an unserer Arbeit und die Bereitschaft Koreferent dieser Arbeit zu sein.
- Tino Cubaynes: Es hat mir sehr viel Spaß gemacht, unter deiner wissenschaftlichen Betreuung den PhD durchzuführen. Vielen Dank für deine unermüdliche Motivation, perfekte Betreuung und unzähligen Erklärungen und natürlich auch das ausführliche Korrekturlesen dieser langen Arbeit. Ich hoffe, du verstehst mein Deutsch mittlerweile ganz gut. En bref, merci beaucoup!
- Aljoscha Auer: Lange ist es her, aber als ich frisch in die Gruppe kam, hast du mir alles gezeigt und auch später noch sehr viel unterstützt, als Beispiel sag ich nur Prevac... Ich habe die gemeinsamen drei Jahre Zusammenarbeit sehr genossen, geprägt durch viele experimentelle Herausforderungen - in Erinnerung blieb sicherlich die mehr als dreistündige SEM Operation - aber auch der alltägliche Austausch über die Bahn und vieles mehr.
- Sophie Klingel: Für die gemeinsame Zeit und Diskussionen im Büro und deine positive, motivierende Einstellung, auch wenn Dinge mal nicht so laufen wie geplant. Und natürlich die regelmäßige Kuchenlieferung, die die Nachmittagsarbeit immer wieder aufhellt.
- Christoph Sürgers: Deine Erfahrung und dein Wissensschatz sind unglaublich. Egal bei welchem Problem hast du immer einen Tipp parat oder irgendein (altes) Buch, was man sonst nirgends findet. Ohne deine Unterstützung wäre gute Laborarbeit am PHI unmöglich.
- Allen anderen Mitgliedern der CNT Gruppe: Insbesondere Christoph Wassmer für die Zusammenarbeit im Rahmen seiner Masterarbeit. Ebenso Niklas Martin während seiner Bachelorarbeit und das nervige Debuggen des Renishaw Raman Mikroskops. Ebenfalls nicht fehlen dürfen Mika und Svenja und Rainer auch wenn er offiziell nicht zur Untergruppe gehörte. Die Diskussionen und der Austausch haben aber trotzdem zur schönen Atmosphäre im Büro beigetragen.
- Der ganzen AG für die schöne, unvergessliche Zeit, insbesondere während der Pandemie, aber auch während der BBQs und Volleyballspiele. Viele haben aber auch direkt oder indirekt zum Projekt beigetragen. Besonderer Dank geht an Luca für das Bereitstellen von Plotting Skripten und der Unterstützung bei Maschinen und Spulenwickeln. Ebenfalls möchte ich mich bei Ioannis bedanken, der tatsächlich der einzige ist, der mich vom Beginn des Studiums vor über zehn Jahren bis zur Vollendung dieses PhDs begleitet hat. Vielen Dank für die

schöne gemeinsame Zeit und das gemeinsame Meistern vieler Herausforderungen von Theo Blättern bis hin zum PhD.

- Reinraumteam: Ohne das ständige Engagement und die Unterstützung des NSL Teams wäre die Probenherstellung nie erfolgreich verlaufen. Besonderer Dank geht an Silvia Diewald für die Geduld und Expertise bei der E-beam Lithografie und Unterstützung in allgemeinen Fragen und Lucas Radtke und Aina Quintilla für die Hilfsbereitschaft, den Austausch und die Unterstützung. Zusammen mit den anderen Leuten im Reinraum sorgt ihr tagtäglich für eine sehr angenehme Arbeitsatmosphäre im Reinraum. Neben vielen anderen muss ich hier auch noch Urs Strobel danke sagen. Es war immer schön, sich im Reinraum zu begegnen. Der Austausch über diverse Fabrikationsprobleme oder zum Zeitvertreib während Wartezeiten war immer eine willkommene Abwechslung.

- Di Wang und dem KNMF für die TEM Messungen und C12QE für die Zusammenarbeit bei den Raman Messungen.

- Der Feinmechanik- und Elektronikwerkstatt für alle möglichen Teile ohne die unsere Experimente nicht möglich wären. Besonderer Dank geht an Jannis Ret und Kevin Zych für das (sehr nervige) Löten der PCBs.

- Unserem He-Man Michael Pfirrmann für die Heliumverflüssigung, aber auch für die Modernisierung der Abläufe in der Heliumhalle und die Erhöhung der Benutzerfreundlichkeit, die sich schnell bemerkbar machte.

- Der Hector Fellow Academy: Für die Finanzierung des Großteils des PhDs und die unbeschreibliche, nette Atmosphäre innerhalb der Academy. Die Netzwerkevents und Workshops waren einzigartig und sind natürlich nicht ohne immensen organisatorischen Aufwand zu bewerkstelligen. Vielen Dank dafür an das ganze HFA Team und insbesondere an Stefanie und Sylvia.

- KSQM: Für die Workshops und einzigartigen Retreat Meetings.

- Der KIT SC Laufgruppe: Als ich beigetreten bin in der Mitte meines PhDs hätte ich nie gedacht, dass Laufen mein Leben so prägen würde und eine neue Leidenschaft bekommen sollte. Ihr alle trägt dazu bei, dass aus einem Einzelsport ein Teamsport wird und nur wenn man mal verletzt war weiß man, was das genau bedeutet. Hier geht besonderer Dank an Jannik, ohne den meine Laufkarriere schnell vorbei gewesen wäre, aber auch an Jonas Kämmerer, nicht nur für die Zeit in unserer AG aber auch dafür, dass du mich motiviert hast mit dem Laufen richtig anzufangen.

- Der Mountainbikegruppe des KITs: Auch wenn sich mein Fokus auf Laufen geändert hat, werde ich nie die gemeinsamen Touren, Stammtische und Abenteuer im Schwarzwald und der Pfalz vergessen, die ich nach wie vor fest mit meiner Zeit in Karlsruhe verbinde.

- Allen Personen, die maßgeblich dazu beigetragen haben, den Lebensweg als Physiker einzuschlagen und diese Promotion so erst ermöglicht haben. Allen voran meinem Oberstufenphysiklehrer Herr Tenzer. Man unterschätzt immer schnell welchen Einfluss gute Schulbildung auf den weiteren Lebensweg hat. Merci beaucoup également à Jérémie Viennot und Franck Balestro für die unvergessliche Zeit in Grenoble, die mich motiviert hat, physikalische Forschung in einem ähnlichen Bereich im PhD fortzusetzen.

- Meinen geschätzten Freunden außerhalb des KITs, die großteils schon mehr als die Hälfte meines Lebens prägen, mich unterstützen und auch während des PhDs dazu beigetragen haben, diese Lebensphase einzigartig zu machen. Ihr alle seid es wert, erwähnt zu werden, aber eine Erwähnung jedes Einzelnen würde den Rahmen dieser Danksagung sprengen.

- Meiner Familie, die mich bei allen Schwierigkeiten und ohne wirklich zu verstehen, an was ich forsche, immer unterstützt hat.